COLLECTED PAPERS on Dressed Photon Science and Technology

Vol. 26

August 2010 – July 2011

Prof. Motoichi OHTSU

MEMBERS

(From April 1, 2011)

*[I] The University of Tokyo**

Professor

Motoichi OHTSU(a-d) (Dr. Eng.)

Associate Professor

Takashi YATSUI (Dr. Eng.)

Researcher

Makoto NARUSE (Dr. Eng.)
Senior Researcher, National Institute of Information and Communications Technology (NICT)

Graduate Students (Doctor Candidate)

Yang LIU
Ryoma OYAMA

Graduate Students (Master Course)

Takuro HAYASHI
Kazunori IIJIMA
Takahiro MOCHIZUKI
Fumihiro MORIGAKI
Kosuke NAKANISHI
Hajime TANAKA
Hironao TANOUCHI

Undergraduate Students

Jiang MING
Siddharth SHANKAR
Naoki WADA

Manager

Kazuhiko TAMAKI

Secretary

Sachiyo KOJIMA

a) Also a director "Nanophotonics Research Center, The Institute of Engineering Innovation, School of Engineering The University of Tokyo"
b) Also a director, "Preparatory research phase, Research and Development Program of Innovative Energy Efficiency Technology, and NEDO (New Energy and Industrial Technology Development Organization)
c) Also a director, " Exploratory research phase, Research and Development Program of Innovative Energy Efficiency Technology, and NEDO (New Energy and Industrial Technology Development Organization)
d) Also a director, NPO-Research Institute of Nanophotonics

(*)
Department of Electronics Engineering and Information Systems,
Graduate School of Engineering,
The University of Tokyo
(Room 215, Bldg. Eng. 9)
2-11-16 Yayoi, Bunkyo-ku, Tokyo 113-8656, Japan
Phone: +81-3-5841-1189
FAX: +81-3-5841-1140
E-mail: ohtsu@ee.t.u-tokyo.ac.jp
URL:http://uuu.t.u-tokyo.ac.jp/

東京大学大学院 工学系研究科 電気系工学専攻
〒113-8656 東京都文京区弥生 2-11-16 工学部 9 号館 215 号室
電話: 03-5841-1189, ファックス: 03-5841-1140
E-mail: ohtsu@ee.t.u-tokyo.ac.jp
URL: http://uuu.t.u-tokyo.ac.jp/

*[II] Preparatory research phase, Research and Development Program of Innovative Energy Efficiency Technology, NEDO project**

Professor

Motoichi OHTSU	(Dr. Eng.)

Associate Professor

Takashi YATSUI	(Dr. Eng.)

Researchers

Tadashi KAWAZOE	(Dr. Sci.)
Wataru NOMURA	(Dr. Eng.)
Naoya TATE	(Dr. Info. Sci.)

Research Assistant

Ayako MIZUSHIMA

Secretary

Kumiko NOZAWA

(*)
Department of Electronics Engineering and Information Systems,
Graduate School of Engineering,
The University of Tokyo
(Room 219, Bldg. Eng. 9)
2-11-16 Yayoi, Bunkyo-ku, Tokyo 113-8656, Japan
Phone: +81-3-5841-1670
FAX: +81-3-5841-1140
E-mail: info@ nanophotonics.t.u-tokyo.ac.jp
URL: http://uuu.t.u-tokyo.ac.jp/

東京大学大学院 工学系研究科 電気系工学専攻
〒113-8656 東京都文京区弥生2-11-16 工学部9号館219号室

電話：+81-3-5841-1670, ファックス: +81-3-5841-1140
E-mail: info@ nanophotonics.t.u-tokyo.ac.jp
URL: http://uuu.t.u-tokyo.ac.jp/

*[III] Exploratory research phase, Research and Development Program of Innovative Energy Efficiency Technology, NEDO project**

Professor

Motoichi OHTSU (Dr. Eng.)

Associate Professor

Takashi YATSUI (Dr. Eng.)

Researcher

Kokoro KITAMURA (Dr. Eng.)

Research Assistant

Etsuko OTA

Secretary

Toshiko TERADA

(*)
Department of Electronics Engineering and Information Systems,
Graduate School of Engineering,
The University of Tokyo
(Room 219, Bldg. Eng. 9)
2-11-16 Yayoi, Bunkyo-ku, Tokyo 113-8656, Japan
Phone: +81-3-5841-1670
FAX: +81-3-5841-1140
E-mail: info@ nanophotonics.t.u-tokyo.ac.jp
URL: http://uuu.t.u-tokyo.ac.jp/

東京大学大学院 工学系研究科 電気系工学専攻
〒113-8656 東京都文京区弥生 2-11-16 工学部 9 号館 219 号室
電話：+81-3-5841-1670, ファックス: +81-3-5841-1140
E-mail: info@ nanophotonics.t.u-tokyo.ac.jp
URL: http://uuu.t.u-tokyo.ac.jp/

*[IV]Nanophotonics Research Center**

Director

Motoichi OHTSU, Professor (core member)

Members

Kazuo HOTATE, Professor (core member)
Hitoshi TABATA, Professor (core member)
Masaki TANAKA, Professor (core member)
Takao SOMEYA, Professor
Shinji YAMASHITA, Professor
Zuyuan HE, Project Professor
Yuichiro KATO, Associate Professor
Shinobu OHYA Associate Professor
Masakazu SUGIYAMA, Associate Professor
Takashi YATSUI, Associate Professor
Munetoshi SEKI, Assistant Professor
Masanori KUBOTA, Assistant Professor
Makoto NARUSE, Senior Researcher, (NICT)
Tadashi KAWAZOE, Researcher
Kokoro KITAMURA, Researcher
Wataru NOMURA, Researcher
Naoya TATE, Researcher

(*)
Institute of Engineering Innovation,
School of Engineering, The University of Tokyo
(Room 219, Bldg. Eng. 9)
2-11-16 Yayoi, Bunkyo-ku, Tokyo 113-8656, Japan
Phone: +81-3-5841-1670
FAX: +81-3-5841-1140
E-mail: info@ nanophotonics.t.u-tokyo.ac.jp
URL: http://www.npc.t.u-tokyo.ac.jp/

東京大学大学院 工学系研究科　総合研究機構
〒113-8656 東京都文京区弥生 2-11-16 工学部 9 号館 219 号室

電話：+81-3-5841-1670, ファックス: +81-3-5841-1140
E-mail: info@ nanophotonics.t.u-tokyo.ac.jp
URL: http://www.npc.t.u-tokyo.ac.jp/

*[V] Research Institute of Nanophotonics**

Director

Motoichi OHTSU

(*)
Research Institute of Nanophotonics,
Nonprofit Organization
1-20-10 Sekiguchi, Bunkyo-ku, Tokyo 112-0014, Japan
Phone: +81-3-5225-6432. Fax: +81-3-5225-6435
E-mail: ohtsu-rinps@nanophotonics.t.u-tokyo.ac.jp
URL: http://www.nanophotonics.info/

特定非営利法人 ナノフォトニクス工学推進機構
〒112-0014 東京都文京区関口 1-20-10
電話: 03-5225-6432, ファックス: 03-5225-6435
E-mail: ohtsu-rinps@nanophotonics.t.u-tokyo.ac.jp
URL: http://www.nanophotonics.info/

LIST OF PAPERS

[(pp. XX-XX); pages in this issue of the COLLECTED PAPERS]

[I] ORIGINAL PAPERS

[1] T. Yatsui, K. Hirata, Y. Tabata, Y. Miyake, Y. Akita, M. Yoshimoto, W. Nomura, T. Kawazoe, M. Naruse, and M. Ohtsu, "Self-organized near-field etching of the sidewalls of glass corrugations," Appl. Phys. B- Lasers and Optics, Vol. 103, No. 3, June 2011, pp. 527-530.

(pp. 1-4)

[2] T. Kawazoe, M. Ohtsu, S. Aso, Y. Sawado, Y. Hosoda, K. Yoshizawa, K. Akahane, N. Yamamoto, and M. Naruse, "Two-dimensional array of room-temperature nanophotonic logic gates using InAs quantum dots in mesa structures," Appl. Phys. B- Lasers and Optics, Vol. 103, No. 3, June 2011, pp. 537-546.

(pp. 5-14)

[3] K. Akahane, N. Yamamoto, M. Naruse, T. Kawazoe, T. Yatsui, and M. Ohtsu, "Energy Transfer in Multi-Stacked InAs Quantum Dots," Jap. J. Appl. Phys., Vol. 50, No.4, April 2011, pp. 04DH05 1-4.

(pp. 15-18)

[4] Y. Liu, T. Morishima, T. Yatsui, T. Kawazoe, and M. Ohtsu, "Size control of sol-gel-synthesized ZnO quantum dots using photo-induced desorption," Nanotechnology, Vol. 22, No. 21, March 2011, pp. 215605 1-5.

(pp. 19-23)

[5] M. Naruse, H. Hori, K. Kobayashi, T. Kawazoe, and M. Ohtsu, "Optical pulsation mechanism based on optical near-field interactions," Appl. Phys. B- Lasers and Optics, Vol. 102, No. 4, March 2011, pp. 717-723.

(pp. 25-31)

[6] J. Lin, A. Mohammadizia, A. Neogi, H. Morkoc, and M. Ohtsu, "Surface plasmon enhanced UV emission in AlGaN/GaN quantum well," Appl. Phys. Lett., Vol. 97, No. 22, December 2010, pp. 221104 1-3.

(pp. 33-35)

[7] S. Schmidt, M. Mascheck, M. Silies, T. Yatsui, K. Kitamura, M. Ohtsu, and C.

Lienau, "Distinguishing between ultrafast optical harmonic generation and multi-photon-induced luminescence from ZnO thin films by frequency-resolved interferometric autocorrelation microscopy," Optics Express, Vol. 18, Issue 24, November 2010, pp. 25016-25028.

(pp. 37-49)

[8] M. Naruse, H. Hori, K. Kobayashi, P. Holmström, L. Thylén, and M. Ohtsu, "Lower bound of energy dissipation in optical excitation transfer via optical near-field interactions," Opt. Express, Vol. 18, No. S4, November 2010, pp. A544-A553.

(pp. 51-60)

[9] M. Naruse, E. Runge, K. Kobayashi, and M. Ohtsu, "Efficient optical excitation transfer in layered quantum dot nanostructures networked via optical near-field interactions," Phys. Rev. B, Vol. 82, No. 12, September 2010, pp. 125417 1-8.

(pp. 61-68)

[10] T. Yatsui, K. Hirata, Y. Tabata, W. Nomura, T Kawazoe, M. Naruse, and M. Ohtsu, "*In situ* real-time monitoring of changes in the surface roughness during nonadiabatic optical near-field etching," Nanotechnology, Vol. 21, No. 35, August 2010, pp. 355303 1-5.

(pp. 69-73)

[II] PRESENTATIONS IN INTERNATIONAL CONFERENCES

[1] T. Yatsui, W. Nomura, and M. Ohtsu, “Nanophotonic Polishing of Substrate for Application to Hard-Disk and Optical-Disk Processing,” Technical Digest of Joint International Symposium on Optical Memoroy & Optical Data Storage (ISOM/ODS 2011), Optical Society of America, Washington D. C., USA, July 17-20, 2011, Kauai, HI, USA, paper number OTuA1.
[Invited presentation]

(pp. 75-76)

[2] Y. Liu, T. Yatsui, T. Kawazoe, and M. Ohtsu, “Controlling the size and variance of ZnO quantum dot using photo-assisted Sol-Gel method,” Program & Abstract of 5th TU-SNU-UT Joint Symposium, Beijing, China, June 7-8, 2011, p. 57.

(p. 77)

[3] T. Yatsui, W. Nomura, and M. Ohtsu, “Nanophotonic etching of glass substrate for A-scale surface roughness,” Abstract of the 12th International Symposium on Laser Precision Microfabrication (LPM2011), Japan Laser Processing Society, Tokyo, Japan, June 7-10, 2011, Takamatsu, Kagawa, Japan, paper number Fr2-I-1.
[Invited presentation]

(p. 79)

[4] A. Ishikawa, T. Yatsui, K. Kobayashi, M. Ohtsu, J. Yoo, G.-C. Yi, and H. Ishihara, “Theory of Superradiance by Nano-Array of Quantum-Well Dots,” Abstract of The European Conference on Lasers and Electro-Optics and the XIIth European Quantum Electronics Conference (CLEO/EUROPE-EQEC 2011), European Physical Society, Mulhouse, France, May 22-26, 2011, Munich, Germany, paper number CK.P.14 TUE.

(p. 81)

[5] M. Naruse, H. Hori, K. Kobayashi, T. Kawazoe, and M. Ohtsu “Optical Pulsation Based on Near-Field Interactions at the Nanoscale by Continuous-Wave Light Excitation,” Proceedings of 2011 ICO International Conference on Information Photonics (IP2011), IEEE, NJ, USA, May 18-20, 2011, Ottawa, Canada, paper number SIPN-18-1-4.

(pp. 83-84)

[6] N. Tate, W. Nomura, M. Naruse, T. Kawazoe, T. Yatsui, M. Hoga, Y. Ohyagi, Y. Sekine, H. Fujita, and M. Ohtsu, “Demonstration of Modulatable Nanophotonics based on modulatable optical near-field interactions between dispersed quantum dots,” Proceedings of 2011 ICO International Conference on Information Photonics (IP2011), IEEE, NJ, USA, May 18-20, 2011, Ottawa, Canada, paper number

PI-19-1-5.

(pp. 85-86)

[7] K. Kitamura, T. Yatsui, H. Yasuda, T. Kawazoe, and M. Ohtsu, “Visible light hydrogen generation using ZnO nanorods in a phonon-assisted optical near-field process, ,” Abstract of European Materials Research Society Spring Meeting 2011 (E-MRS Spring Meeting 2011), European Materials Research Society, Strasbourg, France, May 9-12, 2011, Nice, France, paper number 14-8.

(p. 87)

[8] T. Yatsui, Y. Liu, and M. Ohtsu, “Optimizing the energy transfer between near-field optically coupled ZnO quantum dots,” Abstract of European Materials Research Society Spring Meeting 2011 (E-MRS Spring Meeting 2011), European Materials Research Society, Strasbourg, France, May 9-12, 2011, Nice, France, paper number 11-1.

(p. 89)

[9] Y. Liu, T. Yatsui, and M. Ohtsu, “Size control of sol-gel-synthesized ZnO quantum dots using photo-assisted desorption,” Abstract of European Materials Research Society Spring Meeting 2011 (E-MRS Spring Meeting 2011), European Materials Research Society, Strasbourg, France, May 9-12, 2011, Nice, France, paper number C-2.

(p. 91)

[10] T. Yatsui and M. Ohtsu, “Self-Organized Nanophotonic Device,” Abstract of 219th Electrochemical Society Meeting (219th ECS Meeting), Electrochemical Society, Pennington, NJ, USA, May 1-6, 2011, Montreal, QC, Canada, paper number 1265. **[Invited presentation]**

(p. 93)

[11] M. Naruse, F. Peper, K. Leibnitz, K. Akahane, N. Yamamoto, W. Nomura, T. Kawazoe, T. Yatsui, M. Murata, and M. Ohtsu, “Autonomous Excitation Transfer in Quantum Dot Mixtures via Network of Optical Near-Field Interactions at the Nanoscale,” Proceedings of The 30th IEEE Internacional Conference on Computer Communications Workshops (IEEE Infocom 2011), April 10-15, 2011, Shanghai, China , pp. 490-494.

(pp. 95-99)

[12] N. Tate, M. Naruse, T. Yatsui, T. Kawazoe, M. Hoga, Y. Ohyagi, T. Fukuyama, Y. Sekine, M. Kitamura, and M. Ohtsu, “Nanophotonic Hierarchical Hologram: Hierarchical information processing and nanometric data retrieval based on nanophotonics,” Proceedings of SPIE, Practical Holography XXV: Materials and Applications (Photonics West 2011), SPIE, Bellingham, WA, USA, January 23-26,

2011, San Fransisco, CA, USA, 7957-22.

(pp. 101-108)

[13] T. H. H. Le, K. Mawatari, K. Kitamura, T. Yatsui, T. Kawazoe, M. Ohtsu, and T. Kitamori, “Investigation of Phonon-assisted Optical Near-field Effect on Nanostructured TiO_2 Thin Film,” Abstract of 2010 International Chemical Congress of Pacific Basin Societies (PACIFICHEM 2010), American Chemical Society, Washington D. C., USA, December 15-20, 2010, Honolulu, HI, USA, paper number 435.

(p. 109)

[14] K. Mawatari, N. Hasumoto, K. Kitamura, T. Yatsui, T. Kawazoe, M. Ohtsu, and T. Kitamori, “Development of local surface-modification method for fluidic control in extended-nano space using nanopillar and optical near-field,” Abstract of 2010 International Chemical Congress of Pacific Basin Societies (PACIFICHEM 2010), American Chemical Society, Washington D. C., USA, December 15-20, 2010, Honolulu, HI, USA, paper number 456.

(pp. 111-112)

[15] T. Yatsui and M. Ohtsu, , “Increased Spatial Homogeneity in a Light-Emitting InGaN Thin Film Using a Phonon-Assisted Optical Near-Field Process,” Proceedings of The 17th International Display Workshops (IDW’10), The Institute of Image Information and Television Engineers, Tokyo, Japan, December 1-2, 2010, Fukuoka, Japan, pp. 1619-1622, paper number MEET5-1.
[Invited presentation]

(pp. 113-115)

[16] M. Ohtsu, “Nanophotonics: Dressed photon science and technology,” Book of Abstracts France-Japan Workshop on Nanophotonics, November 4-5, 2010, Paris, France, p. 1.
[Invited presentation]

(p. 117)

[17] T. H. H. Le, K. Mawatari, K. Kitamura, T. Yatsui, T. Kawazoe, M. Ohtsu, T. Kitamori, “Investigation of phonon-assisted optical near-field Excitation on nanostructured TiO_2 towards on-chip fuel cell application,” Abstracts, The 14th International Conference on Miniaturized Systems for Chemistry and Life Sciences (μTAS2010), The Chemical and Biological Microsystems Society, San Diego, CA , USA, October 3-7, 2010, Groningen, The Netherlands, paper number W12E.

(pp. 119-121)

[18] M. Ohtsu, “Nanophotonics: Dressed photon science and technology,” Abstracts of 3rd German-Japanese Seminar on Nanophotonics, September 26-29, 2010, Ilmenau,

Germany, p. 1.
[Invited presentation]

(p. 123)

[19] K. Akahane, N. Yamamoto, M. Naruse, T. Kawazoe, T. Yatsui, and M. Ohtsu, "Energy Transfer in Multi-Stacked InAs Quantum Dots," Extended Abstracts of the 2010 International Conference on Solid State Devices and Material s (SSDM 2010), The Japan Society of Applied Physics, Tokyo, Japan, September 22-24, 2010, Tokyo, Japan, pp. 1281-1282.

(pp. 125-126)

[20] D. Leipold, M. Maschek, S. Schmidt, M. Silies, T. Yatsui, K. Kitamura, and M. Ohtsu, "Photon modes and second harmonic generation in ZnO nano-needle arrays," Abstracts, The International Workshop on Nonlinear Optics and Excitation Kinetics in Semiconductors 10 (NOEKS 10), German Research Foundation, Bonn, Germany, August 16, 2010, Paderborn, Germany, paper number 71.

(p. 127)

[21] M. Naruse, H. Hori, K. Kobayashi, and M. Ohtsu, "Minimum Energy Dissipation in Signal Transfer via Optical Near-Field Interactions in the Subwavelength Regime," Proceedings of the 36th European Conference on Optical Communication (ECOC), IEEE, NJ, USA, September 19-23, 2010, Torino, Italy, paper number Mo. 1.E.5.

(pp. 129-131)

[22] M. Ohtsu, "Phonon-assisted nanophotonic fabrication and its application," Book of Abstracts The seventh International Conference on Photo-Excited Processes and Applications (ICPEAP7), August 16-20, 2010, Copenhagen, Denmark, Invited 7, p. 19.
[Invited presentation]

(p. 133)

[23] M. Naruse, N. Tate, and M. Ohtsu, "Information theoretical aspects innanophotonics," Proceedings, SPIE Optics + Photonics 2010, August 1-5, 2010, San Diego, CA, USA, paper number 7757-75.
[Invited presentation]

(pp. 135-136)

[III] REVIEW PAPERS

[1] T. Yatsui and M. Ohtsu, “Nanophotonic Device Using ZnO Nanostructures,” The Review of Laser Engineering, Vol. 39, No.3, March, 2011, pp. 184-187.

【八井崇、大津元一、「ZnO ナノ構造のナノフォトニックデバイスへの応用」、『レーザー研究』、第 39 巻、第 3 号、2011 年 3 月、pp. 184-187】

(pp. 137-140)

[2] M. Ohtsu, “Room-Temperature operated nanophotonic basic devices,” O plus E, Vol. 32, No.12, December, 2010, pp. 1393-1394.

【大津元一、「ついに室温動作したナノフォトニック論理ゲートデバイス」ー一枚の写真ー、『O plus E』、第 32 巻、第 12 号、2010 年 12 月、pp. 1393-1394】

(pp. 141-142)

[3] T. Yatsui and M. Ohtsu, “Nano-Scale Fabrication Using Optical-Near-Field,” The Journal of the Society of Photographic Science and Technology of Japan (JSPSTJ), Vol. 73, No. 6, December, 2010, pp. 297-302.

【八井崇、大津元一、「近接場光を利用した新しい光励起によるナノ材料加工技術」、『日本写真学会誌』、第 72 巻、第 6 号、2010 年 12 月、pp. 297-302】

(pp. 143-148)

[4] M. Naruse, T. Kawazoe, and M. Ohtsu, “Nanophotonics for Energy Applications,” Kogaku Japanese Journal of Optics, Vol. 39, No.10, October, 2010, pp. 476-481.

【成瀬誠、川添忠、大津元一、「低消費エネルギーを実現するナノフォトニクス技術」、『光学』、第 39 巻、第 10 号、2010 年 10 月、pp. 476-481】

(pp. 149-154)

[IV] PUBLISHED BOOKS

[1] G.-C. Yi, T. Yatsui, and M. Ohtsu, “ZnO Nanorods and their Heterostructures for Electrical and Optical Nanodevice Applications,” in *Comprehensive Nanoscience and Technology* Vol. 6, D. Andrews, G. Scholes, and G. Wiederrecht ed., Maryland Heights, November, 2010, pp. 335-374.

(pp. 155-156)

[2] T. Yatsui and M. Ohtsu, “Nanophotonics for Device Operation and Fabrication,” *Handbook of Nanophotonics,* chapter 35, K. D. Sattler ed., CRC Press (Tailor & Francis Group), Boca Raton, September, 2010, pp. 35-1 - 35-13.

(pp. 1157-161)

[VI] AWARDS

M. Ohtsu, Distingnished Service Award, Optoelectronics Industry and Technology Development Association, December 17, 2010.
大津元一，創立 30 周年記念功労者表彰，財団法人光産業技術振興協会，2010 年 12 月 7 日

[I] ORIGINAL PAPERS

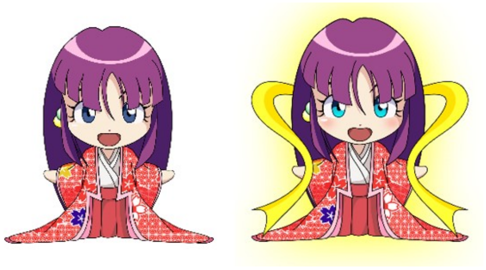

Appl Phys B (2011) 103:527–530
DOI 10.1007/s00340-011-4569-1

Applied Physics B
Lasers and Optics

RAPID COMMUNICATION

Self-organized near-field etching of the sidewalls of glass corrugations

T. Yatsui · K. Hirata · Y. Tabata · Y. Miyake · Y. Akita · M. Yoshimoto · W. Nomura · T. Kawazoe · M. Naruse · M. Ohtsu

Received: 9 April 2011 / Published online: 15 May 2011

Abstract Using soda-lime glass with a nano-stripe pattern as a test specimen, we demonstrated self-organized near-field etching with a continuum-wave laser (λ = 532 nm) light source. Atomic force microscopy confirmed that near-field etching decreases the flank roughness of the corrugations as well as the roughness of the flat surface.

1 Introduction

Reduction of surface roughness (R_a) to less than 1 Å is necessary to minimize light-scattering loss in various applications, such as high-quality, extreme-UV optical components, high-power lasers, and ultra-short pulse lasers [1]. Although chemical-mechanical polishing (CMP) has been used for flattening the surfaces [2], its capacity for reducing the surface roughness R_a is limited to about 2 Å, where the value of R_a is an arithmetical average of the absolute values of the surface height deviations, measured from the best-square fitted plane. This limitation on the reduction of R_a originates with the polishing pad roughness values being as large as 10 µm, and polishing particle diameters as large as 100 nm in the slurry. To overcome this limitation, we have developed a non-contact, self-organized method of near-field etching, utilizing a phonon-assisted photochemical reaction [3–7], which has been successfully applied to reduce the value of R_a to as little as 1.36 Å [3]. To selectively etch away protrusions on a silica surface, a continuum-wave (CW) laser (λ = 532 nm) is used to dissociate the Cl_2 gas. Since this photon energy is lower than the absorption band edge energy of Cl_2 (λ = 400 nm) [8], the conventional Cl_2 adiabatic photochemical reaction is avoided. However, on a nanometer scale rough surface, an optical near-field is also generated. This optical near-field then excites the multiple-mode phonon state. As a result, a quasi-particle, known as a localized exciton-phonon polariton (EPP) [6], is created by the coupling between the optical near-field and multiple phonons. Since this quasi-particle has higher photon energy than that of the incident light photon, it is able to excite a higher molecular vibrational state [5, 6]. Hence, Cl_2 is selectively photo-dissociated to generate radical Cl* atoms (Fig. 1(a)), which etch away the surface roughness. The etching begins automatically when the surface is illuminated by the light, and it proceeds in a self-organized manner. It also ceases automatically when the surface becomes flat enough to stop generating EPP (Fig. 1(b)).

In addition to possessing this unique organizing property, near-field etching is a non-contact method (thus eliminating the need for polishing pads), with anticipated applications to various three-dimensional surfaces, including concave and

---

T. Yatsui (✉) · W. Nomura · T. Kawazoe · M. Naruse · M. Ohtsu
School of Engineering, The University of Tokyo, Bunkyo-ku,
Tokyo 113-8656, Japan
e-mail: yatsui@ee.t.u-tokyo.ac.jp

T. Yatsui · W. Nomura · T. Kawazoe · M. Naruse · M. Ohtsu
Nanophotonics Research Center, The University of Tokyo,
2-11-16 Yayoi, Bunkyo-ku, Tokyo 113-8656, Japan

K. Hirata · Y. Tabata
SIGMA KOKI Co., Ltd., 1-19-9 Midori, Sumida-ku, Tokyo
130-0021, Japan

Y. Miyake · Y. Akita · M. Yoshimoto
Department of Innovative and Engineered Materials, Tokyo
Institute of Technology, 4259-J2-46 Nagatsuta, Midori-ku,
Yokohama, Kanagawa 226-8503, Japan

M. Naruse
National Institute of Information and Communications
Technology, 4-2-1 Nukui-kita, Koganei, Tokyo 184-8795, Japan

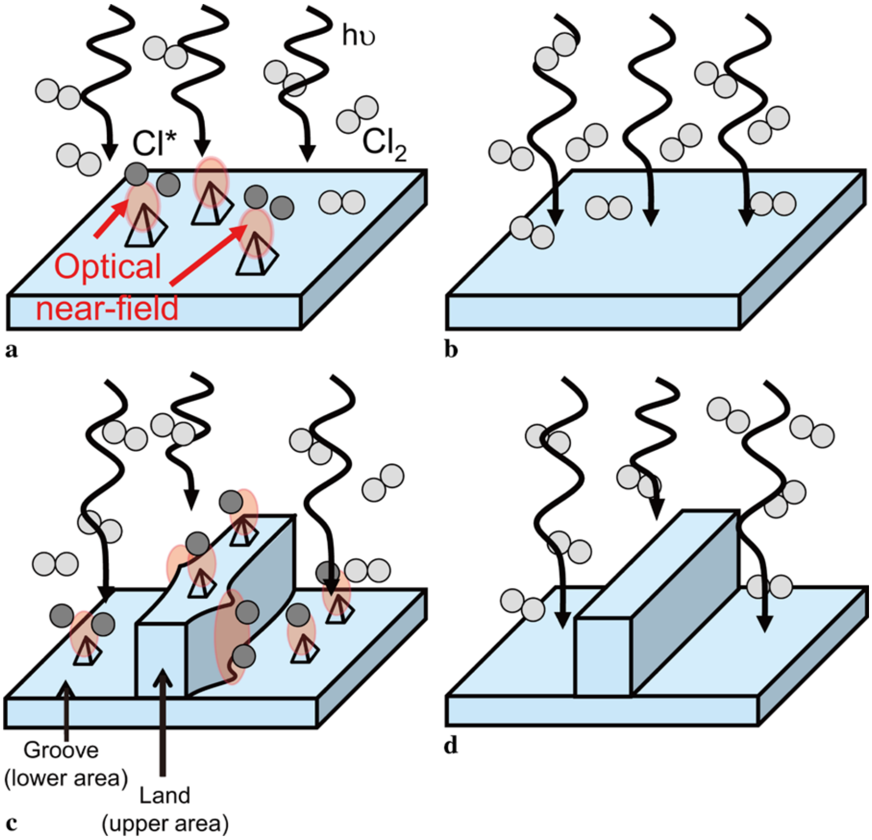

Fig. 1 Schematic diagram of near-field etching of (**a** and **b**) flat and (**c** and **d**) nano-striped substrates

convex lenses, diffraction gratings, and the inner wall surfaces of a cylinder. To confirm this applicability, we utilized the procedure to smooth a substrate with nano-striped corrugation pattern (Figs. 1(c) and (d)).

2 Experiment

The nano-stripe pattern was fabricated on of a soda-lime glass specimen, using a thermal nanoimprint technique with NiO molds [9]. The NiO mold patterns were transferred to the soda-lime glass at 600°C for 5 minutes under 10 MPa of pressure. Figure 2(a) shows a typical atomic force microscopy (AFM) image of the soda-lime glass with the nano-stripe corrugation pattern. The average height and period of the stripes were 13.5 nm and 175 nm, respectively.

Near-field etching was carried out by illuminating the substrate with a CW laser ($\lambda = 532$ nm) having a spatially uniform power density of 0.28 $\mathrm{W/cm^2}$. The Cl_2 pressure in the chamber was maintained at 100 Pa at room temperature with a constant Cl_2 flow rate of 100 sccm (the same conditions used for smoothing a planner substrate of synthetic silica [3]). The surface morphology was evaluated via AFM after near-field etching. The scanning area of the AFM was 1.0 μm × 1.0 µm, and the scanned area was 256 (x-axis) × 256 (y-axis) pixels, with a spatial resolution of 4 nm for each axis.

3 Results and discussion

Figure 2(b) shows a typical AFM image after 30 minutes of near-field etching. When this image is compared to Fig. 2(a) (before near-field etching), significant decreases in flank roughness can be seen. To evaluate the flank roughness reduction, we digitized the AFM images in order to analyze them numerically. Figures 3(a) and (b) show the respective digitized AFM images of Figs. 2(a) and (b); the white and black areas correspond to land and groove areas, respectively. The images were rotated to align them with the y-axis along the corrugations of the nano-stripe pattern. We also evaluated the land widths of white areas in the digitized AFM images. Figures 3(c) and (d) show the respective land width w distributions before and after near-field etching, which were least-square fitted by the black solid Gaussian curves. By comparing these fitted curves, we found that after near-field etching, the central value of the land width w_c at the peak of the Gaussian curve decreased from 94.9 nm to 89.8 nm, and the standard deviation σ decreased from 20.7 nm to 17.6 nm. These simultaneous decreases in w_c and σ indicate that near-field etching effectively reduced

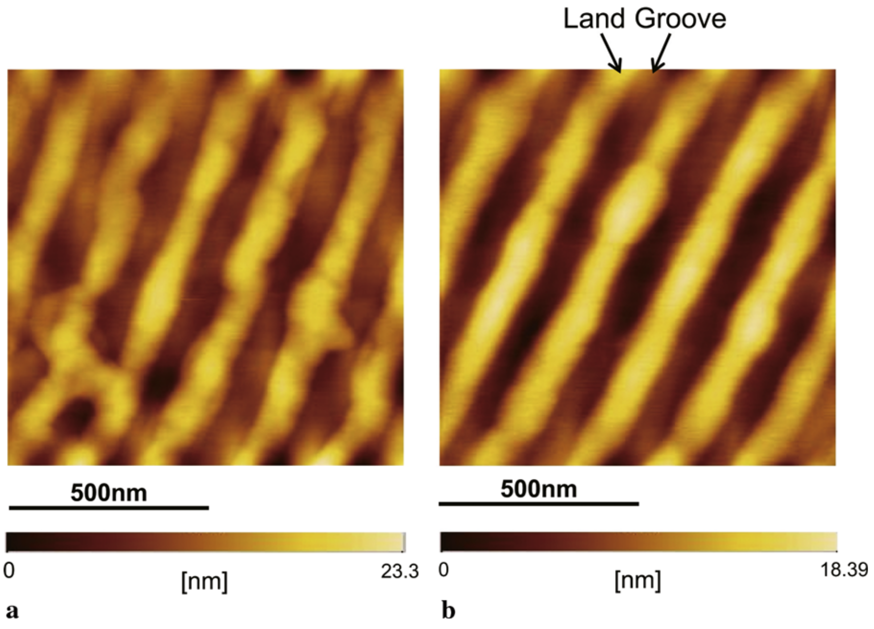

Fig. 2 Typical AFM images of the soda-lime glass (**a**) before and (**b**) after near-field etching (etching time 30 min)

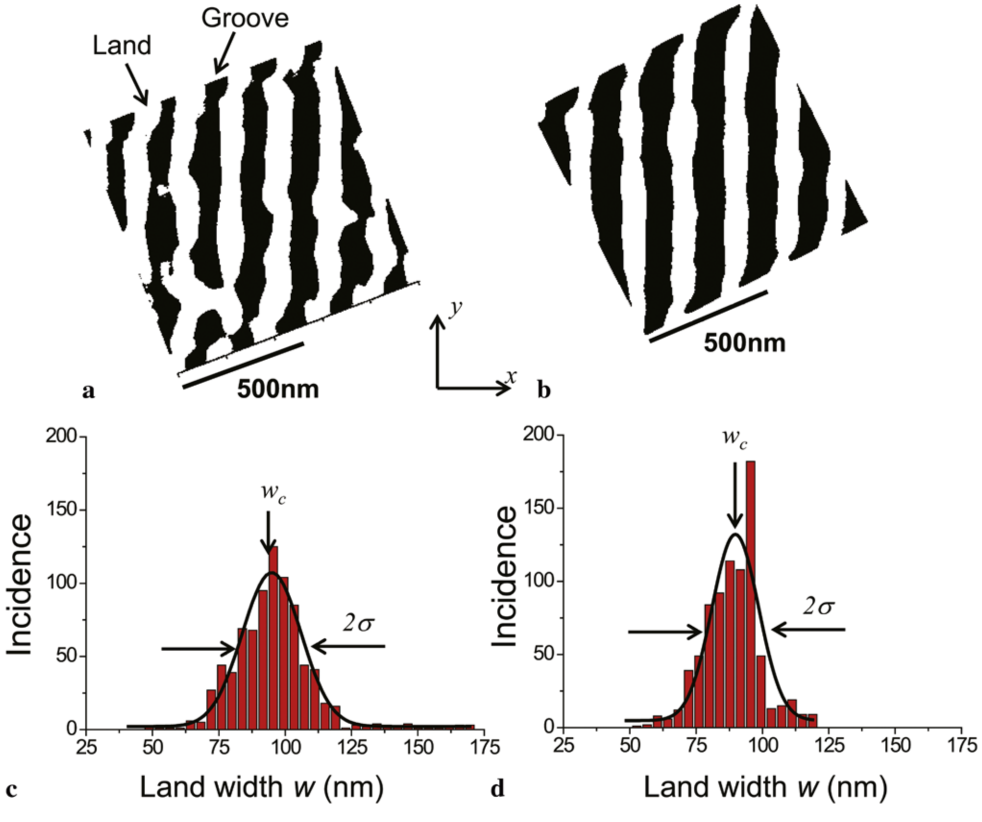

Fig. 3 Digitized AFM images (**a**) before and (**b**) after near-field etching. Land width distributions (**c**) before and (**d**) after near-field etching

the flank roughness of the nano-stripe pattern. In addition to decreased flank roughness, a comparison of Figs. 3(c) and (d) confirms that land with width exceeding 125 nm disappeared, indicating that deburring is also realized by near-field etching. Furthermore, as Fig. 3(d) shows, the incidence of land with 90-nm width greatly exceeded the value of the fitted curve (the black solid curve), which also suggests that the deburring occurred (in other words, larger land was etched, and its width thereby decreased). Since the optical near-field was selectively generated at the protrusions, selective etching of larger land was accomplished by near-field etching.

The roughness of the upper (land area) and lower (groove area) surfaces was also evaluated. We analyzed the surface

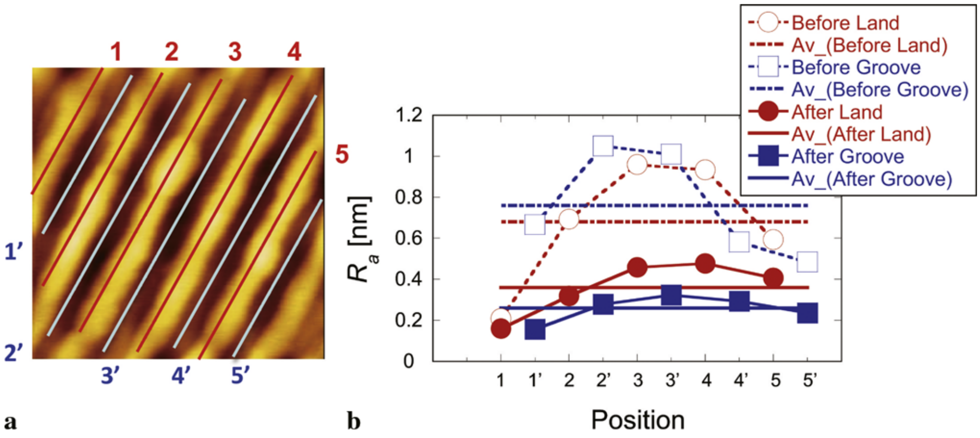

Fig. 4 (**a**) Schematic diagram of lines along land (*solid lines*) and grooves (*dashed lines*). (**b**) R_a values before near-field etching along land (*open circles* and *dashed line*) and grooves (*open squares* and *dashed line*). R_a values after near-field etching along land (*solid circles* and *solid line*) and grooves (*solid squares* and *solid line*). The number of positions corresponds to the number of the lines shown in (**a**). Average R_a: before etching of land—red *dot*-and-*dashed line* (Av_(Before Land)); after etching of land—*red solid line* (Av_(After Land)); before etching of grooves—*blue dot*-and-*dashed line* (Av_(Before Groove)); after etching of grooves—*blue solid line* (Av_(After Groove))

roughness R_a along land and grooves (Fig. 4(a)). Figure 4(b) summarizes the R_a values before and after near-field etching. We found a significant reduction in R_a along each line; the average R_a for land decreased from 0.68 nm before etching (red dot-and-dashed line) to 0.36 nm after etching (red solid line), while the average R_a for grooves decreased from 0.76 nm before etching (blue dot-and-dashed line) to 0.26 nm after etching (blue solid line). Additionally, from the averaged values of R_a, the etching rates for land and grooves were estimated to be 0.64 [nm/hour] and 1.0 [nm/hour], respectively, which were much larger than those of synthetic silica (0.14 [nm/hour]) [3]. Since soda-lime glass has a longer absorption band edge wavelength (350 nm) [10] than synthetic silica (160 nm) [11], this higher etching rate originated of near-field generation caused by the higher absorption coefficient of soda-lime glass.

4 Conclusion

We performed optical near-field etching of three-dimensional nano-stripe structures fabricated on soda-lime glass, with average height and period of 13.5 nm and 175 nm, respectively. Thirty minutes of near-field etching reduced the flank roughness and surface roughness on both land and grooves. Since this technique is a non-contact method (i.e., without a polishing pad), it can be applied not only to the outer surfaces of three-dimensional substrates, but also to the inner wall surfaces of cylinders. Furthermore, the procedure is suitable for mass production.

Acknowledgements This work was partially supported by the New Energy and Industrial Technology Development Organization (NEDO) under the Research and Development Program of Innovative Energy Efficiency Technology and under the program of comprehensive activity for personnel training and industry-academia collaboration based on the NEDO project.

References

1. B. Wua, A. Kumar, J. Vac. Sci. Technol. B **25**, 1743 (2007)
2. L.M. Cook, J. Non-Cryst. Solids **120**, 152 (1990)
3. T. Yatsui, K. Hirata, W. Nomura, M. Ohtsu, Y. Tabata, Appl. Phys. B **93**, 55 (2008)
4. T. Yatsui, K. Hirata, Y. Tabata, W. Nomura, T. Kawazoe, M. Naruse, M. Ohtsu, Nanotechnology **21**, 355303 (2010)
5. T. Kawazoe, K. Kobayashi, S. Takubo, M. Ohtsu, J. Chem. Phys. **122**, 024715 (2005)
6. K. Kobayashi, T. Kawazoe, M. Ohtsu, IEEE Trans. Nanotechnol. **4**, 517 (2005)
7. T. Yatsui, M. Ohtsu, Appl. Phys. Lett. **95**, 043104 (2009)
8. R. Kullmer, D. Büerle, Appl. Phys. A **43**, 227 (1987)
9. Y. Akita, Y. Kato, M. Hosaka, Y. Ono, S. Suzuki, A. Nakajima, M. Yoshimoto, Mater. Sci. Eng. B **161**, 151 (2009)
10. L.B. Glebov, E.N. Boulos, J. Non-Cryst. Solids **242**, 49 (1998)
11. L. Skuja, J. Non-Cryst. Solids **239**, 16 (1998)

Appl Phys B (2011) 103:537–546
DOI 10.1007/s00340-011-4375-9

Applied Physics B
Lasers and Optics

Two-dimensional array of room-temperature nanophotonic logic gates using InAs quantum dots in mesa structures

T. Kawazoe · M. Ohtsu · S. Aso · Y. Sawado · Y. Hosoda · K. Yoshizawa · K. Akahane · N. Yamamoto · M. Naruse

Received: 22 December 2010 / Published online: 10 February 2011

Abstract By growing two layers of InAs quantum dots on a substrate and processing the substrate to form mesa structures, we successfully fabricated for the first time nanophotonic devices that operate at room temperature. We fabricated two types of two-dimensional mesa arrays. The mesa dimensions of the individual arrays were 300 nm × 300 nm × 85 nm and 200 nm × 200 nm × 85 nm, and the areal density was 1×10^8 cm^{-2}. By adjusting the characteristics of energy transfer via dressed photons between two InAs quantum dots in the upper and lower layers of the mesa structures, we implemented devices that operate as AND gates and NOT gates. We fabricated 133 devices (with mesa dimensions of 300 nm on each side), of which 53 devices operated as AND gates and 50 devices operated as NOT gates.

1 Introduction

New nanoscale photonic devices [1–6] and nanoscale fabrication methods [7–10] based on near-field optical interactions through exchange of dressed photons between nanoscale matter have been realized. Dressed photons are virtual quasi-particles representing quantum states in which light is combined with an elementary excitation of matter [1]. A nanoscale optical device that uses dressed photons as signal carriers, i.e., a nanophotonic device, has the following features: (i) The device dimensions are considerably smaller than the wavelength of light. (ii) Since it is possible to utilize electric dipole-forbidden transitions, the loss due to recombination of the elementary excitation is reduced [11]. (iii) Energy consumption is drastically reduced compared with conventional devices [6].

Various types of nanophotonic devices have been proposed, and their operations have been verified, such as AND gates [2, 3], NOT gates [4], XOR gates [12], and optical nanofountains [13] implemented by using quantum dots (QDs) of CuCl, ZnO, or InGaAs. However, these devices were only able to operate at low temperatures below the temperature of liquid nitrogen.

In this research, in order to overcome this shortcoming, we processed two layers of InAs QDs having a low areal density into mesa structures to fabricate AND gates and NOT gates. As a result, of 133 devices (with mesa dimensions of 300 nm on each side) we fabricated, 53 AND gates and 50 NOT gates successfully operated at room temperature.

2 Structure and principles of the devices

Figure 1(a) shows the cross-sectional structure of a nanophotonic device formed of two InAs QDs (QD1, QD2) aligned

---

T. Kawazoe (✉) · M. Ohtsu · M. Naruse
Department of Electrical Engineering and Information Systems, Graduate School of Engineering, The University of Tokyo, 2-11-16 Yayoi, Bunkyo-ku, Tokyo 113-8656, Japan
e-mail: kawazoe@ee.t.u-tokyo.ac.jp
Fax: +81-3-5841-1140

T. Kawazoe · M. Ohtsu
Nanophotonic Research Center, Graduate School of Engineering, The University of Tokyo, 2-11-16 Yayoi, Bunkyo-ku, Tokyo 113-8656, Japan

S. Aso · Y. Sawado · Y. Hosoda · K. Yoshizawa
Pioneer Corporation, 465 Osato-cho, Kofu-shi, Yamanashi 400-0053, Japan

K. Akahane · N. Yamamoto · M. Naruse
National Institute of Information and Communications Technology, Koganei, Tokyo 184-8795, Japan

K. Akahane · N. Yamamoto · M. Naruse
The University of Tokyo, 2-11-16 Yayoi, Bunkyo-ku, Tokyo 113-8656, Japan

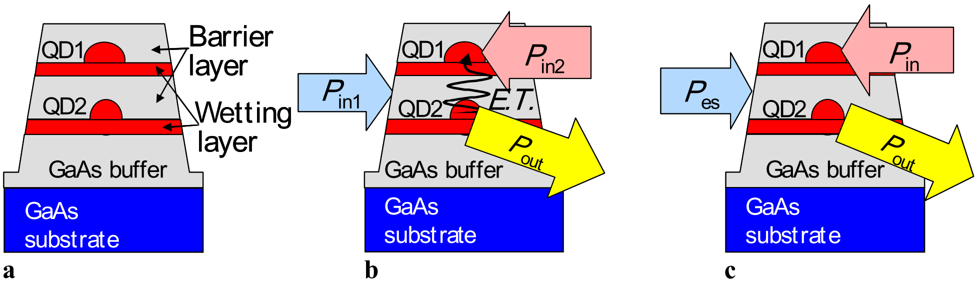

Fig. 1 The structure of a nanophotonic device. (**a**) A nanophotonic device formed of two quantum dots QD1 and QD2 having different sizes. (**b**) AND gate. (**c**) NOT gate

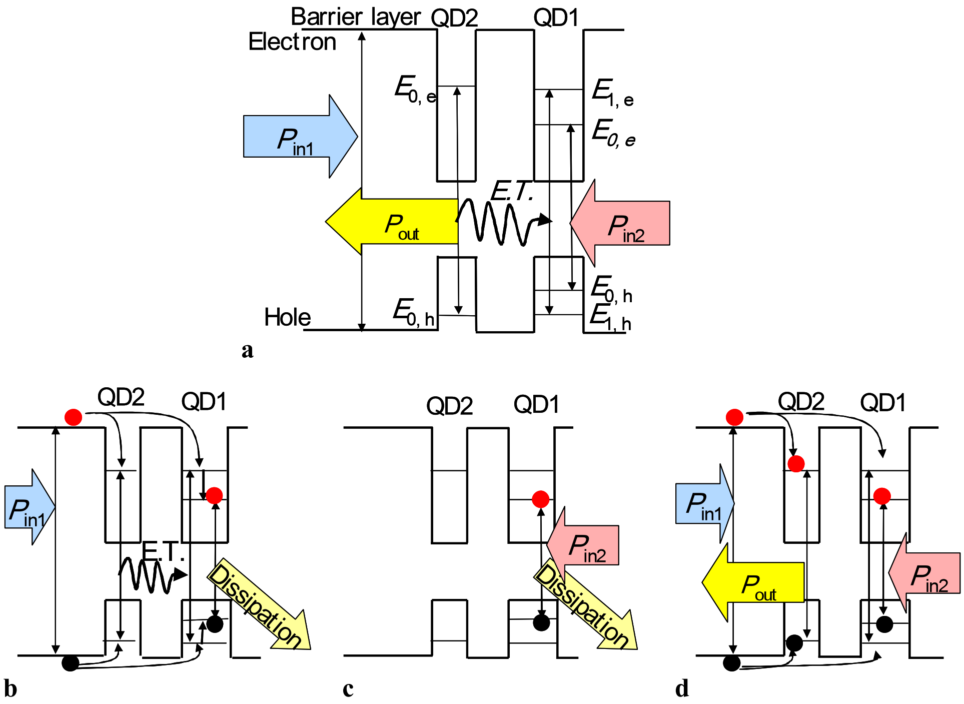

Fig. 2 Energy diagram of QD1 and QD2 that operate as an AND gate by resonance between $E(\mathrm{QD1}{:}E_{1,\mathrm{e}}–E_{1,\mathrm{h}})$ and $E(\mathrm{QD2}{:}E_{0,\mathrm{e}}–E_{0,\mathrm{h}})$. E.T. denotes energy transfer via dressed photons. *Red circles* represent electrons, and *black circles* represent holes. (**a**) Low state ($P_{\mathrm{out}} = 0$; $P_{\mathrm{in1}} \neq 0$, $P_{\mathrm{in2}} = 0$), (**b**) low state ($P_{\mathrm{out}} = 0$; $P_{\mathrm{in1}} = 0$, $P_{\mathrm{in2}} \neq 0$), and (**c**) high state ($P_{\mathrm{out}} \neq 0$; $P_{\mathrm{in1}} \neq 0$, $P_{\mathrm{in2}} \neq 0$)

vertically and having different sizes. These QDs are located in barrier layers in a mesa structure. The barrier layers are thick enough that the wave functions representing the electronic states of the two QDs do not overlap but are thin enough that dressed photons can be exchanged [1]. Figures 2(a) and 3(a) show the quantized energy levels $E_{n,\mathrm{e}}$ and $E_{n,\mathrm{h}}$ ($n = 0, 1$) of electrons and holes in the two QDs. An electronic transition between $E_{n,\mathrm{e}}$ and $E_{n,\mathrm{h}}$ will be referred to as an $E_{n,\mathrm{e}}–E_{n,\mathrm{h}}$ transition. The energies that are absorbed or released with the $E_{n,\mathrm{e}}–E_{n,\mathrm{h}}$ transition of QD1 and QD2 (transition energies) will be denoted as $E(\mathrm{QD1}{:}E_{n,\mathrm{e}}–E_{n,\mathrm{h}})$ and $E(\mathrm{QD2}{:}E_{n,\mathrm{e}}–E_{n,\mathrm{h}})$, respectively. Electric dipole-allowed transitions in QD1 and QD2 are the $E_{0,\mathrm{e}}–E_{0,\mathrm{h}}$ transition and the $E_{1,\mathrm{e}}–E_{1,\mathrm{h}}$ transition [14–16]. An AND gate operation is achieved by controlling the energy levels ($E_{n,\mathrm{e}}$, $E_{n,\mathrm{h}}$) such that the transition energies $E(\mathrm{QD1}{:}E_{1,\mathrm{e}}–E_{1,\mathrm{h}})$ and $E(\mathrm{QD2}{:}E_{0,\mathrm{e}}–E_{0,\mathrm{h}})$ of the two QDs are resonant with each other. On the other hand, in the case where the transition energies $E(\mathrm{QD1}{:}E_{1,\mathrm{e}}–E_{1,\mathrm{h}})$ and $E(\mathrm{QD2}{:}E_{0,\mathrm{e}}–E_{0,\mathrm{h}})$ are slightly off-resonant, if the difference between these energies is not so large, the energy linewidths increase by the many-body effect [4], causing these energies to become resonant with each other. Thus, a NOT gate operation is achieved in this case. In short, it is possible to implement two types of nanophotonic devices that operate in different ways by controlling the energy levels ($E_{n,\mathrm{e}}$, $E_{n,\mathrm{h}}$).

1. Resonant case: The device operates as an AND gate [2, 4] (Figs. 1(b) and 2). Two input light signals (whose powers are denoted by P_{in1} and P_{in2}) generate electron–hole pairs (e–h pairs) in the barrier layer and QD1 serving as input terminals, respectively. The e–h pairs generated in the barrier layer undergo intraband relaxation and then reach the $E_{0,\mathrm{h}}–E_{0,\mathrm{e}}$ level of QD1 or QD2. QD2 serves as an output terminal. The wavy arrows E.T. in the figures represent energy transfer from QD2 to QD1 via dressed photons. At QD2 serving as an output terminal, electrons and holes recombine through the $E_{0,\mathrm{e}}–E_{0,\mathrm{h}}$ transition in QD2 to generate an output light signal (whose power is denoted by P_{out}).

(i) $P_{\mathrm{in1}} \neq 0$, $P_{\mathrm{in2}} = 0$ (Fig. 2(b)): The electrons and holes generated in the barrier layer undergo intraband relaxation while moving to QD1 or QD2. Then, the electrons and holes relax to the levels $E_{0,\mathrm{e}}$ and $E_{0,\mathrm{h}}$ of QD2, respectively. The $E_{0,\mathrm{e}}$–$E_{0,\mathrm{h}}$ transition energy $E(\mathrm{QD2}{:}E_{0,\mathrm{e}}–E_{0,\mathrm{h}})$ of the e–h pairs is transferred to QD1 by resonance via dressed photons (E.T. in Fig. 2(b)). Furthermore, the electrons and holes of the e–h pairs undergo inter-sublevel relaxation to the levels $E_{0,\mathrm{e}}$ and $E_{0,\mathrm{h}}$ of QD1, respectively, and the e–h pairs vanish by recombination of the electrons and holes, whereby the energy input to the device as P_{in1} is dissipated from QD1. Thus, no output signal is generated ($P_{\mathrm{out}} = 0$: low state).

(ii) $P_{\mathrm{in1}} = 0$, $P_{\mathrm{in2}} \neq 0$ (Fig. 2(c)): The e–h pairs generated in QD1 vanish by the $E_{0,\mathrm{e}}$–$E_{0,\mathrm{h}}$ transition, so that no output signal is generated ($P_{\mathrm{out}} = 0$: low state).

(iii) $P_{\mathrm{in1}} \neq 0$, $P_{\mathrm{in2}} \neq 0$ (Fig. 2(d)): The e–h pairs generated in the barrier layer move to QD1 or QD2 and undergo inter-sublevel relaxation. Of the e–h pairs, the transition energy $E(\mathrm{QD2}{:}E_{0,\mathrm{e}}–E_{0,\mathrm{h}})$ of the e–h pairs in QD2 is prohibited from transferring to QD1. This is because the energy levels of electrons and holes in QD1 are already occupied by electrons and holes generated by P_{in1}. The transition energy $E(\mathrm{QD2}{:}E_{0,\mathrm{e}}–E_{0,\mathrm{h}})$ of QD2, which is prohibited from transferring, is released by recombination of electrons and holes through the $E_{0,\mathrm{e}}$–$E_{0,\mathrm{h}}$ transition. As a result, an output signal is generated ($P_{\mathrm{out}} \neq 0$: high state).

2. Slightly off-resonant case: The device operates as a NOT gate [4] (Figs. 1(c) and 3). Light, as the energy source, enters the NOT gate. This light energy is supplied to the barrier layer (same as P_{in1} in case 1, denoted by P_{es} here). QD1 serves as an input terminal. An input signal (same as P_{in2} in case 1, denoted by P_{in} here) generates e–h pairs through the $E_{0,\mathrm{e}}$–$E_{0,\mathrm{h}}$ transition in QD1. QD2 serves as an output terminal, where electrons and holes recombine through the $E_{0,\mathrm{e}}$–$E_{0,\mathrm{h}}$ transition in QD2 to generate an output light signal (P_{out}).

(i) $P_{\mathrm{in}} = 0$ (Fig. 3(b)): The electrons and holes generated in the barrier layer by the light (P_{es}) serving as an energy source move to QD1 and QD2 while undergoing intraband relaxation. The electrons and holes moved to QD1 undergo inter-sublevel relaxation to the levels $E_{0,\mathrm{e}}$ and $E_{0,\mathrm{h}}$ in QD1, respectively, and then the e–h pairs vanish through the $E_{0,\mathrm{e}}$–$E_{0,\mathrm{h}}$ transition. Since $E(\mathrm{QD2}{:}E_{0,\mathrm{e}}–E_{0,\mathrm{h}})$ is not resonant with $E(\mathrm{QD1}{:}E_{1,\mathrm{e}}–E_{1,\mathrm{h}})$, the e–h pairs moved to QD2 are prohibited from moving to QD1 and vanish by recombination of the electrons and holes. Thus, an output signal is generated ($P_{\mathrm{out}} \neq 0$: high state).

(ii) $P_{\mathrm{in}} \neq 0$ (Fig. 3(c)): Since the linewidths of energy levels of QD1 increase by the many-body effect [4], $E(\mathrm{QD1}{:}E_{1,\mathrm{e}}–E_{1,\mathrm{h}})$ and $E(\mathrm{QD2}{:}E_{0,\mathrm{e}}–E_{0,\mathrm{h}})$ come to be resonant with each other. At this time, the e–h pairs generated in the barrier layer by the light serving as an energy source move to QD2 while undergoing intraband relaxation. The transition energy $E(\mathrm{QD2}{:}E_{0,\mathrm{e}}–E_{0,\mathrm{h}})$ of the e–h pairs can transfer to QD1 by resonance (E.T. in Fig. 3(c)). As a result, the e–h pairs in QD2 vanish, so that no output signal is generated ($P_{\mathrm{out}} = 0$: low state).

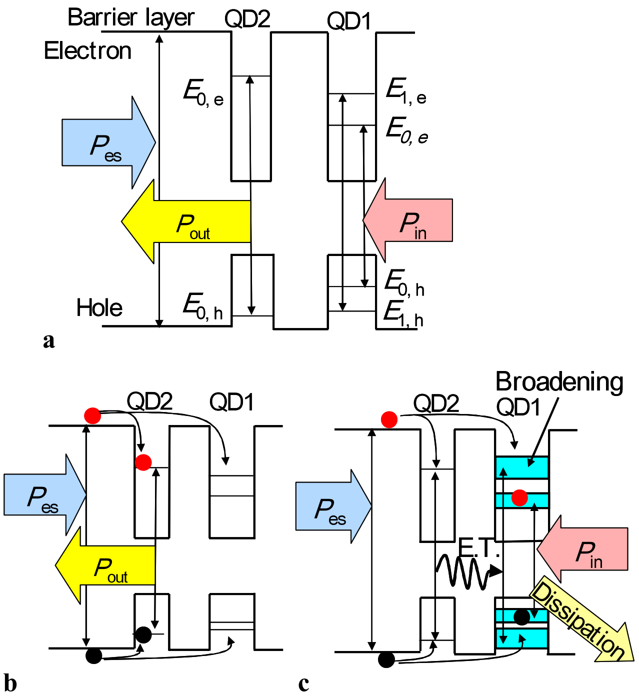

Fig. 3 Energy diagram of QD1 and QD2 in the case where $E(\mathrm{QD1}{:}E_{1,\mathrm{e}}–E_{1,\mathrm{h}})$ and $E(\mathrm{QD2}{:}E_{0,\mathrm{e}}–E_{0,\mathrm{h}})$ are slightly off-resonant, and QD1 and QD2 operate as a NOT gate. (**a**) High state ($P_{\mathrm{out}} \neq 0$; $P_{\mathrm{in}} = 0$) and (**b**) low state ($P_{\mathrm{out}} = 0$; $P_{\mathrm{in}} \neq 0$)

3 Fabrication and evaluation

We used a GaAs wafer as a substrate and grew InAs QDs on the substrate by molecular beam epitaxy (MBE). Figure 4(a) shows the cross-sectional structures of a buffer layer, barrier layers, wetting layers, and QDs grown on the GaAs substrate. The requirements for realizing room-temperature operation and a method we discovered for satisfying the requirements are as follows: (i) Ability to precisely control the distances between QDs (the distance between two QDs constituting a device should be less than or equal to the diameter of a QD, and distances with respect to the other QDs should be greater than the diameter of a QD): By utilizing the phenomenon in which QDs align vertically as a result of growth in the Stranski–Krastanov mode [17], only QDs in the upper layer and the lower layer were placed in proximity to each other. We adjusted the distance between the QDs by controlling the thickness of the barrier layers. Furthermore, we made the areal density of QDs in each layer low by controlling the growth rate. (ii) Satisfying the resonant and slightly off-resonant device operating conditions, described

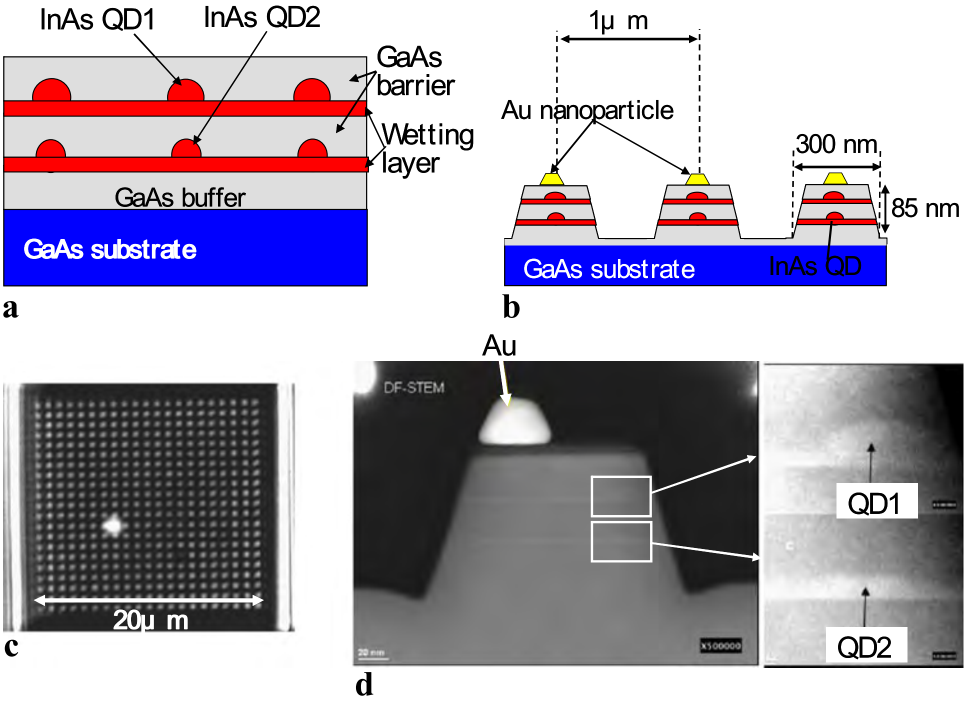

Fig. 4 Mesa structure fabricated by using two layers of InAs QDs. (**a**) The structure of two layers of InAs QDs used for mesa processing. (**b**) A cross-section of the mesa structure. (**c**) Image of the entire two-dimensional array of mesa structures, taken with an optical microscope. (**d**) Cross-sectional image of a mesa, taken with a scanning transmission electron microscope (S-TEM)

in 1 and 2 above, by controlling the quantized energy levels of QD1 and QD2: We controlled the growth rate and deposition thickness of QDs. (iii) Sufficiently high quantum efficiency of photoluminescence at room temperature: We controlled the heating rate under As-source irradiation and the growth temperature of the barrier layers.

The fabrication process satisfying the above requirements (i) to (iii) is as follows. First, we grew a GaAs buffer layer having a thickness of 150 nm on the substrate. Then, we grew 1.8 monolayers of QD2 on the buffer layer (growth temperature, 510°C). Then, we grew a GaAs layer (barrier layer) having a thickness of 24 nm (growth temperature, 475°C) and then grew 1.8 monolayers of QD1 (growth temperature, 510°C). Finally, we grew a GaAs layer (barrier layer) having a thickness of 24 nm (growth temperature, 440°C).

Figure 4(b) shows the cross-sectional structure of the two-dimensional mesa array we fabricated. After fabricating a Ti mask on the quantum dots fabricated as described above by the lift-off method using electron-beam lithography, we formed two-dimensional arrays of two types of mesa devices by Ar-ion milling. The dimensions of the bottom of each mesa structure were 300 nm × 300 nm (Fig. 4(b)) and 200 nm × 200 nm, and the height was 85 nm. The average number of pairs of QD1 and QD2 in each mesa structure, estimated on the basis of the areal density of QDs mentioned earlier, was 4.0 for the 300 nm-size mesa structures and 1.5 for the 200 nm-size mesa structures. We arrayed 20 × 20 mesa devices two-dimensionally at intervals of 1 μm (areal density of 1×10^8 cm^{-2}). Figure 4(c) shows an image of the two-dimensional array, taken with an optical microscope.

Figure 4(d) shows a cross-sectional image of the device, taken with a scanning transmission electron microscope (S-TEM). It will be understood that QD1 is located directly above QD2 and that the distance between QD1 and QD2 is controlled by the thickness of the barrier layer. As will be understood from the image, QD1 and QD2 are aligned vertically, separated by a barrier layer having a thickness of 24 nm. The average dimensions of QD1 were 42 nm in diameter and 11 nm in height. The average dimensions of QD2 were 38 nm in diameter and 10 nm in height. The areal density of QDs was 1.0×10^{10} cm^{-2}. Since the average in-plane interval was 100 nm, requirement (i) was satisfied. Furthermore, as is shown in the image, an Au nanoparticle having a diameter of 50 nm and a height of 30 nm was provided on top of the mesa structure. The Au nanoparticle on the mesa structure was also fabricated by Ar-ion milling using a Ti mask. The Au nanoparticle has the role of improving the efficiency of outputting propagating light as an output signal of the device. That is, since GaAs constituting the barrier layer has a large refractive index, light signals emitted by the device are scattered backward in the direction of the substrate [18]. At this time, the Au nanoparticle serves to discharge a greater portion of the scattered light to the outside of the device.

The white squares in Fig. 5 represent measured values of the spectrum of light emitted by the fabricated QD1 and QD2 at room temperature (300 K). The solid curve is composed of multiple Gaussian curves, representing the result of fitting the measured values. As an excitation light source, we used second harmonic generation (SHG) light of

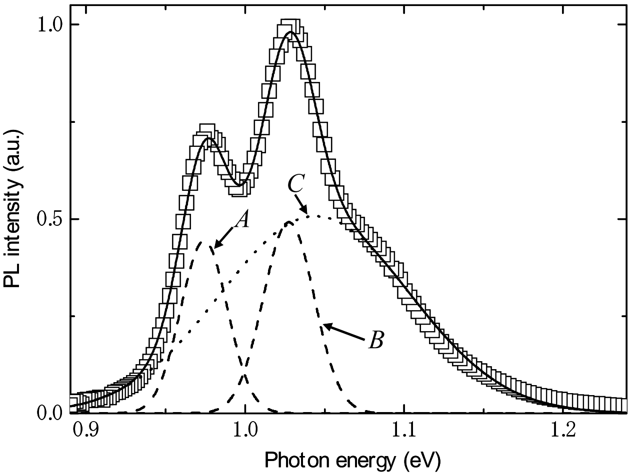

Fig. 5 Spectra of light emitted by the two layers of InAs QDs used for device fabrication. The *curve A* represents the spectrum of light emitted by recombination of electrons and holes through the transition $E_{0,\mathrm{e}}$–$E_{0,\mathrm{h}}$ in QD1. The *curve B* represents the spectrum in which the spectra of light emitted by recombination of electrons and holes through the transition $E_{1,\mathrm{e}}$–$E_{1,\mathrm{h}}$ in QD1 and the transition $E_{0,\mathrm{e}}$–$E_{0,\mathrm{h}}$ in QD2 overlap each other. The *curve C* represents the spectrum of light emitted from wetting layers

an Nd:YAG laser that emits light having a wavelength of 532 nm and an excitation intensity of 20 W/cm^2. We fitted the spectral component of light emitted by recombination of electrons and holes through the $E_{0,\mathrm{e}}$–$E_{0,\mathrm{h}}$ transition of QD1 with a Gaussian curve A. The peak energy of the spectrum ($E(\mathrm{QD1}{:}E_{0,\mathrm{e}}$–$E_{0,\mathrm{h}})$) was 0.974 eV, and the inhomogeneous linewidth of the spectrum was 28 meV. Furthermore, the spectra of light emitted by recombination of electrons and holes through the $E_{1,\mathrm{e}}$–$E_{1,\mathrm{h}}$ transition of QD1 and the $E_{0,\mathrm{e}}$–$E_{0,\mathrm{h}}$ transition of QD2 overlapped each other, and we fitted the spectra with a Gaussian curve B. The peak energy of the spectra ($E(\mathrm{QD1}{:}E_{1,\mathrm{e}}$–$E_{1,\mathrm{h}})$ and $E(\mathrm{QD2}{:}E_{0,\mathrm{e}}$–$E_{0,\mathrm{h}})$) was 1.027 eV, and the inhomogeneous linewidth of the spectra was 31 meV. Furthermore, the curve C represents a broad spectrum of light emitted from the wetting layers. The inhomogeneous linewidth of the spectrum was 119 meV. The sources of these spectra were estimated from the spectra of light emitted from samples in which only QD2 were fabricated and samples in which only QD1 were fabricated and the results of measurement of dependency of these samples on the excitation intensity. The average value of the full width at half maximum (FWHM) of the spectrum of light emitted from a single QD at room temperature, measured by the microscopic photoluminescence method (μ-PL method), was 16 meV. The photoluminescence linewidth obtained from this spectrum substantially coincided with results obtained through other measurements of emitted light [19] and hole burning spectroscopy [20] and can be regarded as the homogeneous linewidth.

Based on the homogeneous linewidth and inhomogeneous linewidth, it is possible to obtain the probability of existence of QD pairs in which $E(\mathrm{QD1}{:}E_{1,\mathrm{e}}$–$E_{1,\mathrm{h}})$ and $E(\mathrm{QD2}{:}E_{0,\mathrm{e}}$–$E_{0,\mathrm{h}})$ are resonant with each other. We assumed that $E(\mathrm{QD1}{:}E_{1,\mathrm{e}}$–$E_{1,\mathrm{h}})$ and $E(\mathrm{QD2}{:}E_{0,\mathrm{e}}$–$E_{0,\mathrm{h}})$ were resonant with each other when the overlapping area of the homogeneous spectral broadenings of these transition energies was greater than half the area of the homogeneous spectral broadening of each one individually. Since the homogeneously broadened spectral shapes of light emitted from $E(\mathrm{QD1}{:}E_{1,\mathrm{e}}$–$E_{1,\mathrm{h}})$ and $E(\mathrm{QD2}{:}E_{0,\mathrm{e}}$–$E_{0,\mathrm{h}})$ of a single QD are represented by Lorentzian curves, $E(\mathrm{QD1}{:}E_{1,\mathrm{e}}$–$E_{1,\mathrm{h}})$ and $E(\mathrm{QD2}{:}E_{0,\mathrm{e}}$–$E_{0,\mathrm{h}})$ are considered as resonant if the distance between the positions of the spectral peaks of these energies is less than the FWHM (16 meV). On the other hand, since the Gaussian linewidth of the inhomogeneously broadened photoluminescence generated with $E(\mathrm{QD1}{:}E_{1,\mathrm{e}}$–$E_{1,\mathrm{h}})$ and $E(\mathrm{QD2}{:}E_{0,\mathrm{e}}$–$E_{0,\mathrm{h}})$ as described above is 31 meV, the probability of existence of a QD pair in which $E(\mathrm{QD1}{:}E_{1,\mathrm{e}}$–$E_{1,\mathrm{h}})$ and $E(\mathrm{QD2}{:}E_{0,\mathrm{e}}$–$E_{0,\mathrm{h}})$ are resonant with each other is expressed by

$$P(\delta x_c, x_h) = \int_0^\infty \int_{x_c}^{x_c+\delta x_c} \exp\left\{-\frac{(x+x_c)^2}{x_h^2}\right\} dx\, dx_c \Big/ \int_0^\infty \int_{x_c}^{\infty} \exp\left\{-\frac{(x+x_c)^2}{x_h^2}\right\} dx\, dx_c. \tag{1}$$

In this equation, the integration variables x and x_c represent photon energies, δx_c represents the homogeneous linewidth, and x_h represents the inhomogeneous linewidth. Assigning the above values, i.e., $\delta x_c = 16$ meV and $x_h = 31$ meV, the value of (1) is $P_1 \equiv P(16\ \mathrm{meV}, 31\ \mathrm{meV}) = 39\%$. Furthermore, we observed the dependency of the spectrum of light emitted by a single QD on the excitation intensity and confirmed that the homogeneous linewidth increased by 2.2 times or more by the many-body effect. Thus, if e–h pairs exist in a QD, the homogeneous linewidth would increase to at least 16 meV × 2.2 = 35 meV. At this time, by assigning $\delta x_c = 16$ meV and $x_h = 31$ meV in (1), it is found that the probability of existence of a resonant QD pair increases to $P_2 \equiv P(35\ \mathrm{meV}, 31\ \mathrm{meV}) = 74\%$. This indicates that QD pairs corresponding to the 35% difference from P_1 experienced a change from the off-resonant to resonant condition by excitation of $E(\mathrm{QD1}{:}E_{1,\mathrm{e}}$–$E_{1,\mathrm{h}})$ and $E(\mathrm{QD2}{:}E_{0,\mathrm{e}}$–$E_{0,\mathrm{h}})$. That is, this indicates that 35% of the QD pairs are slightly off-resonant and thus can operate as NOT gates. From the above discussion, it will be understood that requirement (ii) is satisfied by using the fabricated InAs QDs and that at least 74% of the QD pairs operate as AND gates or NOT gates.

When growing the barrier layer after growing quantum dots by MBE, we raised the temperature of the growth substrate to the growth temperature of the barrier layer under As irradiation. We suppressed diffusion of In by controlling the heating rate and the growth temperature of the barrier layer.

As a result, formation of nonradiative recombination centers due to diffusion of In was suppressed, and the intensity of light emitted from QDs at room temperature increased about tenfold compared with the case without this control. Thus, requirement (iii) was satisfied.

4 Device operation

We verified the device operation at room temperature (300 K) by the μ-PL method. Since the photon energy needed to generate e–h pairs in the GaAs barrier layer is 1.44 eV, we used a cw semiconductor laser with a photon energy of 1.91 eV as a light source for P_{in1} of the AND gates and P_{es} of the NOT gates. The power of input light was 80 μW. Furthermore, we used an optical parametric oscillator (photon energy of 0.965 eV, pulse width of 100 fs, repetition frequency of 80 MHz, and input power of 40 μW) pumped by a Ti:sapphire laser and tuned to $E(\mathrm{QD1}{:}E_{0,\mathrm{h}}\text{–}E_{0,\mathrm{e}})$ of QD1 as a light source for P_{in2} of the AND gates and P_{in} of the NOT gates. The numerical aperture of the objective lens used for the μ-PL method was 0.6, and the spatial resolution was 500 nm.

Light (P_{in1}, P_{es}) from the cw semiconductor laser was made to enter the two-dimensional mesa array, and we measured the spatial distribution of the value of the ratio $R(=P_{\mathrm{out}}/P'_{\mathrm{out}})$ of the output signal power P_{out} in the case where the input signal (P_{in2}, P_{in}) was applied and the output signal power P'_{out} in the case where the input signal was not applied. According to [21], the contrast ratio C of a logic gate is defined as $C(\mathrm{dB}) = 10\log(P_{\mathrm{out,h}}/P_{\mathrm{out},l})$ using P_{out} in a high state ($P_{\mathrm{out,h}}$) and P_{out} in a low state ($P_{\mathrm{out},l}$). Thus, R described above is $R = 10^{C/10}$ for AND gates and $R = 10^{-C/10}$ for NOT gates. Figures 6(a) and (b) show the results of measurement of mesa structures having dimensions of 300 nm and 200 nm on each side, respectively. Here, P_{out} represents a value obtained by integrating the range of photon energy of 1.0533 to 1.0120 eV in the spectrum of the output signal. Spots of yellow to red represent the values of R for AND gates. On the other hand, darker spots of blue to black represent the values of R for NOT gates. Mesa structures having particularly distinct values of R are surrounded by white rings.

Since the values of R fluctuated by as much as 2.2% due to the background noise caused by deep level emission from the GaAs substrate, devices whose average value of C of mesa structures was greater than $10\log(1.025) = 0.11$ dB were defined as AND gates and NOT gates. At this time, in the case of the 300 nm × 300 nm mesa structures, of 133 mesa structures observed, 53 mesa structures operated as AND gates, 50 mesa structures operated as NOT gates, and there were 30 others. In the case of the 200 nm × 200 nm mesa structures, of 126 mesa structures observed, 36 mesa structures operated as AND gates, 36 mesa structures operated as NOT gates, and there were 54 others.

We verified experimentally that the enhancement factor of P_{out} by the 40 nm Au nanoparticle was 3. Furthermore, we excited all the mesa structures in the two-dimensional array with second harmonic generation (SHG) of the mode-locked Ti:sapphire laser and measured the relaxation lifetime of light emission with an avalanche photodiode. As a result, we confirmed that a fast relaxation component having a time constant of 50 ps appeared due to the 40 nm Au nanoparticle. This result suggests that the maximum operation frequency of the device with the Au nanoparticle disposed on the mesa structures is $1/50$ ps (=20 GHz). This point will be published in detail on some other occasion.

5 Discussion

First, C of the device will be discussed. As will be understood from Figs. 6(a) and (b), the maximum value in the spatial distribution of C in the two-dimensional array was $10\log(1.15) = 0.61$ dB for AND gates and $10\log(0.85) = 0.71$ dB for NOT gates. However, these values are underestimated for two reasons: (i) The value obtained by integrating over the range of photon energy of 1.0533–1.0120 eV is used; (ii) Light in the form of short pulses having a low duty ratio and a low repetition frequency (100 fs, 80 MHz) is used as the input signals (P_{in2}, P_{in}).

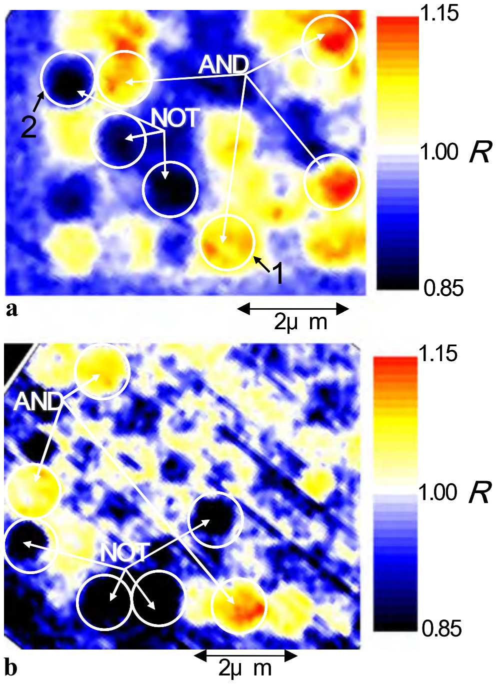

Fig. 6 Spatial distribution of the values of ratio R regarding the two-dimensional mesa array. (**a**) Mesa dimensions 300 nm × 300 nm and (**b**) mesa dimensions 200 nm × 200 nm

Now, reason (i) will be discussed in the context of the AND gate with ring number 1 and the NOT gate with ring number 2 in Fig. 6(a). Figure 7(a) shows the spectra of output light signals of the AND gate at the center of ring number 1 in a high state and a low state by a solid curve and a dashed curve, respectively. C becomes greatest at the position of the arrow in the figure, with a value of $10\ \log(2.0) = 3.0$ dB. Furthermore, Fig. 7(b) shows the spectra of output light signals of the NOT gate with ring number 2 in Fig. 6(a) in a high state and a low state by a solid curve and a dashed curve, respectively. C becomes greatest at the position of the arrow in the figure, again with a value of $10 \log(2.0) = 3.0$ dB. Thus, by choosing the photon energy of P_{out} of each device so that C becomes greatest, C of AND gates and C of NOT gates increase by 2.4 $(=3.0 - 0.61)$ dB and 2.3 $(=3.0 - 0.71)$ dB, respectively.

Next, reason (ii) will be discussed. In the case where light having a high duty ratio is used as the input signals (P_{in2}, P_{in}), the values of C become greater. In the experiment described above, pulse signals are generated both in a high state and a low state. Since P_{out} occurs by recombination of electrons and holes in QD2, the time duration of the pulsed light signals is substantially equal to the recombination lifetime (measured value is 0.38 ns) of the electrons and holes in the device. Furthermore, the pulse repetition time is 12.5 ns $(=1/80$ MHz). That is, since the duty ratio is $0.38\ \text{ns}/12.5\ \text{ns} = 0.03$, by using a light source with a pulse repetition time of 0.38 ns in the experiment and neglecting the effects of saturation, C of AND gates and NOT gates becomes 15 $(=10 \log(1/0.03))$ dB greater compared with (i) above. From the discussion of reasons (i) and (ii), C of AND gates and NOT gates obtained as results of the experiment were both 18 $(=3 + 15)$ dB.

Next, the relationship between the transition energy between quantized energy levels of QDs constituting the device and the reproducibility of the device operation will be discussed. For this purpose, we fitted the spectrum of light emitted from QDs in each mesa structure with a Lorentzian curve and obtained the median of the transition energies of the individual QDs. Figures 8(a) to (c) show the results for AND gates, NOT gates, and other mesa structures, respectively. In Fig. 8(a), the red curve is a fitting curve for the spectrum of light emitted by recombination of electrons and holes through the $E_{0,\text{e}}$–$E_{0,\text{h}}$ transition in QD1. The blue curve is a fitting curve for the spectrum of light emitted by recombination of electrons and holes through the $E_{1,\text{e}}$–$E_{1,\text{h}}$ transition in QD1 and the $E_{0,\text{e}}$–$E_{0,\text{h}}$ transition in QD2 (corresponding to P_{out}). Furthermore, in Fig. 8(b), the red, green, and blue curves are fitting curves for the spectra of light emitted by recombination of electrons and holes through the $E_{0,\text{e}}$–$E_{0,\text{h}}$ transition in QD1, the $E_{1,\text{e}}$–$E_{1,\text{h}}$ transition in QD1, and the $E_{0,\text{e}}$–$E_{0,\text{h}}$ transition in QD2 (corresponding to P_{out}). The FWHM of the green curve is wider than that of the red curve. This is because the $E_{1,\text{e}}$–$E_{1,\text{h}}$ transition is fourfold degenerate, causing quick phase relaxation between degenerate levels, and because inter-sublevel relaxation of electrons and holes to the $E_{0,\text{e}}$ and the $E_{0,\text{h}}$ levels occurs quickly, whereby the FWHM of the spectrum of emitted light increases [14–16]. Figure 8(c) shows the spectrum of light emitted from the other mesa structures. We fitted the spectrum with multiple Lorentzian curves having different center positions.

Figure 9 shows the results of plotting the photon energies at the center positions of the Lorentzian curves obtained by the fitting described above as a function of R. The white triangles, white circles, and black squares in the figure correspond to AND gates ($R = 10^{C/10}$), NOT gates ($R = 10^{-C/10}$), and the other mesa structures, respectively. The white triangles and circles distributed in the vicinity of the red curve A represent the photon energies of light emission by recombination of electrons and holes through the $E_{1,\text{e}}$–$E_{1,\text{h}}$ transition in QD1. On the other hand, white triangles and circles distributed in the vicinity of the red curve B represent the photon energies of light emission by recombination of electrons and holes through the $E_{1,\text{e}}$–$E_{1,\text{h}}$ transition in QD1 and the $E_{0,\text{e}}$–$E_{0,\text{h}}$ transition in QD2.

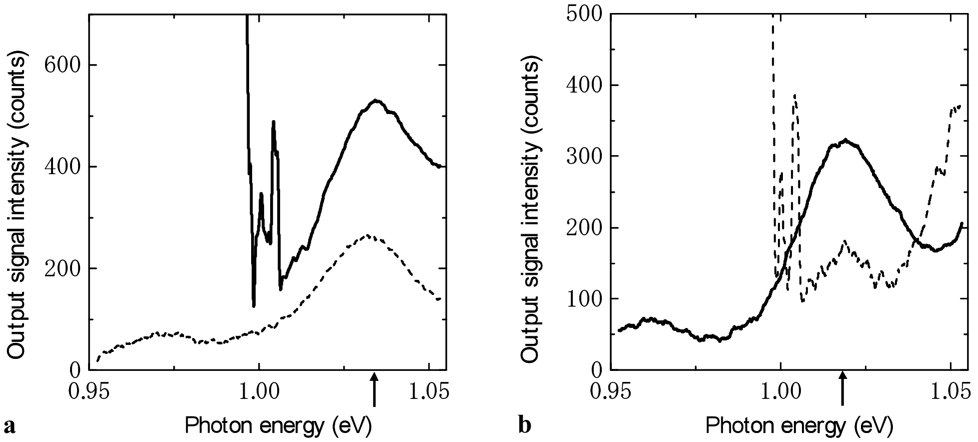

Fig. 7 Spectra of output signals. (**a**) Spectra of P_{out} of the AND gate with ring number 1 (*dashed curve* for low state ($P_{\text{out}} = 0$; $P_{\text{in1}} \neq 0$, $P_{\text{in2}} = 0$), *solid curve* for high state ($P_{\text{out}} \neq 0$; $P_{\text{in1}} \neq 0$, $P_{\text{in2}} \neq 0$)). (**b**) Spectra of P_{out} of the NOT gate with ring number 2 (*dashed curve* for low state ($P_{\text{out}} = 0$; $P_{\text{in}} \neq 0$), *solid curve* for high state ($P_{\text{out}} \neq 0$; $P_{\text{in}} = 0$))

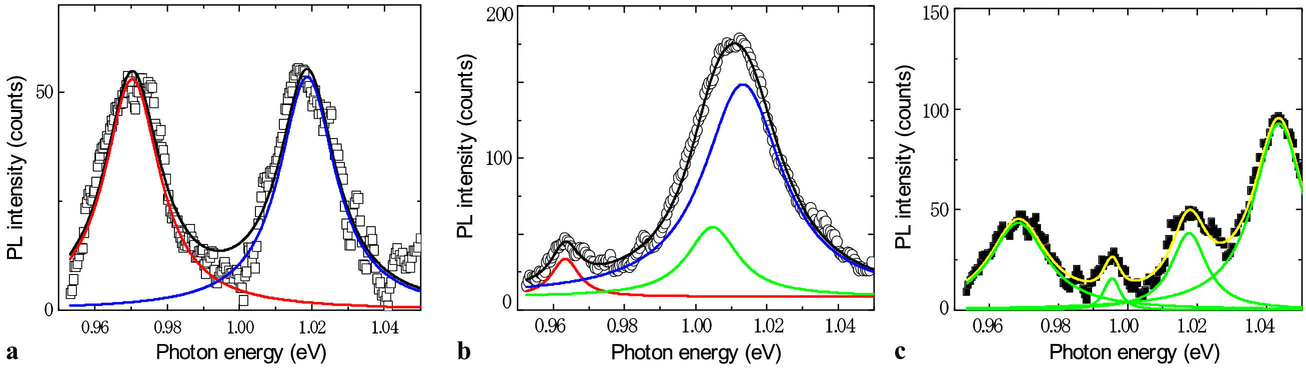

Fig. 8 Spectra of light emitted by different mesa structures. The *solid curves* represent the results of fitting with Lorentzian curves. (**a**) Mesa structures that operate as AND gates. (**b**) Mesa structures that operate as NOT gates. (**c**) Other mesa structures

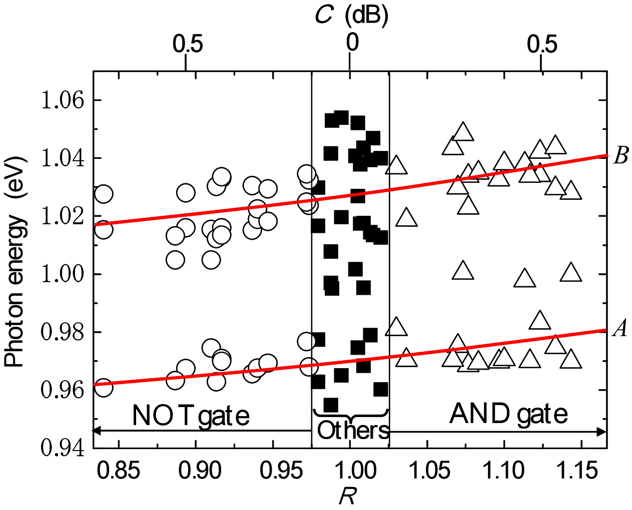

Fig. 9 Result of plotting the photon energies at the center positions of the Lorentzian curves obtained by the fitting shown in Fig. 8 as a function of R of individual mesa structures, together with the values of C. The *white triangles*, *white circles*, and *black squares* represent results obtained from the spectra of light emitted by AND gates, NOT gates, and the other mesa structures, respectively. The *curve A* represents the photon energy of $E(\mathrm{QD1}{:}E_{0,\mathrm{e}}–E_{0,\mathrm{h}})$, and the *curve B* represents the photon energy in which $E(\mathrm{QD1}{:}E_{1,\mathrm{e}}–E_{1,\mathrm{h}})$ and $E(\mathrm{QD2}{:}E_{0,\mathrm{e}}–E_{0,\mathrm{h}})$ overlap

As indicated by the black squares, mesa structures other than AND gates and NOT gates have a large number of peaks in the emitted light spectra, with the center positions of the Lorentzian curves considerably deviated from the red curves A and B. That is, the transition energies of two QDs in these mesa structures are not resonant or slightly off-resonant, and do not satisfy the operating conditions of AND gates or NOT gates. The differences in photon energy at the peaks were large, averaging at 42 meV. The probability of existence of a QD having a peak of light emission at such a photon energy position is greater than the probability of existence obtained from the value of the inhomogeneous width (31 meV) of the quantized energy level of QDs before the processing into mesa structures. That is, according to (1), the probability of existence of such a QD is estimated as 17% before the processing; whereas the measured value after the mesa processing was 30%. This is presumably attributable to changes in the quantized energy levels of QDs through the mesa processing. The changes presumably occur mainly in the periphery of mesa structures, where damage is likely to occur. Thus, by alleviating damage to QDs by adding a passivation regime in the mesa periphery, improvement in the device fabrication yield can be expected [22].

Finally, the meanings of "resonant" and "slightly off-resonant" device operation conditions described in Sect. 2 will be clarified, and it will be pointed out that the device operates by way of energy transfer via dressed photons instead of the ordinary Förster mechanism. Light emission by recombination of electrons and holes through the $E_{1,\mathrm{e}}–E_{1,\mathrm{h}}$ transition in QD1 and the $E_{0,\mathrm{e}}–E_{0,\mathrm{h}}$ transition in QD2 contribute to the white triangles and circles in the vicinity of the red curve B in Fig. 9. Thus, two Lorentzian curves overlap. Figure 10 shows the results of plotting the energy difference $E(\mathrm{QD2}{:}E_{0,\mathrm{e}}–E_{0,\mathrm{h}}) - E(\mathrm{QD1}{:}E_{1,\mathrm{e}}–E_{1,\mathrm{h}})$ between the peaks of the two Lorentzian curves for AND gates and NOT gates. White circles in the figure are distributed in a range of the absolute value of $E(\mathrm{QD2}{:}E_{0,\mathrm{e}}–E_{0,\mathrm{h}}) - E(\mathrm{QD1}{:}E_{1,\mathrm{e}}–E_{1,\mathrm{h}})$ between 10 and 20 meV. Thus, it is understood that "slightly off-resonant," which is to be satisfied by $E(\mathrm{QD1}{:}E_{1,\mathrm{e}}–E_{1,\mathrm{h}})$ and $E(\mathrm{QD2}{:}E_{0,\mathrm{e}}–E_{0,\mathrm{h}})$ of two QDs constituting a NOT gate, refers to a state of detuning from resonance by approximately 10 to 20 meV. On the other hand, as for AND gates, as indicated by white triangles in the figure, of 14 devices examined, $E(\mathrm{QD2}{:}E_{0,\mathrm{e}}–E_{0,\mathrm{h}}) - E(\mathrm{QD1}{:}E_{1,\mathrm{e}}–E_{1,\mathrm{h}}) = 0$ (i.e., separation by fitting was not possible due to their homogeneous broadening) for 11 devices. By comparing these values, it is understood that $E(\mathrm{QD1}{:}E_{1,\mathrm{e}}–E_{1,\mathrm{h}})$ and $E(\mathrm{QD2}{:}E_{0,\mathrm{e}}–E_{0,\mathrm{h}})$ are resonant with each other and QD1 and QD2 operate as an AND gate if $E(\mathrm{QD1}{:}E_{1,\mathrm{e}}–E_{1,\mathrm{h}})$ and $E(\mathrm{QD2}{:}E_{0,\mathrm{e}}–E_{0,\mathrm{h}})$ are close

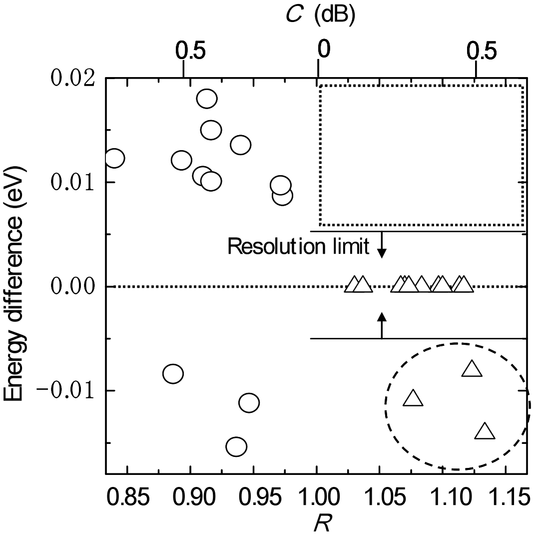

Fig. 10 Result of plotting the energy difference $E(\mathrm{QD2}{:}E_{0,\mathrm{e}}\text{–}E_{0,\mathrm{h}}) - E(\mathrm{QD1}{:}E_{1,\mathrm{e}}\text{–}E_{1,\mathrm{h}})$ of peaks of light emission along the *curve B* in Fig. 9 as a function of R of individual mesa structures, together with the values of C. The *white triangles* represent AND gates, and the *white circles* represent NOT gates

enough to each other that these energies are inseparable due to their homogeneous broadenings.

The devices indicated by three white triangles in a broken ellipse in Fig. 10 are considered to operate as AND gates by resonance between the energy $E(\mathrm{QD1}{:}E_{1,\mathrm{e}}\text{–}E_{0,\mathrm{h}})$ of the electric dipole-forbidden transition ($E_{1,\mathrm{e}}\text{–}E_{0,\mathrm{h}}$ transition) in QD1 and the energy $E(\mathrm{QD2}{:}E_{0,\mathrm{e}}\text{–}E_{0,\mathrm{h}})$ of the electric dipole-allowed transition ($E_{0,\mathrm{e}}\text{–}E_{0,\mathrm{h}}$ transition) in QD2 instead of the operation condition $E(\mathrm{QD2}{:}E_{0,\mathrm{e}}\text{–}E_{0,\mathrm{h}}) - E(\mathrm{QD1}{:}E_{1,\mathrm{e}}\text{–}E_{1,\mathrm{h}}) = 0$. This is because of the following two reasons: (i) The photon energy of $E(\mathrm{QD1}{:}E_{1,\mathrm{e}}\text{–}E_{0,\mathrm{h}})$ of the electric dipole-forbidden transition estimated on the basis of the band offset of InAs and GaAs [23] is 11 meV lower than that of $E(\mathrm{QD1}{:}E_{1,\mathrm{h}}\text{–}E_{1,\mathrm{e}})$. This value substantially coincides with the value of $E(\mathrm{QD2}{:}E_{0,\mathrm{e}}\text{–}E_{0,\mathrm{h}}) - E(\mathrm{QD1}{:}E_{1,\mathrm{e}}\text{–}E_{1,\mathrm{h}})$ of the devices indicated by the three white triangles in the broken ellipse in Fig. 10. (ii) We were unable to find AND gates in the region where electric dipole-forbidden transitions as in (i) above are absent ($E(\mathrm{QD2}{:}E_{0,\mathrm{e}}\text{–}E_{0,\mathrm{h}}) - E(\mathrm{QD1}{:}E_{1,\mathrm{e}}\text{–}E_{1,\mathrm{h}}) > 0$; the dotted rectangular region at the upper right part of Fig. 10). The occurrence of energy transfer via electric dipole-forbidden transitions indicates that the device operates through energy transfer between QDs via exchange of dressed photons instead of the ordinary Förster mechanism [1, 11].

6 Conclusions

By using mesa structures of InAs QDs, we succeeded for the first time in fabricating nanophotonic logic gates that operated at room temperature. The mesa dimensions were 300 nm × 300 nm × 85 nm and 200 nm × 200 nm × 85 nm, and the mesa structures were arrayed two-dimensionally on a GaAs substrate at an areal density of $1 \times 10^8\ \mathrm{cm}^{-2}$. A device is formed of two quantum dots vertically aligned in a mesa structure. Of 133 mesa structures having dimensions of 300 nm on each side, 53 operated as AND gates and 50 operated as NOT gates. Of 126 devices having dimensions of 200 nm on each side, 36 operated as AND gates and 36 operated as NOT gates. In order to fabricate a NOT gate, the absolute value of the energy difference between $E(\mathrm{QD2}{:}E_{0,\mathrm{e}}\text{–}E_{0,\mathrm{h}})$ and $E(\mathrm{QD1}{:}E_{1,\mathrm{e}}\text{–}E_{1,\mathrm{h}})$ must be 10 to 20 meV. On the other hand, an AND gate operates if $E(\mathrm{QD2}{:}E_{0,\mathrm{e}}\text{–}E_{0,\mathrm{h}}) = E(\mathrm{QD1}{:}E_{1,\mathrm{e}}\text{–}E_{1,\mathrm{h}})$, and also operates if the condition $E(\mathrm{QD2}{:}E_{0,\mathrm{e}}\text{–}E_{0,\mathrm{h}}) = E(\mathrm{QD1}{:}E_{1,\mathrm{e}}\text{–}E_{0,\mathrm{h}})$ is satisfied, even in the condition of an electric dipole-forbidden transition. By precisely controlling the quantized energy levels of QDs through optimization of the mesa processing and use of the photo-assisted size-controlled growth [24], the device fabrication yield is expected to improve even further.

Acknowledgement This paper belongs to “Innovative nanophotonics components development project” which OITDA contracted with The New Energy and Industrial Technology Development Organization (NEDO) since 2006.

References

1. M. Ohtsu, T. Kawazoe, T. Yatsui, M. Naruse, IEEE J. Sel. Top. Quantum Electron. **14**, 1404 (2008)
2. T. Kawazoe, K. Kobayashi, S. Sangu, M. Ohtsu, Appl. Phys. Lett. **82**, 2957 (2003)
3. T. Yatsui, S. Sangu, T. Kawazoe, M. Ohtsu, S.J. An, J. Yoo, G.C. Yi, Appl. Phys. Lett. **90**, 223110 (2007)
4. T. Kawazoe, K. Kobayashi, K. Akahane, M. Naruse, N. Yamamoto, M. Ohtsu, Appl. Phys. B: Laser Opt **84**, 243 (2006)
5. S. Sangu, K. Kobayashi, A. Shojiguchi, M. Ohtsu, Phys. Rev. B **69**, 115334 (2004)
6. M. Naruse, H. Hori, K. Kobayashi, P. Holmstrom, L. Thylen, M. Ohtsu, Opt. Express **18**, A544 (2010)
7. T. Kawazoe, K. Kobayashi, S. Takubo, M. Ohtsu, J. Chem. Phys. **122**, 024715 (2005)
8. H. Yonemitsu, T. Kawazoe, K. Kobayashi, M. Ohtsu, J. Lumin. **122–123**, 230 (2007)
9. T. Yatsui, K. Hirata, W. Nomura, Y. Tabata, M. Ohtsu, Appl. Phys. B **93**, 55 (2008)
10. K. Kobayashi, A. Sato, T. Yatsui, T. Kawazoe, M. Ohtsu, Appl. Phys. Express **2**, 075504 (2009)
11. T. Kawazoe, K. Kobayashi, J. Lim, Y. Narita, M. Ohtsu, Phys. Rev. Lett. **88**, 067404 (2002)
12. K. Kobayashi, S. Sangu, T. Kawazoe, M. Ohtsu, J. Lumin. **112**, 117 (2005)
13. T. Kawazoe, K. Kobayashi, M. Ohtsu, Appl. Phys. Lett. **86**, 103102 (2005)
14. G.A. Narvaez, A. Zunger, Phys. Rev. B **74**, 045316 (2006)
15. K.H. Schmidt, G. Medeiros-Ribeiro, M. Oestreich, P.M. Petroff, Phys. Rev. B **54**, 11346 (1996)
16. L. He, G. Bester, Z. Su, A. Zunger, Phys. Rev. B **76**, 035313 (2007)

17. S. Guha, A. Madhukar, K.C. Rajkumar, Appl. Phys. Lett. **57**, 2110 (1990)
18. V. Zwiller, H. Blom, P. Jonsson, N. Panev, S. Jeppesen, T. Tsegaye, E. Goobar, M.E. Pistol, L. Samuelson, G. Björk, Appl. Phys. **78**, 2476 (2001)
19. Z. Mi, P. Bhattacharya, J. Appl. Phys. **98**, 023510 (2005)
20. P. Borri, W. Langbein, J. Mørk, J.M. Hvam, F. Heinrichsdorff, M.-H. Mao, D. Bimberg, Phys. Rev. B **60**, 7784 (1999)
21. F. Yu, J. Suganda, Y. Shizuhuo (eds.), *Introduction to Information Optics* (Academic Press, San Diego/London, 2001), p. 202
22. R. Dylewicza, R.M. De La Rue, R. Wasielewski, P. Mazur, G. Mezősi, A.C. Bryce, J. Vac. Sci. Technol. B **28**, 882 (2010)
23. D.J. Arent, K. Deneffe, C. Van Hoof, J. De Boeck, G. Borghs, J. Appl. Phys. **66**, 1739 (1989)
24. T. Yatsui, M. Ohtsu, Appl. Phys. Lett. **95**, 043104 (2009)

Japanese Journal of Applied Physics **50** (2011) 04DH05 **REGULAR PAPER**
DOI: 10.1143/JJAP.50.04DH05

Energy Transfer in Multi-Stacked InAs Quantum Dots

Kouichi Akahane[1]*, Naokatsu Yamamoto[1], Makoto Naruse[1,2,3],
Tadashi Kawazoe[2,3], Takashi Yatsui[2,3], and Motoichi Ohtsu[2,3]

[1] *National Institute of Information and Communications Technology, Koganei, Tokyo 184-8795, Japan*
[2] *Department of Electrical Engineering and Information Systems, Graduate School of Engineering, The University of Tokyo, Bunkyo, Tokyo 113-8656, Japan*
[3] *Nanophotonics Research Center, Graduate School of Engineering, The University of Tokyo, Bunkyo, Tokyo 113-8656, Japan*

Received September 21, 2010; accepted November 1, 2010; published online April 20, 2011

We fabricated a modulated stacked quantum dot (QD) structure to investigate energy transfer among QDs using a strain compensation technique that allowed us to fabricate a vertically aligned, highly stacked structure without any degradation in crystal quality. Enhanced photoluminescence (PL) intensity for the ground state of large QDs was clearly observed in a sample where the ground state of small QDs was resonant to the first excited state of large QDs, indicating energy transfer from small QDs to large QDs. Long-range energy transfer reached approximately 200 nm and can be considered from the measurement of N dependence of PL intensity. © 2011 The Japan Society of Applied Physics

1. Introduction

Excitation energy transfer between semiconductor quantum dots (QDs) is attracting considerable research interest, with interlayer excitation energy transfer between QDs widely investigated based on carrier tunneling,[1–4] dipole-dipole interactions,[5] optical near-field interaction,[6,7] and carrier hopping[8,9] in self-assembled QDs systems. It is important to evaluate the energy transfer length for applications such as extremely small, low-power signal processors and high efficiency solar cells, since their performance is based on these phenomena. However, it is difficult to evaluate energy transfer length systematically in a self-assembled QD system, because QDs are distributed randomly on the semiconductor surface. Even with QDs aligned vertically in a stacked structure, fabrication of a stacking structure with multiple layers is difficult because of the accumulation of strain energy, which generates defects and dislocations in the structure.[10,11] Therefore, almost all of the investigations have been conducted using two QD systems.

We have developed a method of stacking InAs QDs grown on InP(311)B using a strain compensation scheme.[12,13] In this scheme, spacer layers with a lattice constant slightly smaller than that of the substrate are used to embed the QD layers. Using this method, we successfully stacked 300 InAs QD layers without any degradation in QD quality.[14] We believe that there is no limit to the number of QD layers that can be stacked using this method. This enables use of the optimum number of QD layers for any given application. In addition, emission wavelength can be changed by altering QD growth thickness without degrading crystal quality, as long as the strain compensation condition is satisfied. Therefore, this material system is considered to be ideal for investigating energy transfer length among QDs. In this paper, we investigate energy transfer in highly stacked QDs using the photoluminescence (PL) method.

2. Experiments

All samples were fabricated using conventional solid-source molecular beam epitaxy (MBE). We fabricated the highly stacked QD structures on an InP(311)B substrate. The value of the lattice constant of InP lies between the values of those of GaAs and InAs. This means that the lattice constant of InGaAlAs can be varied continuously around that of InP by controlling its composition. Thus, strain compensation can be achieved by capping the InAs QDs with an InGaAlAs layer, the lattice constant of which is slightly smaller than that of the InP substrate. We defined the strain-compensation conditions as

$$d_{\mathrm{QD}} \cdot \varepsilon_{\mathrm{QD}} = -d_{\mathrm{s}} \cdot \varepsilon_{\mathrm{spacer}}, \tag{1}$$

$$\varepsilon_{\mathrm{QD}} = \frac{a_{\mathrm{QD}} - a_{\mathrm{sub}}}{a_{\mathrm{sub}}}, \tag{2}$$

$$\varepsilon_{\mathrm{spacer}} = \frac{a_{\mathrm{spacer}} - a_{\mathrm{sub}}}{a_{\mathrm{sub}}}, \tag{3}$$

where d_{QD} and d_{s} are the thicknesses of the deposited QDs and spacer layers, respectively, and a_{QD}, a_{sub}, and a_{spacer} are the lattice constants of the InAs, InP, and InGaAlAs spacer layers, respectively. This definition is based on the simple approximation that the total strain energy of a set, containing one layer of QDs and one spacer layer, is zero. First, we fabricated two 60-layer stacked samples with $d_{\mathrm{QD}}/d_{\mathrm{spacer}} = 3\,\mathrm{ML}/15\,\mathrm{nm}$ and $d_{\mathrm{QD}}/d_{\mathrm{spacer}} = 4\,\mathrm{ML}/20\,\mathrm{nm}$ to check the emission wavelength. We then fabricated modulated sample, continuously stacked N layers/one layer/$N+1$ layers, where N and $N+1$ layers correspond to a 3-ML QD layer and one layer corresponds to a 4-ML QD layer. We fabricated three samples of $N = 5$, 10 and 20. Post-growth surface morphology was observed using an atomic force microscope (AFM) under normal atmospheric conditions. Photoluminescence (PL) measurements were carried out using the 532-nm line of a YVO laser, 250-mm monochromator, and electrically cooled PbS detector.

3. Results and Discussion

Figure 1 shows AFM images of a 60-layer stacked sample with (a) 3- and (b) 4-ML QDs. While degradation of the surface morphology is usually observed in a large number of stacks of normal QD structures, such as InAs QDs on GaAs, this sample shows good surface morphology with the formation of uniform QDs, even though 60 QD layers were stacked. The average lateral size in the $[\bar{2}33]$ direction, height, and density of the QDs were (a) 42.8 nm, 2.7 nm, and $8.4 \times 10^{10}/\mathrm{cm}^2$ and (b) 47.9 nm, 4.5 nm, and $9.0 \times 10^{10}/\mathrm{cm}^2$, respectively. The larger QDs were fabricated in the sample with the 4-ML QDs.

Figure 2 shows the PL spectra of 3- and 4-ML QDs measured at room temperature. Four-ML QDs shows longer

---

*E-mail address: akahane@nict.go.jp

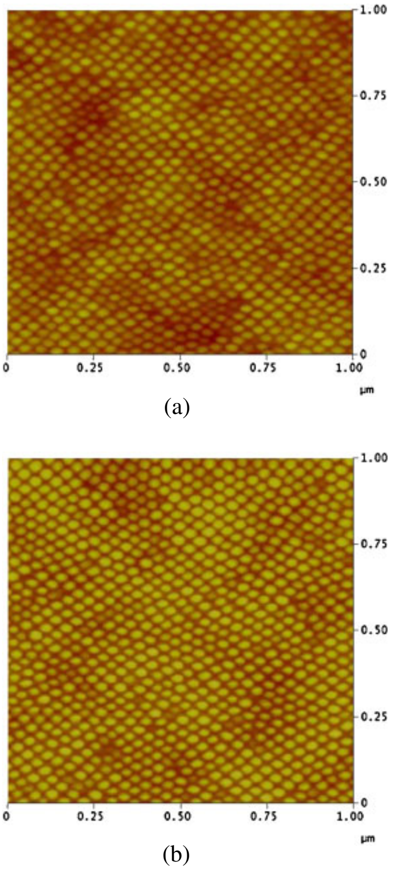

(a)

(b)

Fig. 1. (Color online) AFM images 60-layer stacked QDs with thickness of (a) 3- and (b) 4-ML.

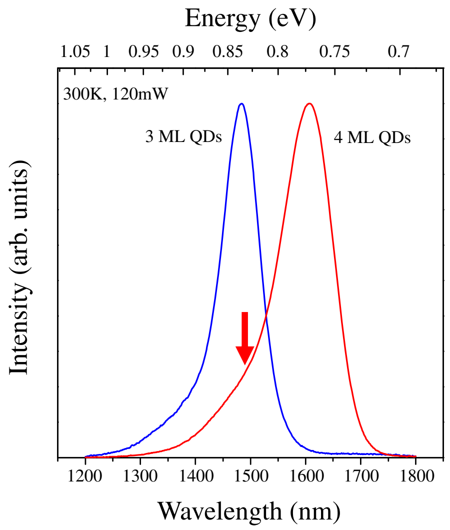

Fig. 2. (Color online) PL spectra of 60-layer stacked QDs with thickness of 3- and 4-ML.

wavelength emissions at 1607 nm, which corresponds to the ground state of 4-ML QDs, depending on the size of the QDs. This emission wavelength shows similar value of our previous calculation.[13)] There are small peaks in the shorter wavelength region of the main peak corresponding to the excited states of 4-ML QDs (as indicated by arrow). This peak energy is the same as the main emission of 3-ML QDs (ground state, 1484 nm). Therefore, the energy transfer from 3-ML QDs to 4-ML QDs is enhanced when 3- and 4-ML QDs exist in the same sample because the ground state of 3-ML QDs is resonant to the first excited state of 4-ML QDs.

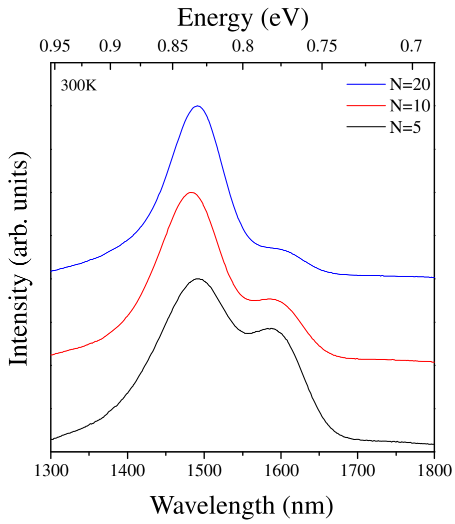

Fig. 3. (Color online) N dependence of PL spectra of modulated stacking structure of QDs.

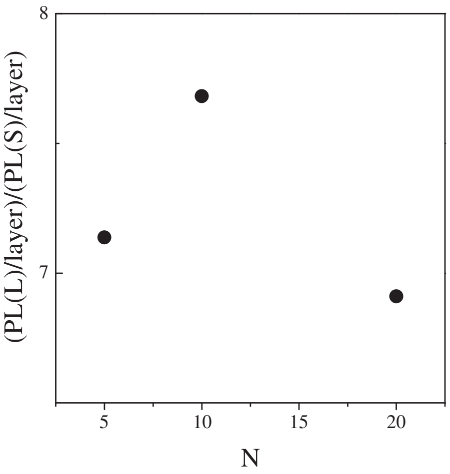

Fig. 4. N dependence of the ratio of PL intensity per QD layers.

Figure 3 shows the PL spectrum for modulated samples $N = 5$, 10, and 20. The ground state emission of 4-ML QDs shows a large intensity even if there is only one layer of 4-ML QDs in these samples. For example, although the ratio of the 4-ML QD layer to the 3-ML QD layer is 0.1, the peak intensity of 4-ML QDs is 0.71 times as strong as that of 3-ML QDs. This clearly shows that energy transfer occurs from small QDs to large QDs. These amplified PL emissions of 4-ML QDs were observed in all of the samples we fabricated ($N = 5$, 10, and 20).

We evaluated the ratio of PL intensity per dot layer as

$$\frac{\mathrm{PL(large\ QD)/layer}}{\mathrm{PL(small\ QD)/layer}}, \qquad (4)$$

where PL(small QD) and PL(large QD) denotes the PL intensity of 3- and 4-ML QDs. Figure 4 shows the N dependence of the ratio of PL intensity per dot layer. The ratio of PL intensity per dot layer increased with increasing

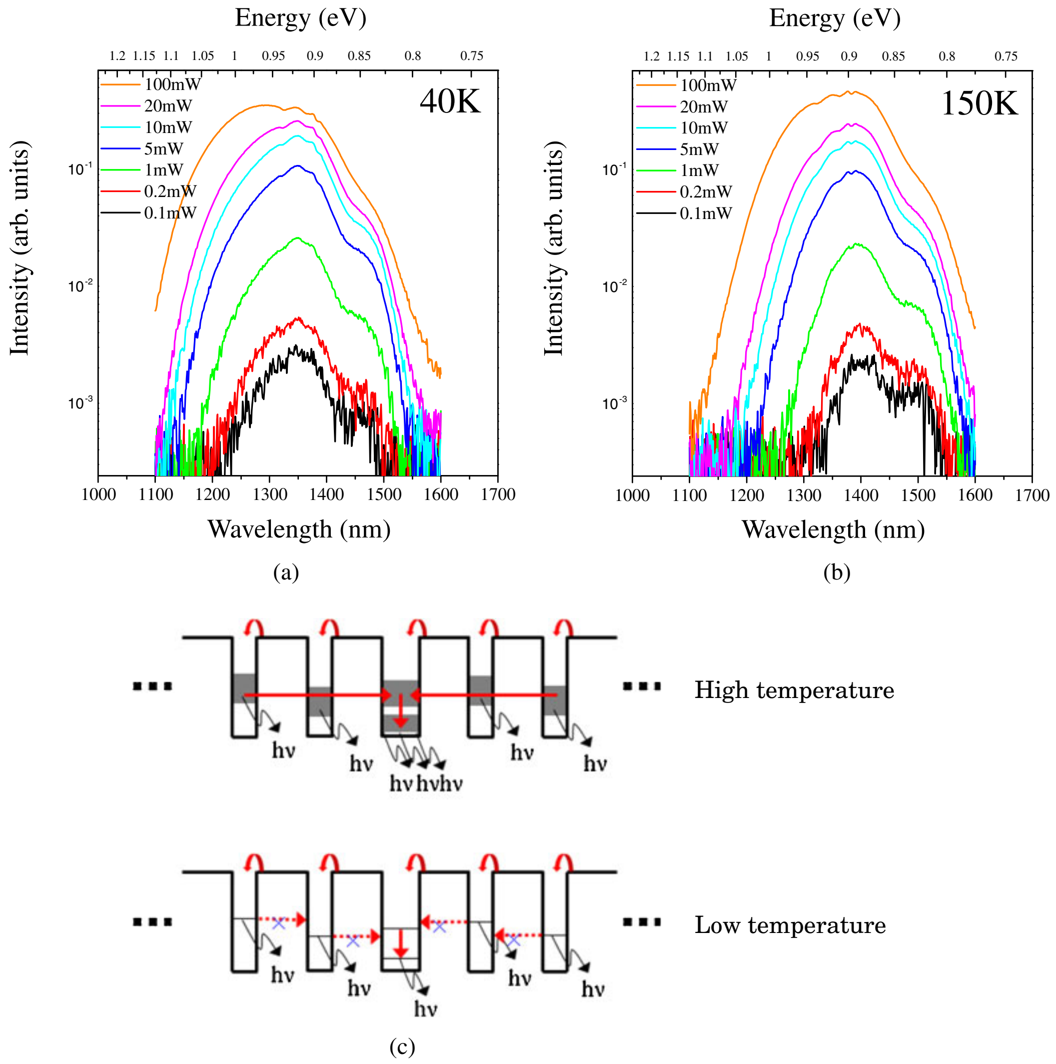

(a)

(b)

(c)

Fig. 5. (Color online) Excitation intensity dependence of PL spectra at (a) 40 and (b) 150 K. (c) Schematic mechanisms of energy transfer.

N then decreased with increasing N. The maximum ratio of PL intensity per dot layer is around $N = 10$. This result implies that long-range energy transfer of about 200 nm should occur in these samples.

The energy transfer length should depend on excitation intensity and temperature. We therefore investigated the dependence of excitation intensity and temperature for the PL spectrum. Figures 5(a) and 5(b) shows the excitation intensity dependence for PL spectra at 40 and 150 K, respectively. At 40 K, the relationship of PL intensity between 3- and 4-ML QDs was similar in the dependence of excitation intensity. At 150 K, the relationship of PL intensity between small and large QDs has changed in the dependence of excitation intensity. PL intensity for small and large QDs at low excitation is almost same so that a number of excited carriers, or excitons, were transferred from small QDs to large QDs. The ratio of PL intensity of small QDs and large QDs increased with increasing excitation intensity. We consider the mechanisms of these phenomena to be as shown in Fig. 5(c). At higher temperatures, the homogeneous energy width of QDs will expand, and energy transfer will occur with a strong probability. In contrast, at lower temperatures, the homogeneous energy width of QDs will contract, and energy transfer will be restricted because there are certain differences in energy with an inhomogeneous size distribution of QDs. We conclude that it is important to control both the size uniformity of QDs, which has implications for QD energy levels, and the homogeneous broadening of the QD state for complete control of energy transfer between QDs.

4. Conclusions

We fabricated a modulated stacked QD structure to investigate energy transfer among QDs. We fabricated a high-quality, highly stacked InAs QDs structure on an InP(311)B substrate using the strain compensation technique. Energy transfer from small QDs to large QDs was clearly observed in the sample where the ground state of small QDs is resonant to the first excited state of large QDs. Long-range energy transfer, which reached approximately 200 nm, can be considered from the measurement of N dependence of PL intensity. The importance of controlling both the size uniformity of QDs and the homogeneous broadening of the QD state was clarified from the dependence of PL spectra on excitation intensity and temperature for complete control of energy transfer between QDs.

Acknowledgements

We would like to acknowledge the staff of the Photonic Device Laboratory at NICT for their technical support in device fabrication.

---

1) R. Heitz, I. Mukhametzhanov, P. Chen, and A. Madhukar: Phys. Rev. B **58** (1998) R10151.
2) A. Tackeuchi, T. Kuroda, K. Mase, Y. Nakata, and N. Yokoyama: Phys. Rev. B **62** (2000) 1568.
3) Yu. I. Mazur, Zh. M. Wang, G. G. Tarasov, M. Xiao, G. J. Salamo, J. W. Tomm, V. Talalaev, and H. Kissel: Appl. Phys. Lett. **86** (2005) 063102.
4) Yu. I. Mazur, X. Wang, Z. M. Wang, G. J. Salamo, M. Xiao, and H. Kissel: Appl. Phys. Lett. **81** (2002) 2469.
5) C. R. Kagan, C. B. Murray, M. Nirmal, and M. G. Bawendi: Phys. Rev. Lett. **76** (1996) 1517.
6) M. Ohtsu and H. Hori: *Near-Field Nano-Optics: From Basic Principles to Nano-Fabrication and Nano-Photonics* (Kluwer, Dordrecht, 1999).
7) M. Ohtsu, K. Kobayashi, T. Kawazoc, S. Sangu, and T. Yatsui: IEEE J. Sel. Top. Quantum Electron. **8** (2002) 839.
8) Z. Y. Xu, Z. D. Lu, X. P. Yang, Z. L. Yuan, B. Z. Zheng, J. Z. Xu, W. K. Ge, Y. Wang, J. Wang, and L. L. Chang: Phys. Rev. B **54** (1996) 11528.
9) A. Polimeni, A. Patanè, M. Henini, L. Eaves, and P. C. Main: Phys. Rev. B **59** (1999) 5064.
10) K. Shiramine, Y. Horisaki, D. Suzuki, S. Itoh, Y. Ebiko, S. Muto, Y. Nakata, and N. Yokoyama: Jpn. J. Appl. Phys. **37** (1998) 5493.
11) K. M. Kim, Y. J. Park, C. H. Roh, Y. M. Park, E. K. Kim, C. K. Hyon, J. H. Park, and T. W. Kim: Jpn. J. Appl. Phys. **42** (2003) 54.
12) K. Akahane, N. Ohtani, Y. Okada, and M. Kawabe: J. Cryst. Growth **245** (2002) 31.
13) K. Akahane, N. Yamamoto, S. Gozu, A. Ueta, N. Ohtani, and M. Tsuchiya: Proc. Int. Conf. Indium Phosphide and Related Materials (IPRM'06), 2006, p. 192.
14) K. Akahane, N. Yamamoto, and T. Kawanishi: to be published in Phys. Status Solidi A.

Size control of sol–gel-synthesized ZnO quantum dots using photo-induced desorption

2011 Nanotechnology 22 215605

(http://iopscience.iop.org/0957-4484/22/21/215605)

IOP Publishing Nanotechnology

Nanotechnology **22** (2011) 215605 (5pp) doi:10.1088/0957-4484/22/21/215605

Size control of sol–gel-synthesized ZnO quantum dots using photo-induced desorption

Y Liu[1], T Morishima[1], T Yatsui[1,2], T Kawazoe[1,2] and M Ohtsu[1,2]

[1] Department of Electrical Engineering and Information Systems, School of Engineering, The University of Tokyo, Tokyo 113-8656, Japan
[2] Nanophotonics Research Center, The University of Tokyo, Tokyo 113-8656, Japan

E-mail: ryu@nanophotonics.t.u-tokyo.ac.jp

Received 4 December 2010, in final form 8 March 2011
Published 30 March 2011
Online at stacks.iop.org/Nano/22/215605

Abstract

We developed a sol–gel method using photo-induced desorption for size-controlled ZnO quantum dots (QDs). This method successfully controlled the size and size variance of ZnO QDs, and size fluctuations decreased from 23% to 18% depending on the illuminated light intensity. The sol–gel synthesis effectively reduced the number of defect levels that originated from oxygen defects.

(Some figures in this article are in colour only in the electronic version)

1. Introduction

Optical near-field energy transfer between quantum dots (QDs) has been applied to the production of nanophotonic devices [1–4] because it decreases the device size beyond the diffraction limit of light and achieves novel functions unattainable using conventional propagating light. Furthermore, it drastically decreases the magnitude of power consumption [5]. Logic devices, including AND gates [6] and NOT gates [7], light-harvesting nanofountains [8], and nanophotonic couplers [9] have been demonstrated as nanophotonic devices. Several semiconductor materials, including CuCl [10], InAs [11], InGaAs [12], and CdCe [9], have been used for QDs. Additionally, ZnO is a promising candidate material because of its large exciton binding energy [13]. Moreover, AND-gate operation has been demonstrated using ZnO nanorod multi-quantum wells [14].

For more advanced nanophotonic devices using ZnO, it is advantageous to replace the nanorod quantum wells with QDs for larger confinement energies. For this replacement, QD size should be controlled to ensure that the quantized energy levels are resonant, facilitating efficient optical near-field interaction. For ZnO QDs that are 5 nm, the size-mismatching between the QDs must be within 10% (i.e., 0.5 nm) to maintain the resonance condition, as estimated based on the broadening (30 meV) of the discrete energy levels of excitons, which is determined by the magnitude of the thermal energy at room temperature [3]. Among the methods used to grow ZnO QDs, such as laser ablation [15] and molecular beam epitaxy [16], synthetic methods using liquid solutions are advantageous because they result in high productivity and size-controlled ZnO QDs [17]. However, the size distributions of the QDs fluctuate depending on the thermal equilibrium condition of the chemical reaction [18], and the fluctuation can be as large as 25% for the conventional sol–gel method [2, 17].

This study introduced photo-induced desorption to the sol–gel method to reduce size fluctuations. When synthesized ZnO QDs are illuminated by light with photon energies higher than their bandgap energy, electron–hole pairs trigger an oxidation–reduction reaction in the QDs; thus, the ZnO atoms depositing on the QD surface are desorbed. The growth rate is controlled by the absorbed light intensity and wavelength, which control the QD size. Related methods for size-controlled QDs using photo-induced chemical processes have been reported for CdSe [19] and Si [20]. However, they were limited to etching the materials after growth, and particle size distributions were not quantitatively evaluated.

This paper discusses the role of photo-induced desorption in the sol–gel synthesis of ZnO QDs and the decrease in luminescence intensity due to the defect levels in ZnO QDs.

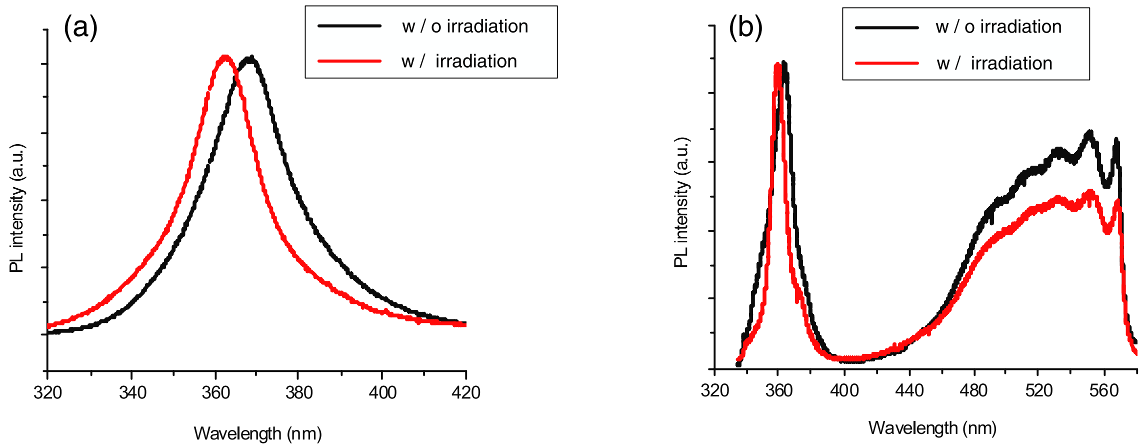

Figure 1. (a) PL spectra of ZnO QDs grown for six days (320–420 nm view) with a growth temperature of 300 K, without irradiation: ZnO QDs grown without light irradiation ($IPL_{w/o}$); and with irradiation: ZnO QDs grown with 325 nm laser irradiation ($IPL_{w/325}$). (b) PL spectra of ZnO QDs grown for six days (300–600 nm view) with a growth temperature of 293 K, without irradiation: ZnO QDs grown without light irradiation; and with irradiation: ZnO QDs grown with 325 nm laser irradiation.

2. Experimental technique

For the sol–gel synthesis of ZnO QDs, 1.1 g of zinc acetate dihydrate and 0.29 g of lithium hydroxide monohydrate were dissolved in ethanol (50 ml) individually, and then the two solutions were mixed at 273 K [2, 18]. The mixed solution was kept at room temperature (300 K) to grow the ZnO QD particles. After the ZnO QDs grew to the desired size, the solution was mixed with 300 ml of hexane to remove the lithium, which was used to accelerate the growth. Then, the ZnO QD growth was halted; thus, the size of the ZnO QDs was controlled. A continuum-wave (CW) He–Cd laser was used as a light source, and its wavelength ($\lambda = 325$ nm) was shorter than the absorption edge wavelength ($\lambda = 340$ nm). The irradiating laser (CW $\lambda = 325$ nm) had a uniform power density of 8 mW cm^{-3} and irradiated over the mixed solution during whole growing process.

3. Results and discussion

The synthesized ZnO QDs were dispersed uniformly over a sapphire substrate and were excited by the fourth harmonic ($\lambda = 266$ nm, power = 2 mW) of a YAG laser to measure their photoluminescence (PL) spectra at room temperature. The black and red curves in figure 1(a) show the measured profiles of QDs that were grown for six days either without light irradiation ($IPL_{w/o}$) or with irradiation from a 325 nm laser ($IPL_{w/325}$). The PL peak wavelength of $IPL_{w/325}$ was 6 nm blue-shifted compared with that of $IPL_{w/o}$, indicating that the growth rate decreased for the ZnO QDs under 325 nm laser irradiation.

To quantitatively analyze the mechanism of size control under light irradiation, we evaluated the ZnO QD diameters. The shape of the QDs synthesized by the sol–gel method is known to be spherical, although the crystalline structure of ZnO QDs is wurtzite [21]. In the present study, the QD shape was assumed to be spherical. The QD diameter was calculated using the effective mass approximation, in which the emission energy E_{em} from the recombination of free excitons confined in the QD can be described by the following equation [22]:

$$E_{em} = 3.37 + \frac{2\pi^2\hbar^2}{(m_e + m_h)ed^2} - \frac{13.6\mu}{m_0\varepsilon^2}. \qquad (1)$$

Here d is the QD diameter, m_e and m_h are the effective masses of electron and hole, m_0 is the electron mass of 9.11×10^{-31} (kg), μ is the translation mass described by $m_e m_h/(m_e + m_h)$, and e is the elementary electric charge. The third term in equation (1) is the correction term. The QD diameter d and the emission energy E_{em} were determined as the average diameter using transmission electron microscopy (TEM) images (figures 2(a)–(c)), and the respective PL spectra (figure 2(d)), and they are plotted as open circles in figure 2(e). Using these obtained data, we determined m_e and m_h. To obtain the black solid curve in figure 2 we used $m_e = 0.32m_0$, $m_h = 0.42m_0$. These values are in good agreement with the reported values in [23] ($m_e = 0.24m_0$ and $m_h = 0.45m_0$). Thus, we consider that the QD diameter can be determined using the effective mass approximation and the emission is originated from the recombination of free excitons confined in the QD. Based on the above estimation, we obtained the relationship between the growth time and the diameter (figure 3), showing that the growth rate decreased as irradiation power increased. The detailed irradiation power dependence analyzed using the rate equation will be discussed later.

Figures 4(a) and (b) show TEM images of ZnO QDs grown for three days without and with light irradiation, respectively. The lattice fringes of the ZnO QDs can be identified very clearly in the magnified images. The lattice spacings were estimated to be 0.274 nm (figure 4(a)) and 0.270 nm (figure 4(b)), which agree well with that of ZnO QDs along the c-axis [24], confirming sufficiently high-quality single-crystal growth. Figures 4(c) and (d) show the distribution of the ZnO QD diameters measured by the binarized TEM images shown in figures 4(a) and (b), respectively. Table 1 summarizes the diameters and diameter distributions of the ZnO QDs. The average diameter grown

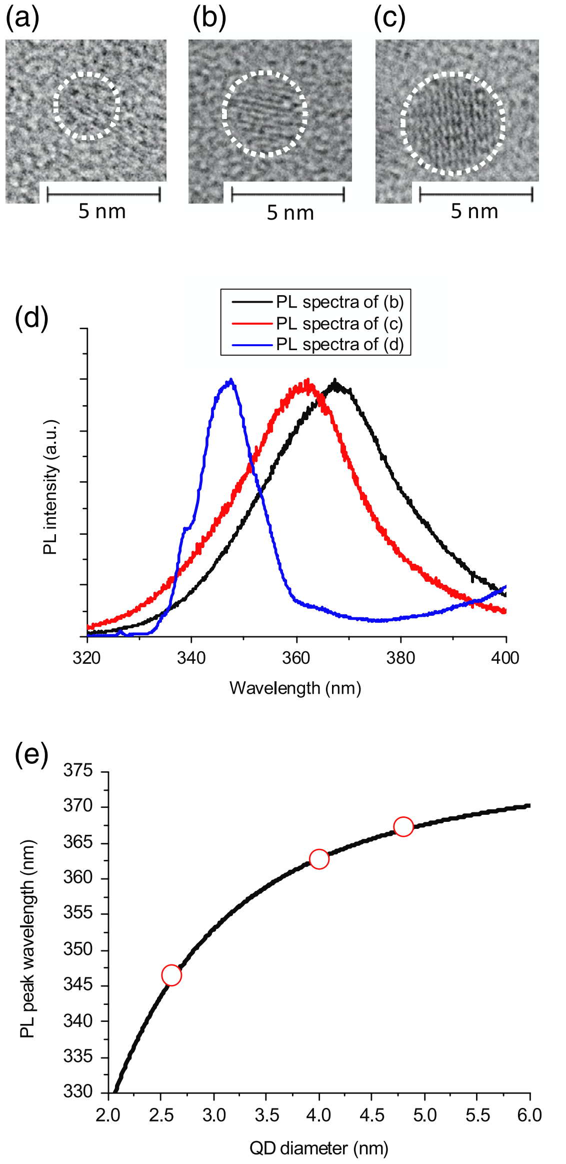

Figure 2. (a)–(c) Typical TEM images of ZnO QDs. (d) The respective PL spectra of the ZnO QDs of (a)–(c). (e) Relationship between QD diameter and PL peak wavelength. The open circles are plotted from the diameter determined using the TEM images ((a)–(c)) and the respective PL spectra (d). Using these obtained data, we determined m_e and m_h. The black solid curves are plotted using the values $m_e = 0.32m_0$, $m_h = 0.42m_0$ for equation (1).

with 325 nm laser irradiation was 4.1 nm, but it increased to 4.9 nm without light irradiation. These values agree well with the values estimated from the PL spectral peak wavelength in figure 3 (5.05 nm in diameter for ZnO QDs obtained through normal growth without light irradiation and 4.26 nm in diameter for ZnO QDs grown with 325 nm laser irradiation). Table 1 also shows that the full width at half maximum (FWHM) of the diameter distributions was 1.09 nm for ZnO QDs grown without light irradiation, whereas it was 0.71 nm for ZnO QDs grown with 325 nm light irradiation. This result indicates that the fluctuation in diameters decreased from 23% to 18% by introducing photo-desorption, confirming highly accurate particle size control.

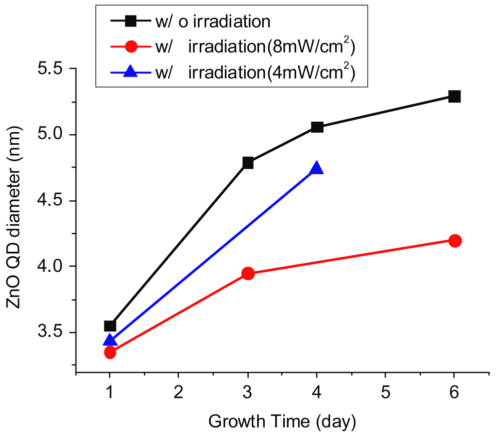

Figure 3. Dependence of ZnO QD diameter on growth time.

Table 1. ZnO QD diameter and diameter variance for respective growth conditions.

	QD diameter (nm)	FWHM of distribution (nm)	Variance (%)
Without irradiation	4.8	1.09	23
With irradiation	4.1	0.71	17

The ZnO QD growth rate was analyzed using a rate equation:

$$dV/dt = \alpha S - \beta V I, \qquad (2)$$

where V and S are the volume and the surface area of the QD, respectively. α and β are the proportionality constants. The first term of equation (2) represents the growth rate, which is proportional to the amount of the material to be adsorbed on the QD surface and is therefore proportional to S. The second term represents the desorption rate, which is proportional to the light intensity absorbed by QDs and is therefore proportional to V. By assuming a spherical shape, S is equal to $4\pi(3V/4\pi)^{2/3}$.

By fitting equation (2) to the experimental values obtained without light irradiation ($I = 0$ mW cm^{-2}), the value of α was 2.81. Next, by fitting to the experimental values for $I = 8$ mW cm^{-2}, $\beta_{I=8\ \mathrm{mW\ cm^{-2}}}$ was 0.032. Furthermore, $\beta_{I=4\ \mathrm{mW\ cm^{-2}}}$ was 0.029 for $I = 4$ mW cm^{-2}, which agrees well with the result for $\beta_{I=8\ \mathrm{mW\ cm^{-2}}}$. Thus, the above model is valid, indicating that particle sizes can be controlled in proportion to light intensity. Since we have confirmed that the spectral linewidth of ZnO single-quantum structures remained constant at excitation power densities ranging from 0.5 to 5 W cm^{-2} of CW light source ($\lambda = 325$ nm) [25], indicating that the increase in the temperature was negligible, it is therefore possible to decrease the size variance below 10% by increasing the light intensity without adverse effect on the QD properties.

The ability to excite defect levels of ZnO QDs suggests that the region causing these defect levels can be removed by photo-induced desorption. A defect level originates from an oxygen defect or an impurity in the ZnO QDs, and the energy level corresponding to such a defect level is lower than the bandgap energy. Thus, as the amount of defect levels increases,

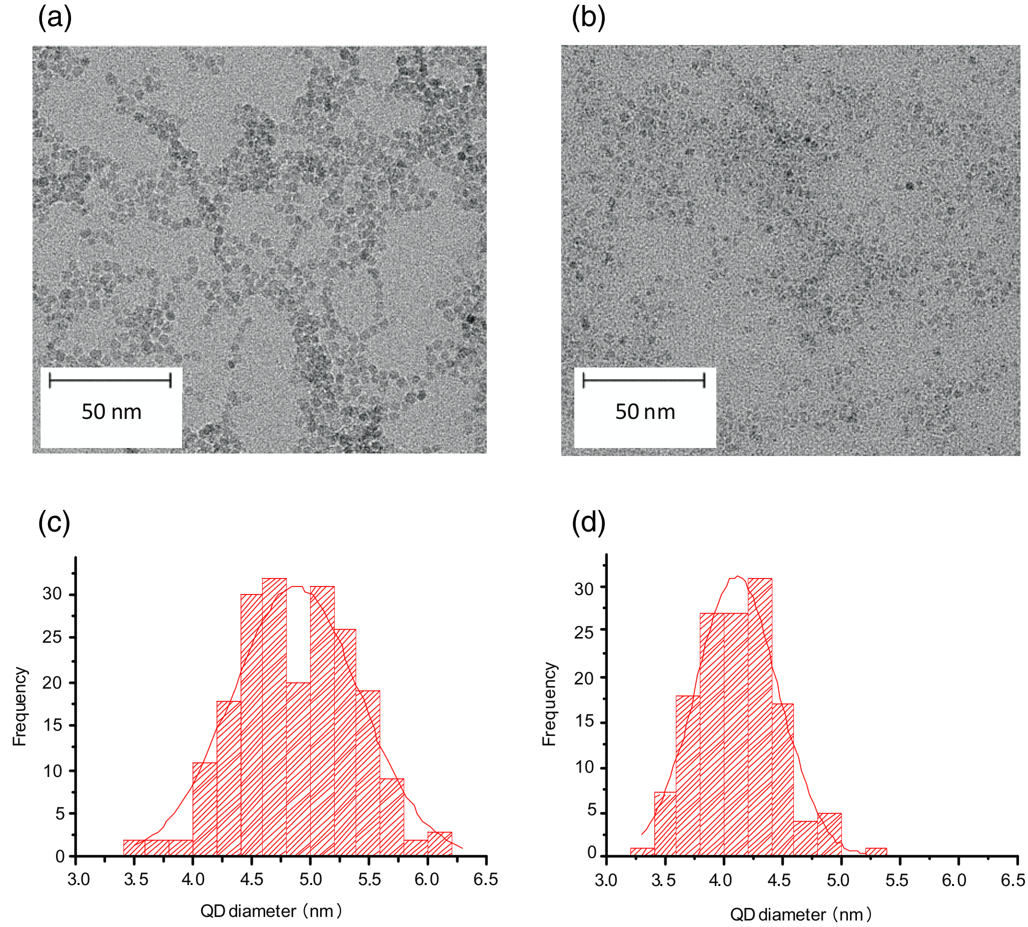

Figure 4. (a) TEM image of ZnO QDs deposited without light irradiation. (b) TEM image of ZnO QDs deposited with 325 nm laser irradiation. (c) Size distribution of ZnO QDs produced without light irradiation. (d) Size distribution of ZnO QDs produced with 325 nm laser irradiation.

the quantum efficiency of the ZnO QDs decreases. However, with this method, defect levels were removed preferentially because photo-induced desorption occurred in defect portions due to local oxidation–reduction reactions after the excited electron–hole pairs relaxed to those defect portions in the ZnO QDs. To confirm this phenomenon, PL spectra, including long wavelengths, for QDs grown for six days were analyzed (figure 1(b)). Compared with the PL spectrum without light irradiation (black solid curve), the PL intensity of QDs grown with 325 nm light irradiation (red solid curve) decreased by around 50 nm, indicating that higher crystallinity with fewer defect levels was achieved using photo-induced desorption.

4. Conclusion

We developed a sol–gel method using photo-induced desorption for size-controlled ZnO QDs and successfully controlled the QD size and size variance. Because size control was proportional to light irradiation power, we applied light irradiation with photon energy greater than the bandgap during ZnO QD growth. We analyzed changes in deposition rate based on light irradiation power using a theoretical model and a rate equation, and the results were in a good agreement with the experimental data. We also reduced the QD size variance from 23% to 18%, and further reduction in size variance can be expected by irradiating with higher intensity. Furthermore, this method achieved higher crystallinity; thus, higher energy transmission efficiency for nanophotonic devices using QDs is expected.

Acknowledgments

This research was partially supported by a grant for the Global COE Program, Secure-Life Electronics, from the Ministry of Education, Culture, Sports, Science and Technology of Japan, and by a research grant from The Murata Science Foundation.

References

[1] Kawazoe T, Kobayashi K, Lim J, Narita Y and Ohtsu M 2002 *Phys. Rev. Lett.* **88** 067404
[2] Yatsui T, Jeong H and Ohtsu M 2008 *Appl. Phys.* B **93** 199
[3] Ohtsu M, Kawazoe T, Yatsui T and Naruse M 2008 *IEEE J. Sel. Top. Quantum Electron.* **14** 1404
[4] Yatsui T, Ryu Y, Morishima T, Nomura W, Kawazoe T, Yonezawa T, Washizu M, Fujita H and Ohtsu M 2010 *Appl. Phys. Lett.* **96** 133106

[5] Naruse M, Hori H, Kobayashi K, Holmstrom P, Thylen L and Ohtsu M 2010 *Opt. Express* **18** A544
[6] Kawazoe T, Kobayashi K, Sangu S and Ohtsu M 2003 *Appl. Phys. Lett.* **82** 2957
[7] Kawazoe T, Kobayashi K, Akahane K, Naruse M, Yamamoto N and Ohtsu M 2006 *Appl. Phys.* B **84** 243
[8] Kawazoe T, Kobayashi K and Ohtsu M 2005 *Appl. Phys. Lett.* **86** 103102
[9] Nomura W, Yatsui T, Kawazoe T and Ohtsu M 2007 *J. Nanophoton.* **1** 011591
[10] Kawazoe T, Kobayashi K, Sangu S and Ohtsu M 2003 *J. Microsc.* **209** 261
[11] Nishibayashi K, Kawazoe T, Ohtsu M, Akahane K and Yamamoto N 2009 *J. Lumin.* **129** 1912
[12] Matsumoto T, Ohtsu M, Matsuda K, Saiki T, Saito H and Nishi K 1999 *Appl. Phys. Lett.* **75** 3346
[13] Sun H D, Makino T, Segawa Y, Kawasaki M, Ohtomo A, Tamura K and Koinuma H 2002 *J. Appl. Phys.* **91** 1993
[14] Yatsui T, Sangu S, Kobayashi K, Kawazoe T, Ohtsu M, Yoo J and Yi G C 2009 *Appl. Phys. Lett.* **94** 083113
[15] Besner S, kabashin A V, Winnik F M and Meunier M 2008 *Appl. Phys.* A **93** 955
[16] Wu H Z, Qiu D J, Cai Y J, Xu X L and Chen N B 2002 *J. Cryst. Growth* **245** 50
[17] Meulenkamp E A 1998 *J. Phys. Chem.* B **102** 5566
[18] Hendriks E M 1984 *Z. Phys.* B **57** 307
[19] Torimoto T, Murakami S, Sakuraoka M, Iwasaki K, Okazaki K, Shibayama T and Ohtani B 2006 *J. Phys. Chem.* B **110** 13314
[20] Koyama H and Koshida N 1993 *J. Appl. Phys.* **74** 6365
[21] Zhang L, Yin L W, Wang C, Lun N and Qi Y 2010 *Appl. Mater. Interface* **2** 1769
[22] Yoffe A D 2002 *Adv. Phys.* **2** 799 51
[23] Wood A, Giersig M, Hilgendorff M, Vilas-Campos A, Liz-Marzan L M and Mulvaney P 2003 *Aust. J. Chem.* **56** 1051
[24] Ozfu U, Alivov Ya l, Liu C, Teke A, Reshchikov M A, Dogan S, Avrutin V, Cho S J and Horkoc H 2005 *J. Appl. Phys.* **98** 041301
[25] Yatsui T, Ohtsu M, Yoo J, An S J and Yi G-C 2005 *Appl. Phys. Lett.* **87** 033101

Appl Phys B (2011) 102: 717–723
DOI 10.1007/s00340-010-4295-0

Applied Physics B
Lasers and Optics

Optical pulsation mechanism based on optical near-field interactions

M. Naruse · H. Hori · K. Kobayashi · T. Kawazoe · M. Ohtsu

Received: 26 October 2010 / Published online: 20 November 2010

Abstract We theoretically demonstrate optical pulsation based on optical near-field interactions between quantum nanostructures. It is composed of two quantum dot systems, each of which consists of a combination of smaller and larger quantum dots, so that optical excitation transfer occurs. With an architecture in which the two systems take the role of a timing delay and frequency up-conversion, we observe pulsation in populations pumped by continuous-wave light irradiation. The pulsation is induced with suitable setting of parameters associated with the optical near-field interactions. This will provide critical insights toward the design and implementation of experimental nanophotonic pulse generating devices.

1 Introduction

Nanophotonics, which is based on local interactions between nanometer-scale materials via optical near-field interactions, has been intensively studied in order to understand its unique physical attributes [1, 2] as well as for a wide range of industrial applications [3, 4]. System aspects of nanophotonics have been investigated in order to realize the basic functionalities required for information and communications technology (ICT) [5–7]. Generating an optical pulse train is one of the most important functionalities required for optical systems [8, 9], and pulsed signals are indispensable in digital systems in general. However, conventional principles of optical pulse generation are based on optical energy build-up in a cavity whose size is much larger than the optical wavelength; thus, the volume and the energy efficiency of the entire system have serious limitations. Therefore, for nanophotonics applications, novel principles should be developed for pulse generation based on light-matter interactions on the nanometer scale.

Shojiguchi et al. theoretically investigated the possibility of generating superradiance in N two-level systems interacting with optical near-fields [10]. This approach, however, requires precise control of the initial states of all of the N dipoles, which is not straightforward to implement. Also, the resultant pulse train cannot be sustained for a duration longer than the carrier lifetime dissipated to the far-field due to free photon emission.

Optical excitation transfer between quantum dots (QDs) via optical near-field interactions is one unique function available on the nanometer scale. Its theoretical fundamentals have been studied through the development of dressed photon models [1, 11], and experimental demonstrations have been shown, such as logic gates [12, 13], energy concentration [14, 15], and interconnects [16, 17].

In this paper, we propose and theoretically demonstrate a mechanism of optical pulsation based on optical excitation transfer via optical near-field interactions in quantum dot systems pumped by continuous-wave (CW) light irradiation. With an architecture composed of two subsystems taking the role of a timing delay and frequency up-conversion, re-

---

M. Naruse (✉)
National Institute of Information and Communications Technology, 4-2-1 Nukui-kita, Koganei, Tokyo 184-8795, Japan
e-mail: naruse@nict.go.jp
Fax: +81-42-3277035

M. Naruse · T. Kawazoe · M. Ohtsu
Department of Electrical Engineering and Information Systems and Nanophotonics Research Center, School of Engineering, The University of Tokyo, 2-11-16 Yayoi, Bunkyo-ku, Tokyo 113-8656, Japan

H. Hori · K. Kobayashi
Interdisciplinary Graduate School of Medicine and Engineering, University of Yamanashi, Kofu, Yamanashi 400-8511, Japan

spectively, we observe pulsation in the populations based on a model system using a density-matrix formalism. The experimental technology of optical excitation transfer, including long-range signal transfer [17], and fabrication technology of geometry-controlled quantum nanostructures, such as stacked QDs [18] or QD rings by droplet epitaxy [19] etc., has shown rapid progress; thus, it is important to design a fundamental mechanism of optical pulsation and to analyze important parameters associated with optical near-field interactions, which is the primary focus of this paper.

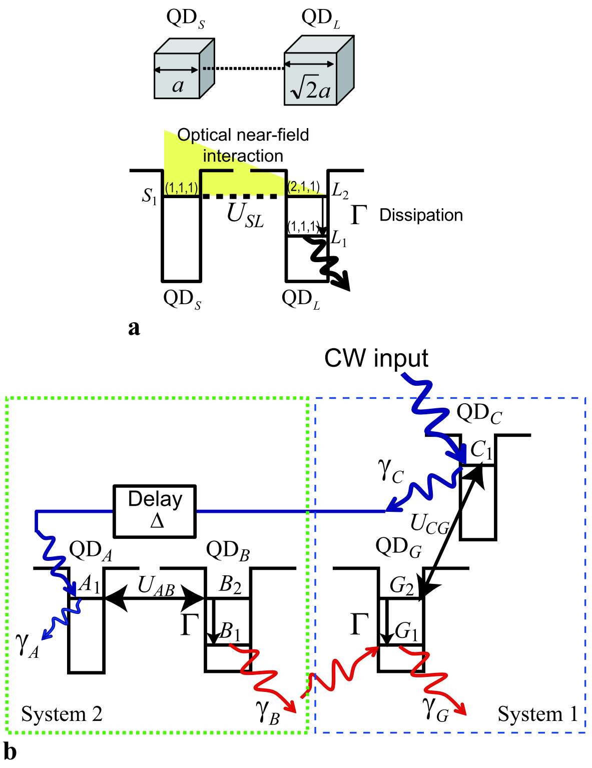

Fig. 1 (**a**) Optical excitation transfer from a smaller quantum dot (QD$_S$) to a larger one (QD$_L$) via optical near-field interaction. (**b**) The system architecture of pulsation based on optical excitation transfer. The two subsystems (System 1 and System 2) are each composed of smaller QDs (QD$_C$ and QD$_A$) and larger QDs (QD$_G$ and QD$_B$). The optical excitation transfer in System 1 is changed when the state filling effect occurs at the destination quantum dot, which originates from the change in System 1 with a certain delay time provided by System 2. System 1 is irradiated with continuous-wave (CW) light, taking the role of power supply for the pulsation

2 Theoretical elements of optical excitation transfer via optical near-field interaction

We first briefly review the principles of optical excitation transfer involving optical near-field interactions [1]. Conventionally, in the interaction Hamiltonian between an electron and an electric field, the operator corresponding to the electric field is assumed to be a constant (i.e., long-wavelength approximation), since the electric field of propagating light is uniform on the nanometer scale. As a consequence, the optical selection rule tells us that, in the case of cubic quantum dots, transitions to states described by quantum numbers containing an even number are prohibited. In the case of optical near-field interactions, on the other hand, due to the nanometrically localized nature of optical near-fields in the vicinity of nanometer-scale matter, an optical transition that violates conventional optical selection rules is allowed. Optical excitations in nanostructures, such as quantum dots, can be transferred to neighboring ones via optical near-field interactions. For instance, assume that two cubic quantum dots QD$_S$ and QD$_L$, whose side lengths are a and $\sqrt{2}a$, respectively, are located close to each other, as shown in Fig. 1a. Suppose that the energy eigenvalues for the quantized exciton energy level specified by quantum numbers (n_x, n_y, n_z) in the QD with side length $a(\mathrm{QD}_S)$ are given by

$$E_{(n_x,n_y,n_z)} = E_B + \frac{\hbar^2\pi^2}{2Ma^2}\left(n_x^2 + n_y^2 + n_z^2\right), \qquad (1)$$

where E_B is the energy of the bulk exciton, and M is the effective mass of the exciton. According to (1), there exists a resonance between the level of quantum number (1, 1, 1) of QD$_S$ and that of quantum number (2, 1, 1) of QD$_L$. There is an optical near-field interaction, which is denoted by U_{SL}, due to the localized electric field in the vicinity of QD$_S$. It is known that the inter-dot optical near-field interaction is given by a Yukawa-type potential [1]. Therefore, excitons in QD$_S$ can move to the (2, 1, 1)-level in QD$_L$. Note that such a transfer is prohibited for propagating light, since the (2, 1, 1)-level in QD$_L$ contains an even number. In QD$_L$, the exciton sees a sublevel energy relaxation, denoted by Γ, which is faster than the near-field interaction, and so the exciton relaxes to the (1, 1, 1)-level of QD$_L$.

Here, when the lower level of QD$_L$ is populated by external input, the optical excitation occurring in QD$_S$ cannot be transferred to QD$_L$, because the lower energy level in QD$_L$ is busy, which is called the state filling effect [1]. Putting it another way, the population of the (1, 1, 1)-level in QD$_S$ is changed by the external input applied to L_1 in QD$_L$. In other words, if we see the external input affecting the lower energy level of QD$_L$ as the input to the system and regard the radiation from QD$_S$ as the output signal, frequency upconversion is realized.

Now, the optical pulsation based on optical excitation transfer comes from the idea that the externally applied change induced in L_1 can be provided in a self-induced manner by S_1 with certain timing delay. If QD$_S$ is irradiated with continuous input light, such a change should last continuously with certain timing interval; that is, a pulsed signal should result, as explained in detail below.

3 Optical pulsation mechanism based on optical near-field interaction

We prepare two quantum dot systems, each of which is composed of one smaller and one larger QD, as shown in Fig. 1b. One system, called System 1 hereafter, serves as a primary system, represented by one smaller dot (QD$_C$) and one larger dot (QD$_G$). In the upper level of QD$_C$, a continuous-wave input is provided, which serves as the power supply for the pulsation. The optical near-field interaction between QD$_C$ and QD$_G$ is denoted by U_{CG}.

Another system, called System 2, is also represented by one smaller QD (QD$_A$) and one larger QD (QD$_B$). QD$_A$, accepts radiation from QD$_C$ in System 1; that is, the change of the states in QD$_C$ is transferred to QD$_A$. The optical excitation induced in QD$_A$ is transferred to QD$_B$ via the optical near-field interaction between QD$_A$ and QD$_B$ denoted by U_{AB}. The output from QD$_B$ then influences the lower energy level of QD$_G$.

The role of System 2 is, as discussed in detail below, to provide a delay time. Physically, a longer delay time is made possible by multiple use of smaller and larger dots, as already experimentally realized in Ref. [17]. Also, quantum dot arrangements of graded size, such as the optical nanofountain demonstrated by Kawazoe et al. [20] or exciton recycling realized by Franzl et al. [15], provide energy transfer from smaller to larger dots involving many QDs in the system as a whole. However, modeling the delay made of multiple QDs makes the discussion of pulsation mechanisms unnecessarily complicated; thus, we assume an arbitrary delay time applied to the input signal of System 2, denoted by Δ, followed by the last two quantum dots in the delay system, namely, a smaller QD (QD$_A$) and a larger QD (QD$_B$), as indicated in Fig. 1b.

We describe the details of the above modeling based on a density-matrix formalism. First, for System 1, there are in total three energy levels (namely, C_1 in QD$_C$, G_1 and G_2 in QD$_G$); thus, the number of different states occupying those energy levels is $2^3 (= 8)$. The radiative relaxation rates from C_1 and G_1 are, respectively, given by γ_C and γ_G. The quantum master equation of System 1 is then given by [21]

$$\begin{aligned}\frac{d\rho^{\text{Sys1}}(t)}{dt} &= -\frac{i}{\hbar}\left[H_{\text{int}} + H_{\text{ext}}^{\text{CW}}(t) + H_{\text{ext}}^{G}(t), \rho^{\text{Sys1}}(t)\right] \\ &\quad + \sum_{i=C_1,G_1} \frac{\gamma_i}{2}\big(2R_i\rho^{\text{Sys1}}(t)R_i^\dagger - R_i^\dagger R_i\rho^{\text{Sys1}}(t) \\ &\quad - \rho^{\text{Sys1}}(t)R_i^\dagger R_i\big) + \frac{\Gamma}{2}\big(2S\rho^{\text{Sys1}}(t)S^\dagger \\ &\quad - S^\dagger S\rho^{\text{Sys1}}(t) - \rho^{\text{Sys1}}(t)S^\dagger S\big), \end{aligned} \tag{2}$$

where H_{int} represents the interaction Hamiltonians. The two external Hamiltonian, denoted by $H_{\text{ext}}^{\text{CW}}(t)$ and $H_{\text{ext}}^{G}(t)$, are introduced later below. Let the (i,i) and (j,j) elements of the density matrix $\rho^{\text{Sys1}}(t)$, respectively, indicate two states that are transformable between each other via an optical near-field interaction denoted by U_{CG}. The (i,j) and (j,i) elements of the interaction Hamiltonian H_{int} are given by U_{CG}. The matrices $R_i (i = C_1, G_1)$ are annihilation operators that, respectively, annihilate excitations in C_1 and G_1 via radiative relaxations. The matrices $R_i^\dagger (i = C_1, G_1)$ are, respectively, creation operators given by the transposes of the matrices of R_i. The matrix S is an annihilation operator that annihilates an excitation in G_2 via sublevel relaxations. The external Hamiltonian $H_{\text{ext}}^{\text{CW}}(t)$ is the Hamiltonian representing the continuously irradiated external input light into QD$_C$, or the energy level of C_1, given by

$$H_{\text{ext}}^{\text{CW}}(t) = CW(t) \times \left(R_{C_1}^\dagger + R_{C_1}\right), \tag{3}$$

where $CW(t)$ specifies the amplitude of the external input light applied to QD$_C$. The other external Hamiltonian, $H_{\text{ext}}^{G}(t)$, is the Hamiltonian representing the external input correlated with the radiation from the lower energy level of System 1 affecting the energy lower energy level of QD$_G$ or G_2, which is given by

$$H_{\text{ext}}^{G}(t) = \alpha_G \times \rho_{B1}^{\text{Sys2}}(t) \times \left(R_{G_1}^\dagger + R_{G_1}\right), \tag{4}$$

where $\rho_{B1}^{\text{Sys2}}(t)$ indicates the population involving energy level B_1 in System 2, which is introduced in the following, and α_G indicates the coupling efficiency from System 2 to System 1.

Second, System 2 also has in total three energy levels (namely, A_1 in QD$_A$, B_1 and B_2 in QD$_B$), and the quantum master equation of System 2 is similar to (2) above:

$$\begin{aligned}\frac{d\rho^{\text{Sys2}}(t)}{dt} &= -\frac{i}{\hbar}\left[H_{\text{int}}^{\text{Sys2}} + H_{\text{ext}}^{A}(t), \rho^{\text{Sys2}}(t)\right] \\ &\quad + \sum_{i=A_1,B_1} \frac{\gamma_i}{2}\big(2R_i\rho^{\text{Sys2}}(t)R_i^\dagger - R_i^\dagger R_i\rho^{\text{Sys2}}(t) \\ &\quad - \rho^{\text{Sys2}}(t)R_i^\dagger R_i\big) + \frac{\Gamma}{2}\big(2S\rho^{\text{Sys2}}(t)S^\dagger \\ &\quad - S^\dagger S\rho^{\text{Sys2}}(t) - \rho^{\text{Sys2}}(t)S^\dagger S\big), \end{aligned} \tag{5}$$

where the radiative relaxation rates from C_1 and G_1 are, respectively, given by γ_C and γ_G. Γ is the sublevel relaxation rate in QD$_B$. The interaction Hamiltonian $H_{\text{int}}^{\text{Sys2}}$ has the same structure as that in System 1, while the optical near-field interaction between A_1 and B_2 is given by U_{AB}. The external Hamiltonian, $H_{\text{ext}}^{A}(t)$, is the Hamiltonian representing the external input affecting the energy level in QD$_A$ by the radiation from QD$_C$ in System 1, which is given by

$$H_{\text{ext}}^{A}(t) = \alpha_A \times \rho_{C1}^{\text{Sys1}}(t - \Delta) \times \left(R_{A_1}^\dagger + R_{A_1}\right), \tag{6}$$

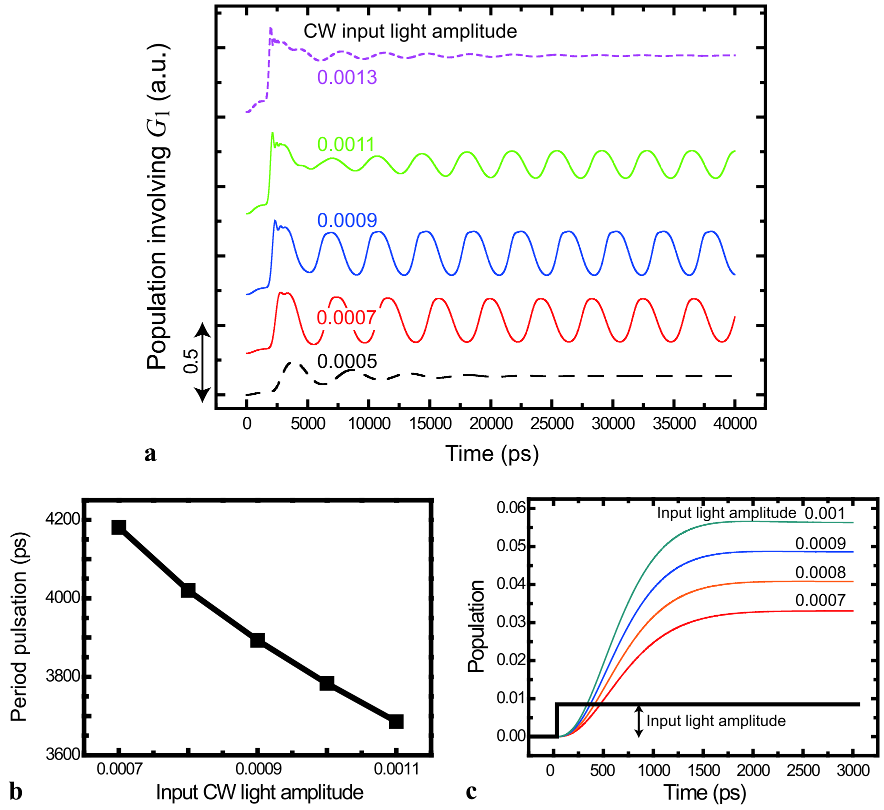

Fig. 2 (**a**) Evolution of population in the lower energy level of QD$_G$ with different CW input light amplitudes. Amplitudes that are too small and too large do not yield pulsation. (**b**) Evaluated pulse cycles as a function of CW light amplitude. (**c**) In a virtually isolated system of energy transfer, the evolution of the population is evaluated with different input amplitudes. A higher amplitude provides more rapid reaction of the system, which is consistent with the amplitude dependence in (**b**)

where $\rho_{C1}^{\mathrm{Sys1}}(t)$ indicates the population involving the energy level C_1 in System 1, and α_A indicates the coupling efficiency from System 1 to System 2. The populations in both System 1 and System 2 can be evaluated by simultaneously solving the master equations given by (2) and (5).

First we assume the following typical parameter values based on experimental observations of energy transfer observed in ZnO nanorods [22]: (i) inter-dot optical near-field interaction $U_{CG}^{-1} = U_{AB}^{-1} = 144$ ps, (ii) sublevel relaxation $\Gamma^{-1} = 10$ ps, and (iii) radiative decay times of the smaller dot $\gamma_C^{-1} = \gamma_A^{-1} = 443$ ps and the large ones $\gamma_G^{-1} = \gamma_B^{-1} = 190$ ps. We assume the coupling efficiencies of α_G and α_A to be 0.1 and 0.01, respectively.

Figure 2a shows the evolution of the populations involving the lower level of QD$_G$, or G_1, for different CW input light amplitudes. Input light of extremely small amplitude does not induce an optical pulsation, as indicated in the dashed curve in Fig. 2a. Also, input light of too large an amplitude does not lead to pulsation either, as shown by the dotted curve. With appropriate input light amplitudes, optical pulsation is successfully observed, as demonstrated by the solid curves in Fig. 2a. The period of pulsation depends on the input CW light amplitude, as shown in Fig. 2b, where the period of pulsation decreases as the CW light amplitude increases. This is due to the fact that QD$_G$ is populated more rapidly with higher input irradiation. Virtually subtracting System 1 from the entire system, Fig. 2c evaluates the evolution of the population of the lower level of QD$_G$ with light irradiation beginning at $t = 0$. The rise time of the population becomes smaller as the amplitude of the radiation increases, which yields a shorter period of pulsation.

Next we examine the dependence on the delay time Δ in (6). Figure 3a shows the evolution of the population involving G_1 assuming a constant CW input amplitude (specifically, 7×10^{-4}) while the delay is varied. First, no pulsation is observed when the delay time Δ is too small, as shown by dashed curves in Fig. 3a. This is attributed to the fact that the changes in the populations involving C_1 in System 1 are instantaneously delivered to QD$_G$, even by way of System 1, resulting in convergence to a steady state. As shown in Fig. 3b, the period of pulsation, T, is proportional to the delay Δ which is given by $T = a \times \Delta + b$, where a and b, respectively, denote the slope and the intercept. As shown in Fig. 3c, the slope is constant regardless of the CW input amplitude, whereas the intercept of the curve decreases as the input light increases, which agrees with the results shown in Fig. 2b.

Next, we examine the dependence on the optical near-field interactions and radiation lifetime of the quantum dots in the system. Figure 4a shows the evolution of the population for different near-field interactions in System 1 (U_{CG}). Optical pulsation occurs in a limited parameter regime of U_{CG}. With interactions that are too weak, as in the case

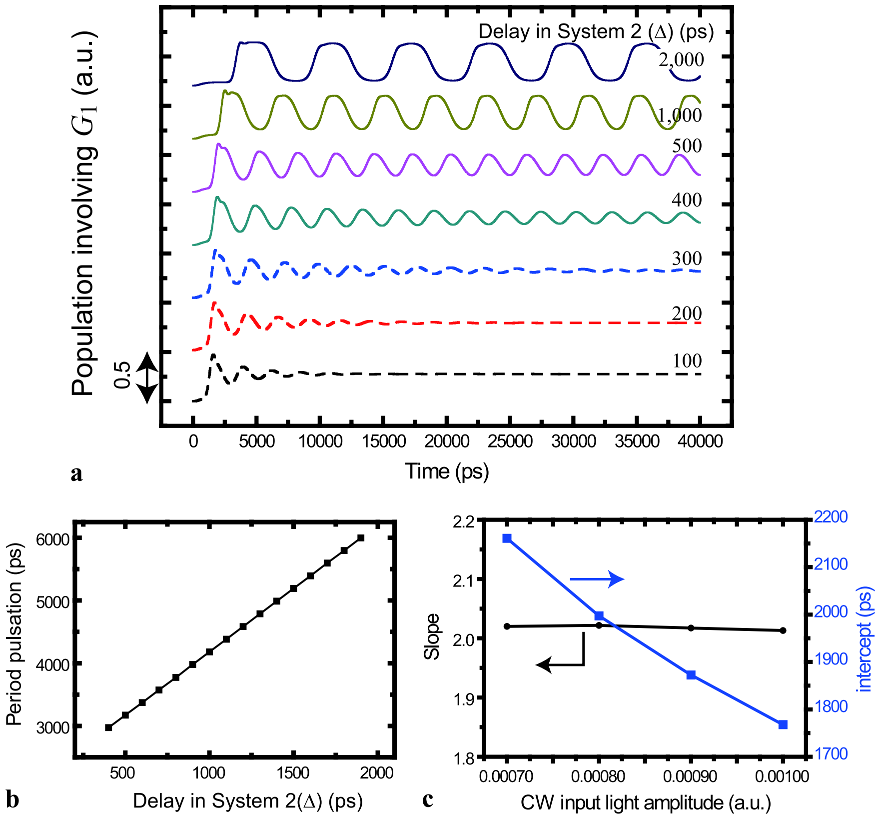

Fig. 3 (**a**) Evolution of population as a function of delay in System 2. (**b**) Linear dependence of the period of pulsation on the delay in System 2. (**c**) Changes of the linear dependence on the delay with different CW inputs

where U_{CG}^{-1} is 300 ps (dotted curve in Fig. 4a), and also with interactions that are too strong, as shown by the case U_{CG}^{-1} of 100 ps and 120 ps (dashed curves in Fig. 4a), the amplitude of the pulsation is attenuated. Square marks in Fig. 4c show the peak-to-peak value of the pulsation in populations as a function of the optical near-field interactions. With optical near-field interactions that are too weak, the optical excitation occurring in C_1 cannot be transferred to QD$_G$, and, thus, optical pulsation does not occur. To investigate the detailed processes, we again virtually subtracted System 1 from the entire system and investigated the dependence on the near-field interaction. The square marks in Fig. 4d show the steady-state population involving the lower energy level of destination QD (or G_1) as a function of the near-field interaction between QD$_C$ and QD$_G$. With a larger interaction time (i.e., weaker near-field interaction), the population in G_1 decreases. Therefore the decaying of the peak-to-peak populations in the optical pulsation may be due to the lack of optical excitation to be transferred from QD$_C$ to QD$_G$.

Figure 4b summarizes the evolution of the population for different radiation lifetimes γ_C^{-1} of QD$_C$ in System 1. The smaller radiation lifetimes of 100, 200, and 300 ps do not yield an optical pulsation, as shown by the dashed curves in Fig. 4b. The circular marks in Fig. 4c show the peak-to-peak value of the pulsation as a function of radiation lifetime in QD$_C$. To seek the origin of such behavior, we again investigate the virtually isolated System 1. The circular marks in Fig. 4d represent the steady-state populations involving G_1 as a function of the radiation lifetime of QD$_C$. Increasing the radiation lifetime of QD$_C$ allows an exciton generated in QD$_C$ to be transferrable during that lifetime, thus increasing the possibility of transition to QD$_G$. However, with an interaction that is too weak, the quantity of the transfer from QD$_C$ to QD$_G$ decreases. Note that the population involving G_1 when the optical pulsation vanishes, $\gamma_C^{-1} = 300$ ps in Fig. 4c, is around 0.02, as shown in Fig. 4d, which is nearly the same as the population when U_{CG}^{-1} is 230 ps, where the optical pulsation also vanishes in Fig. 4c. Such a coincidence, or an unified understanding of two different parameter dependencies, indicates that the optical energy transfer from the smaller QD to the larger QD plays a crucial role for the pulsation.

4 Conclusion

In summary, we theoretically demonstrated pulsations in populations based on optical excitation transfer via optical near-field interactions in quantum dot systems pumped by continuous-wave light irradiation. The optical pulsation is induced with proper setting of parameters associated with the optical near-field interactions, since the successive occurrence of optical excitation transfer is the fundamental

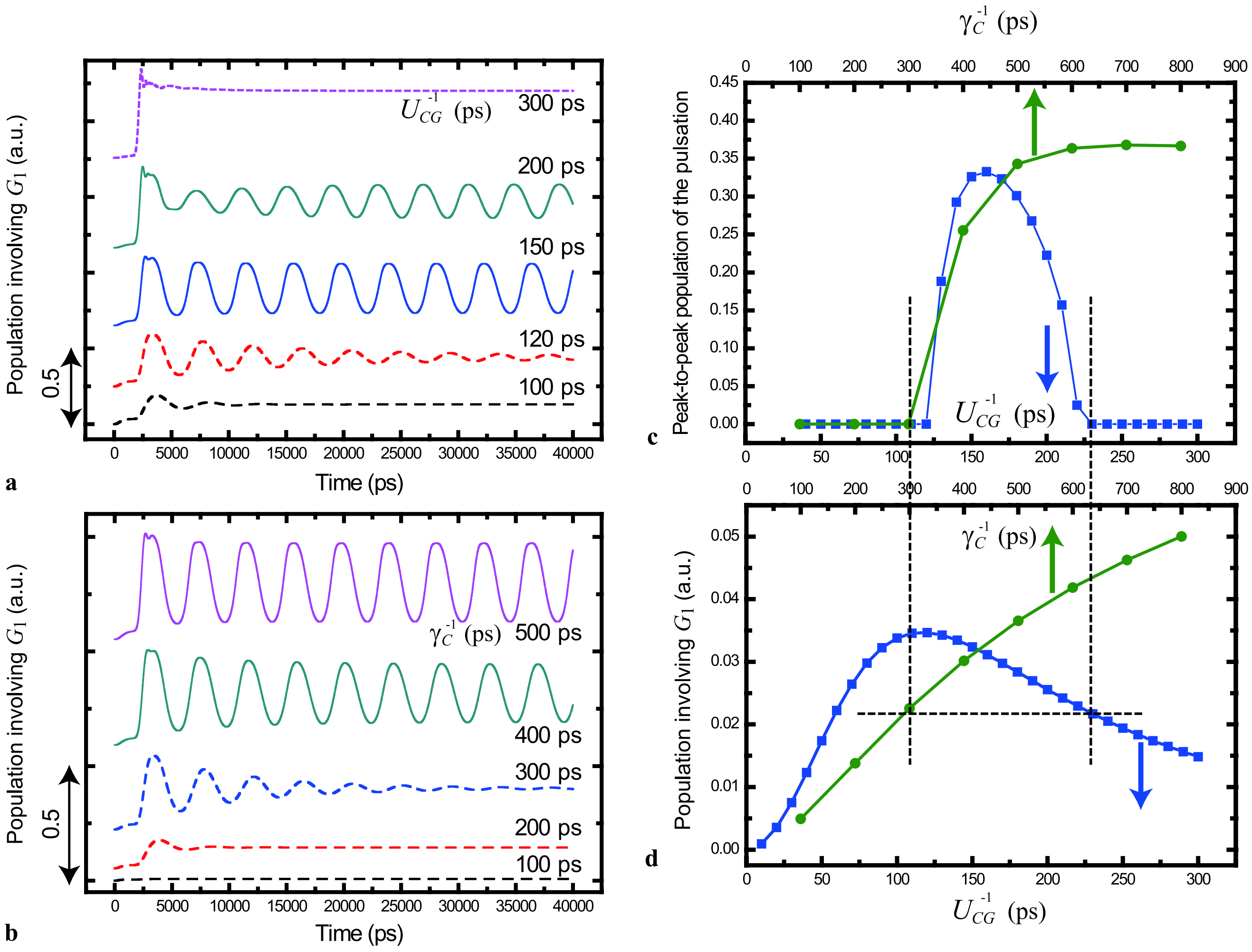

Fig. 4 Evolution of population involving G_1 (**a**) with different inter-dot optical near-field interactions (U_{CG}) between QD$_C$ and QD$_G$, and (**b**) with different radiation lifetimes in QD$_C$(γ_C). (**c**) Peak-to-peak value of pulsations in population involving G_1 as a function of U_{CG} (*square marks*) and γ_C (*circular marks*). (**d**) Analysis of the subsystem System 1. Steady-state population involving G_1 as a function of U_{CG} and γ_C. The population involving G_1 is about 0.02 both of the dependences to U_{CG} and γ_C when the pulsation disappears in (**c**)

basis. We will further investigate the design and the implementation of nanometer-scale pulse generators, based on the critical insights gained in the work described in this paper, while developing enabling nanophotonics device technologies.

References

1. M. Ohtsu, K. Kobayashi, T. Kawazoe, T. Yatsui, M. Naruse, *Principles of Nanophotonics* (Taylor & Francis, Boca Raton, 2008)
2. V.I. Klimov, *Nanocrystal Quantum Dots* (Taylor & Francis, Boca Raton, 2010)
3. MONA consortium, A European roadmap for photonics and nanotechnologies (2008). http://www.ist-mona.org/
4. *Nanophotonics: Accessibility and Applicability* (National Academies Press, Washington, 2008)
5. M. Naruse, T. Miyazaki, T. Kawazoe, S. Sangu, K. Kobayashi, F. Kubota, M. Ohtsu, IEICE Trans. Electron. **E88-C**, 1817 (2005)
6. M. Naruse, H. Hori, K. Kobayashi, M. Ishikawa, K. Leibnitz, M. Murata, N. Tate, M. Ohtsu, J. Opt. Soc. Am. B **26**, 1772 (2009)
7. L. Thylén, P. Holmström, A. Bratkovsky, J. Li, S.-Y. Wang, IEEE J. Quantum Electron. **46**, 518 (2010)
8. K. Iga, R.B. Miles, *Fundamentals of Laser Optics* (Plenum, New York, 1994)
9. A. Weiner, *Ultrafast Optics* (Wiley, Hoboken, 2009)
10. A. Shojiguchi, K. Kobayashi, S. Sangu, K. Kitahara, M. Ohtsu, J. Phys. Soc. Jpn. **72**, 2984 (2003)
11. M. Ohtsu, K. Kobayashi, T. Kawazoe, S. Sangu, T. Yatsui, IEEE J. Sel. Top. Quantum Electron. **8**, 839 (2002)
12. T. Kawazoe, K. Kobayashi, S. Sangu, M. Ohtsu, Appl. Phys. Lett. **82**, 2957 (2003)
13. T. Yatsui, S. Sangu, T. Kawazoe, M. Ohtsu, S.J. An, J. Yoo, G.-C. Yi, Appl. Phys. Lett. **90**, 223110 (2007)
14. M. Naruse, T. Kawazoe, R. Ohta, W. Nomura, M. Ohtsu, Phys. Rev. B **80**, 125325 (2009)
15. T. Franzl, T.A. Klar, S. Schietinger, A.L. Rogach, J. Feldmann, Nano Lett. **4**, 1599 (2004)

16. M. Naruse, T. Kawazoe, S. Sangu, K. Kobayashi, M. Ohtsu, Opt. Express **14**, 306 (2006)
17. W. Nomura, T. Yatsui, T. Kawazoe, M. Naruse, M. Ohtsu, Appl. Phys. B **100**, 181 (2010)
18. K. Akahane, N. Yamamoto, M. Tsuchiya, Appl. Phys. Lett. **93**, 041121 (2008)
19. T. Mano, N. Koguchi, J. Cryst. Growth **278**, 108 (2005)
20. T. Kawazoe, K. Kobayashi, M. Ohtsu, Appl. Phys. Lett. **86**, 103102 (2005)
21. H.J. Carmichael, *Statistical Methods in Quantum Optics 1* (Springer, Berlin, 1999)
22. T. Yatsui, H. Jeong, M. Ohtsu, Appl. Phys. B **93**, 199 (2008)

Surface plasmon enhanced UV emission in AlGaN/GaN quantum well

J. Lin,[1] A. Mohammadizia,[1] A. Neogi,[1,a)] H. Morkoc,[2] and M. Ohtsu[3]
[1]*Department of Physics, University of North Texas, Denton, Texas 76203-5370, USA*
[2]*Department of Electrical Engineering, Virginia Commonwealth University, Richmond, Virginia 23284, USA*
[3]*Department of Electrical Engineering and Information System, University of Tokyo, 2-11-16 Yayoi, Bunkyo-ku, Tokyo 113-8656, Japan*

(Received 6 July 2010; accepted 18 October 2010; published online 1 December 2010)

The surface plasmon (SP) energy for resonant enhancement of light has shown to be modified by the epitaxial substrate and the overlying metal thin film. The modification of SP energy in AlGaN/GaN epitaxial layers is studied using spectroscopic ellipsometry for enhanced UV-light emission. Silver induced SP can be extended to the UV wavelength range by increasing the aluminum concentration in $Al_xGa_{1-x}N$ epilayer. A threefold increase in the UV-light emission is observed from AlGaN/GaN quantum well due to silver induced SP. Photoluminescence lifetime measurements confirm the resonant plasmon induced increase in Purcell factor as observed from the PL intensity measurements. © *2010 American Institute of Physics*. [doi:10.1063/1.3515419]

GaN/InGaN nitride quantum well based light emitters were one of the first III-V semiconductor material systems that were employed to demonstrate resonant exciton-surface plasmon polariton (SPP) coupling,[1,2] leading to the enhancement of light emission in the visible wavelength regime.[3,4] Surface plasmon (SP) coupled to excitons or free carriers in AlGaN/GaN system offers an attractive alternative to enhance the light emission in the UV wavelength range. The internal quantum efficiency of AlGaN/GaN emitters is rather low compared to the InGaN system,[5] and AlGaN/GaN emitters are therefore ideal for plasmonic enhancement. The efficiency of UV emission is currently restricted by the lattice mismatch of AlGaN epitaxial layers to sapphire substrate or the cost effectiveness of AlGaN substrates.[6] In the present paper, we study the factors influencing the SP coupling in AlGaN/GaN quantum well system and demonstrate SP induced enhancement of light emission in the UV wavelength region.

SPP induced light emission depends on the resonant interaction of the SP modes with the exciton emission at a certain wavelength. In nanoscale emitters, the resonant interaction can be achieved by using an appropriate metal with a SP energy resonant to the emission wavelength of the light emitter, which can be tuned by changing the dimension of the nanoscale emitter such as the width of a quantum well (QW) or wire or the diameter of a quantum dot.[7] The SP energy at the interface of a metal thin film and a semiconductor can also be influenced by the dielectric constant of the substrate.[8] Silver induced SPP has been reported as the most effective means for visible light enhancement in nitride semiconductors. The surface plasmon energy at the Ag-GaN interface has been reported[1] to be 2.95 eV, which renders Ag induced plasmon ineffective for the UV wavelength regime. However, as the refractive index of AlN reduces by nearly 19.5% compared to GaN,[9,10] a corresponding change in the SP energy is expected for GaN nitride quantum well based UV-light emitters capped with AlGaN layers. We therefore investigate the change in the surface plasmon energy for Ag metal film with various Al concentrations in $Al_xGa_{1-x}N$ epilayer and the effect of various metals on GaN for the design of UV-light emitters.

The details of the epitaxially grown wurtzite AlGaN alloy films used to study the compositional variation of the surface plasmon energy are described elsewhere.[11] The AlGaN layers were coated with 10 nm thin Ag metal layer using electron beam evaporation. The SP energy at the metal semiconductor interface was estimated from the effective dielectric constant measured using a Woollam spectroscopic ellipsometer. The measurements were carried out at room temperature at an incident angle of 75° for the 300–450 nm wavelength range. The dielectric constants were measured using a conventional multilayer model[9] including the surface and interface roughness of the metal layer after deposition and the semiconductor epilayer before the metal deposition. From Fig. 1, it is observed that the SP energy at the Ag/AlGaN interface increases from 2.97 to 3.7 eV as the Al mole fraction increases from 0% to 100%. Therefore this increase in the SP energy with Al concentration provides us an option to couple high energy photons from QWs in the UV range to the SPP modes that normally cannot be coupled in the case of Ag-GaN system.

The inset of Fig. 2(a) shows the schematic of the sample that has been used to study the SPP enhanced light interaction in the UV regime. The AlGaN/GaN QW structure was synthesized using molecular beam epitaxy and capped with

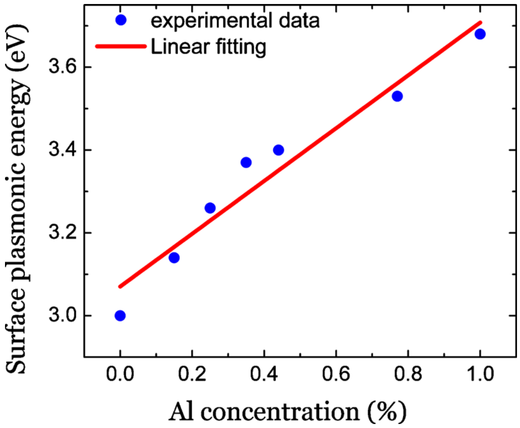

FIG. 1. (Color online) Variation of silver induced surface plasmon with Al mole fraction in AlGaN epilayer measured by spectroscopic ellipsometry.

[a)] Author to whom correspondence should be addressed. Electronic mail: arup@unt.edu.

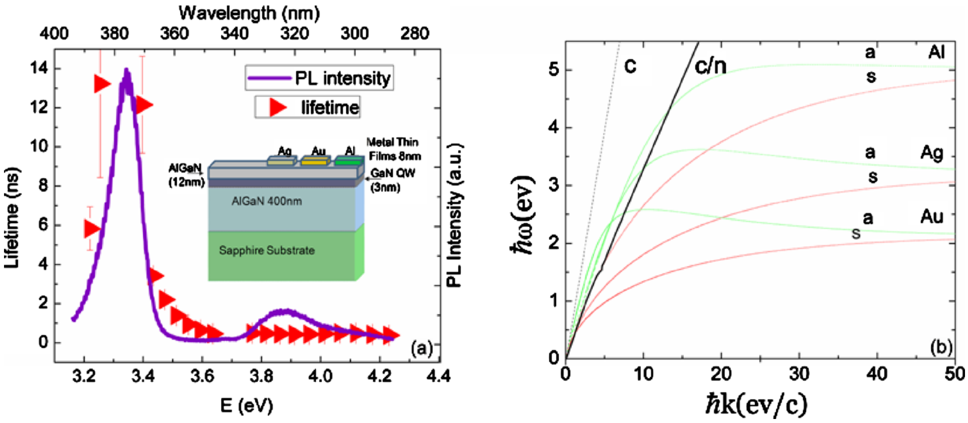

FIG. 2. (Color online) (a) The schematic of AlGaN/GaN quantum well structure used for studying the effect of surface plasmon enhancement (inset). PL spectrum and recombination lifetime measured using time-resolved PL spectroscopy measured at 10 K. (b) Dispersion relations for 8 nm Al, Ag, and Au layers on AlGaN/GaN/AlGaN quantum well showing the normal/antisymmetric (A) and the tangential/symmetric branches (S).

various metals for exciting SPP. A 3 nm GaN QW layer with 3 periods has been grown on a $Al_{0.23}Ga_{0.67}N$ buffer layer with a 12 nm $Al_{0.23}Ga_{0.67}N$ cap layer to enable SPP coupling. Photoluminescence (PL) emission intensity measurements were performed using a continuous wave (cw) 18 mW HeCd laser at 325 nm. The PL lifetime was measured using a tripled Ti:Sapphire femtosecond laser excitation at 267 nm wavelength (4.64 eV) with 60 mW average power. The PL signal was monodispersed using a spectrometer, and the lifetime was measured using a Hamamatsu Streak camera with an effective resolution of 15 ps. The time-integrated PL spectrum and the corresponding lifetime of the carriers within the GaN/AlGaN QW measured at 10 K are shown in Fig. 2(a). The pump laser excites the carriers into the AlGaN barrier, which results in an emission at ~3.8–4.0 eV, whereas the emission from the GaN quantum well is observed at ~3.34 eV. The lifetime of the carrier in the quantum well is relatively longer than that in the AlGaN barrier layer, which is dictated by the carrier recombination due to the carrier capture into the GaN well and nonradiative recombination at the interface.

Figure 2(b) shows the theoretical estimate of SPP dispersion[12] for 8 nm metal films on a multilayer structure composed of AlGaN (12 nm)/GaN (3 nm)/AlGaN (400 nm)/sapphire. For the 8 nm thin metal layer, the SPs at the air-metal and the metal-AlGaN interfaces couple together, generating symmetric and antisymmetric plasma oscillations. The dielectric constants used in the calculation were interpolated from tabulated[10,13] values. For large wave vectors, the symmetric modes asymptotically approach an energy, which agrees closely with the spectral position of the plasmon resonance in a system.[1,2] The portions of the antisymmetrical plasmon branch between the c and c/n light lines must have a complex wave vector. The antisymmetric branches are "leaky" plasmon modes, which are not confined to the interface, but can propagate into the AlGaN layer due to the small wave vector to the left of the c/n light line, which can lead to an enhancement in plasmon enhanced coupling to excitons in QWs.

Figure 3(a) shows the surface plasmon induced modification of the cw PL emission from the GaN quantum well due to Au, Ag, and Al thin films with 8 nm thickness. The cw PL measurements were made using the 325 nm (3.81 eV) excitation of a HeCd laser with an average incident power of 18 mW. The metal films were deposited using electron beam evaporation, and a top excitation geometry (with the source and detector being above the metallic side of the sample) was used[1,2] to study the effect of surface plasmon coupling. It is observed that for an excitation below the barrier level, the Al and Ag thin films show an enhancement in PL emission compared to bare sample, whereas the Au coated QW shows a slight quenching at 300 K. From the theoretical estimates in Fig. 2(b), it is observed that the leakage of the SP modes for the Ag/Air interface into the AlGaN/GaN QW results in coupling with the exciton in the quantum well and results in the enhancement in light emission as observed in certain quantum confined structures.[14] The SPP induced enhancement in PL emission is similar to that observed in the InGaN system,[3] though in the present case, the samples were excited from the top instead of the back illumination geometry applied by Okamoto *et al.*[7] In case of the InGaN/GaN QWs excited from the top, the emission from the wells is actually quenched due to the resonant plasmon coupling in the presence of Ag thin film.[2] So to investigate the origin of enhancement, the recombination lifetime has been measured as the spontaneous emission rate of carriers are enhanced due to SPP coupling.[2,3]

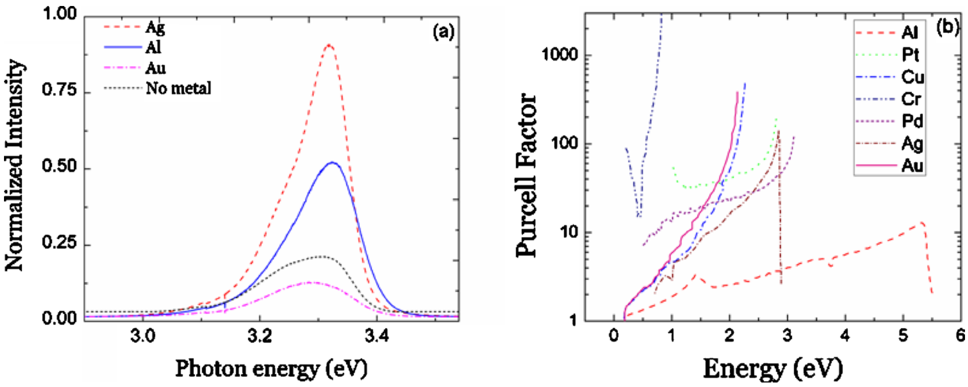

FIG. 3. (Color online) (a) The comparison of room temperature PL emission from AlGaN/GaN quantum well in the presence of Al, Ag, and Au induced metal surface plasmon at 300 K (excitation wavelength at 325 nm). (b) An estimation of Purcell enhancement in AlGaN/GaN quantum well due to surface plasmon interaction induced by various metals on the GaN cap layer.

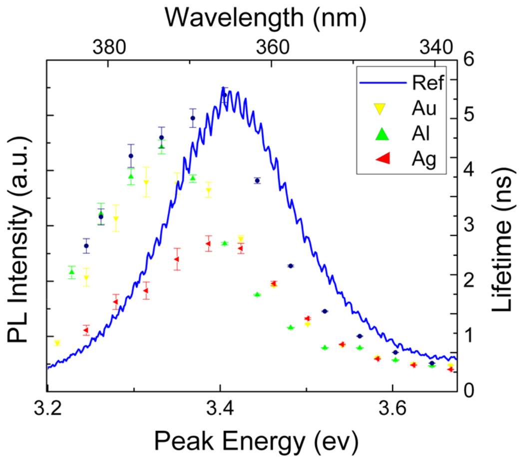

FIG. 4. (Color online) The comparison of time-integrated photoluminescence and PL recombination lifetime in the presence of metal induced surface plasmon polariton measured using time-resolved PL (excitation wavelength at 267 nm). Rectangles: reference sample (no metal); pyramid (green): Al; inverted pyramid (yellow): Au; and side-flipped pyramid (red): Ag.

As the surface plasmon energy of the Au-GaN layer is below the emission wavelength of QW, the surface plasmon modes due to Au does not play any role in the spontaneous emission process. A slight quenching of the PL in Fig. 3(a) is observed in the case of Au due to the absorption of the incident HeCd laser light as well as the PL emission by the metal layer. Though Al metal has a relatively higher energy SPP mode, which is more suitable for coupling to UV photons, in the present case, Ag is observed to be more effective at 3.34 eV as in the case of visible light enhancement from the InGaN/GaN QW system. We thereby also present a theoretical estimation of the Purcell enhancement factor for various metals coupled to GaN/AlGaN QW (in Fig. 2), which is regarded as the figure of merit for surface plasmon based emitters.[1] The Purcell enhancement factor is obtained from the ratio of the surface plasmon induced spontaneous recombination rate (Γ_p) to the radiative recombination rate (Γ_o) of the QW,

$$F_p(\omega) = \frac{\Gamma_p(\omega) + \Gamma_0(\omega) + \Gamma_{\mathrm{nr}}(\omega)}{\Gamma_0(\omega) + \Gamma_{\mathrm{nr}}(\omega)} \approx 1 + \frac{\Gamma_p}{\Gamma_0}, \qquad (1)$$

where Γ_{nr} is the nonradiative recombination rate and is considered to be negligible compared to the plasmon mediated radiative recombination process. The modified light emission depends on the density of the surface plasmon modes $\rho(\hbar\omega)$.

Utilizing the plasmon energy of various metals[15] and the optical constants of GaN/AlGaN,[16] the Purcell enhancement factor for various metal/GaN interface has been estimated using Eq. (1). It is observed that Al can couple to deep UV photons due to higher SP energy but has a relatively an order lower enhancement factor compared to Ag or Pt, which can enhance the light emission up to ~2.9 eV. Au and Cu can resonantly enhance visible wavelength emission at around 2.2–2.4 eV with a higher Purcell factor compared to Ag. Chromium has one of the highest Purcell enhancement factor and can be effective for resonant SP coupling, the near-infrared wavelength range including the communication wavelength intersubband devices at 1.55 μm.[17]

Figure 4 shows the time-resolved PL measurement for the AlGaN/GaN QWs in the presence of various metal layers. It is observed that below and around the emission edge of the QW, the PL recombination lifetime is not influenced by the Au or Al thin films, whereas the Ag surface plasmon induced recombination process is significantly fast implying radiative decay though SPP channels. At the QW emission edge, the surface plasmon induced contribution due to Al increases and the PL recombination lifetime becomes comparable to the silver surface plasmon induced recombination process. Within the width of the emission spectrum, the Ag induced SP decay rates are nearly three times faster than the spontaneous decay rate of the AlGaN/GaN quantum well. This enhancement in the decay rate is similar to the magnitude of the PL enhancement observed in the cw measurement [Fig. 3(a)].

In conclusion, we present the enhancement of UV-light emission from AlGaN/GaN quantum wells based on resonant surface plasmon interaction. We demonstrate that the surface plasmon energy of Ag/AlGaN material system can be increased to the ultraviolet wavelength regime by increasing the Al concentration in the AlGaN cap layer of the light emitter. We also study the applicability of various metals on GaN semiconductor for the surface plasmon enhanced light emission. The increase in the light emission from AlGaN/GaN quantum well due to being Ag and Al induced corresponds to the enhancement in the spontaneous emission rate.

The authors acknowledge the support from the Global COE program at the University of Tokyo. J.L. is supported by a U.S. Department of Energy research grant. H.M. acknowledges the support of the Air Force Office of Scientific Research. The authors acknowledge the discussions with Nagraj, Dr. C. W. Lee, and Dr. H. Everitt for the calculation of the SP dispersion relation.

[1] I. Gontijo, M. Boroditsky, E. Yablonovitch, S. Keller, U. K. Mishra, and S. P. DenBaars, Phys. Rev. B **60**, 11564 (1999).
[2] A. Neogi, C.-W. Lee, H. O. Everitt, T. Kuroda, A. Tackeuchi and E. Yablonovitch, Phys. Rev. B **66**, (2002) 153305.
[3] K. Okamoton, A. Scherer, and Y. Kawakami, Phys. Status Solidi C **5**, 2822 (2008).
[4] Y.-C. Lu, Y.-S. Chen, F.-J. Tsai, J.-Y. Wang, C. Lin, C. Chen, Y. C. C. Yang, Appl. Phys. Lett. **94**, 233113 (2009).
[5] K. Iida, T. Kawashima, A. Miyazaki, H. Kasugai, S. Mishima, A. Honshio, Y. Miyake, M. Iwaya, S. Kamiyama, H. Amano, and I. Akasaki, Jpn. J. Appl. Phys., Part 2 **43**, L499 (2004).
[6] V. N. Jmerik, A. M. Mizerov, A. A. Sitnikova, P. S. Kop'ev, S. V. Ivanov, E. V. Lutsenko, N. P. Tarasuk, N. V. Rzheutskii, and G. P. Yablonskii, Appl. Phys. Lett. **96**, 141112 (2010).
[7] K. Okamoto, I. Niki, A. Scherer, Y. Narukawa, T. Mukai, and Y. Kawakami, Appl. Phys. Lett. **87**, 071102 (2005).
[8] K. C. Vernon, A. M. Funston, C. Novo, D. E. Gómez, P.Mulvaney, and T. J. Davis, Nano Lett. **10**, 2080 (2010).
[9] T. Suzuki H. Yaguchi, H. Okumura, Y. Ishida, S. Yoshida, Jpn. J. Appl. Phys., Part 2 **39**, L497 (2000).
[10] N. A. Sanford L. H. Robins, A. V. Davydov, A. Shapiro, D. V. Tsvetkov, A. V. Dmitriev, S. Keller, U. K. Mishra, and S. P. DenBaars, J. Appl. Phys. **94**, 2980 (2003).
[11] U. Ozgur, G. Webb-Wood, H. O. Everitt, F. Yun, and H. Morkoc, Appl. Phys. Lett. **79**, 4103 (2001).
[12] J. Burke, G. I. Stegeman, and T. Tamir, Phys. Rev. B **33**, 5186 (1986).
[13] See http://savannah.nongnu.org/projects/freesnell for estimation of metal refractive index.
[14] N. Ganesh, I. D. Block, P. C. Mathias, W. Zhang, E. Chow, V. Malyarchuk, and B. T. Cunningham, Opt. Express **16**, 21626 (2008).
[15] D. E. Gray, *American Institute of Physics Handbook*, 3rd ed. (McGraw-Hill, New York, 1972), pp. 6–149.
[16] D. Brunner, H. Angerer, E. Bustarret, F. Freudenberg, R. Hopler, R. Dimitrov, O. Ambacher, and M. Stutzmann, J. Appl. Phys. **82**, 5090 (1997).
[17] M. Tchernycheva, H. Macchadani, L. Nevou, J. Mangeney, F. H. Julien, P. K. Kandaswamy, A. Wirthmüller, E. Monroy, A. Vardi, S. Schacham, and G. Bahir, Phys. Status Solidi A **207**, 1421 (2010).

Distinguishing between ultrafast optical harmonic generation and multi-photon-induced luminescence from ZnO thin films by frequency-resolved interferometric autocorrelation microscopy

**S. Schmidt,[1] M. Mascheck,[1] M. Silies,[1] T. Yatsui,[2] K. Kitamura,[2]
M. Ohtsu,[2] and C. Lienau[1,*]**

[1] Institut für Physik Carl von Ossietzky Universität, 26129 Oldenburg, Germany
[2]School of Engineering, University of Tokyo, Tokyo 113-8656, Japan
**christoph.lienau@uni-oldenburg.de*

Abstract: The nonlinear optical properties of thin ZnO film are studied using interferometric autocorrelation (IFRAC) microscopy. Ultrafast, below-bandgap excitation with 6-fs laser pulses at 800 nm focused to a spot size of 1 µm results in two emission bands in the blue and blue-green spectral region with distinctly different coherence properties. We show that an analysis of the wavelength-dependence of the interference fringes in the IFRAC signal allows for an unambiguous assignment of these bands as coherent second harmonic emission and incoherent, multiphoton-induced photoluminescence, respectively. More generally our analysis shows that IFRAC allows for a complete characterization of the coherence properties of the nonlinear optical emission from nanostructures in a single-beam experiment. Since this technique combines a very high temporal and spatial resolution we anticipate broad applications in nonlinear nano-optics.

OCIS codes: (320.7110) Ultrafast nonlinear optics; (190.4180) Multiphoton processes (250.5230) Photoluminescence.

References and links

1. M. R. Beversluis, A. Bouhelier, and L. Novotny, “Continuum generation from single gold nanostructures through near-field mediated intraband transitions,” Phys. Rev. B **68**(11543), 1–10 (2003).
2. D. Coquillat, G. Vecchi, C. Comaschi, A. M. Malvezzi, J. Torres, and M. Le Vassor d’Yerville, “Enhanced second- and third-harmonic generation and induced photoluminescence in a two-dimensional GaN photonic crystal,” Appl. Phys. Lett. **87**(10), 101106 (2005).
3. A. B. Djurišić, and Y. H. Leung, “Optical properties of ZnO nanostructures,” Small **2**(8-9), 944–961 (2006).
4. Ü. Özgür, Ya. I. Alivov, C. Liu, A. Teke, M. A. Reshchikov, S. Dŏgan, V. Avrutin, S.-J. Cho, and H. Morkoç, “A comprehensive review of ZnO materials and devices,” J. Appl. Phys. **98**(4), 041301 (2005).
5. J. Fallert, R. J. B. Dietz, J. Sartor, D. Schneider, C. Klingshirn, and H. Kalt, “Co-existence of strongly and weakly localized random laser modes,” Nature Photon. **3**(5), 279–282 (2009).
6. C. F. Zhang, Z. W. Dong, K. J. Liu, Y. L. Yan, S. X. Qian, and H. Deng, “Multiphoton absorption pumped ultraviolet stimulated emission from ZnO microtubes,” Appl. Phys. Lett. **91**(14), 142109 (2007).
7. T. Tritschler, O. D. Mücke, M. Wegener, U. Morgner, and F. X. Kärtner, “Evidence for third-harmonic generation in disguise of second-harmonic generation in extreme nonlinear optics,” Phys. Rev. Lett. **90**(21), 217404 (2003).
8. U. Neumann, R. Grunwald, U. Griebner, G. Steinmeyer, and W. Seeber, “Second-harmonic efficiency of ZnO nanolayers,” Appl. Phys. Lett. **84**(2), 170–172 (2004).
9. D. C. Dai, S. J. Xu, S. J. Shi, M. H. Xie, and C. M. Che, “Observation of Both Second-Harmonic and Multiphoton-Absorption-Induced Luminescence In ZnO,” IEEE Photon. Technol. Lett. **18**(14), 1533–1535 (2006).
10. N. S. Han, H. S. Shim, S. Min Park, and J. K. Song, “Second-harmonic Generation and Multiphoton Induced Photoluminescence in ZnO,” Bull. Korean Chem. Soc. Vol. **30**(10), 2199–2200 (2009).

#136025 - $15.00 USD Received 4 Oct 2010; revised 7 Nov 2010; accepted 7 Nov 2010; published 16 Nov 2010

11. C. F. Zhang, Z. W. Dong, G. J. You, R. Y. Zhu, S. X. Qiana, H. Deng, H. Cheng, and J. C. Wang, "Femtosecond pulse excited two-photon photoluminescence and second harmonic generation in ZnO nanowires," App, Phys. Lett. **89**, 042117 (2006).
12. S. W. Liu, H. J. Zhou, A. Ricca, R. Tian, and M. Xiao, "Far-field second-harmonic fingerprint of twinning in single ZnO rods," Phys. Rev. B **77**(11), 113311 (2008).
13. K. Pedersen, C. Fisker, and T. G. Pedersen, "Second-harmonic generation from ZnO nanowires," Phys. Status Solidi **5**(8), 2671–2674 (2008).
14. S. K. Das, M. Bock, C. O'Neill, R. Grunwald, K. M. Lee, H. W. Lee, S. Lee, and F. Rotermund, "Efficient second harmonic generation in ZnO nanorod arrays with broadband ultrashort pulses," Appl. Phys. Lett. **93**(18), 181112 (2008).
15. Y. C. Zhong, K. S. Wong, A. B. Djurisic, and Y. F. Hsu, "Study of optical transitions in an individual ZnO tetrapod using two-photon photoluminescence excitation spectrum," Appl. Phys. B **97**(1), 125–128 (2009).
16. A. F. Kohan, G. Ceder, D. Morgan, and C. G. Van de Walle, "First-principles study of native point defects in ZnO," Phys. Rev. B **61**(22), 15019–15027 (2000).
17. H. L. Wang, J. Shah, T. C. Damen, and L. N. Pfeiffer, "Spontaneous emission of excitons in GaAs quantum wells: The role of momentum scattering," Phys. Rev. Lett. **74**(15), 3065–3068 (1995).
18. S. Haacke, R. A. Taylor, R. Zimmermann, I. Bar-Joseph, and B. Deveaud, "Resonant femtosecond emission from quantum well excitons: The role of Rayleigh scattering and luminescence," Phys. Rev. Lett. **78**(11), 2228–2231 (1997).
19. M. Gurioli, F. Bogani, S. Ceccherini, and M. Colocci, "Coherent vs Incoherent Emission from Semiconductor Structures after Resonant Femtosecond Excitation," Phys. Rev. Lett. **78**(16), 3205–3208 (1997).
20. G. Stibenz, and G. Steinmeyer, "Interferometric frequency-resolved optical gating," Opt. Express **13**(7), 2617–2626 (2005), http://www.opticsinfobase.org/oe/abstract.cfm?URI=oe-13-7-2617.
21. A. B. Djurišić, W. C. H. Choy, V. A. L. Roy, Y. H. Leung, C. Y. Kwong, K. W. Cheah, T. K. Gundu Rao, W. K. Chan, H. Fei Lui, and C. Surya, "Photoluminescence and Electron Paramagnetic Resonance of ZnO Tetrapod Structures," Adv. Funct. Mater. **14**(9), 856–864 (2004) (and references therein).
22. G. Stibenz, C. Ropers, C. Lienau, C. Warmuth, A. S. Wyatt, I. A. Walmsley, and G. Steinmeyer, "Advanced methods for the characterization of few-cycle light pulses: a comparison," Appl. Phys. B **83**(4), 511–519 (2006).
23. A. Anderson, K. S. Deryckx, X. G. Xu, G. Steinmeyer, and M. B. Raschke, "Few-femtosecond plasmon dephasing of a single metallic nanostructure from optical response function reconstruction by interferometric frequency resolved optical gating," Nano Lett. **10**(7), 2519–2524 (2010).
24. C. Cohen-Tannoudji, J. Dupont-Roc, and G. Grynberg, *Atom-photon interactions: Basic processes and Applications* (Wiley, 1998).

---

1. Introduction

When illuminating semiconducting or metallic solid state nanostructures with intense and broadband ultrashort optical pulses, a variety of nonlinear optical processes such as second or third harmonic generation (SHG, THG), multiphoton-induced luminescence (MPL), photoemission and others are induced. Quite often several of these phenomena occur simultaneously under the same experimental conditions, making it sometimes difficult to distinguish between them. Prominent examples having attracted considerable recent interest are the competition between SHG and multiphoton-induced visible photoluminescence in gold nanoparticles [1] or SHG, THG and MPL in wide bandgap semiconductors such as gallium nitride [2].

Particularly well-studied examples are ZnO films and nanostructures. The wide band gap energy of ZnO of 3.37 eV at room temperature and its large exciton binding energy of ~60meV makes it a highly interesting material for various optoelectronics applications [3,4]. Also, ZnO powders and nanorods present an interesting prototypical material for exploring random lasing [5,6]. Consequently, the nonlinear optical properties of a variety of different ZnO thin films [7–10] and nanostructures [11–15] have been studied extensively. Quite generally, it is found that nonlinear optical efficiencies in ZnO nanostructures can be significantly larger than those of ZnO thin films but that the relative intensities of the different harmonic generation and photoluminescence contributions depend critically on the structural and morphological characteristics of the nanostructures as well as on the nature and concentration of defects in these samples [16].

Being able to clearly distinguish between optical harmonic generation (OHG) and luminescence processes is therefore crucial for a further optimization of their device performance. In general, this requires a complete characterization of the coherence properties

#136025 - $15.00 USD Received 4 Oct 2010; revised 7 Nov 2010; accepted 7 Nov 2010; published 16 Nov 2010

of the light being re-emitted from the nanostructures. Whereas OHG is a fully phase-coherent resonant scattering process, phase coherence to the driving laser is lost in incoherent MPL emission. Even though the coherence properties of the emitted radiation have been studied in great detail for linear light scattering from, e.g., semiconductor quantum wells [17–19], such analyses are scarce for nonlinear light scattering from nanostructures.

Here we show that interferometric frequency-resolved autocorrelation (IFRAC) spectroscopy, a technique recently introduced to characterize ultrashort laser pulses [20], can quantitatively discriminate between OHG and MPL from semiconducting nanostructures. By experimentally and theoretically analyzing IFRAC spectra from thin ZnO films, we show that IFRAC probes the most important difference between SHG and MPL, i.e., their phase correlation with the excitation pulse. Due to its high temporal (< 6 fs) and spatial (< 500 nm) resolution, we foresee a variety of applications of this technique in probing the optical nonlinearities of individual nanostructures.

2. Experimental setup

The experimental setup used in this work is schematically shown in Fig. 1(a). Few-cycle laser pulses with an energy of 2.5 nJ and a duration of 6 fs are generated in a commercial Ti:sapphire oscillator (Femtolasers Rainbow) operating at a repetition rate of 82 MHz. The pulse dispersion is controlled by a pair of chirped mirrors with a group delay dispersion (GDD) of –45 fs^2/bounce (Femtolasers GSM014). A pair of wedges (Femtolasers UA124, angle 2°48′, Suprasil 1) is used to fine-tune the dispersion. Appropriately pre-compensated pulses with a GDD of < –200fs^2 enter a dispersion-balanced, unstabilized Michelson interferometer with low-dispersion broadband dielectric beamsplitters. In the interferometer, a collinearly propagating pair of pulses with variable time delay τ is generated. The pulse delay is controlled using a hardware-linearized single-axis piezo scanner (Physik Instrumente P-621.1CD PI-Hera). Fluctuations of τ due to mechanical vibrations of the interferometer and the finite precision of the piezo scanner are less than 30 as. The pulse pair is expanded to a beam size of 15 mm in an all-reflective Kepler telescope. The beam is then focused to its diffraction limit using an all-reflective, aluminum-coated 36x Cassegrain (Davin Optronics, 5004-000) microscope objective with a numerical aperture (NA) of 0.5. The spatial intensity profile of the focused spot is characterized by collecting the laser light through an aluminum coated near-field optical fiber (Veeco Instruments) with an aperture diameter of ~300nm, fabricated by focused-ion-beam milling. The tip is mounted on a hardware-linearized three-axis piezo stage (Physik Instrumente NanoCube) with a positioning accuracy of better than 10 nm. The intensity of the collected laser light is detected with a photomultiplier tube while scanning the tip through the focus. The spatial intensity distribution of the beam in the focus of the Cassegrain objective is shown in Fig. 1(b). The full width at half maximum of this distribution is 1.0 µm. The rather pronounced Airy fringes result from the obscuration of the central part of the beam by the inner mirror of the objective.

Received 4 Oct 2010; revised 7 Nov 2010; accepted 7 Nov 2010; published 16 Nov 2010

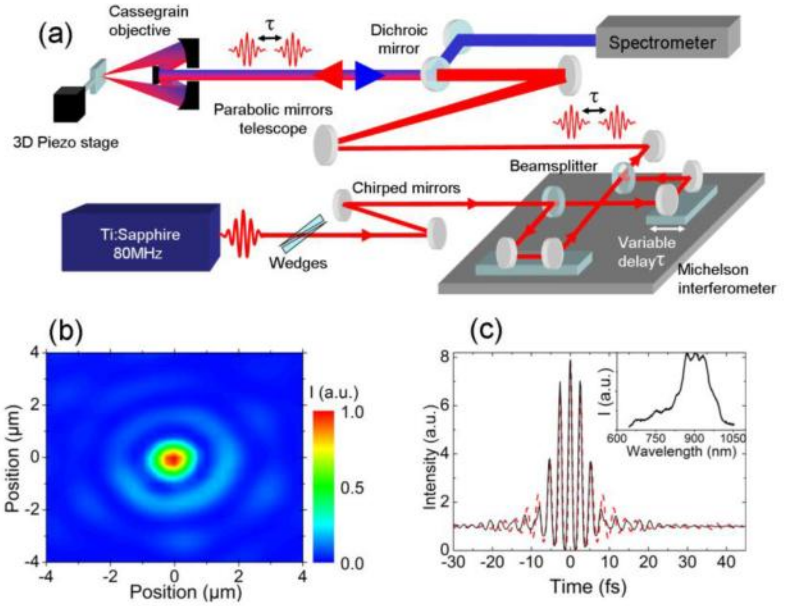

Fig. 1. (a) Experimental setup for interferometric frequency resolved autocorrelation (IFRAC) microscopy. A phase-locked pair of two 6-fs-optical pulses centered at 800 nm derived from a mode-locked Ti:Sapphire oscillator operating at 80 MHz repetition rate is generated in a dispersion-balanced Michelson interferometer. Pulses with an energy of 1 nJ are focused to the diffraction limit of about 1 µm onto the sample using an all-reflective Cassegrain objective. The emission from the sample is collected in a reflection geometry, spectrally dispersed in a monochromator and detected with a cooled CCD detector as a function of the time delay τ between both pulses. (b) Spatial intensity profile in the focal plane recorded by scanning a near-field fiber tip through the focus. (c) Interferometric autocorrelation (IAC) trace of the focused laser pulses (solid line). A simulation of the IAC trace based on the measured laser spectrum (inset) is shown as a dashed line.

To record the time structure of the focused pulses, the tip is replaced with a 10 µm thick BBO crystal and interferometric autocorrelation (IAC) traces are recorded in the laser focus. In Fig. 1(c), a typical IAC trace of the laser pulses in the focus of the Cassegrain objective is shown. The spectrum of the incident laser pulses extending from 650 to 1050 nm is shown in the inset. A simulation of the IAC trace (Fig. 1(c), red dashed line) based on the measured pulse spectrum gives evidence that the focusing with the Cassegrain objective results in essentially bandwidth-limited pulses with a temporal duration of 6.0 fs (full width at half maximum of the pulse intensity) focused to a spot size of 1.0 µm.

Thin ZnO layers with a thickness of 430 nm are deposited on a sapphire substrate using a sputtering technique. The films are sputter-deposited for 50 min at a RF power of 200 W and an Ar flow rate of 16 sccm. A scanning electron microscope (SEM) image of the ZnO film recorded under a viewing angle of 30° in shown in the inset of Fig. 2. The sputtering technique results in a slightly granular surface morphology with a typical grain size of about 50 nm, much smaller than the wavelength of light. For the optical measurements reported here, the ZnO thin film can therefore be considered as a spatially homogeneous layer. Photoluminescence spectra are recorded at room temperature by exciting the sample at 337 nm with a N_2-laser. For the nonlinear optical measurements, the film is illuminated with 6-fs Ti:sapphire pulses focused through the Cassegrain objective. The emission from the ZnO sample is collected in reflection geometry, spectrally dispersed in a monochromator (SpectraPro-2500i, Acton) and detected with a deep-depletion liquid-nitrogen cooled CCD camera (Spec-10, Princeton Instruments). Interferometric frequency-resolved autocorrelation (IFRAC) traces are recorded by illuminating the film with a pair of phase-locked 6-fs laser pulses and monitoring the nonlinear emission spectrum as a function of the delay τ between these pulses.

3. Experimental results

A room-temperature photoluminescence spectrum of the ZnO layer recorded for above bandgap excitation at 337 nm is displayed in Fig. 2. As known for such films [21], it shows a strong and spectrally narrow free-exciton emission centered at 392 nm and a spectrally broad, defect-related blue-green emission band extending from 400 to 550 nm. The origin of the blue-green emission has strongly been debated in the literature [21] and it is generally believed that this emission involves multiple defects and/or defect complexes.

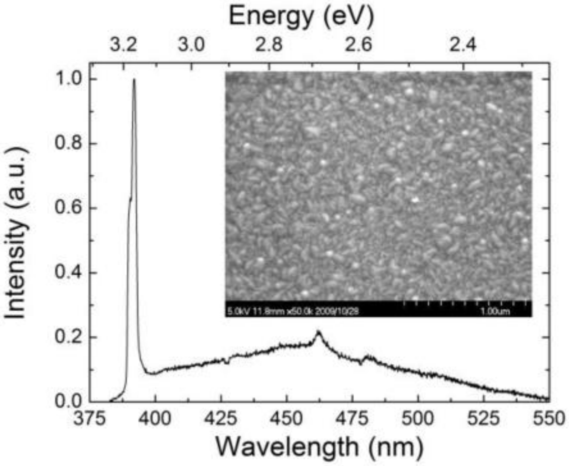

Fig. 2. Room-temperature photoluminescence spectrum of the ZnO layer for one-photon, above-bandgap excitation at 337 nm. The spectrally narrow free-exciton emission around 392 nm and the defect-related blue-green emission band extending from 400 to 550 nm are clearly distinguished. Inset: Scanning electron microscope image of the sputtered 400-nm-thick ZnO film.

Nonlinear optical spectra recorded for below-band gap excitation with 6-fs-laser pulses centered at around 800 nm are shown in Fig. 3(a). Two prominent emission bands are found. The first one is centered at around 400 nm, slightly below the free-exciton resonance. The second emission band is centered around 500 nm. The intensity of both bands depends very differently on the laser intensity. The intensity I_1 of the 400-nm-band (red circles in Fig. 3(b)) scales essentially as the second power of the laser power P, $I_1 \propto P^{b1}$ with $b1 = 1.85 \pm 0.1$ (solid line in Fig. 3(b)). This suggests that this emission arises predominantly from resonantly enhanced second harmonic generation (SHG) from the ZnO film. The drop in SHG intensity at $\lambda < 380$ nm is then attributed to the reabsorption of SH radiation in the ZnO film. This assignment is in agreement with recent studies using more narrowband, spectrally tunable below-bandgap excitation [9]. The intensity I_2 of the blue-green emission band (red circles in Fig. 3(c)) depends much more strongly on the laser power, $I_2 \propto P^{b2}$ with $b2 = 3.5 \pm 0.3$ (solid line in Fig. 3(c)). A similarly pronounced power dependence has been observed before [9] and has led the authors to conclude that this emission band can be assigned to a multiphoton-induced luminescence band. Since the spectral shape in Fig. 3 is independent on the excitation power we conclude that stimulated emission processes, well known in ZnO nanostructures, can be neglected under excitation conditions chosen in our experiments.

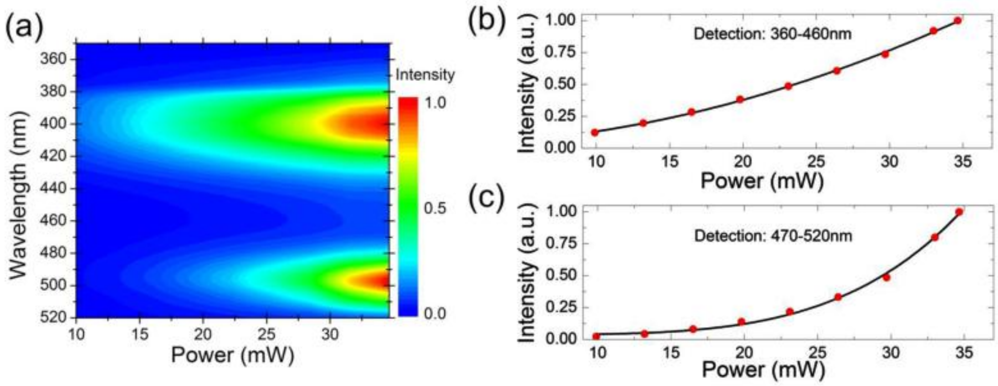

Fig. 3. (a) Spectrally resolved nonlinear optical emission from a ZnO film. The sample is excited with 6-fs laser pulses pulses centered at 800 nm. The emission spectra are recorded as a function of the average laser power. Two emission bands, a blue emission around 400 nm and a blue-green emission around 500 nm are discerned. (b) Power dependence of the blue band, integrated between 360 and 460 nm (red circles) and allometric fit $I \propto P^{b1}$ with $b1 = 1.85 \pm 0.1$ (black solid line). (c) Power dependence of the blue-green band, integrated between 470 and 520 nm (red circles) and allometric fit $I \propto P^{b2}$ with $b2 = 3.5 \pm 0.3$ (black solid line).

To further characterize the two nonlinear optical emission bands, we induce this emission by a phase-locked pair of collinearly propagating 6-fs laser pulses and record the emission intensity $I_{IF}\left(\tau, \lambda_d\right)$ as a function of the interpulse delay τ and the emission wavelength λ_d. Such interferometric frequency resolved autocorrelation (IFRAC) measurements have successfully been used to characterize ultrashort laser pulses [20, 22] and very recently also to probe the optical nonlinearity of a single metallic nanotip [23]. An IFRAC trace $I_{IF}\left(\tau, \lambda_d\right)$ from the ZnO-layer recorded with pulses having an energy of 0.44 nJ (laser power 35 mW) is shown in Fig. 4(a). Here, the time delay τ between the two pulses is varied between –30 fs and + 30 fs and the spectral emission is detected between 370 nm and 520 nm. As in Fig. 3, two distinct emission bands, the blue emission around 400 nm and the blue-green band around 500 nm are discerned. The IFRAC signals of both bands show distinctly different dynamics and, most importantly, very different interference fringe patterns. In the blue emission band, the modulation period, i.e., the time difference between two fringe maxima, in a narrow region around $\tau = 0$ is $T = 2\lambda_d / c = 4\pi / \omega_d$ (ω_d: detection frequency) and varies linearly with the detection wavelength. This is schematically illustrated by the dotted lines in Fig. 4(a). At $\lambda = 400$ nm we find $T = 2.69 \pm 0.05$ fs, in good agreement with the expected value of 2.67 fs. For larger τ, the fringe spacing reduces to half this value. The wavelength-dependence of the fringes is more clearly seen when looking at the magnitude of the Fourier transforms $\tilde{I}_{IF}\left(\omega_\tau, \lambda_d\right) = \int I_{IF}\left(\tau, \lambda_d\right) \exp\left(-i\omega_\tau \tau\right) d\tau$ along the delay axis τ (Fig. 4(b)). This Fourier transform shows peaks around $\omega_\tau = 0$ (the DC component), $\omega_\tau = \pm\omega_d / 2$ (the fundamental sidebands) and $\omega_\tau = \pm\omega_d$ (the second order sidebands). It is important to note that in an off-resonant, coherent second harmonic experiment, the center frequencies of the fundamental and second order sidebands are proportional to the detection frequency [20].

Received 4 Oct 2010; revised 7 Nov 2010; accepted 7 Nov 2010; published 16 Nov 2010

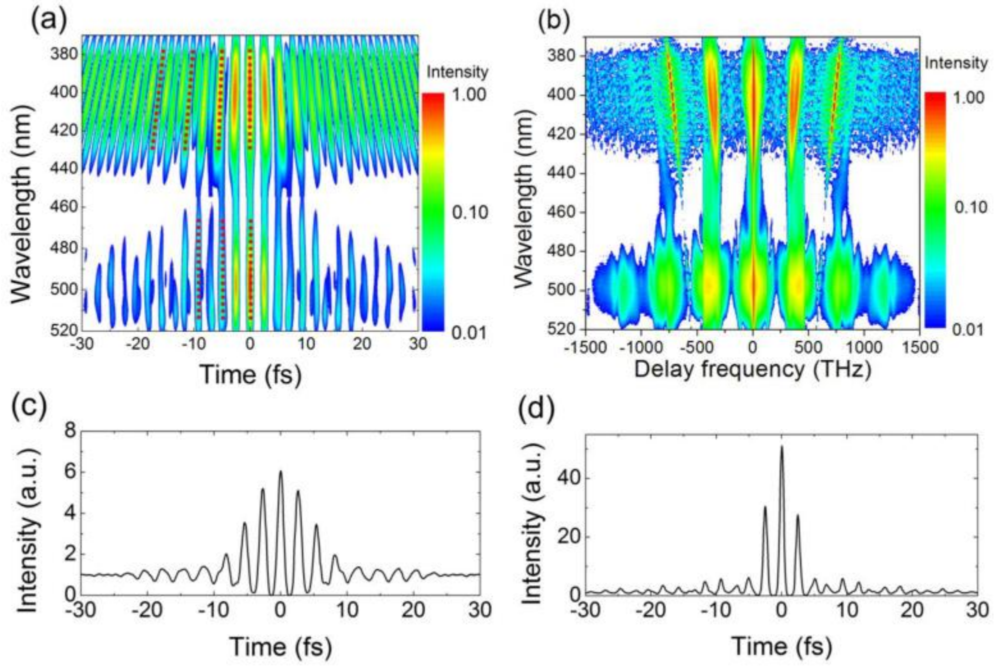

Fig. 4. (a) Experimental IFRAC traces from a 400-nm-thick ZnO layer plotted on a logarithmic scale. Two distinct emission-bands, the blue emission around 400 nm and a blue-green emission around 500 nm are discerned. Detection-wavelength dependent interference fringes with a period $T = 2\lambda_d / c$, λ_d : detection wavelength, c : speed of light, are observed in the wavelength range between 380 nm and 450 nm. This points to a coherent optical harmonic emission process. In the range between 460 nm and 520 nm, however, the interference fringes are independent of the detection-wavelength and modulation period of $T = 2.4$ fs, indicating that the emission arises from an incoherent multiphoton-induced PL process. The different shape of the coherent and the incoherent emission is illustrated by dotted lines. (b) Spectral Fourier transformations of the IFRAC traces plotted on logarithmic intensity scale (c,d) IAC trace obtained by spectrally integrating the data in (a) from 380nm to 460nm and from 460nm to 520nm, respectively.

Very different fringe patterns are observed in the IFRAC signal of the blue-green emission band (Fig. 4(a)). Here, pronounced fringes are only seen in a narrow region around $\tau = 0$ due to the large ($b2 = 3.5$)nonlinear power dependence. Moreover, we observe, in the entire detection wavelength range between 460 and 520 nm, a fringe spacing $T = 2.40 \pm 0.05$ fs which is independent of the detection wavelength. The detection-wavelength-independence of the fringe spacing is confirmed by looking at the Fourier transform $\tilde{I}_{IF}(\omega_\tau, \lambda_d)$. This signal is arguably much more complex than the corresponding signal in the blue emission band. In addition to the fundamental and second order sideband peaks it shows third order sideband peaks. Weak sidebands at the fourth and even fifth order (not shown) are also resolved when plotting $\tilde{I}_{IF}(\omega_\tau, \lambda_d)$ on a logarithmic scale. Most notably, however, the center frequency ω_τ of all sidebands is independent of the detection frequency. Regular interferometric autocorrelation (IAC) traces $I_{IAC}(\tau) = \int I_{IF}(\tau, \lambda_d)\, d\lambda_d$ are deduced from the data in Fig. 4a by spectral integration over the wavelength range from 380 to 460 nm (blue-emission band) and 460 to 520 nm (blue-green emission band). The IAC traces are shown in Fig. 4(c) and (d), respectively. Notable in the IAC trace of the blue emission is the enhancement factor $\eta = I_{IAC}(\tau = 0) / \lim_{\tau \to \infty} I_{IAC}(\tau)$ of 6, which agrees well with $\eta = 2^{2\cdot 1.85} / 2 = 6.5$ expected for the observed nonlinear power dependence of 1.85. This IAC trace appears slightly broader than that recorded with a BBO crystal (Fig. 1(c)). The IAC trace of the blue-green emission (Fig. 4(d)) displays a much larger enhancement factor of $\eta = 50$, close to the value of 64 resulting from the strong power dependence of the involved optical nonlinearity. Consequently, the IAC extends over essentially only three cycles of the light field in the time domain.

4. Discussion

Apart from their different dynamics, the most notable difference between the interferometric frequency-resolved autocorrelation functions recorded in the blue and blue-green emission is the different detection wavelength dependence of the fringe spacing T. While $T = 2\lambda_d / c$ in the blue band, T is found to be independent of λ in the blue-green band. For a coherent, off-resonant second harmonic process, the wavelength scaling of T is readily explained. Here, the interferometric SH signals recorded when exciting the sample with a phase-locked pulse pair are $I_{IAC}(\tau) = \int \left| \left(E(t) + E(t-\tau) \right)^2 \right|^2 dt$ and $I_{IF}(\tau, \omega_d) = \left| \int \left(E(t) + E(t-\tau) \right)^2 \exp(-i\omega_d t) dt \right|^2$. For excitation with a spectrally narrow-band laser pulse $E = \varepsilon(t) \exp(-i\omega_L t)$ one readily sees that $T = 4\pi / \omega_d$. For excitation with spectrally broad-band few-cycle pulses the analysis is slightly more involved and has been given in [20]. Here, the fringes in the IFRAC signal at early delay times are governed by the fundamental sideband which oscillates as $\cos\left(\frac{\omega_d \tau}{2} \right)$ [20]. The fringe spacing is thus $T = 4\pi / \omega_d$. At longer delay times, pronounced fringes with half the spacing are seen which reflect the second order sideband.

In case of an incoherent, spontaneous emission process (photoluminescence), the expected IFRAC signals are fundamentally different. Here the phase relation between the excitation laser and re-emitted electric field form the sample is lost and the emitted intensity is proportional to the incoherent carrier population n_e in the light-emitting state. We emphasize that despite of the incoherent nature of the emission, coherences fringes can be observed in autocorrelation measurements. Such fringes necessarily result from interferences in the excitation process of the system. This is readily understood by considering a dipole-allowed one-photon transition of a simple two-level system impulsively excited with a short pulse $n_e \approx \left| d \cdot \tilde{E}(\omega_r) \right|^2 / \hbar^2$. Here, d is the transition dipole moment and $\tilde{E}(\omega_r)$ is the amplitude of the Fourier component of the laser electric field $E(t)$ at the transition frequency ω_r between the ground and excited state of the system. The equality holds if the duration of the laser pulse is much shorter than the dephasing time of the two-level system. When impulsively exciting the system with a pair of pulses, a large population n_e is therefore created if the field components at ω_r interfer contructively. The fringe spacing therefore is $T = 2\pi / \omega_r$. It is thus defined only by the energetics of the optically excited system and independent of the detection frequeny. It is important to note that in case of an incoherent emission process the emission frequency ω_d may differ from the transition frequency ω_r since the optically excited state may be coupled to the emitting state by inelastic relaxation processes.

For multiphoton-excitation of a two-level system, the Rabi frequency $\Omega_r(t) = d \cdot E(t) / \hbar$ can be replaced by a generalized Rabi frequency $\Omega_r(t) = \alpha \cdot E(t)^n / \hbar$ [24]. Here, α is the transition matrix element for an n-photon transition between ground and excited state. The

#136025 - $15.00 USD Received 4 Oct 2010; revised 7 Nov 2010; accepted 7 Nov 2010; published 16 Nov 2010

impulsively excited carrier density is $n_e \approx \left| d \cdot E^n(\omega_r) \right|^2 / \hbar^2$, where $E^n(\omega_r)$ is the Fourier component of the n-th harmonic of the laser field at ω_r. This results in a fringe-spacing $T = 2n\pi / \omega_r$, which is – again – independent of the detection wavelength.

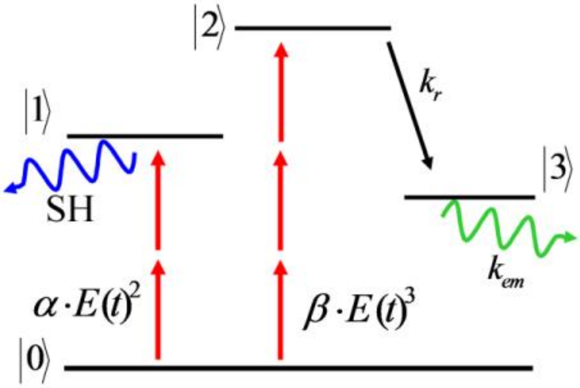

Fig. 5. Schematic illustration of a four-level system with displaying both harmonic emission and multi-photon-induced photoluminescence. We assume that the electronic system is excited by an ultrafast laser pulse with electric field E(t) coupling the ground state $|0\rangle$ to an excited state $|1\rangle$ by two-photon absorption and to an excited state $|2\rangle$ by three-photon absorption. Second harmonic radiation is emitted from $|1\rangle$ whereas carriers in $|2\rangle$ are assumed to relax non-radiatively at rate k_r to a state $|3\rangle$ from which they return to the ground state by PL emission.

We therefore conclude very generally that coherent and incoherent emission processes result in fundamentally different IFRAC signals. Coherent emission processes such as Rayleigh scattering or optical harmonic generation result in a fringe spacing which is proportional to the detection wavelength. Incoherent spontaneous emission processes, however, are characterized by a detection-wavelength independent fringe spacing. This spacing is governed by the energy of the optically excited state which may differ from that of the light-emitting state. IFRAC measurements can therefore distinguish between coherent and incoherent emission and provide a full characterization of the coherence properties of the re-emitted light.

This leads us to conclude that in the case of the ZnO films studied in this work, the IFRAC signal in the blue emission region in Fig. 4(a) results predominantly from coherent second harmonic generation in the ZnO film whereas the IFRAC signal in the blue-green region in Fig. 4(a) reflects multiphoton-absorption in the ZnO film followed by incoherent, spontaneous emission from below-bandgap defect states. The short fringe spacing of $T = 2.4$ fs and the strong power dependence of the of the optical nonlinearity $b2 = 3.5$ indicates that, here, multiphoton-absorption creates carriers in the conduction band of ZnO which then relax into the light-emitting below-bandgap defect states.

For a more quantitative analysis of the data in Fig. 4(a), we have simulated these results within the framework of optical Bloch equations. As schematically illustrated in Fig. 5, we model the ZnO film as an effective 4-level-system with a ground state $|0\rangle$ and three excited states $|1\rangle$ - $|3\rangle$. We assume that state $|1\rangle$ is coupled to the ground state by two-photon absorption, whereas $|2\rangle$ couples to $|0\rangle$ by three-photon absorption. We also assume that carriers $|2\rangle$ can relax at a rate k_r to the low-lying state $|3\rangle$ from where they can spontaneously emit light. The Hamiltonian of the isolated system is then given as $H_0 = \sum \hbar\omega_i \left|i\right\rangle\left\langle i\right|$, $i = 0...3$, and that for light-matter interaction is $H_I = \hbar\Omega_{r1}(t)\left(\left|0\right\rangle\left\langle 1\right| + \left|1\right\rangle\left\langle 0\right|\right) + \hbar\Omega_{r2}\left(\left|0\right\rangle\left\langle 2\right| + \left|2\right\rangle\left\langle 0\right|\right)$, with generalized Rabi frequencies $\Omega_{r1}(t) = \alpha E(t)^2/\hbar$ and $\Omega_{r2}(t) = \beta E(t)^3/\hbar$. Here α (β) denotes the matrix element for two-photon (three-photon) interaction between states $\left|0\right\rangle$ and $\left|1\right\rangle$ ($\left|0\right\rangle$ and $\left|2\right\rangle$). For simplicity, we assume real matrix elements. The time-evolution of the density matrix of the system is obtained by solving the Liouville-von Neumann equation $\frac{\partial}{\partial t}\rho = -\frac{i}{\hbar}\left[H,\rho\right] + \left.\frac{\partial}{\partial t}\rho\right|_{rel}$. The last term includes possible dephasing and relaxation processes. The equations of motion for the relevant polarizations then read

$$\dot{\rho}_{01} = \overline{\dot{\rho}_{10}} = -i\Omega_{r1}\left(\rho_{11} - \rho_{00}\right) - i\left(\omega_1 - \omega_0\right)\rho_{01} - \frac{1}{T2_1}\rho_{01} \tag{1}$$

$$\dot{\rho}_{02} = \overline{\dot{\rho}_{10}} = -i\Omega_{r2}\left(\rho_{22} - \rho_{00}\right) - i\left(\omega_2 - \omega_0\right)\rho_{02} - \left(\frac{1}{T2_2} + \frac{k_r}{2}\right)\rho_{02} \tag{2}$$

Polarization dephasing times $T2_1$ and $T2_2$ are introduced phenomenologically. The population dynamics are deduced from

$$\dot{\rho}_{00} = -2\Omega_{r1}\,\mathrm{Im}\left(\rho_{01}\right) - 2\Omega_{r2}\,\mathrm{Im}\left(\rho_{02}\right) + k_{em}\rho_{33} \tag{3}$$

$$\dot{\rho}_{11} = 2\Omega_{r1}\,\mathrm{Im}\left(\rho_{01}\right) \tag{4}$$

$$\dot{\rho}_{22} = 2\Omega_{r2}\,\mathrm{Im}\left(\rho_{02}\right) - k_r\rho_{22} \tag{5}$$

$$\dot{\rho}_{33} = k_r\rho_{22} - k_{em}\rho_{33} \tag{6}$$

Here k_{em}^{-1} denotes the radiative lifetime of state $\left|3\right\rangle$. The second harmonic field emitted from the sample is taken as $E_{SH}(t) = d_1 \cdot \mathrm{Re}\left(\rho_{01}(t)\right)$ with d_1 being the one-photon transition dipole matrix element of states $\left|0\right\rangle$ and $\left|1\right\rangle$. The spontaneous emission intensity from level $\left|3\right\rangle$ is modeled as $I_{PL}(\lambda) \propto \rho_{33}(t_0) \cdot PL(\lambda)$ with $\rho_{33}(t_0)$ being the population in level $\left|3\right\rangle$ at a finite delay time t_0 after the arrival of the laser pulse and $PL(\lambda)$ being the emission spectrum in the blue-green region deduced from Figs. 3 and 4. The experimental data are modeled by taking a phase-locked pair of unchirped 6-fs-pulses as the input field $E(t)$. The IFRAC traces are then simulated using $I_{IF}(\tau,\omega_d) = \left|\int E_{SH}(\tau)\exp(-i\omega_d t)dt\right|^2 + I_{PL}(\tau,\omega_d)$. Model simulations have been performed taking unchirped laser pulses with a Gaussian spectrum and with the spectrum seen in Fig. 1(c). Results of such simulations for optimized system parameters are shown in Fig. 6(a). Obviously the salient features of the experiment, specifically the different wavelength dependence of the fringe spacings in the blue and blue-green emission band are rather well reproduced. To reach good agreement with experiment, a few assumptions about the properties of the four-level-system are necessary:

(i) The energy of the SH-emitting state $\left|1\right\rangle$ should be chosen around 3.1 eV (400 nm), slightly below the ZnO bandgap, and a short, yet finite, dephasing time $T2_1 = 7 \pm 2$ fs should be assumed to match the IFRAC traces in the blue range. Good agreement is found when taking bandwidth-limited pulses with the spectrum shown in Fig. 1(c) and a dephasing time of 7 fs.

#136025 - $15.00 USD Received 4 Oct 2010; revised 7 Nov 2010; accepted 7 Nov 2010; published 16 Nov 2010

(ii) A large energy of the three-photon active state $\left|2\right\rangle$ of 5.1 eV (240 nm), far above the ZnO bandgap, should be chosen to match the detection-wavelength independent fringe spacing of 2.4 fs in the blue-green emission band. The dephasing time $T2_2$ should not be longer than 3 fs to match the time dynamics of the experimentally-recorded IFRAC trace.

With these assumptions the wavelength-dependence and the dynamics of the IFRAC traces are reasonably well reproduced. Also the dynamics of the spectrally-integrated IAC traces in Fig. 6(c,d) are similar to those in the experiment (Fig. 4(c,d)). The IFRAC signal in the blue range shows a fringe spacing $T = 4\pi / \omega_d$. Clearly, the blue emission results almost entirely from coherent second harmonic emission. A closer comparison between the IFRAC simulations for coherent second harmonic emission (Fig. 6a) and the experimental data in the blue emission band (Fig. 4a) shows the following important features: (i) At sufficiently long delay times, all fringes have comparable signal intensities. These fringes persist even if the pulse delay τ is much larger than the dephasing time $T2_1$. They result from the interference of the second harmonic fields E_{SH} generated by each of the two temporally well-separated pulses (s. Eq. (4) in Ref. 20). They persist until τ becomes larger than the inverse spectral resolution of the monochromator used for IFRAC detection. These fringes give rise to the spectrally narrow second order sideband in the Fourier spectra.

(ii) At early times also second harmonic signals induced by the direct interference of the laser fields of the two pulses on the sample contribute. These signals results in a rather complex temporal and spectral IFRAC pattern arising from the interference between both pulses and the coherent polarizations induced in the nonlinear medium. They therefore persist only for delays similar to $T2_1$. Essentially, we find that “even” fringes at $\tau = 4n\pi / \omega_d,\ n \in \mathbb{Z}$ extend over the full range of detection wavelength range. The “odd” fringes at $\tau = (2n+1) 2\pi / \omega_d,\ n \in \mathbb{Z}$, however, have high intensity only for short detection wavelengths, $\omega_d \le \omega_1 - \omega_0$, yet weak intensity for longer wavelengths. For the “even” harmonics, the fields at the fundamental laser frequency and at the second harmonic frequency are in phase, and constructive interference is seen for all detection wavelengths. For the “odd” harmonics, however, the interference pattern apparently depends on the phase of the second harmonic polarization ρ_{01} which exhibits a phase jump at ω_d and hence gives rise to constructive interference for $\omega_d \le \omega_1 - \omega_0$, yet destructive interference at longer wavelengths. A full analysis of these interference patterns is currently underway and will be given elsewhere.

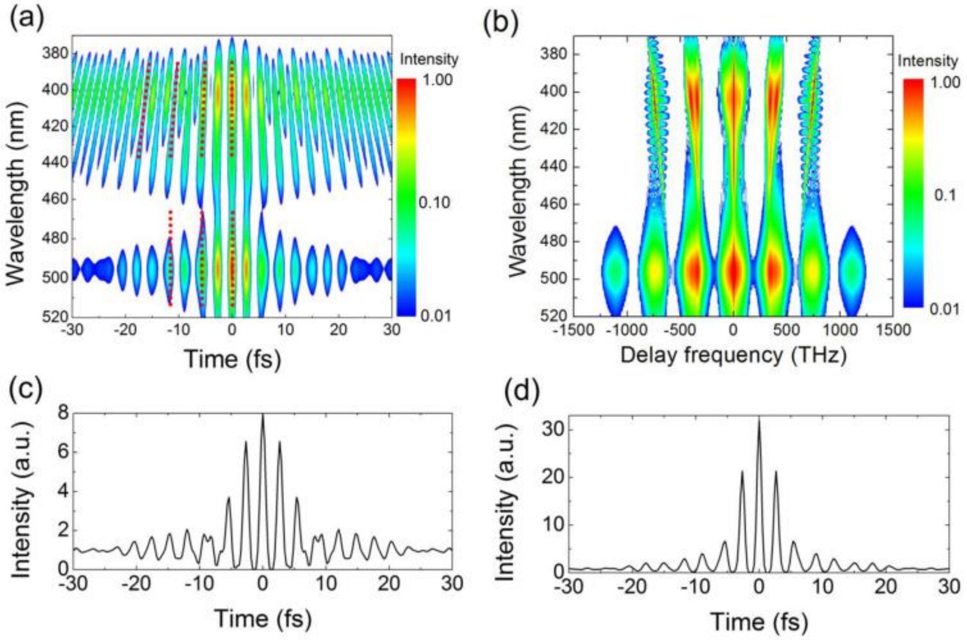

Fig. 6. (a) Simulation of an IFRAC trace for the model system illustrated in Fig. 5 after excitation with a 6-fs-laser pulse plotted on a logarithmic scale. In agreement with the experimental data in Fig. 4(a), the simulation shows emission-wavelength-dependent interference fringes in the region around 440 nm, reflecting coherent second harmonic emission. The wavelength-independent fringes around 500 nm reflect incoherent three-photon-induced photoluminescence. (b) Spectral Fourier transformations of the IFRAC traces plotted on logarithmic intensity scale. (c) IAC trace obtained by spectrally integrating the data in (a) from 380nm to 460nm. (d) IAC trace obtained by integrating the data in (a) from 460nm to 520nm.

In the region of the blue-green emission, the data in Fig. 6(a) show interference fringes with a spacing which is independent on the detection-wavelength. We take this a a clear signature that the blue-green emission arises predominantly from an incoherent photoluminescence process. A closer comparison between the Fourier-transformed IFRAC signals in Fig. 4(b) and 6(b) indicates, however, that the microscopic mechanisms resulting in the blue-green emission are certainly much more complicated than a three-photon-induced absorption into a higher-lying electronic state far above the bandgap. The strong power dependence of the nonlinear optical signal ($b2 = 3.5$) and the complex IFRAC-spectrum in Fig. 6(b) may probably be explained by an interference between different nonlinear optical processes. It is likely that this strong power dependence results from field-induced ionization processes, i.e., the generation of a dense electron-hole plasma in the ZnO film by below-band gap excitation. Its effect on the optical nonlinearities of ZnO nanostructures will be subject of further investigations.

5. Conclusions

In summary, we have studied the nonlinear optical properties of thin zinc oxide films using interferometric frequency-resolved autocorrelation (IFRAC) microscopy following impulsive excitation with 6-fs optical pulses focused to a spot size of 1 µm. Two emission bands with distinctly different coherence properties are observed in the blue and blue-green emission region. Both bands display very different wavelength dependencies of the interference patterns of their IFRAC signals. A new IFRAC analysis based on solutions of optical Bloch equations shows that this can directly be traced back to the different coherence properties of the two emission channels. This analysis allows us to unambiguously assign the blue band as resonantly enhanced coherent second harmonic emission close to the band gap of ZnO. The blue-green emission band, displaying detection-wavelength independent fringes, results from multiphoton-absorption-induced incoherent spontaneous emission from below bandgap defect states. Our results show that IFRAC microscopy is a new and elegant way to fully characterize the coherence properties of the optical emission from nanostructures. With its high time resolution of a few fs only, it can directly probe the dynamics of coherent optical polarizations in nanostructures in the time domain. Its high spatial resolution makes it interesting for studying the nonlinear optical properties of single nanostructure and/or for coherent nonlinear optical microscopy.

Acknowledgments

This research was supported by the Japan Science and Technology Agency (JST) and the Deutsche Forschungsgemeinschaft (DFG) under the strategic Japanese-German Cooperative program on "Nanoelectronics". Support by the DFG (SPP 1391) and by the Korea Foundation for International Cooperation of Science & Technology (Global Research Laboratory project, K20815000003) is acknowledged.

Received 4 Oct 2010; revised 7 Nov 2010; accepted 7 Nov 2010; published 16 Nov 2010

Lower bound of energy dissipation in optical excitation transfer via optical near-field interactions

Makoto Naruse,[1,2,*] **Hirokazu Hori,**[3] **Kiyoshi Kobayashi,**[3]
Petter Holmström,[4] **Lars Thylén,**[4,5] **and Motoichi Ohtsu**[2]

[1] *National Institute of Information and Communications Technology, 4-2-1 Nukui-kita, Koganei, Tokyo 184-8795, Japan*
[2] *Department of Electrical Engineering and Information Systems and Nanophotonics Research Center, School of Engineering, The University of Tokyo, 2-11-16 Yayoi, Bunkyo-ku, Tokyo 113-8656, Japan*
[3] *Interdisciplinary Graduate School of Medicine and Engineering, University of Yamanashi, Kofu, Yamanashi 400-8511, Japan*
[4] *Laboratory of Photonics and Microwave Engineering, Royal Institute of Technology (KTH), SE-164 40 Kista, Sweden*
[5] *Hewlett-Packard Laboratories, Palo Alto, CA 94304 USA*
**naruse@nict.go.jp*

Abstract: We theoretically analyzed the lower bound of energy dissipation required for optical excitation transfer from smaller quantum dots to larger ones via optical near-field interactions. The coherent interaction between two quantum dots via optical near-fields results in unidirectional excitation transfer by an energy dissipation process occurring in the larger dot. We investigated the lower bound of this energy dissipation, or the intersublevel energy difference at the larger dot, when the excitation appearing in the larger dot originated from the excitation transfer via optical near-field interactions. We demonstrate that the energy dissipation could be as low as 25 μeV. Compared with the bit flip energy of an electrically wired device, this is about 10^4 times more energy efficient. The achievable integration density of nanophotonic devices is also analyzed based on the energy dissipation and the error ratio while assuming a Yukawa-type potential for the optical near-field interactions.

OCIS codes: (260.2160) Energy transfer; (230.5590) Quantum-well, -wire and -dot devices; (200.3050) Information processing; (180.4243) Near-field microscopy.

References and links

1. ITU-T Focus Group on ICTs and Climate Change, http://www.itu.int/ITU-T/focusgroups/climate/index.html.
2. L. B. Kish, "Moore's law and the energy requirement of computing versus performance," IEE Proc., Circ. Devices Syst. **151**(2), 190–194 (2004).
3. J. Gea-Banacloche, "Minimum energy requirements for quantum computation," Phys. Rev. Lett. **89**(21), 217901 (2002).
4. The Green Grid, http://www.thegreengrid.org/.
5. R. S. Tucker, R. Parthiban, J. Baliga, K. Hinton, R. W. A. Ayre, and W. V. Sorin, "Evolution of WDM Optical IP Networks: A Cost and Energy Perspective," J. Lightwave Technol. **27**(3), 243–252 (2009).
6. K. Sato, and H. Hasegawa, "Prospects and Challenges of Multi-Layer Optical Networks," IEICE Trans. Commun, E **90-B**, 1890–1902 (2007).
7. M. Ohtsu, K. Kobayashi, T. Kawazoe, T. Yatsui, and M. Naruse, *Principles of Nanophotonics* (Taylor and Francis, Boca Raton, 2008).
8. L. Thylén, P. Holmström, A. Bratkovsky, J. Li, and S.-Y. Wang, "Limits on Integration as Determined by Power Dissipation and Signal-to-Noise Ratio in Loss-Compensated Photonic Integrated Circuits Based on Metal/Quantum-Dot Materials," IEEE J. Quantum Electron. **46**(4), 518–524 (2010).
9. T. Kawazoe, K. Kobayashi, J. Lim, Y. Narita, and M. Ohtsu, "Direct observation of optically forbidden energy transfer between CuCl quantum cubes via near-field optical spectroscopy," Phys. Rev. Lett. **88**(6), 067404 (2002).
10. M. Naruse, T. Kawazoe, R. Ohta, W. Nomura, and M. Ohtsu, "Optimal mixture of randomly dispersed quantum dots for optical excitation transfer via optical near-field interactions," Phys. Rev. B **80**(12), 125325 (2009).

#132260 - $15.00 USD Received 2 Aug 2010; revised 31 Aug 2010; accepted 23 Sep 2010; published 5 Oct 2010

11. T. Franzl, T. A. Klar, S. Schietinger, A. L. Rogach, and J. Feldmann, "Exciton Recycling in Graded Gap Nanocrystal Structures," Nano Lett. **4**(9), 1599–1603 (2004).
12. J. H. Lee, Zh. M. Wang, B. L. Liang, K. A. Sablon, N. W. Strom, and G. J. Salamo, "Size and density control of InAs quantum dot ensembles on self-assembled nanostructured templates," Semicond. Sci. Technol. **21**(12), 1547–1551 (2006).
13. K. Akahane, N. Yamamoto, and M. Tsuchiya, "Highly stacked quantum-dot laser fabricated using a strain compensation technique," Appl. Phys. Lett. **93**(4), 041121 (2008).
14. T. Mano, and N. Koguchi, "Nanometer-scale GaAs ring structure grown by droplet epitaxy," J. Cryst. Growth **278**(1-4), 108–112 (2005).
15. W. I. Park, G.-C. Yi, M. Y. Kim, and S. J. Pennycook, "Quantum Confinement Observed in ZnO/ZnMgO Nanorod Heterostructures," Adv. Mater. **15**(6), 526–529 (2003).
16. T. Kawazoe, K. Kobayashi, S. Sangu, and M. Ohtsu, "Demonstration of a nanophotonic switching operation by optical near-field energy transfer," Appl. Phys. Lett. **82**(18), 2957–2959 (2003).
17. T. Yatsui, S. Sangu, T. Kawazoe, M. Ohtsu, S. J. An, J. Yoo, and G.-C. Yi, "Nanophotonic switch using ZnO nanorod double-quantum-well structures," Appl. Phys. Lett. **90**(22), 223110 (2007).
18. M. Naruse, T. Kawazoe, S. Sangu, K. Kobayashi, and M. Ohtsu, "Optical interconnects based on optical far- and near-field interactions for high-density data broadcasting," Opt. Express **14**(1), 306–313 (2006).
19. M. Naruse, T. Miyazaki, F. Kubota, T. Kawazoe, K. Kobayashi, S. Sangu, and M. Ohtsu, "Nanometric summation architecture based on optical near-field interaction between quantum dots," Opt. Lett. **30**(2), 201–203 (2005).
20. H. Hori, "Electronic and Electromagnetic Properties in Nanometer Scales," in *Optical and Electronic Process of Nano-Matters*, M. Ohtsu, ed. (Kluwer Academic, 2001), pp. 1–55.
21. P. Kocher, J. Jaffe, and B. Jun, "Introduction to Differential Power Analysis and Related Attacks," http://www.cryptography.com/resources/whitepapers/DPATechInfo.pdf.
22. M. Naruse, H. Hori, K. Kobayashi, and M. Ohtsu, "Tamper resistance in optical excitation transfer based on optical near-field interactions," Opt. Lett. **32**(12), 1761–1763 (2007).
23. H. Haug, and S. W. Koch, *Quantum Theory of the Optical and Electronic Properties of Semiconductors* (World Scientific, Singapore, 2004).
24. S. Sangu, K. Kobayashi, A. Shojiguchi, T. Kawazoe, and M. Ohtsu, "Excitation energy transfer and population dynamics in a quantum dot system induced by optical near-field interaction," J. Appl. Phys. **93**(5), 2937–2945 (2003).
25. H. J. Carmichael, *Statistical Methods in Quantum Optics 1* (Springer-Verlag, Berlin, 1999).
26. T. Yatsui, H. Jeong, and M. Ohtsu, "Controlling the energy transfer between near-field optically coupled ZnO quantum dots," Appl. Phys. B **93**(1), 199–202 (2008).
27. W. Nomura, T. Yatsui, T. Kawazoe, and M. Ohtsu, "The observation of dissipated optical energy transfer between CdSe quantum dots," J. Nanophoton. **1**(1), 1–8 (2007).
28. W. Nomura, T. Yatsui, T. Kawazoe, M. Naruse, and M. Ohtsu, "Structural dependency of optical excitation transfer via optical near-field interactions between semiconductor quantum dots," Appl. Phys. B **100**(1), 181–187 (2010).
29. M. Ohtsu, and K. Kobayashi, *Optical Near Fields* (Springer, Berlin, 2004).
30. S. Haykin, *Communication Systems* (John Wiley & Sons, New York, 1983).
31. M. Naruse, T. Inoue, and H. Hori, "Analysis and Synthesis of Hierarchy in Optical Near-Field Interactions at the Nanoscale Based on Angular Spectrum," Jpn. J. Appl. Phys. **46**(No. 9A), 6095–6103 (2007).
32. K. Ohmori, K. Kodama, T. Muranaka, Y. Nabetani, and T. Matsumoto, "Tunneling of spin polarized excitons in ZnCdSe and ZnCdMnSe coupled double quantum wells," Phys. Status Solidi **7**(6), 1642–1644 (2010).
33. J. Seufert, G. Bacher, H. Schömig, A. Forchel, L. Hansen, G. Schmidt, and L. W. Molenkamp, "Spin injection into a single self-assembled quantum dot," Phys. Rev. B **69**(3), 035311 (2004).
34. H. Imahori, "Giant Multiporphyrin Arrays as Artificial Light-Harvesting Antennas," J. Phys. Chem. B **108**(20), 6130–6143 (2004).
35. H. Tamura, J.-M. Mallet, M. Oheim, and I. Burghardt, "Ab Initio Study of Excitation Energy Transfer between Quantum Dots and Dye Molecules," J. Phys. Chem. C **113**(18), 7548–7552 (2009).
36. V. P. Carey, and A. J. Shah, "The Exergy Cost of Information Processing: A Comparison of Computer-Based Technologies and Biological Systems," J. Electron. Packag. **128**(4), 346–352 (2006).

1. Introduction

Energy efficiency is an issue of increasing importance in today's information and communications technology (ICT) in order to abate CO_2 production [1]. Various approaches have been intensively studied regarding energy efficiency, ranging from analysis of fundamental physical processes [2,3] to system-level smart energy management [4]. Energy efficiency involving optical processes has also been considered in terms of, for example, how we can fully exploit the low-loss, wavelength-multiplexed, high-bandwidth nature of optical communications for efficient energy usage [5,6].

The fundamental physical attributes of photons exploited so far are, however, typically just the ability to utilize fully optical end-to-end connections and the multiplexing nature of

#132260 - $15.00 USD Received 2 Aug 2010; revised 31 Aug 2010; accepted 23 Sep 2010; published 5 Oct 2010

propagating light. One of the primary objectives of this paper is to note another unique attribute available on the nanometer scale, that is, optical near-field interactions [7]. In related issues, the limit on the integration density determined by power dissipation and signal-to-noise ratio was studied by Thylén et al. in systems composed of metal and quantum dots [8]. However, the fundamental physical mechanisms studied so far are based on a dipole coupling, which is significantly different from the optical excitation transfer via optical near-field interactions discussed in this paper. Here we theoretically demonstrate that the energy dissipation in optical excitation transfer via optical near-field interactions could be as low as 25 μeV, which is about 10^4 times smaller than the bit flip energy in a conventional electrically wired device.

As discussed in detail later, optical excitations could be transferred from smaller quantum dots (QDs) to larger ones via optical near-field interactions that allow transitions even to conventionally electric-dipole forbidden energy levels. Such optical excitation transfers have been experimentally demonstrated in various materials, such as CuCl [9], CdSe [10], and CdTe [11]. Geometry-controlled nanostructures are also seeing rapid progress, such as in size- and density-controlled InAs QDs [12], stacked InAs QDs [13], ring-shaped QDs [14], and ZnO nanorods [15]. Theoretical foundations have been constructed, such as the dressed photon model that unifies photons and material excitations on the nanometer scale, validating the non-zero transition probabilities even for conventionally electric-dipole forbidden energy levels [7]. Based on these principles and enabling technologies, a wide range of device operations have been demonstrated, such as logic gates [16,17], interconnects [18], energy concentration [11,19], and so forth. In considering a bit flip in nanophotonic logic gates, we need to combine multiple optical excitation transfers from smaller QDs to larger ones among multiple quantum dots; for instance, three QDs are needed in the case of an AND gate [16,18]. Therefore, this paper, dealing with the energy dissipation in optical excitation transfer composed of two dots, constitutes a foundation for nanophotonic devices in general.

The energy dissipation in such an optical excitation transfer from a smaller QD to a large one is the energy relaxation processes that occur at the destination QD (namely, the larger QD). In other words, the coherent interaction between two QDs via optical near-fields results in a unidirectional excitation transfer from a smaller QD to a larger one by the energy dissipation occurring in the larger QD [20]. In electrically wired devices, the dissipation occurring in external circuits is crucial in completing signal transfer. Such a fundamental principle also impacts tamper resistance against non-invasive attacks; tampering of information could easily be possible by monitoring power consumption patterns in electrically wired devices [21], whereas it is hard in optical excitation transfer since energy dissipation occurs at the destination QDs [22]. In this paper, we quantitatively investigate how such energy dissipation at the destination QD could be minimized. Here, it should be noted that the primary objective of this paper is to reveal the theoretical limitations of the principle provided by optical excitation transfer. We start our discussion with a theoretical model for cubic quantum dots and assume typical values for the inter-dots distance and interaction time, and so on. However we can extend the theoretical investigation into the parameter range where one of the ideal dots corresponds practically to a coupled quantum dot system in which inter-dot electron transfer takes place between energy level with a separation much smaller than those feasible by a single quantum dot.

2. Modeling

We begin with the interaction Hamiltonian between an electron–hole pair and an electric field, which is given by

$$\hat{H}_{int} = -\int d^3r \sum_{i,j=e,h} \hat{\psi}_i^{\dagger}(\mathbf{r}) e\mathbf{r}\bullet\mathbf{E}(\mathbf{r})\hat{\psi}_j(\mathbf{r}), \tag{1}$$

where e represents a charge, $\hat{\psi}_i^{\dagger}(\mathbf{r})$ and $\hat{\psi}_j(\mathbf{r})$ are respectively creation and annihilation operators of either an electron ($i, j=e$) or a hole ($i, j=h$) at $\boldsymbol{r}$, and $\boldsymbol{E}(\boldsymbol{r})$ is the electric field [23].

In usual light–matter interactions, $\boldsymbol{E}(\boldsymbol{r})$ is a constant since the electric field of diffraction-limited propagating light is homogeneous on the nanometer scale. Therefore, as is well known, we can derive optical selection rules by calculating the dipole transition matrix elements. As a consequence, in the case of cubic quantum dots for instance, transitions to states containing an even quantum number are prohibited. In the case of optical near-field interactions, on the other hand, due to the steep electric field of optical near-fields in the vicinity of nano-scale material, an optical transition that violates conventional optical selection rules is allowed. A detailed physical discussion is found in Ref [7].

Using near-field interactions, optical excitations in quantum dots can be transferred to neighboring ones. For instance, assume two cubic quantum dots whose side lengths are a and $\sqrt{2}a$, which we call QD_S and QD_L, respectively, as shown in Fig. 1(a). Suppose that the energy eigenvalues for the quantized exciton energy level specified by quantum numbers (n_x, n_y,n_z) in a QD with side length L are given by

$$E_{(n_x,n_y,n_z)} = E_B + \frac{\hbar^2\pi^2}{2ML^2}(n_x^2 + n_y^2 + n_z^2), \tag{2}$$

where E_B is the transition energy of the bulk exciton, and M is the effective mass of the exciton. According to Eq. (2), there exists a resonance between the level of quantum number (1,1,1) for QD_S and that of quantum number (2,1,1) for QD_L. Hereafter, the (1,1,1)-level of QD_S is denoted by E_S, and the (2,1,1)-level of QD_L is called E_{L_2}. There is an optical near-field interaction, which is denoted by U_{SL_2}, due to the steep electric field in the vicinity of QD_S. Therefore, excitons in S can move to L_2 in QD_L. Note that such a transfer is prohibited in propagating light since the (2,1,1)-level in QD_L contains an even number. In QD_L, the exciton undergoes intersublevel energy relaxation due to exciton–phonon coupling, denoted by Γ, which is faster than the near-field interaction [9,24], and so the exciton relaxes to the (1,1,1)-level of QD_L, which is called E_{L_1} hereafter. We should note that the intersublevel relaxation determines the uni-directional exciton transfer from QD_S to QD_L. Also, we assume far-field input light irradiation at the optical frequency ω_{ext}.

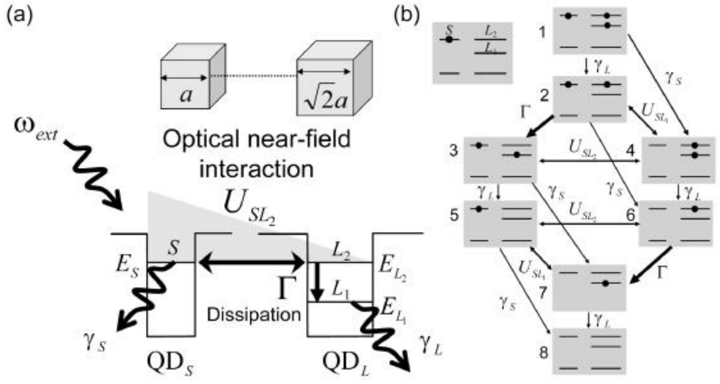

Fig. 1. (a) Optical near-field interaction between a smaller quantum dot (QD_S) and a larger one (QD_L). The input light is given by external propagating light at an optical frequency ω_{ext}. (b) State transition diagram of the two-dot system.

Here we first introduce quantum mechanical modeling of the total system based on a density matrix formalism. There are in total eight states where either zero, one, or two exciton(s) can sit in the energy levels of S, L_1, and L_2 in the system, as schematically summarized in the diagram shown in Fig. 1(a). Here, the interactions between QD_S and QD_L are denoted by U_{SL_i} (i=1,2), and the radiative relaxation rates from E_S and E_{L_1} are respectively given by γ_S and γ_L. Then, letting the (i,i) element of the density matrix

#132260 - $15.00 USD Received 2 Aug 2010; revised 31 Aug 2010; accepted 23 Sep 2010; published 5 Oct 2010

correspond to the state denoted by *i* in Fig. 1(b), the quantum master equation of the total system is given by [25]

$$\begin{aligned}\frac{d\rho(t)}{dt} &= -\frac{i}{\hbar}\left[H_{int}+H_{ext}(t),\rho(t)\right]+\frac{\gamma_S}{2}\left(2S\rho(t)S^{\dagger}-S^{\dagger}S\rho(t)-\rho(t)S^{\dagger}S\right)\\ &+\frac{\Gamma}{2}\left(2L_2\rho(t)L_2^{\dagger}-L_2^{\dagger}L_2\rho(t)-\rho(t)L_2^{\dagger}L_2\right)+\frac{\gamma_L}{2}\left(2L_1\rho(t)L_1^{\dagger}-L_1^{\dagger}L_1\rho(t)-\rho(t)L_1^{\dagger}L_1\right),\end{aligned} \tag{3}$$

where the interaction Hamiltonian H_{int} is given by

$$H_{int}=\begin{pmatrix}0&0&0&0&0&0&0&0\\0&0&0&U_{SL_1}e^{i(\Omega_S-\Omega_{L_1})}&0&0&0&0\\0&0&0&U_{SL_2}e^{i(\Omega_S-\Omega_{L_2})}&0&0&0&0\\0&U_{SL_1}e^{-i(\Omega_S-\Omega_{L_1})}&U_{SL_2}e^{-i(\Omega_S-\Omega_{L_2})}&0&0&0&0&0\\0&0&0&0&0&U_{SL_2}e^{i(\Omega_S-\Omega_{L_2})}&U_{SL_1}e^{i(\Omega_S-\Omega_{L_1})}&0\\0&0&0&0&U_{SL_2}e^{-i(\Omega_S-\Omega_{L_2})}&0&0&0\\0&0&0&0&U_{SL_1}e^{-i(\Omega_S-\Omega_{L_1})}&0&0&0\\0&0&0&0&0&0&0&0\end{pmatrix}, \tag{4}$$

where Ω_S, Ω_{L_1}, and Ω_{L_2} respectively indicate eigenenergy levels associated with E_S, E_{L_1}, and E_{L_2}. The matrices $S^{\dagger}$, $L_1^{\dagger}$, and $L_2^{\dagger}$ respectively are creation operators that create excitations in E_S, E_{L_2}, and E_{L_1}, defined by

$$S^{\dagger}=\begin{pmatrix}0&0&0&1&0&0&0&0\\0&0&0&0&0&1&0&0\\0&0&0&0&0&0&1&0\\0&0&0&0&0&0&0&0\\0&0&0&0&0&0&0&1\\0&0&0&0&0&0&0&0\\0&0&0&0&0&0&0&0\\0&0&0&0&0&0&0&0\end{pmatrix},L_2^{\dagger}=\begin{pmatrix}0&0&0&0&0&0&0&0\\0&0&1&0&0&0&0&0\\0&0&0&0&0&0&0&0\\0&0&0&0&0&0&0&0\\0&0&0&0&0&0&0&0\\0&0&0&0&0&0&1&0\\0&0&0&0&0&0&0&0\\0&0&0&0&0&0&0&0\end{pmatrix},L_1^{\dagger}=\begin{pmatrix}0&1&0&0&0&0&0&0\\0&0&0&0&0&0&0&0\\0&0&0&0&1&0&0&0\\0&0&0&0&0&1&0&0\\0&0&0&0&0&0&0&0\\0&0&0&0&0&0&0&0\\0&0&0&0&0&0&0&1\\0&0&0&0&0&0&0&0\end{pmatrix}, \tag{5}$$

and *S*, L_1, and L_2 in Eq. (4) are respectively annihilation operators given by the transposes of the matrices of Eq. (5). H_{ext} indicates the Hamiltonian representing the interaction between the external input light at frequency ω_{ext} and the quantum dot system, given by

$$\begin{aligned}H_{ext}(t)=gate(t)\times\Big[&\left(\exp(i(\Omega_S-\omega_{ext})S^{\dagger}+\exp(-i(\Omega_S-\omega_{ext})S\right)\\ &+\left(\exp(i(\Omega_{L_1}-\omega_{ext}))L_1^{\dagger}+\exp(-i(\Omega_{L_1}-\omega_{ext}))L_1\right)\Big],\end{aligned} \tag{6}$$

where *gate*(*t*) specifies the duration and the amplitude of the external input light. Also, note that the input light could couple to the (1,1,1)-level E_S in QD$_S$, and to the (1,1,1)-level E_{L_1} in QD$_L$, because those levels are electric dipole-allowed energy levels. Setting the initial condition as an empty state, and giving the external input light in Eq. (6), the time evolution of the population is obtained by solving the master equation given by Eq. (3).

3. Lower bound of energy dissipation in the optical excitation transfer

Then we introduce two different system setups to investigate the minimum energy dissipation in the optical excitation transfer modeled above. In the first one, System A in Fig. 2(a), two quantum dots are closely located in the region where the optical excitation transfer from QD$_S$ to QD$_L$ occurs. We assume $U_{SL_2}^{-1}$ of 100 ps in System A, denoted by U_{A}^{-1} in Fig. 2(a), which

#132260 - $15.00 USD Received 2 Aug 2010; revised 31 Aug 2010; accepted 23 Sep 2010; published 5 Oct 2010

is close to typical values of optical near-field interactions experimentally observed in CuCl QDs (130 ps) [16], ZnO quantum-well structures (130 ps) [17], ZnO QDs (144 ps) [26], and CdSe QDs (135 ps) [27]. The intersublevel relaxation time, due to exciton–phonon coupling, is in the 1–10 ps range [9,24,28], and here we assume $\Gamma^{-1} = 10\,\text{ps}$. In System B on the other hand, shown in Fig. 2(b), the two quantum dots are located far away from each other. Therefore the interactions between QD_S and QD_L are negligible, and thus the optical excitation transfer from QD_S to QD_L does not occur, and the radiation from QD_L should normally be zero. We assume $U_{SL_2}^{-1} = 10{,}000$ ps for System B, denoted by U_{B}^{-1} in Fig. 2(b), indicating effectively no interactions between the quantum dots.

One remark here is that the particular value of the inter-dot interaction time of System A and System B is related to the distance between two quantum dots. The optical near-field interaction between two nanoparticles is known to be expressed as a screened potential using a Yukawa function, given by

$$U = \frac{A\exp(-\mu r)}{r}, \tag{7}$$

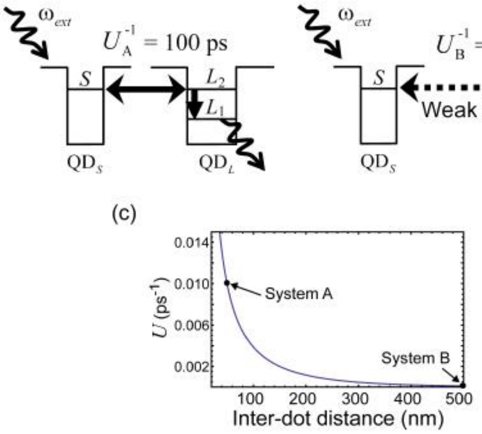

Fig. 2. Two representative quantum dot systems: (a) System A, where the inter-dot interaction is strong (100 ps), and (b) System B, where the interaction is negligible (10,000 ps). (c) Yukawa-type screened potential of an optical near-field interaction between two QDs as a function of the inter-dot distance.

where r is the distance between the two [29]. In this representation, the optical near-field is localized around nanoparticles, and its decay length is equivalent to the particle size. Here it should be noted that the inter-dot distance of System B indicates how closely independent functional elements can be located. In other words, the interaction time of System B is correlated with the *integration density* of the total system. In order to analyze such spatial density dependences, we assume that $U_{SL_2}^{-1}$ values of 100 ps and 10,000 ps correspond to the inter-dot distances of 50 and 500 nm, respectively. Here, the stronger interaction (100 ps) has been assumed, as already mentioned, based on a typical interaction time between closely separated quantum dots [7]. We also assume that the negligible magnitude of the interaction (10,000 ps) corresponds to a situation when the inter-dot distance is around optical wavelengths. Figure 2(c) shows the Yukawa-type potential curve given by Eq. (7). Further discussion on the integration density will be given at the end of this paper.

The energy dissipation in the optical excitation transfer from QD_S to QD_L is the intersublevel relaxation in QD_L given by $\Delta = E_{L_2} - E_{L_1}$. Therefore, the issue is to derive the minimum of Δ. When this energy difference is too small, the input light may directly couple to L_1, resulting in output radiation from QD_L, even in System B. In other words, we would not be able to recognize the origin of the output radiation from QD$_L$ if it involves the optical excitation transfer from QD$_S$ to QD$_L$ in System A, or it directly couples to L_1 in System B. Therefore, the *intended* proper system behavior is to observe higher populations from L_2 in System A while at the same time observing lower populations from L_2 in System B.

We first assume pulsed input light irradiation with a duration of 150 ps at 3.4 eV (wavelength 365 nm), and assume that the energy level S is resonant with the input light. Also, we assume the radiation lifetime of QD$_L$ to be $\gamma_L^{-1} = 1\,\mathrm{ns}$ and that of QD$_S$ to be $\gamma_S^{-1} = 2^{3/2} \times 1 \sim 2.83\,\mathrm{ns}$ since it is inversely proportional to the volume of the QDs [10]. The solid and dashed curves in Fig. 3 respectively represent the evolutions of populations related to the radiation from the energy level of E_{L_1} and E_S for both System A and System B, assuming three different values of Δ: (i) Δ=2.5 meV, (ii) Δ = 17 μeV, and (iii) Δ = 0.25 μeV.

In the case of (i), there is nearly zero population in System B from E_{L_1}, which is the expected proper behavior of the system since there are no interactions between the quantum dots. The radiation from QD$_S$ is observed with its radiation decay rate (γ_S). In System A, on the other hand, populations from E_{L_1} do appear. Note that the population involving the output energy level E_{L_1} is only 0.17 when the input pulse is terminated (t = 150 ps), whereas the population involving E_S at t = 150 ps is 0.81. Therefore, the increased population from E_{L_1} after t = 150 ps is due to the optical excitation transfer from QD$_S$ to QD$_L$. In the case of (iii), due to the small energy difference, the input light directly couples with L_1; therefore, both System A and System B yield higher populations from E_{L_1}, which is an unintended system behavior. Finally, in case (ii), the population from L_1 in System B is not as large as in case (iii), but it exhibits a non-zero value compared with case (i), indicating that the energy difference Δ = 17 μeV may be around the middle of the intended and unintended system operations involving optical excitation transfer between QD$_S$ and QD$_L$.

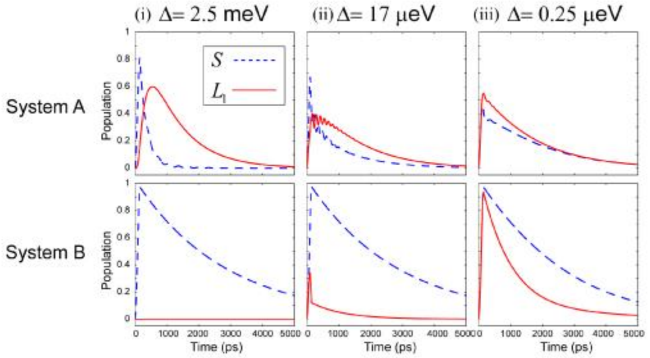

Fig. 3. Evolutions of the populations of the radiation from QD$_S$ (dashed curve) and QD$_L$ (solid curve) with 150 fs-duration input pulse radiating both System A and System B. The energy dissipation in QD$_L$ is arranged to be (i) 2.5 meV, (ii) 17 μeV, and (iii) 0.25 μeV.

When we assume a longer duration of the input light, the population converges to a steady state. Radiating a pulse with a duration of 10 ns at the same wavelength (365 nm), Fig. 4(a) summarizes the steady state output populations involving energy level E_{L_1} evaluated at t = 10 ns as a function of the energy dissipation. The intended system behavior, that is, higher output population in System A and lower one in System B, is obtained in the region where energy dissipation is larger than around 25 μeV.

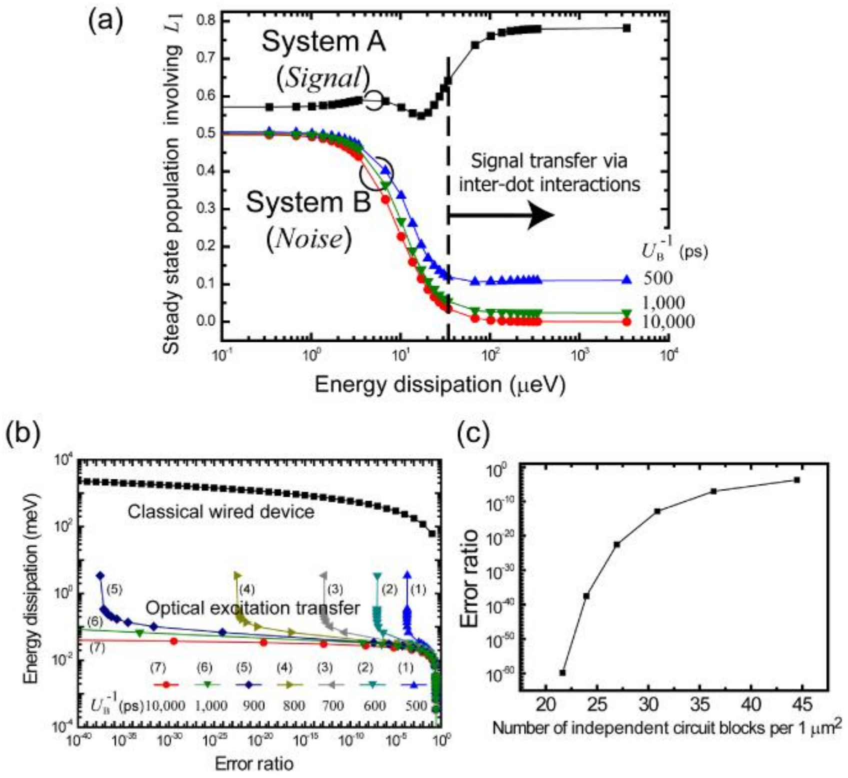

Fig. 4. (a) Steady-state population involving energy level E_{L_1} in System A (squares) and System B as a function of the energy dissipation. For System B, three different cases are shown, with U_B^{-1} of 500, 1,000, and 10,000 ps respectively indicated by ▲, ▼, and ● marks. (b) Energy dissipation as a function of error ratio regarding optical excitation transfer and classical electrically wired device (more specifically a CMOS logic gate) based on Ref [2]. The energy dissipation of optical excitation transfer is about 10^4 times lower than that in classical electrically wired devices. (c) As the optical near-field interaction time of System B decreases, the lower bound of the error ratio increases, indicating that the performance could be degraded with increasing integration density. The error ratio is evaluated as the number of independent functional blocks within an area of 1 μm^2.

If we treat the population from System A as the amplitude of the "signal" and that from System B as "noise", the signal-to-noise ratio (SNR) can be evaluated based on the numerical values obtained in Fig. 4(a). To put it another way, from the viewpoint of the destination QD (or QD$_L$), the signal should come from QD$_S$ in its proximity (as in the case of System A), not from QD$_S$ far from QD$_L$ (as in the case of System B); such a picture will aid in understanding the physical meaning of the SNR defined here. Also, here we suppose that the input data are coded in an external system, and the input light at frequency ω_{ext} irradiates QD$_S$. With SNR, the error ratio (P_E), or equivalently Bit Error Rate (BER), is derived by the formula $P_E = (1/2)erfc(\sqrt{SNR}/2\sqrt{2})$ where $erfc(x) = 2/\sqrt{\pi}\int_x^{\infty}\exp(-x^2)dx$, called the complementary error function [30]. The circles in Fig. 4(b) represent the energy dissipation as a function of the error ratio assuming the photon energy used in the above study (3.4 eV). According to Ref [2], the minimum energy dissipation (E_d) in classical electrically wired devices (specifically, energy dissipation required for a single bit flip in a CMOS logic gate) is given by

#132260 - $15.00 USD Received 2 Aug 2010; revised 31 Aug 2010; accepted 23 Sep 2010; published 5 Oct 2010

$$E_d = k_B T \ln\left(\frac{\sqrt{3}}{2} P_E\right) \tag{8}$$

which is indicated by the squares in Fig. 4(b). For example, when the error ratio is 10^{-6}, the minimum Δ in the optical excitation transfer is about 0.024 meV, whereas that of the classical electrical device is about 303 meV; the former is about 10^4 times more energy efficient than the latter.

As mentioned earlier, the performance of System B depends on the distance between the QDs. When the interaction time of System B (U_{B}^{-1}) gets larger, such as 500 ps, the steady state population involving L_1 is as indicated by the triangular marks in Fig. 4(a); the population stays higher even with increasing energy dissipation compared with the former case of $U_{\mathrm{B}}^{-1} =$ 10,000 ps. This means that the lower bound of the SNR results in a poorer value. In fact, as demonstrated by the triangular marks (1) in Fig. 4(b), the BER cannot be smaller than around 10^{-4}, even with increasing energy dissipation. The lower bound of the BER decreases as the interaction time U_{B}^{-1} increases (namely, weaker inter-dot interaction), as demonstrated by the triangular and square marks (2) to (6) in Fig. 4(b).

Now, suppose that an independent nanophotonic circuit needs a spatial area specified by the square of the inter-dot distance corresponding to U_{B} so that no interference occurs between adjacent circuits; this gives the integration density of nanophotonic circuits in a unit area. When the energy cost paid (namely, the energy dissipation) is 3.4 meV, the BER of the system is evaluated as the square marks in Fig. 4(c) as a function of the number of independent functional blocks within an area of 1 μm^2; we can observe that the system likely sacrifices more errors as the integration density increases.

Finally, here we make a few remarks regarding the discussion above. First, we assume arrays of “identical” independent circuits in the above density discussion. Therefore, two circuits need spatial separations given by U_{B} so that unintended behavior does not occur. However, when two adjacent nanophotonic circuits are operated with different optical frequencies so that they can behave independently [18], those two circuits could be located more closely, which would greatly improve the integration density as a whole. Hierarchical properties of optical near-fields [31] would also impact the integration density. Further analysis and design methodologies of complex nanophotonic systems, as well as comparison to electronic devices, will be another issue to pursue in future work. Second, the energy separation in a single destination QD being limited by its size is lying in the range of meV, so that the results of energy separations in μeV range correspond to the cases where the destination dot QD_L represents a theoretical model of a coupled quantum dot system such as a pair of quantum dots. It exerts optical near-field interactions with QD_S followed by inter-dot electron transfer resulting in optical radiation. In fact, one of the authors’ research group have recently demonstrated a spin-dependent carrier transfer leading to optical radiation between a coupled double quantum wells system composed of magnetic and nonmagnetic semiconductors [32], which can be applicable to quantum dot systems [33]. Third, as mentioned in the introduction, in considering a bit flip in nanophotonic devices, we need to combine multiple optical excitation transfers from smaller dots to larger ones in systems composed of multiple quantum dots, for instance, three dots in the case of an AND gate [16]. In a future study, we will investigate the required energy for nanophotonic devices in general based on the results shown in this paper.

4. Summary

In summary, we theoretically investigated the lower bound of energy dissipation required for optical excitation transfer from smaller quantum dots to larger ones via optical near-field interactions. A quantum mechanical formulation of quantum dot systems provides systematic and quantitative analysis of the intended and unintended behaviors of optical excitation transfer as a function of the energy dissipation, or intersublevel relaxation, occurring at the destination quantum dot. We demonstrated that the energy dissipation is as low as 25 μeV, which is about 10^4 times more energy efficient than the bit flip energy in a conventional electrically wired device. We also discussed the integration density of nanophotonic devices by taking account of energy dissipation, bit error rate, and the optical near-field interactions whose spatial nature is characterized by a Yukawa-type potential.

We will also investigate the energy efficiency by comparing this approach to light harvesting antennae observed in nature [34,35] whose physical mechanism is known to be similar to optical excitation transfer between QDs. More generally, it has been known that the energy efficiency in biological systems is 10^4 times superior to today's electrical computers [36]. We will also seek how to realize computational systems by combinations of optical excitation transfer, whose elemental energy efficiency could be comparable to that of biological systems.

#132260 - $15.00 USD Received 2 Aug 2010; revised 31 Aug 2010; accepted 23 Sep 2010; published 5 Oct 2010

PHYSICAL REVIEW B **82**, 125417 (2010)

Efficient optical excitation transfer in layered quantum dot nanostructures networked via optical near-field interactions

Makoto Naruse,[1,2] Erich Runge,[3] Kiyoshi Kobayashi,[4] and Motoichi Ohtsu[2]
[1]*National Institute of Information and Communications Technology, 4-2-1 Nukui-kita, Koganei, Tokyo 184-8795, Japan*
[2]*Department of Electrical Engineering and Information Systems and Nanophotonics Research Center, School of Engineering, The University of Tokyo, 2-11-16 Yayoi, Bunkyo-ku, Tokyo 113-8656, Japan*
[3]*Institute of Physics and Institute of Micro- and Nanotechnologies, Ilmenau University of Technology, 98684 Ilmenau, Germany*
[4]*Interdisciplinary Graduate School of Medicine and Engineering, University of Yamanashi, Kofu, Yamanashi 400-8511, Japan*
(Received 11 February 2010; revised manuscript received 17 August 2010; published 9 September 2010)

We investigated the efficient optical excitation transfer in layered quantum dot structures by introducing a network of optical near-field interactions. With a density-matrix-based formalization of interdot near-field interactions, our theoretical approach allows systematic analysis of layered CdTe quantum dot systems, revealing dominant factors contributing to the efficient optical excitation transfer and demonstrating good agreement with previous experimental observations. We also show that the efficiency of optical excitation transfer could be further improved by optimizing the interaction network.

DOI: 10.1103/PhysRevB.82.125417 PACS number(s): 78.67.Bf, 74.25.Gz, 73.63.Kv

I. INTRODUCTION

Optical near-field interactions on the nanometer scale have been studied intensively both theoretically and experimentally because of their potential impact in a wide range of applications. One of their unique enabling functions is optical excitation transfer between nanoscale matter, such as semiconductor quantum dots (QDs), via optical near-field interactions.[1] This offers various applications, including subwavelength-scale optical devices beyond the diffraction limit of light,[2–5] light harvesting systems,[6–9] nanofabrication,[10] and many others. Experimental materials exploiting optical near-field interactions have been seeing rapid progress, such as randomly diffused quantum dots,[11–14] geometry-controlled quantum dot arrangements,[15,16] ZnO nanorods,[17] and others. Theoretical fundamentals have also been built, such as in the dressed photon model,[1] which explains the possibility of optical transitions between conventionally electric dipole forbidden energy levels, thanks to the localized nature of a photon dressed by material excitations in its vicinity.[18]

One of the most interesting consequences of optical excitation transfer is energy concentration to larger quantum dots from smaller ones via optical near-field interactions. Those have been observed in some materials, most notably CuCl,[3,6] CdSe,[14,15] CdTe,[19,20] and InAs quantum dots.[21] In Refs. 19 and 20, the Feldmann group experimentally demonstrated *superefficient* energy concentration, where the radiation from layered graded-size CdTe quantum dots exhibits a signal nearly four times larger than that from structures composed of uniform-size quantum dots, which has been called *exciton recycling*[19] or *superefficient exciton funneling*.[20]

In the literature, dipole-dipole interactions such as Förster resonant energy transfer are typically used in explaining energy transfer from smaller QDs to larger ones.[15,22] However, it should be noted that such point-dipole-based modeling does not allow optical transitions to dipole-forbidden energy sublevels, which is often the case with the experimental conditions of two closely located QDs of slightly different size (rigorously, with a size ratio of 1.45 in the case of spherical QDs, as discussed in Sec. II). Also, recent experimental observations in light harvesting antenna indicate the inaccuracy of dipole-based modeling.[9,23] On the other hand, as mentioned already above, the localized nature of optical near fields frees us from conventional optical selection rules, meaning that optical excitation could excite QDs to energy levels that are conventionally electric dipole forbidden.[1,4] This has been demonstrated experimentally and validated theoretically in, e.g., logic devices and systems,[24] and energy concentration applications.[3,6]

In this paper, we analyze the superefficient energy concentration in layered QD systems like those experimentally reported in Refs. 19 and 20 within the theoretical framework of optical near-field interactions. We formulate an interaction network among layered nanostructures whereby the dynamics of the structure-dependent optical excitation transfer involving electric dipole forbidden energy levels is systematically analyzed based on a density-matrix formalism. We demonstrate that the increase in the radiation from the graded-size quantum dot system shows good agreement between the experiment and theory.

This paper is organized as follows. In Sec. II, we first review the experimental observations in layered CdTe quantum dot nanostructures reported so far and describe theoretical elements of optical excitation transfer via optical near-field interactions. In Sec. III, we demonstrate the modeling of the interaction networks in the layered quantum dot systems. In Sec. IV, we quantitatively analyze the structure-dependent optical excitation transfer, including its agreement with the experiments. Also, we demonstrate another system showing further improved efficiency in optical excitation transfer. Section V concludes the paper.

II. REVIEW OF EXPERIMENTAL AND THEORETICAL ELEMENTS OF OPTICAL NEAR-FIELD INTERACTIONS

First we briefly summarize the experimental observations reported in Ref. 19 that shows optical excitation transfer in

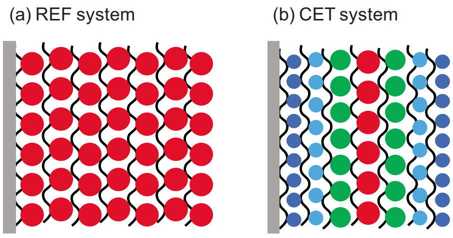

FIG. 1. (Color online) (a) Layered quantum dot system consisting of uniform-sized elements, called the REF system. (b) Layered quantum dot system consisting of four different, graded-sized elements, called the CET system.

two kinds of representative layered nanostructures. One kind is a system consisting of quantum dots of the same size, as schematically shown in Fig. 1(a), called a reference (REF) system. It consists of seven layers of 3.5-nm-diameter CdTe quantum dots. The other system, called a cascaded energy transfer (CET) system, shown in Fig. 1(b), also has a seven-layer structure, but the diameters are stepwise increasing in the first four layers (1.7, 2.5, 3.2, and 3.5 nm) and stepwise decreasing in the subsequent three layers (3.2, 2.5, and 1.7 nm). These REF and CET systems were synthesized using layer-by-layer assembly methods.[25,26]

With optical excitation at a wavelength of 350 nm, the CET system exhibits nearly four times larger photoluminescence than the REF system at emission wavelengths around 612 nm, which corresponds to the radiation from the 3.5-nm-diameter CdTe QDs.[19] Note that there is only one layer of 3.5-nm-diameter QDs in the CET system, whereas the REF system has seven layers of those QDs. Note that the experimental quantum yield of the REF system is very low, on the order of 2%, compared with a quantum yield of about 20% for isolated dots. The authors of Refs. 19 and 20 interpret their findings consistently in terms of nonradiative trap states and exciton recycling from the trap states of larger dots into QD states of smaller dots. It has been reported that these trap states are actually Te-related hole traps on the surface of the CdTe QDs.[27] In this paper, we call QDs having trap states *dark* dots.

In this section, we describe elements of the theoretical framework, which will be later applied in the analysis of the REF and CET systems in Sec. III. The present paper transfers the concept of layered CET systems to layered systems of QDs, such as those studied in Refs. 2 and 14 where excitation transfer via optical near-field interactions takes place between the ground states of smaller dots QD_S (radius R_S) and the first excited states of larger dots QD_L (radius R_L). The condition that these energy levels are in resonance can, for spherical QDs, be discussed using the simple, but widely used estimation of Brus[28] for the energy eigenvalues of QD states specified by the orbital angular momentum quantum number l and the magnetic quantum number m,[29]

$$E_{(n,l)} = E_g + \frac{\hbar^2 \alpha_{nl}^2}{2R^2}\left(\frac{1}{m_e} + \frac{1}{m_h}\right) - 1.8\frac{e^2}{\varepsilon R}. \qquad (1)$$

Here, E_g is the band-gap energy of the bulk semiconductor, $m_e(m_h)$ is the effective mass of the electron (hole), ε is the dielectric constant, and α_{nl} are determined from the boundary conditions, for example, $\alpha_{n0}=n\pi$, $\alpha_{11}=4.49$.

According to Eq. (1), there exists a resonance between the level of quantum number (1,0) of QD_S and that of quantum number (1,1) of QD_L when the size ratio R_L/R_S is appropriately configured. Based on the material parameters for CdTe QDs (Ref. 30) used in the experiment described above, whose radii range from around 1–4 nm, such a resonance occurs when $R_L/R_S \sim 1.45$ is satisfied. The nominal ratio of the diameters of adjacent CdTe QDs in the experimental CET system does not exactly satisfy this condition. However, it is known that QD sizes could typically tolerate a ±10% deviation from the optimal condition,[31] which includes the experimental combinations of the diameters of the QDs used.

It should be noted that optical transitions to the (1,1) level in QD_L are prohibited in conventional optical selection rules; only transitions to states specified by $l=m=0$ are allowed, where l and m are the orbital angular momentum quantum number and magnetic quantum number, respectively.[29] However, when those two QDs are closely located, thanks to the large spatial inhomogeneity of the localized optical near fields at the surface of nanoscale material, an optical transition that violates conventional optical selection rules is permitted.[1] Therefore, an exciton in the (1,0) level in QD_S could be transferred to the (1,1) level in QD_L. In QD_L, due to the sublevel energy relaxation, which is faster than the near-field interaction, the exciton relaxes to the (1,0) level. Therefore, unidirectional optical excitation transfers from QD_S to QD_L is accomplished.

III. NETWORK OF OPTICAL NEAR-FIELD INTERACTIONS IN LAYERED QUANTUM DOTS

A. Analysis of the REF system

1. Modeling of the REF system

We now consider optical excitation transfer in the REF and CET systems introduced in Sec. II with a network of interactions between QDs via optical near fields. First we consider modeling of the REF system. As shown in Fig. 2(a), we represent the REF system as a 5-row × 7-column system composed of the same-sized QDs and assume that only one QD in the system yields output radiation, whereas all of the others are dark. That is, the concentration of bright QD is $1/(5\times 7)\sim 2.9\%$, which is comparable to the experimental value of about 2% luminescence yield. Each of the quantum dots is identified by the notation QD_{S_i}, where the suffixes S and i, respectively, specify its horizontal position $S=\{A,B,C,D,E,F,G\}$ and vertical position $i=\{-2,-1,0,1,2\}$. We suppose that those QDs have two energy levels: the (1,0)-energy level in QD_{S_i} denoted by $S_i^{(1,0)}$ and the (1,1) level denoted by $S_i^{(1,1)}$. The sublevel relaxation constant from $S_i^{(1,1)}$ to $S_i^{(1,0)}$ is given by Γ_{S_i}, which is faster than the radiative or nonradiative relaxation constant from $S_i^{(1,0)}$, denoted by γ_{S_i}.

We assume interdot interactions in the (1,1) level as follows. The interactions between horizontally adjacent quantum dots are denoted by $U_{S_iT_i}$, where the suffixes are given

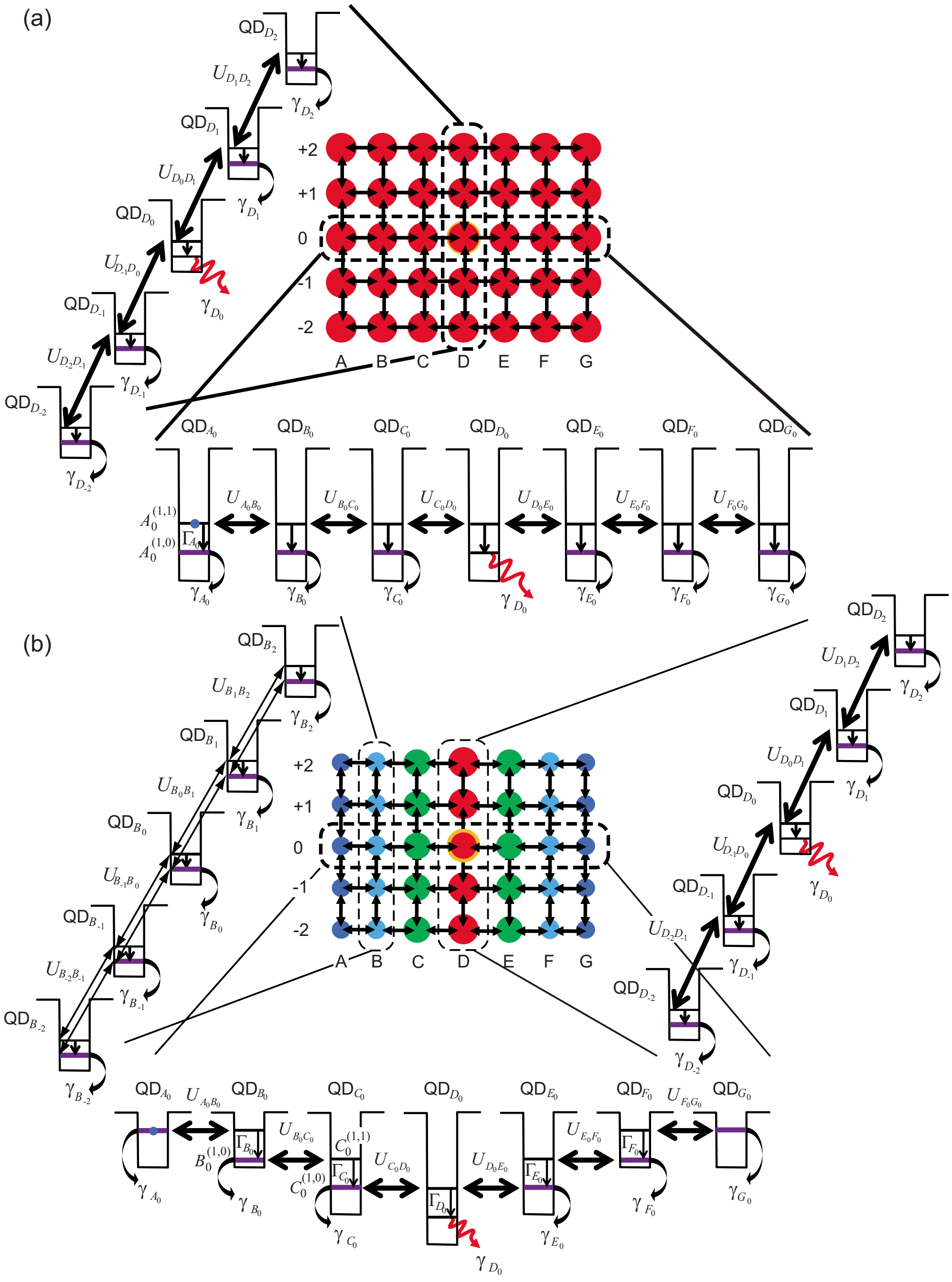

FIG. 2. (Color online) Theoretical modeling of (a) the REF system and (b) the CET system. The radiative relaxation from the center QD, denoted by QD_{D_0}, contributes to the output.

by $(S,T)=\{(A,B),(B,C),(C,D),(D,E),(E,F),(F,G)\}$ and $i=\{-2,\ldots,2\}$. At the bottom of Fig. 2(a), horizontal interactions among QDs located in row $i=0$ are schematically indicated. Also, the interactions between vertically adjacent quantum dots are given by $U_{S_iS_{i+1}}$, where $S=\{A,\ldots,G\}$ and $i=\{-2,-1,0,1\}$. The left-hand side of Fig. 2(a) schematically shows the array of QDs in column D.

Now, the interaction Hamiltonian regarding one-exciton states where an exciton exists at one of the energy levels of $S_i^{(1,1)}$ is given by submatrices H_i and $H_{i,j}$,

$$H_{\text{int}}^{(1,1)}=\begin{pmatrix} H_2 & H_{1,2} & O & O & O \\ H_{1,2} & H_1 & H_{0,1} & O & O \\ O & H_{0,1} & H_0 & H_{-1,0} & O \\ O & O & H_{-1,0} & H_{-1} & H_{-2,1} \\ O & O & O & H_{-2,1} & H_{-2} \end{pmatrix}, \tag{2}$$

where O represents an empty matrix. The diagonal elements in Eq. (2) specify horizontal interactions given by

$$H_i = \hbar \begin{pmatrix} 0 & U_{A_iB_i} & 0 & 0 & 0 & 0 & 0 \\ U_{A_iB_i} & 0 & U_{B_iC_i} & 0 & 0 & 0 & 0 \\ 0 & U_{B_iC_i} & 0 & U_{C_iD_i} & 0 & 0 & 0 \\ 0 & 0 & U_{C_iD_i} & 0 & U_{D_iE_i} & 0 & 0 \\ 0 & 0 & 0 & U_{D_iE_i} & 0 & U_{E_iF_i} & 0 \\ 0 & 0 & 0 & 0 & U_{E_iF_i} & 0 & U_{F_iG_i} \\ 0 & 0 & 0 & 0 & 0 & U_{F_iG_i} & 0 \end{pmatrix}, \quad (3)$$

where $i=\{-2,\ldots,2\}$ and $\hbar$ is Planck's constant divided by 2π. The nondiagonal elements in Eq. (2) describe the vertical interactions in the system, given by

$$H_{i,j} = \hbar\ \mathrm{diag}(U_{A_iA_j}, U_{B_iB_j}, U_{C_iC_j}, U_{D_iD_j}, U_{E_iE_j}, U_{F_iF_j}, U_{G_iG_j}), \quad (4)$$

where $(i,j)=\{(-2,-1),(-1,0),(0,1),(1,2)\}$. The sublevel relaxation from the energy levels of $S_i^{(1,1)}$ is described by a diagonal matrix $N_\Gamma^{(1,1)}$ whose diagonal elements are given by Γ_{S_i}. Letting $\rho^{(1,1)}(t)$ be the density matrix corresponding to the Hamiltonian introduced above and $H^{(0)}$ be the unperturbed Hamiltonian, the master equation for the system is given by[32]

$$\frac{d\rho^{(1,1)}(t)}{dt} = -\frac{i}{\hbar}[(H^{(0)}+H_{\mathrm{int}}^{(1,1)}),\rho^{(1,1)}(t)] - N_\Gamma^{(1,1)}\rho^{(1,1)}(t) - \rho(t)^{(1,1)}N_\Gamma^{(1,1)}. \quad (5)$$

The lower level in QD_{S_i}, namely, the (1,0) level denoted by $S_i^{(1,0)}$, could be filled via the sublevel relaxation denoted by Γ_{S_i} from $S_i^{(1,1)}$. The relaxation constants from $S_i^{(1,0)}$ are given by a diagonal matrix $N_\Gamma^{(1,0)}$ whose diagonal elements are given by γ_{S_i}.

Now, remember that only one QD in the system is bright and all the rest are dark. That is, most of the energy levels of $S_i^{(1,0)}$ should be treated as trap states. In representing those trap states in the REF system, we assume that there are no interactions between QDs among the energy levels of $S_i^{(1,0)}$. Letting $\rho^{(1,0)}(t)$ be the density matrix corresponding to the energy level of $S_i^{(1,0)}$, the master equation for the system is given by

$$\frac{d\rho^{(1,0)}(t)}{dt} = -\frac{i}{\hbar}[H_0,\rho^{(1,0)}(t)] - N_\Gamma^{(1,0)}\rho^{(1,0)}(t) - \rho^{(1,0)}(t)N_\Gamma^{(1,0)} + P_\Gamma[\rho^{(1,1)}(t)], \quad (6)$$

where P_Γ represents the relaxations from the energy levels of $S_i^{(1,1)}$.

2. Numerical evaluation of the REF system

In the numerical calculation, we assume that the horizontal and vertical interactions are equal; namely, we assume $U_{S_iT_i}^{-1}=U_{S_kS_{k+1}}^{-1}=100$ ps. The radiation lifetime of the bright CdTe quantum dot is assumed to be 2 ns. The sublevel relaxation constants in QD_{S_i} are given by $\Gamma_{S_i}^{-1}=10$ ps. We consider that QD_{D_0}, located in the center, is a bright one whose population regarding the (1,0) level gives an output signal, whereas all the other dots are dark ones whose (1,0)-level populations do not contribute to the output. Also, we regard the nonradiative relaxation time $\gamma_{S_i}^{-1}=40$ ns $(S_i \neq D_0)$ from the (1,0) level of QD_{S_i} to be 20 times larger than the radiative relaxation time $\gamma_{D_0}^{-1}=2$ ns. In experiments, the interdot interaction time between CdTe quantum dots has been reported to be 254 ps, and the possibility of 100 ps was discussed in Ref. 26; we investigate the interaction-time dependence later in Sec. IV. The radiation lifetime of CdTe QDs can range from hundreds of picoseconds up to hundreds of nanoseconds.[33] In this paper, as stated above, we set the radiation lifetime as $\gamma_{D_0}^{-1}=2$ ns in agreement with the experimental findings in Ref. 34.

Then we assume that there is an initial exciton in either one of the (1,1) levels of the QDs in the system. Here, since the (1,1) level is an electric dipole forbidden energy level for propagating light, such an initial state is physically unreasonable. However, since the primary interest in this paper is to highlight the effects of interdot optical excitation transfer involving electric dipole forbidden energy levels, which play a critical role in the CET system described below, we assume such an initial condition, so that the input exciton could have the possibility of interacting with the adjacent dots.

Finally, by solving quantum master equations given by Eqs. (5) and (6), the time evolution of the (1,0) level of QD_{D_0} with initial excitation at the (1,1) level of QD_{S_i} is obtained, which is denoted by $\rho_{D_0}(t;S_i)$. For example, Fig. 3(a) dem-

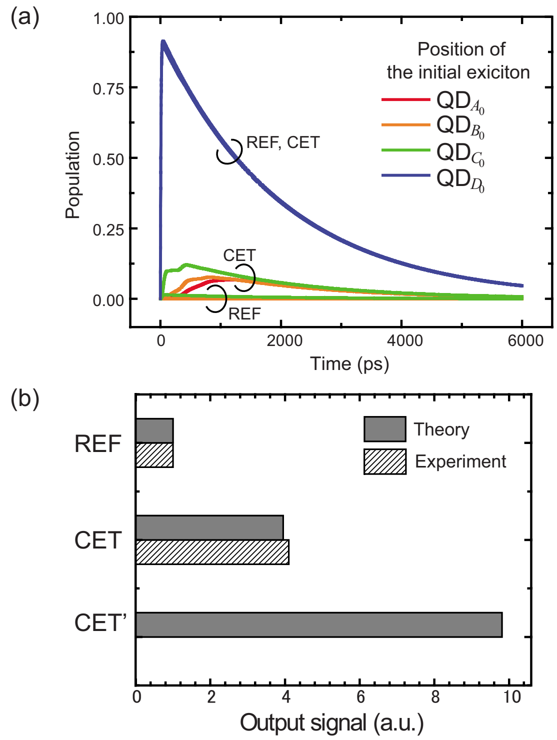

FIG. 3. (Color online) (a) Evolutions of the populations of the (1,0) level of QD_{D_0} from the REF and CET systems with their initial excitons in QD_{A_0}, QD_{B_0}, QD_{C_0}, or QD_{D_0}. (b) Comparison of the total output signal between the REF, CET, and CET' systems.

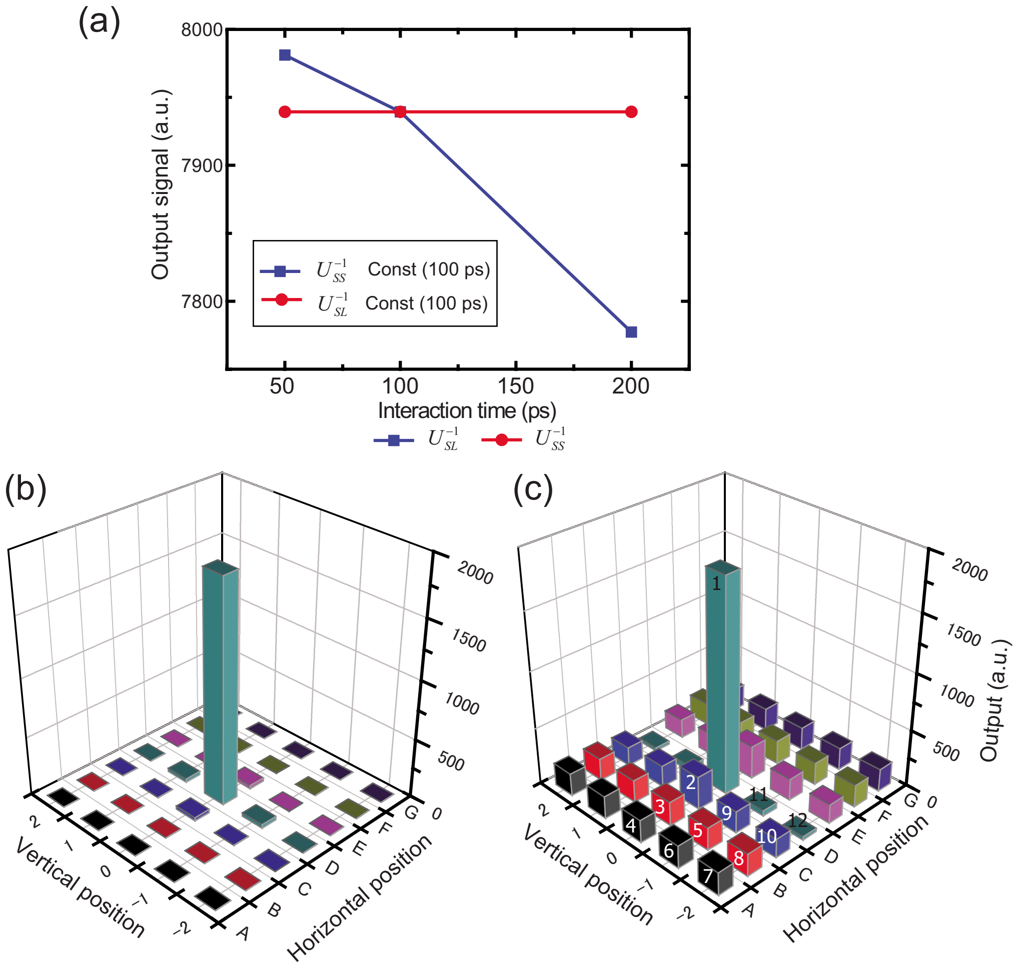

FIG. 4. (Color online) (a) Output signal dependency on the interdot horizontal and vertical near-field interactions. [(b) and (c)] Comparison of the output signal level as a function of initial position of the input exciton. The numbers attached to the bars in Fig. 4(c) indicate the order of the magnitude of the output signal.

onstrates $\rho_{D_0}(t;A_0)$, $\rho_{D_0}(t;B_0)$, and $\rho_{D_0}(t;C_0)$, all of which stay nearly at zero level. This is due to the fact that nearly all of the populations are trapped at the energy levels $A_0^{(1,0)}$, $B_0^{(1,0)}$, and $C_0^{(1,0)}$. The curve of $\rho_{D_0}(t;D_0)$ exhibits a higher population thanks to the sublevel relaxation from the (1,1) level to the (1,0) level in QD_{D_0}. The output signal for the initial excitation at S_i is obtained by integrating the time evolutions of $\rho_{D_0}(t;S_i)$ between 0 and 10 ns,

$$\gamma_{D_0}\int \rho_{D_0}(t;S_i)dt, \tag{7}$$

where $i=\{-2,\ldots,2\}$. The results are discussed and compared with those of the CET system in Figs. 3(b) and 4 in Sec. IV.

B. Analysis of the CET system

1. Modeling of the CET system

Next, with respect to the CET system, Fig. 2(b) represents a 5-row × 7-column system composed of four kinds of quantum dots. The identification of each of the QDs is the same as with the REF system. Along the columns, the sizes of the quantum dots are uniform. The QDs located in the central column (column D) have the largest radius. The QDs located in their proximity, that is, in columns C and E, are smaller than those in column D and their radii are tuned such that, according to Eq. (1), the (1,0) levels of QD_{C_i} and QD_{E_i}, namely, $C_i^{(1,0)}$ and $E_i^{(1,0)}$, are resonant with those of the (1,1)-energy level of QD_{D_i}, that is, $D_i^{(1,1)}$. Similarly, we assume resonances between two levels in adjacent layers: $B_i^{(1,0)}=C_i^{(1,1)}=F_i^{(1,0)}=E_i^{(1,1)}$ and $A_i^{(1,0)}=B_i^{(1,1)}=G_i^{(1,0)}=F_i^{(1,1)}$.

Now, we formulate interdot interactions by introducing an interaction Hamiltonian. It is a block diagonal given by

$$H_{\text{int}}=\begin{pmatrix} H_{AB} & O & O & O & O \\ O & H_{BC} & O & O & O \\ O & O & H_{CDE} & O & O \\ O & O & O & H_{EF} & O \\ O & O & O & O & H_{FG} \end{pmatrix}. \tag{8}$$

If state indices of H_{BC}, for example, are spanned by the order of $B_2^{(1,1)}$, $C_2^{(1,0)}$, $B_1^{(1,1)}$, $C_1^{(1,0)}$, $B_0^{(1,1)}$, $C_0^{(0,1)}$, $B_{-1}^{(1,1)}$, $C_{-1}^{(1,0)}$, $B_{-2}^{(1,1)}$, and $C_{-2}^{(1,0)}$, which are energetically degenerate, H_{BC} is given by

$$H_{BC}=\hbar\begin{pmatrix} 0 & U_{B_2C_2} & U_{B_1B_2} & 0 & 0 & 0 & 0 & 0 & 0 & 0 \\ U_{B_2C_2} & 0 & 0 & U_{C_1C_2} & 0 & 0 & 0 & 0 & 0 & 0 \\ U_{B_1B_2} & 0 & 0 & U_{B_1C_1} & U_{B_0B_1} & 0 & 0 & 0 & 0 & 0 \\ 0 & U_{C_1C_2} & U_{B_1C_1} & 0 & 0 & U_{C_0C_1} & 0 & 0 & 0 & 0 \\ 0 & 0 & U_{B_0B_1} & 0 & 0 & U_{B_0C_0} & U_{B_{-1}B_0} & 0 & 0 & 0 \\ 0 & 0 & 0 & U_{C_0C_1} & U_{B_0C_0} & 0 & 0 & U_{C_{-1}C_0} & 0 & 0 \\ 0 & 0 & 0 & 0 & U_{B_{-1}B_0} & 0 & 0 & U_{B_{-1}C_{-1}} & U_{B_{-2}B_{-1}} & 0 \\ 0 & 0 & 0 & 0 & 0 & U_{C_{-1}C_0} & U_{B_{-1}C_{-1}} & 0 & 0 & U_{C_{-2}C_{-1}} \\ 0 & 0 & 0 & 0 & 0 & 0 & U_{B_{-2}B_{-1}} & 0 & 0 & U_{B_{-2}C_{-2}} \\ 0 & 0 & 0 & 0 & 0 & 0 & 0 & U_{C_{-2}C_{-1}} & U_{B_{-2}C_{-2}} & 0 \end{pmatrix}, \tag{9}$$

where $U_{B_iC_i}$ represents the horizontal interactions between QD_{B_i} and QD_{C_i}, whereas $U_{C_iC_{i+1}}$ indicates vertical interactions between QD_{C_i} and $\mathrm{QD}_{C_{i+1}}$ through the energy level of $B_i^{(1,0)}(=C_i^{(1,1)})$. The relaxation constants for the corresponding states are given by

$$N_\Gamma^{BC}=\mathrm{diag}\left(\frac{\gamma_{B_2}}{2},\frac{\Gamma_{C_2}}{2},\frac{\gamma_{B_1}}{2},\frac{\Gamma_{C_1}}{2},\frac{\gamma_{B_0}}{2},\frac{\Gamma_{C_0}}{2},\frac{\gamma_{B_0}}{2},\frac{\Gamma_{C_{-1}}}{2},\frac{\gamma_{B_{-1}}}{2},\frac{\Gamma_{C_{-2}}}{2},\frac{\gamma_{B_{-2}}}{2}\right). \tag{10}$$

Letting $\rho_{BC}(t)$ be the density matrix for the above Hamiltonian, the master equation is given by

$$\frac{d\rho_{BC}(t)}{dt}=-\frac{i}{\hbar}[(H^{(0)}+H_{BC}),\rho_{BC}(t)]-N_\Gamma^{BC}\rho_{BC}(t)-\rho_{BC}(t)N_\Gamma^{BC}+P_\Gamma^{BC}[\rho_{AB}(t)]. \tag{11}$$

The last term on the right-hand side of Eq. (11) takes into account the fact that the lower level in QD_{B_i}, namely, the (1,0) level denoted by $B_i^{(1,0)}$, can be filled via the sublevel relaxation denoted by Γ_{B_i} from the upper level $B_i^{(1,1)}$, whose behavior is given by the differential equations that corresponds to Eq. (11) and whose density matrix is given by $\rho_{AB}(t)$.

2. Numerical evaluation of the CET system

In the numerical calculation, we first assume that the horizontal and vertical interactions are equal; namely, $U_{S_iT_i}^{-1}=U_{S_kS_{k+1}}^{-1}=100$ ps. As in the REF system, the radiation lifetime of the bright QDs located in the center is $\gamma_{D_0}^{-1}=2$ ns, and the sublevel relaxation time is $\Gamma_{S_i}^{-1}=10$ ps. Again, we assume that only the relaxation from the (1,0) level in the center, that is, QD_{D_0}, contributes to the output. We assume that the system has an initial exciton in either the (1,1) level in QD_{S_i}($S=B,C,D,E,F$) or the (1,0) level in QD_{S_i}($S=A,G$).

IV. STRUCTURE-DEPENDENT EFFICIENCY OF OPTICAL EXCITATION TRANSFER

What is particularly notable in the CET system is that the excitons trapped in the trap states in columns A, B, C, E, F, and G have the chance to be transferred to the adjacent energy level through near-field interactions. Therefore, the probability of exciton transfer to the (1,0) level in D_0 from other dots could significantly improve. In fact, as shown in Fig. 3(a), $\rho_{D_0}(t;A_0)$, $\rho_{D_0}(t;B_0)$, and $\rho_{D_0}(t;C_0)$ in the CET system exhibit higher populations than in the REF system.

Finally, the output signal in the CET system is obtained by following the same procedure defined by Eq. (7), which is represented as the gray bar graph in Fig. 3(b); the enhancement factor with respect to the REF system is about 3.95, which agrees well with the experimental observations shown in Sec. II, indicated as the dashed bars in Fig. 3(b).

Figure 4(a) illustrates the dependency of the horizontal and vertical interdot interactions in the CET system. The circular marks in Fig. 4(a) show the output signal as a function of vertical interaction time ($U_{S_iS_{i+1}}^{-1}$) while the horizontal interactions remain constant ($U_{S_iT_i}^{-1}=100$ ps). The output is nearly constant. On the other hand, the output increases as the horizontal interaction time ($U_{S_iT_i}^{-1}$) decreases keeping the vertical interactions constant ($U_{S_iS_{i+1}}^{-1}=100$ ps), as shown by the square marks in Fig. 4(a). This clearly indicates that the energy transfers between the different-sized quantum dots via optical near-field interactions along the horizontal directions allow excitons to avoid being dissipated in trap states, leading to increased output signal.

Figures 4(b) and 4(c) summarizes the integrated output populations from QD_{D_0} as a function of the input excitation position for both the REF and CET systems. As is evident, the output populations from QD_{D_0} in the REF system are constituted almost entirely of an initial exciton located in QD_{D_0}, whereas in the CET system, the input excitons geometrically located far from QD_{D_0} can have an impact on the radiation from QD_{D_0}. Interestingly, regarding QDs in rows $i=-2$ and -1, distant QDs contribute to the output from

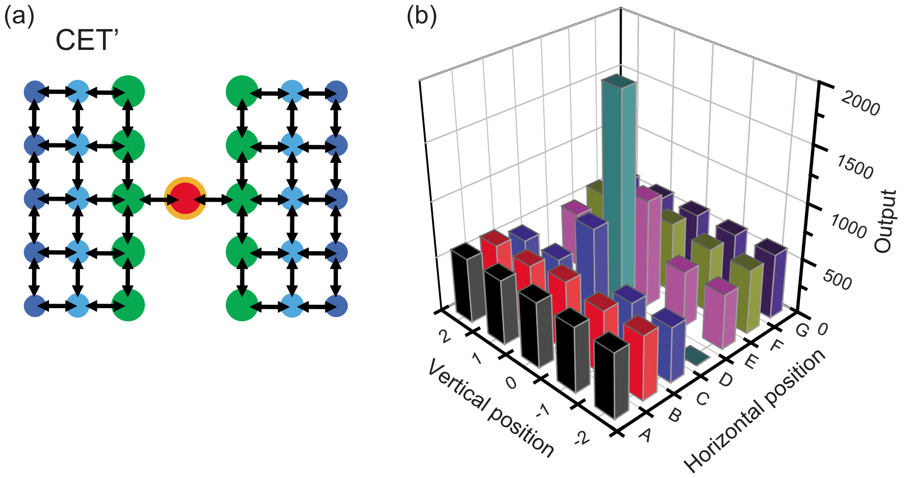

FIG. 5. (Color online) (a) Near-field interaction network in the CET' system where the nonradiative largest QDs are eliminated from the CET system. (b) The total excitation transfer in the CET' system is about 9.8 times larger than that in the REF system [see Fig. 3(b)].

QD_{D_0} more than the geometrically closer QDs do. For instance, QDs B_{-1} and B_{-2} contribute to the radiation from QD_{D_0} more than QDs such as C_{-1} and C_{-2} do. This is due to the fact that, for input excitons in QDs B_{-1} and B_{-2}, the chance of being trapped at QDs D_{-1} and D_{-2} is reduced.

Those internal mechanisms of optical excitation transfer in the CET system indicate that the output populations could be further improved by an appropriate design of the interaction network. For example, by removing the largest dark dots, namely, QDs D_{-2}, D_{-1}, D_1, and D_2, from the CET system, the output population should greatly improve because it eliminates the possibility of input excitons to be trapped at those QDs. Figure 5(a) schematically shows such a modified system denoted by CET'. As expected, the output populations from QD_{D_0} improved as shown in Fig. 5(b). As a total system, the output signal is about 9.8 times larger than that from the REF system.

V. CONCLUSION

We investigated the efficient optical excitation transfer in layered quantum dot structures by introducing a network of optical near-field interactions. With density-matrix-based modeling of the layered, graded-sized quantum dot systems, our theoretical analysis allows systematic handling of structure-dependent interdot interactions and reveals dominant factors contributing to the efficient optical excitation transfer. Our analysis shows good agreement with the experimental observations, where a graded-sized seven-layer QD system exhibits nearly four times larger photoluminescence compared with a uniform-sized QD system. We also show that the efficiency could be further improved by optimizing the interaction network.

We should also emphasize that the theoretical modeling strategy demonstrated in Sec. III can be applied to interaction networks other than the REF, CET, and CET' systems discussed in this paper. General properties that emerge from networks of optical near-field interactions on the nanometer-scale will be one important research challenge in the future. Experimentally, Akahane *et al.* realized stacked InAs QD devices consisting of more than 100 layers based on molecular-beam epitaxy.[16] Also, the sizes of QDs could potentially be controlled layer by layer. We will seek further theoretical and experimental insights in layered QD systems regarding their energy transfer efficiencies, as well as achieving functionalities for a wide range of system applications. Those pursuits will provide us with a further understanding of the network of optical near-field interactions in QD systems.

ACKNOWLEDGMENTS

This work was supported by the Japan Science and Technology Agency (JST) and the German Research Foundation (DFG) under the Strategic Japanese-German Cooperative Program. The authors acknowledge Thomas A. Klar of Ilmenau University of Technology for important suggestions. The authors acknowledge Christoph Lienau of the University of Oldenburg, the German-side principal investigator of the above Japan-Germany bilateral program, for fruitful discussions.

---

[1] M. Ohtsu, K. Kobayashi, T. Kawazoe, T. Yatsui, and M. Naruse, *Principles of Nanophotonics* (Taylor & Francis, Boca Raton, 2008).

[2] M. Ohtsu, K. Kobayashi, T. Kawazoe, S. Sangu, and T. Yatsui, IEEE J. Sel. Top. Quantum Electron. **8**, 839 (2002).

[3] M. Naruse, T. Miyazaki, F. Kubota, T. Kawazoe, K. Kobayashi, S. Sangu, and M. Ohtsu, Opt. Lett. **30**, 201 (2005).

[4] T. Unold, K. Mueller, C. Lienau, T. Elsaesser, and A. D. Wieck, Phys. Rev. Lett. **94**, 137404 (2005).

[5] P. Vasa, R. Pomraenke, S. Schwieger, Y. I. Mazur, V. Kunets, P. Srinivasan, E. Johnson, J. E. Kihm, D. S. Kim, E. Runge, G. Salamo, and C. Lienau, Phys. Rev. Lett. **101**, 116801 (2008).

[6] T. Kawazoe, K. Kobayashi, and M. Ohtsu, Appl. Phys. Lett. **86**, 103102 (2005).

[7] H. Tamura, J.-M. Mallet, M. Oheim, and I. Burghardt, J. Phys. Chem. C **113**, 7548 (2009).

[8] H. Imahori, J. Phys. Chem. B **108**, 6130 (2004).

[9] M. Kubo, Y. Mori, M. Otani, M. Murakami, Y. Ishibashi, M. Yasuda, K. Hosomizu, H. Miyasaka, H. Imahori, and S. Nakashima, J. Phys. Chem. A **111**, 5136 (2007).

[10] T. Kawazoe, K. Kobayashi, and M. Ohtsu, Appl. Phys. B **84**, 247 (2006).

[11] C. R. Kagan, C. B. Murray, M. Nirmal, and M. G. Bawendi, Phys. Rev. Lett. **76**, 1517 (1996).

[12] O. I. Mićić, K. M. Jones, A. Cahill, and A. J. Nozik, J. Phys. Chem. B **102**, 9791 (1998).

[13] S. V. Kershaw, M. T. Harrison, A. L. Rogach, and A. Kornowski, IEEE J. Sel. Top. Quantum Electron. **6**, 534 (2000).

[14] M. Naruse, T. Kawazoe, R. Ohta, W. Nomura, and M. Ohtsu, Phys. Rev. B **80**, 125325 (2009).

[15] S. A. Crooker, J. A. Hollingsworth, S. Tretiak, and V. I. Klimov, Phys. Rev. Lett. **89**, 186802 (2002).

[16] K. Akahane, N. Yamamoto, and M. Tsuchiya, Appl. Phys. Lett. **93**, 041121 (2008).

[17] T. Yatsui, S. Sangu, T. Kawazoe, M. Ohtsu, S. J. An, J. Yoo, and G.-C. Yi, Appl. Phys. Lett. **90**, 223110 (2007).

[18] T. Kawazoe, K. Kobayashi, J. Lim, Y. Narita, and M. Ohtsu, Phys. Rev. Lett. **88**, 067404 (2002).

[19] T. Franzl, T. A. Klar, S. Schietinger, A. L. Rogach, and J. Feldmann, Nano Lett. **4**, 1599 (2004).

[20] T. A. Klar, T. Franzl, A. L. Rogach, and J. Feldmann, Adv. Mater. **17**, 769 (2005).

[21] K. Nishibayashi, T. Kawazoe, K. Akahane, N. Yamamoto, and M. Ohtsu, Appl. Phys. Lett. **93**, 042101 (2008).

[22] T. Förster, Ann. Phys. **437**, 55 (1948).

[23] G. D. Scholes and G. R. Fleming, J. Phys. Chem. B **104**, 1854 (2000).

[24] M. Ohtsu, T. Kawazoe, T. Yatsui, and M. Naruse, IEEE J. Sel. Top. Quantum Electron. **14**, 1404 (2008).

[25] A. A. Mamedov, A. Belov, M. Giersig, N. N. Mamedova, and N. A. Kotov, J. Am. Chem. Soc. **123**, 7738 (2001).

[26] T. Franzl, D. S. Koktysh, T. A. Klar, A. L. Rogach, J. Feldmann, and N. Gaponik, Appl. Phys. Lett. **84**, 2904 (2004).

[27] A. L. Rogach, T. Franzl, T. A. Klar, J. Feldmann, N. Gaponik, V. Lesnyak, A. Shavel, A. Eychmüller, Y. P. Rakovich, and J. F. Donegan, J. Phys. Chem. C **111**, 14628 (2007).

[28] L. E. Brus, J. Chem. Phys. **80**, 4403 (1984).

[29] H. Haug and S. W. Koch, *Quantum Theory of the Optical and Electronic Properties of Semiconductors* (World Scientific, Singapore, 2004).

[30] A. L. Rogach, L. Katsikas, A. Kornowski, D. Su, A. Eychmüller, and H. Weller, Ber. Bunsenges. Phys. Chem. **100**, 1772 (1996).

[31] S. Sangu, K. Kobayashi, A. Shojiguchi, T. Kawazoe, and M. Ohtsu, J. Appl. Phys. **93**, 2937 (2003).

[32] H. J. Carmichael, *Statistical Methods in Quantum Optics 1* (Springer-Verlag, Berlin, 1999).

[33] A. M. Kapitonov, A. P. Stupak, S. V. Gaponenko, E. P. Petrov, A. L. Rogach, and A. J. Eychmüller, J. Phys. Chem. B **103**, 10109 (1999).

[34] S. Mayilo, J. Hilhorst, A. S. Susha, C. Hhl, T. Franzl, T. A. Klar, A. L. Rogach, and J. Feldmann, J. Phys. Chem. C **112**, 14589 (2008).

In situ real-time monitoring of changes in the surface roughness during nonadiabatic optical near-field etching

2010 Nanotechnology 21 355303

(http://iopscience.iop.org/0957-4484/21/35/355303)

IOP Publishing Nanotechnology

Nanotechnology **21** (2010) 355303 (5pp) doi:10.1088/0957-4484/21/35/355303

In situ real-time monitoring of changes in the surface roughness during nonadiabatic optical near-field etching

T Yatsui[1,2], K Hirata[3], Y Tabata[3], W Nomura[1,2], T Kawazoe[1,2], M Naruse[1,2,4] and M Ohtsu[1,2]

[1] School of Engineering, The University of Tokyo, Bunkyo-ku, Tokyo 113-8656, Japan
[2] Nanophotonics Research Center, The University of Tokyo, 2-11-16 Yayoi, Bunkyo-ku, Tokyo 113-8656, Japan
[3] SIGMA KOKI Co., Ltd, 1-19-9 Midori, Sumida-ku, Tokyo 130-0021, Japan
[4] National Institute of Information and Communications Technology, 4-2-1 Nukui-kita, Koganei, Tokyo 184-8795, Japan

E-mail: yatsui@ee.t.u-tokyo.ac.jp

Received 5 March 2010, in final form 21 July 2010
Published 6 August 2010
Online at stacks.iop.org/Nano/21/355303

Abstract

We performed *in situ* real-time monitoring of the change in surface roughness during self-organized optical near-field etching. During near-field etching of a silica substrate, we detected the scattered light intensity from a continuum wave (CW) laser ($\lambda = 633$ nm) in addition to the etching CW laser ($\lambda = 532$ nm) light source. We discovered that near-field etching not only decreases surface roughness, but also increases the number of scatterers, as was confirmed by analyzing the AFM image. These approaches provide optimization criteria for the etching parameter and hence for further decreases in surface roughness.

(Some figures in this article are in colour only in the electronic version)

1. Introduction

A reduction of the surface roughness (R_a) to less than 1 Å to minimize light scattering losses is required in various applications such as high-quality, extreme-UV optical components, high-power lasers, and ultra-short pulse lasers [1]. R_a is formally defined as the arithmetic average of the absolute values of the surface height deviations from the best-fitting plane. Although chemical–mechanical polishing (CMP) has been used to flatten the surfaces [2], it is generally limited to reducing R_a to about 2 Å because the polishing pad roughness is as large as 10 μm, and the polishing-particle diameters in the slurry are as large as 100 nm. We therefore developed a non-contact self-organized method of near-field etching that succeeded in reducing the R_a to as small as 1.36 Å [3].

Near-field etching utilizes a nonadiabatic photochemical reaction [3–6]. To photochemically etch the silica nonadiabatically, a continuum wave (CW) laser ($\lambda = 532$ nm) was used to dissociate the Cl_2 gas. As this photon energy is lower than the absorption band edge energy of Cl_2 ($\lambda = 400$ nm) [7], the conventional Cl_2 adiabatic photochemical reaction is avoided. However, on a surface with nanometer-scale roughness, generation of a strong optical near field would be expected. As a virtual exciton–phonon–polariton can be excited at this roughness, unlike on the flat part of the surface, a higher molecular vibrational state can be excited [4, 5]. Cl_2 is therefore selectively photo-dissociated to generate radical Cl^* atoms wherever the optical near field is generated. The Cl^* atoms etch away the surface roughness; the etching process automatically stops when the surface becomes flattened.

In a previous near-field etching study [3], the reduction in R_a was confirmed using an atomic force microscope (AFM) after etching. Because the scanning area of the AFM measurement was restricted to less than 10 μm × 10 μm, R_a had to be obtained as an average of several scanning areas. Furthermore, scattering loss reduction at the surface could not be confirmed.

For the present investigations, we performed an *in situ* real-time monitoring of the scattered light at the substrate surface during near-field etching. In addition, we obtained

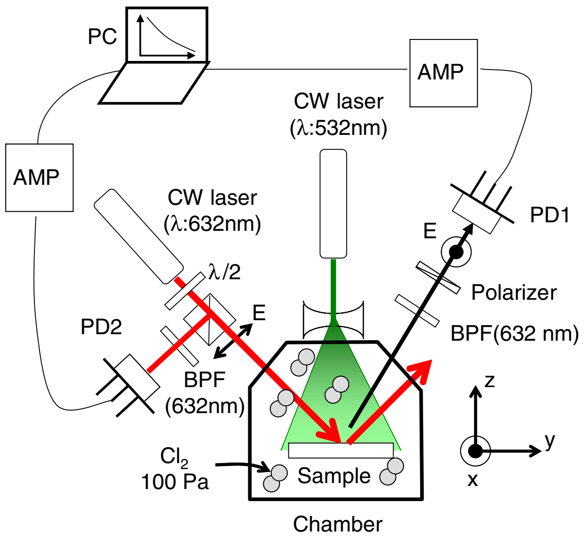

Figure 1. Schematic of the *in situ* real-time monitoring of the surface roughness during the near-field etching.

the correlation length of the surface roughness, allowing estimation of the structural change due to the near-field etching. These approaches allowed us to optimize the etching parameters to further decrease the surface roughness.

2. Experiment

We used 30 mm diameter planar synthetic silica substrates synthesized by vapor-phase axial deposition with an OH group concentration of less than 1 ppm [8]. The substrates were preliminarily polished by CMP prior to the near-field etching. The near-field etching was done with a CW laser ($\lambda = 532$ nm) having a uniform power density of 0.28 W cm^{-2} over the substrate (see figure 1). The Cl_2 pressure in the chamber was maintained at 100 Pa at room temperature. The scattered light was generated with a CW laser with wavelength 632 nm, power density 0.127 W cm^{-2} and spot size diameter 1 mm. As this photon energy is lower than both the absorption band edge energy of Cl_2 ($\lambda = 400$ nm) and the light source for the near-field etching ($\lambda = 532$ nm), it does not contribute to the near-field etching. To increase the sensitivity and selectivity for detection of the scattered light, the incident light was polarized perpendicular to the x-axis (P-polarized light), and the polarized light parallel to the x-axis (S-polarized light) was detected after passing through a $\lambda = 632$ nm $\pm$ 1.5 nm band pass filter (BPF) and a polarizer. The scattered light intensity, detected by a photodetector (PD1), was normalized to the incident light intensity detected by another photodetector (PD2). The surface roughness was also evaluated with the AFM after near-field etching. As the scanning area of the AFM was much smaller than the substrate, we measured the surface roughness R_a in nine representative areas, each 10 μm × 10 μm and separated by 100 μm. The scanned area was 8192 (x-axis) × 256 (y-axis) pixels with a spatial resolution of 1.2 nm (x-axis) and 40 nm (y-axis), respectively.

3. Results and discussion

Figures 2(a) and (b) show typical AFM images of the scanned 10 μm × 10 μm silica substrate area before and after 30 min of near-field etching, respectively. Figure 2(c) shows the cross-sectional profiles of figures 2(a) and (b), where the near-field etching yielded a dramatic decrease in peak-to-valley measurements from 1.73 nm (curve B) to 1.05 nm (curve A).

The solid curve in figure 3 shows the normalized scattered light intensity, obtained during the near-field etching. The normalized scattered light intensity was at maximum at an etching time of 13 min (indicated by the downward arrow in figure 3), and it decreased steadily as etching time increased. The etching time dependence of the average $\bar{R}_a$ for the nine R_as, also plotted in this figure, indicates that $\bar{R}_a$ decreases as the etching time increases. The minimum $\bar{R}_a$ was 1.35 Å at an etching time of 30 min. This increase in normalized scattered light intensity during the near-field etching accompanied by the decrease in $\bar{R}_a$ might originate from the increase in the number of scatterers. The details are discussed below.

We calculated the spatial power spectral density and the correlation length from the AFM images; these provided the data from which the structural changes in the surface morphology could be analyzed. First, we calculated the power spectral density based on the Yule–Walker method [9, 10] using a cross-sectional profile along the x-axis at the center of the AFM image. The etching time dependence of the power spectral density (figure 4(a)) shows that the spectral density reached maximum at a 20 min etching time. Although $\bar{R}_a$ only contains information about the individual scatterers, both the scattered light and power spectra yield lateral surface information about the scatterer. Thus, the increase in the normalized scattered intensity and the spectral density were originated from the increase in the number of scatterers. Furthermore, we also obtained the etching time dependence of the lower- and higher spatial frequency components of the spectral density. Figure 4(b) shows the results, where the low and high-frequency components were fixed at scales of 1.0×10^{-3} (nm^{-1}) (solid circles) and 1.3×10^{-1} (nm^{-1}) (solid squares), respectively. From the lines fitted to these values by the least-squares method, it was found that the low-frequency component decreased with increased etching time, whereas the high-frequency components increased. These results indicate that the size of the scatterer decreased as etching time increased. To confirm this postulate, we calculated the correlation length of the AFM images.

For the given surface function $f(u)$, the correlation function, $C_f(u)$, defined by

$$C_f(u) = \lim_{L\to\infty} \frac{1}{2L} \int_{-L}^{+L} f(z) f(z+u)\,\mathrm{d}u, \qquad (1)$$

is a measure of the correlation between two points on the surface separated by a distance u. For stationary stochastic processes, the correlation function is a monotonically decreasing function of the correlation length L_c, where L_c corresponds to the average protrusion width in the surface profile, i.e., the width of the scatterer. This correlation

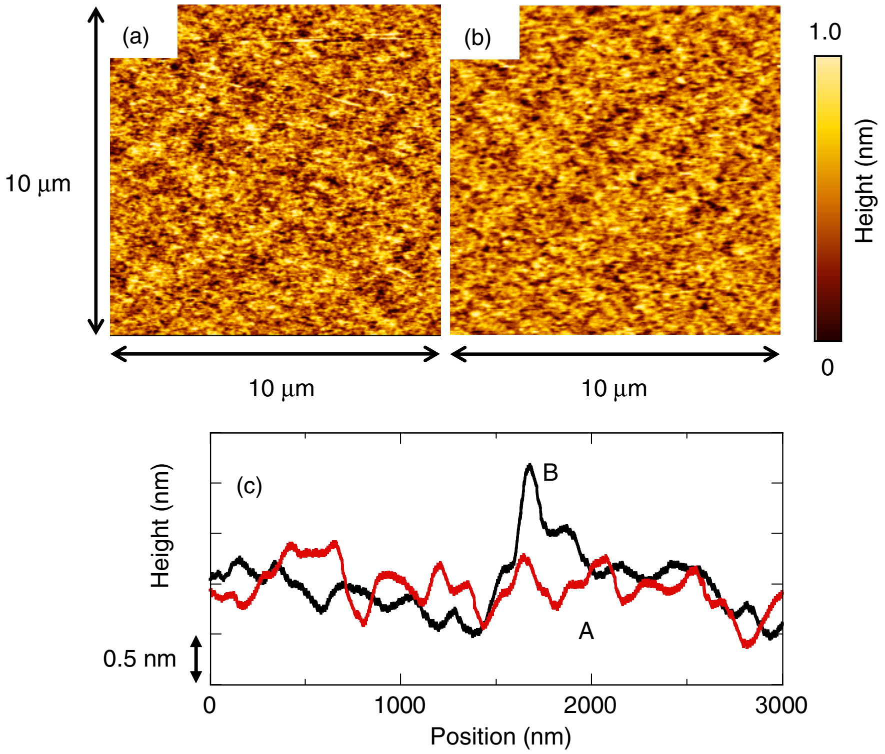

Figure 2. Typical AFM images of the silica substrate (a) before and (b) after the near-field etching (etching time of 30 min). (c) Cross-sectional profiles for (a) (curve B) and (b) (curve A).

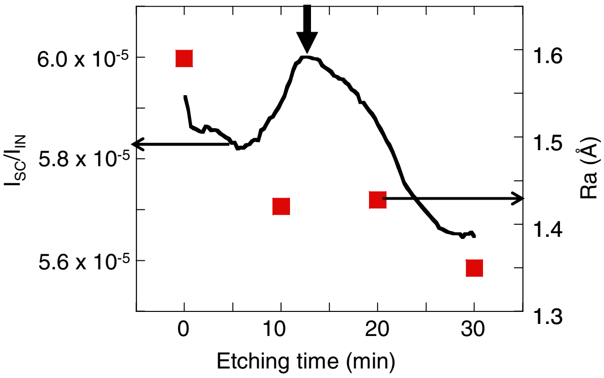

Figure 3. The etching time dependence of the normalized scattered light intensity (I_{SC}/I_{IN}, solid curve) and the $\bar{R}_a$ (solid squares). I_{SC}, detected scattered intensity using PD1; I_{IN}, detected incident light intensity using PD2.

function is well approximated with an exponential model of the form [11]

$$C_f(u) = \delta_f^2 \exp(-u/L_c) \tag{2}$$

where δ_f is the standard deviation of the roughness function. Another important roughness quantity is its power spectrum, $S(\sigma)$, where σ represents the spatial frequencies present in the roughness function. The correlation function $C_f(u)$ and the power spectrum $S(\sigma)$ are linked to each other through the Wiener–Khintchine relations [12]

$$C_f(u) = \int_{-\infty}^{\infty} \exp(\mathrm{i}\sigma u) S_f(\sigma)\, \mathrm{d}\sigma \tag{3}$$

$$S_f(\sigma) = \frac{1}{2\pi} \int_{-\infty}^{\infty} \exp(-\mathrm{i}\sigma u) C_f(\sigma)\, \mathrm{d}u. \tag{4}$$

Using the defining equation (4), the power spectrum associated with the exponential model is in the form of a Lorentzian

$$S_f(\sigma) = \frac{\delta_f^2}{\pi} \frac{L_c}{1 + L_c \sigma^2} \tag{5}$$

where, as noted previously, σ, δ_f, and L_c are the spatial frequencies, the standard deviation of the roughness function, and the correlation length, respectively [11, 12]. From this simple relation between power spectrum and correlation length, we see that as L_c decreases, the low-frequency components decrease, whereas the high-frequency components increase. This can be understood by considering that a decrease in the size of the scatterer results in a decrease in the low-frequency components and simultaneously results in an increase in high-frequency components. Using equations (1) and (2), we derived L_c and δ_f of surface profile along the x-axis at the center of the AFM images. Figure 5(a) shows the etching time dependence of L_c; L_c decreased to as little as 80 nm as the near-field etching time proceeded. This result agrees with the power spectral density change shown in figures 4(a) and (b). In addition, we found a reduction in the standard deviation of the roughness function δ_f (see solid squares in figure 5(a)), indicating that the substrate surface was etched uniformly across the substrate. This high spatial uniformity indicated that the near-field etching is a self-organized process.

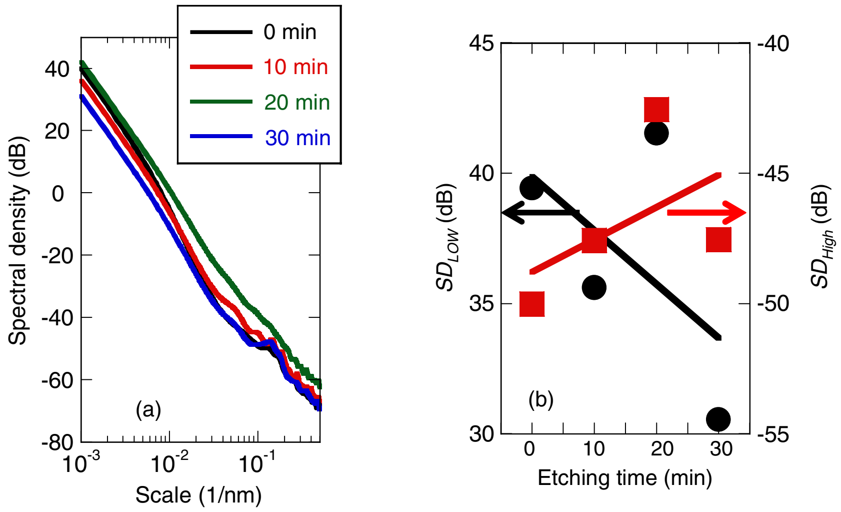

Figure 4. (a) Etching time dependence of the power spectrum. (b) Etching time dependence of the spectral density at a scale of 1.0×10^{-3} (nm^{-1}) ($\mathrm{SD_{Low}}$) and spectral density at high frequency of 1.3×10^{-1} (nm^{-1}) ($\mathrm{SD_{High}}$).

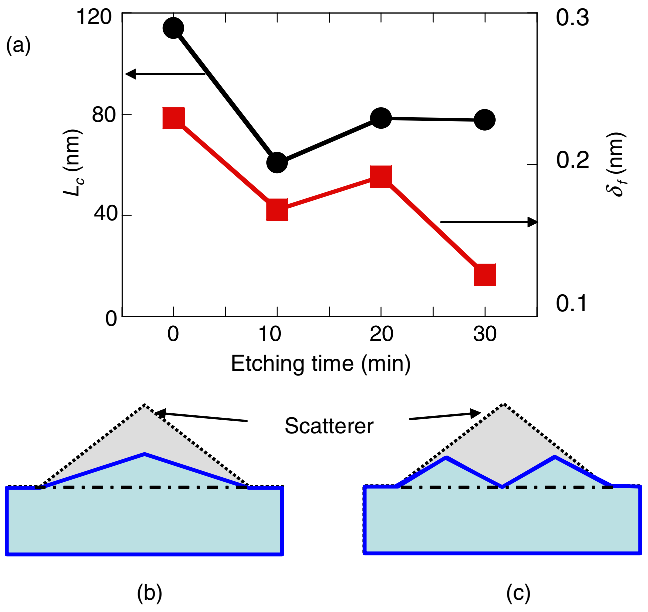

Figure 5. (a) Etching time dependence of the correlation length L_c and the standard deviation of the roughness function δ_f. (b) and (c) Schematic of structural change of the scatterer. Dashed, solid, and dash-dotted lines show the surface profiles before, during, and after near-field etching, respectively.

Based on these time dependences, we then considered structural change during near-field etching. The decrease in L_c rules out the possibility of structural change when the number of the scatterers remains constant (figure 5(b)) because for this structural change L_c, i.e., the width of the scatterer, remains constant. The increase in scattered light intensity and spectral density should originate from the increase in the number of scatterers, as shown schematically by the solid line in figure 5(c). This structural change is supported by the fact that the L_c halved at an etching time of 10 min (figure 5(a)).

To visually understand the above postulate, we analyzed the AFM images numerically. First, the AFM images were digitized with a threshold height of 0.5 nm. Figures 6(a)–(d) show the respective AFM images for 0–30 min etching time; the white area corresponds to the protruding area, i.e., the scatterer. Second, we evaluated the diameters of the scatterer by approximating them as circles of equal area. Figure 6(e) shows the diameter distributions of the scatterers fitted by the log-normal curves. Here, we found that the number of scatterers increased with etching times of 10 and 20 min, whereas the peak diameter decreased. Figure 6(f) shows the comparison of L_c, previously presented as the solid circles in figure 5(a), and the obtained peak diameters of the scatterers. The coincidence of both etching time dependences agrees with the above postulate that the width of the scatterers decreases as etching time increases. Figure 6(g) shows the comparison of the number of scatterers and the scattered light intensity (I_{SC}/I_{IN}), previously plotted as the solid line in figure 3. This comparison indicates that both values are maximum at an etching time of 10 min, meaning that the near-field etching produces smaller scatterers, i.e., an increase in the number of scatterers, resulting in an increase in the scattered light intensity.

4. Conclusion

We performed *in situ* real-time monitoring of surface roughness during optical near-field etching by detecting the scattered light intensity. This method yields both the surface roughness and lateral surface information for the scatterer. Comparison of the etching time dependence of the surface roughness and the power spectrum showed that near-field etching not only decreased the surface roughness, but also increased the number of scatterers, as was confirmed by analyzing the AFM image. The longer wavelength for the dissociation light source is expected to suppress the adiabatic photochemical reaction [5] and realize a smaller surface roughness. Optimizing the etching parameters, i.e., the

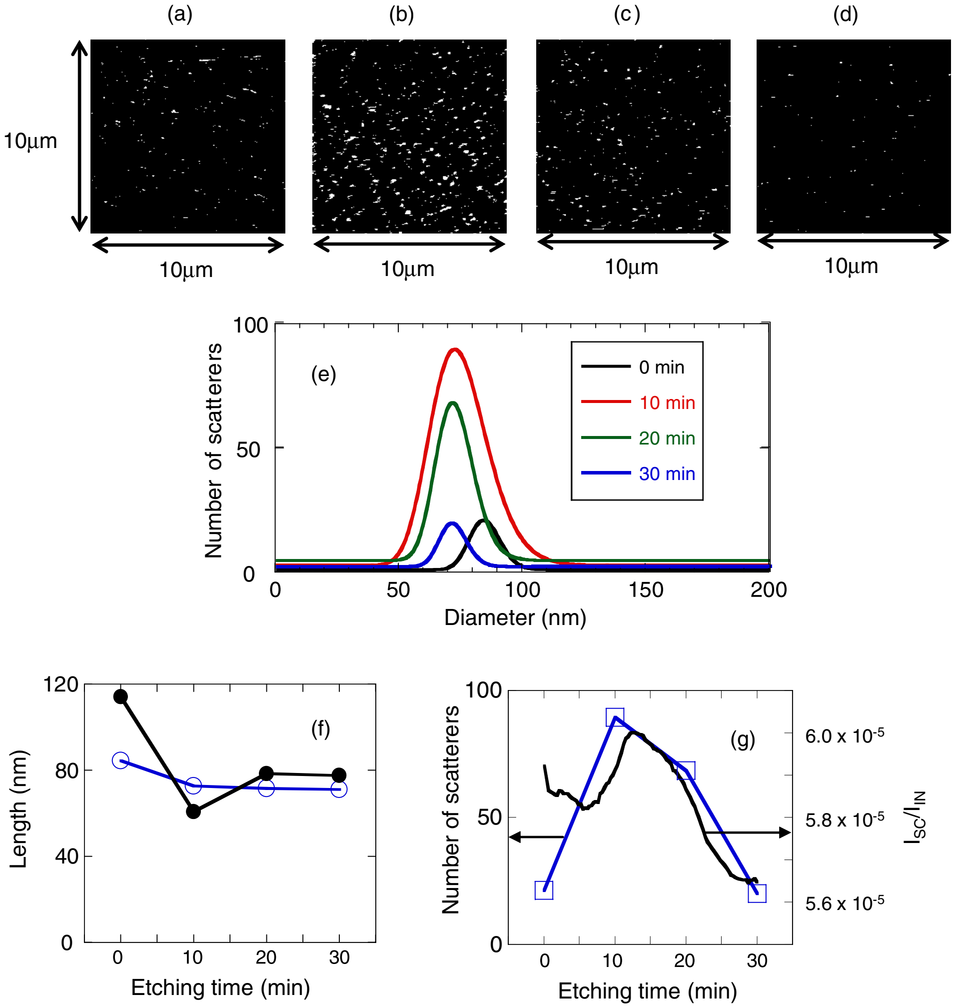

Figure 6. (a)–(d) Digitized AFM image of etching time of 0, 10, 20, 30 min, respectively. (e) Scatterer diameter distribution for (a)–(d). (f) The comparison of L_c (same as the solid circles in figure 5(a)) and the obtained peak diameter of the scatterer. (g) Comparison of scatterer number and scattered light intensity I_{SC}/I_{IN} (previously plotted as the solid line in figure 3).

wavelength, power density, etching time, etc, should further decrease the surface roughness.

Acknowledgments

This work was partially supported by the New Energy and Industrial Technology Development Organization (NEDO) under the program of Strategic Development on Rationalization Technology using Energy and under the program of Comprehensive Activity for Personnel Training and Industry-Academia Collaboration based on the NEDO project.

References

[1] Wua B and Kumar A 2007 *J. Vac. Sci. Technol.* B **25** 1743
[2] Cook L M 1990 *J. Non-Cryst. Solids* **120** 152
[3] Yatsui T, Hirata K, Nomura W, Ohtsu M and Tabata Y 2008 *Appl. Phys.* B **93** 55
[4] Kawazoe T, Kobayashi K, Takubo S and Ohtsu M 2005 *J. Chem. Phys.* **122** 024715
[5] Kobayashi K, Kawazoe T and Ohtsu M 2005 *IEEE Trans. Nanotechnol.* **4** 517
[6] Yatsui T and Ohtsu M 2009 *Appl. Phys. Lett.* **95** 043104
[7] Kullmer R and Büerle D 1987 *Appl. Phys.* A **43** 227
[8] Izawa T and Inagaki N 1980 *Proc. IEEE* **68** 1184
[9] Stoica P and Moses R 1997 *Introduction to Spectral Analysis* (Upper Saddle River: Prentice-Hall)
[10] Naruse M, Yatsui T, Nomura W, Hirata K, Tabata Y and Ohtsu M 2009 *J. Appl. Phys.* **105** 063516
[11] Ladouceur F 1997 *J. Light. Technol.* **15** 1020
[12] Koopmans L H 1974 *The Spectral Analysis of Time Series* (New York: Academic)

[II] PRESENTATIONS

IN INTERNATIONAL CONFERENCES

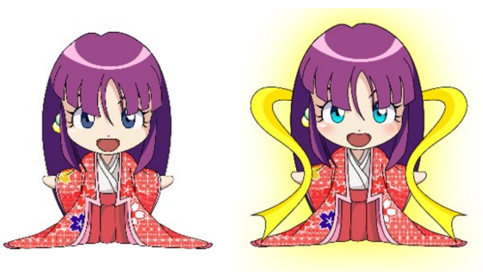

Nanophotonic Polishing of Substrate for Application to Hard-Disk and Optical-Disk Processing

Takashi Yatsui, Wataru Nomura, and Motoichi Ohtsu
School of Engineering, The University of Tokyo
2-11-16 Yayoi, Bunkyo-ku, Tokyo, Japan 113-8656
Email: yatsui@ee.t.u-tokyo.ac.jp

A reduction of the surface roughness (R_a) to less than 1 Å is required in various applications such as hard-disk and optical-disk processing. R_a is formally defined as the arithmetic average of the absolute values of the surface height deviations from the best-fitting plane. Although chemical-mechanical polishing (CMP) has been used to flatten the surfaces [1], it is generally limited to reducing R_a to about 2 Å because the polishing pad roughness is as large as 10 μm, and the polishing-particle diameters in the slurry are as large as 100 nm. We therefore developed a new polishing method that uses near-field etching based on an autonomous phonon-assisted process, which does not use any polishing pad, with which we obtained ultra-flat silica surface with angstrom-scale average roughness (see Fig. 1) [2,3]. Since this technique is a non-contact method without a polishing pad, it can be applied not only to flat substrates but also to three-dimensional substrates that have convex or concave surfaces, such as micro-lenses, optical-disk, and the inner wall surface of cylinders. Furthermore, this method is also compatible with mass-production.

References

1. L. M. Cook, J. Non-Crystalline Solids, **120**, 152 (1990).
2. T. Yatsui, K. Hirata, W. Nomura, M. Ohtsu, and Y. Tabata, Appl. Phys. B, **93**, 55 (2008).
3. T. Yatsui, K. Hirata, Y. Tabata, W. Nomura, T. Kawazoe, M. Naruse, and M. Ohtsu, Nanotechnology **21**, 355303 (2010).

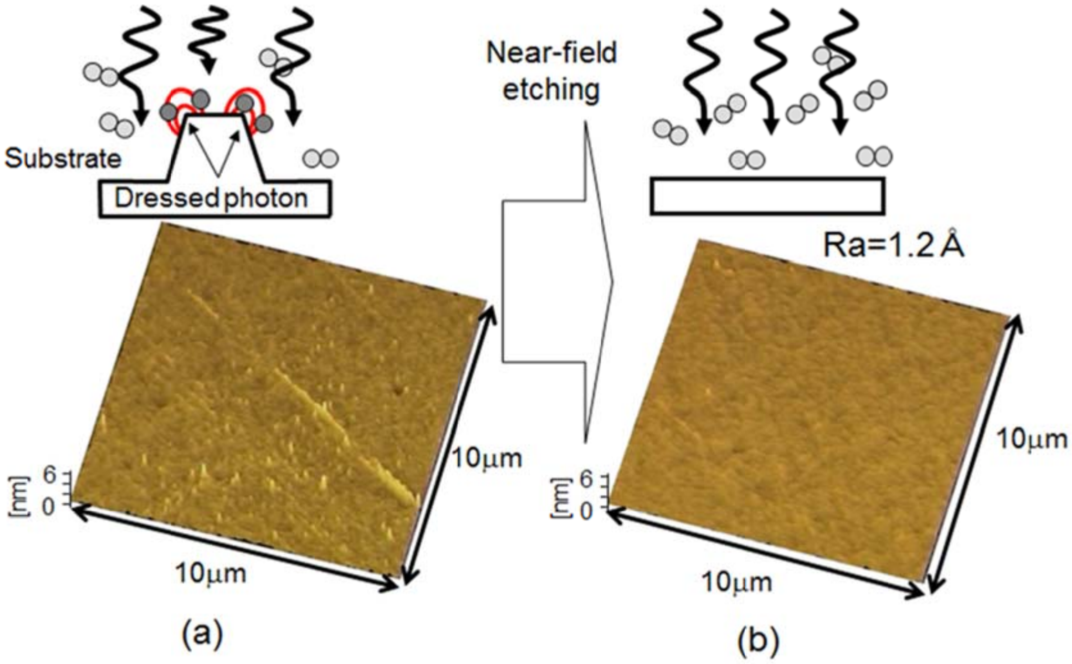

Fig. 1. Schematic of near-field etching. Atomic force microscopic images of (a) before and (b) after the optical near-field etching.

Controlling the Size and Variance of ZnO Quantum Dot Using Photo-Assisted Sol-Gel Method

Yang Liu, Takashi Yatsui, Tadashi Kawazoe, and Motoichi Ohtsu
Department of Electrical Engineering and Information Systems,
School of Engineering, The University of Tokyo
ryu@nanophotonics.t.u-tokyo.ac.jp

In order to carry out highly performance in device using quantum dots (QD), it is necessary to resonate the discrete level of excitons in the QDs. With this assumption, size variance of QD must be controlled. But in conventional sol-gel method which is an effective method for synthesizing ZnO QD, the size variance must be improved. To solve this problem, we developed a new sol-gel method employing optically assisted. With this new method, we improved the size variance from 23% to 17%. Furthermore we succeed to control the size of ZnO QD by selecting specific wavelength of assisting light.

Biography of Yang Liu

Yang Liu was born in Changchun, Jilin, China, on December 16, 1985. He received his Bachelor and Master degrees in Electronic Engineering from University of Electro -Communications and The University of Tokyo, in March 2008 Year and March 2010, respectively. He is currently working in pursuing a doctorate degree at the Department of Electrical Engineering and Information Systems, School of Engineering, The University of Tokyo. His research interest is in nano-scale photonics and ZnO crystal growth area.

Nanophotonic etching of glass substrate for Å-scale surface roughness

T. Yatsui, **W. Nomura, and M. Ohtsu**

School of Engineering, The University of Tokyo
2-11-16 Yayoi, Bunkyo-ku, Tokyo, Japan 113-8656

yatsui@ee.t.u-tokyo.ac.jp

A reduction of the surface roughness (R_a) to less than 1 Å is required in various applications such as hard-disk and optical-disk processing. Ra is formally defined as the arithmetic average of the absolute values of the surface height deviations from the best-fitting plane. Although chemical-mechanical polishing (CMP) has been used to flatten the surfaces [1], it is generally limited to reducing R_a to about 2 Å because the polishing pad roughness is as large as 10 μm, and the polishing-particle diameters in the slurry are as large as 100 nm. We therefore developed a new polishing method that uses near-field etching based on a phonon-assisted process, which does not use any polishing pad, with which we obtained ultra-flat silica surface with angstrom-scale average roughness (see Fig. 1) [2,3]. Since this technique is a non-contact method without a polishing pad, it can be applied not only to flat substrates but also to three-dimensional substrates that have convex or concave surfaces, such as micro-lenses, optical-disk, and the inner wall surface of cylinders. Furthermore, this method is also compatible with mass-production.

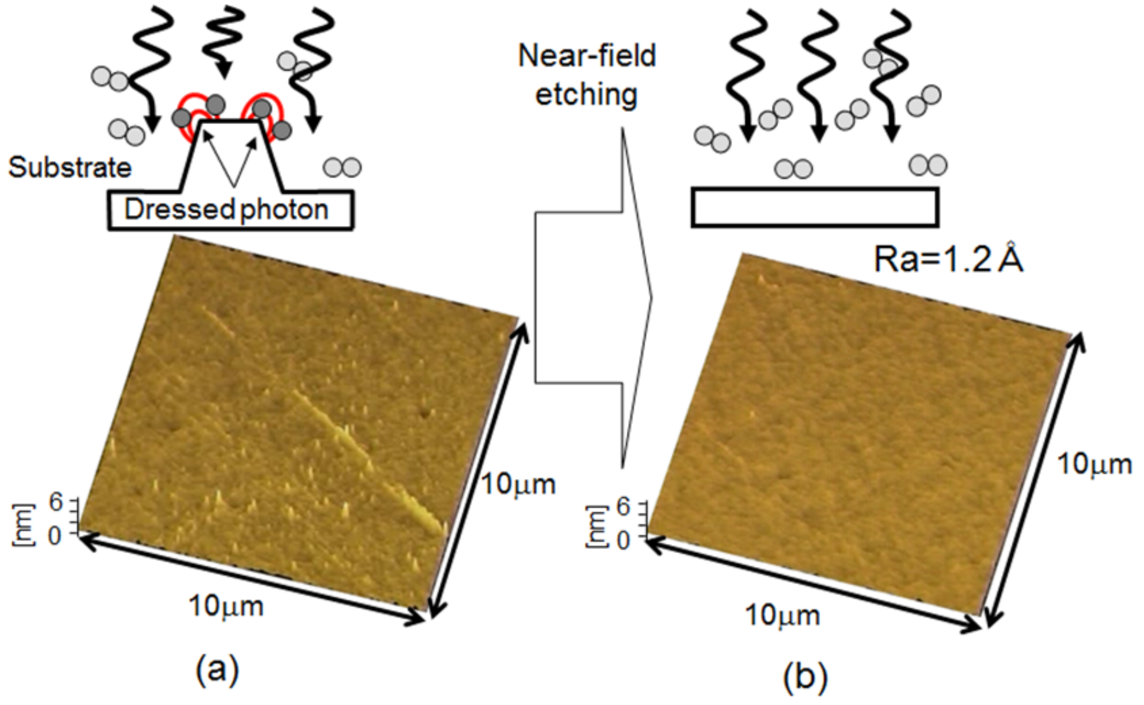

Figure 1 Schematic of near-field etching. Atomic force microscopic images of (a) before and (b) after the optical near-field etching.

[1] L. M. Cook, J. Non-Crystalline Solids, **120**, 152 (1990).
[2] T. Yatsui, K. Hirata, W. Nomura, M. Ohtsu, and Y. Tabata, Appl. Phys. B, **93**, 55 (2008).
[3] T. Yatsui, K. Hirata, Y. Tabata, W. Nomura, T. Kawazoe, M. Naruse, and M. Ohtsu, Nanotechnology **21**, 355303 (2010).

Theory of Superradiance by Nano-Array of Quantum-Well Dots

A. Ishikawa[1], T. Yatsui[2], K. Kobayashi[1], M. Ohtsu[2], J. Yoo[3], G.-C. Yi[4], and H. Ishihara[5]
1. Interdisciplinary Graduate School of Medicine and Engineering, The University of Yamanashi, Takeda, Kofu 400-8511, Japan
2. School of Engineering, The University of Tokyo, Bunkyo-ku, Tokyo 113-8656, Japan
3. Department of Materials Science and Engineering, POSTECH, Pohang, Gyoungbuk 790-784, Republic of Korea
4. National Creative Research Initiative Center for Semiconductor Nanorods, and Department of Physics and Astronomy, Seoul National University, Seoul 151-747, Republic of Korea
5. Graduate School of Engineering, Osaka Prefecture University, Gakuen-cho, Sakai, Osaka 599-8531, Japan

The superradiance had been predicted by Dicke in 1954 theoretically [1] and observed in atomic and molecular systems experimentally [2]. In the recent experiments, the superradiance and superfluorescence by nano-structures of solid-state materials such as an ensemble of quantum dots were observed [3, 4]. The superradiance by solid-state materials has advantage for the application of devices as compared with that by other materials such as atoms and molecules. Our group also observed the superradiant behaviour of emissions from a semiconductor nano-rod as shown in Fig. 1 (a). This sample is a nano-array of quantum-well dots (QWDs) with the width of 3.25 nm and barrier layers with the width of 9 nm. The diameter of the rod is 80 nm. The number of QWDs is about ten. In order to clarify the mechanism of the new type of superradiance by solid-state materials, we constructed the full-quantum-mechanical theory of superradiance [5], in which theory, the fundamental equations of the superradiant photoluminescence were derived by the scheme of the semiconductor luminescence equations [6]. The important development of our theory is an introduction of a correlation between polarizations via a radiation field which is the origin of superradiance. Here we will clarify the characteristics of superradiant emissions from the nano-array of QWDs and prove that the superradiance by our sample of the nano-rod can be realized theoretically.

In our theoretical model, all QWDs were assumed to be two-level systems which do not interact with each other and do with the photon field. We ignored the dependence of QWDs on the position in a real space because the length of the array is smaller than the wavelength of the radiation field which is resonant to QWDs. We calculated the time evolution of the peak intensity of photoluminescence as shown in Fig. 1 (b) and the population as shown in Fig. 1 (c). The parameters were set as follows: the number of QWDs $N = 10$ and the excitation density n_{ex} is from 0.1 to 1.0. From Fig. 1 (b), we find that the time profile of emissions changes from the curve of an exponential decay to the pulse-like curve when n_{ex} becomes larger than 0.5. In short, the superradiance can occur by our sample of the nano-rod when the population inversion is realized in each QWD. We also confirmed numerically that the origin of this superradiance is the correlation between polarizations in QWDs. From Fig. 1 (c), we find that the decay of the population becomes more rapid when $n_{\mathrm{ex}} > 0.5$ as an evidence of superradiance. In contrast to the above case of the population inversion, the decay of the population is restrained when $n_{\mathrm{ex}} < 0.5$. This shows that the subradiant emissions occur in the case of the low-density excitation by a nature of two-level systems of our sample. As a next step, we included the anisotropic interaction between QWDs and the photon field caused by the thin forms of QWDs. The dependence of superradiance on the direction of emissions was researched numerically. Thus, we clarified the mechanism of superradiant emissions and proved that the superradiance can be realized by our sample of the nano-array of QWDs.

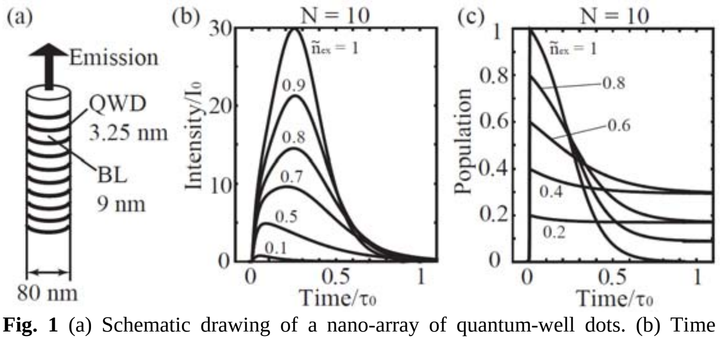

Fig. 1 (a) Schematic drawing of a nano-array of quantum-well dots. (b) Time evolution of the peak intensity of photoluminescence. (c) Time evolution of the population. N and n_{ex} are the number of quantum-well dots and the excitation density.

References

[1] R. H. Dicke, “Coherence in Spontaneous Radiation Processes,” Phys. Rev. **93**, 99 (1954).
[2] H. M. Gibbs, Q. H. F. Vrehen, and H. M. J. Hikspoors, “Single-Pulse Superfluorescence in Cesium,” Phys. Rev. Lett. **39**, 547 (1977).
[3] M. Scheibner et al., “Superradiance of quantum dots,” Nature Phys. **3**, 106 (2007).
[4] K. Miyajima, Y. Kagotani, S. Saito, M. Ashida, and T. Itoh, “Superfluorescenct pulsed emission from biexcitons in an ensemble of semiconductor quantum dots,” J. Phys.: Condens. Matter **21**, 195802 (2009).
[5] A. Ishikawa and H. Ishihara, “Theory of superradiance by biexcitons in optically correlative quantum dots,” International Conference on Excitonic Processes in Condensed Matters (EXCON 08) (Kyoto, June, 2008), THY-P-26.
[6] M. Kira and S. W. Koch, “Quantum-optical spectroscopy of semiconductors,” Phys. Rev. A **73**, 013813 (2006).

Optical Pulsation Based on Near-Field Interactions at the Nanoscale by Continuous-Wave Light Excitation

Makoto Naruse[1], Hirokazu Hori[2], Kiyoshi Kobayashi[2], Tadashi Kawazoe[3], and Motoichi Ohtsu[3]
[1] National Institute of Information and Communications Technology, 4-2-1 Nukui-kita, Koganei, Tokyo 184-8795, Japan
[2] Interdisciplinary Graduate School of Medicine and Engineering, University of Yamanashi, Yamanashi 400-8511, Japan
[3] Dept. Electric. Eng. and Info. Systems and Nanophotonics Research Center, The University of Tokyo, Tokyo 113-8656, Japan

***Abstract*- We theoretically demonstrate optical pulsation based on optical near-field interactions at the nanoscale. We observe pulsation in populations pumped by continuous-wave light excitation based on optical energy transfer from smaller to larger quantum dots. This will provide critical insights toward the design and implementation of experimental nanophotonic pulse generating devices.**

I. INTRODUCTION

Generating an optical pulse train is one of the most important functionalities required for optical systems. However, conventional principles of optical pulse generation are based on optical energy build-up in a cavity whose size is much larger than the optical wavelength; thus, the volume and the energy efficiency of the entire system have serious limitations. For nanophotonic applications [1], novel principles should be developed on the nanometer scale. Shojiguchi et al. theoretically investigated the possibility of generating superradiance in N two-level systems interacting with optical near-fields [2]. This approach, however, requires precise control of the initial states, which is not straightforward to implement. In this paper, we theoretically demonstrate a mechanism of optical pulsation based on optical near-field interactions at the nanometer scale pumped by continuous-wave (CW) light irradiation [3]. With an architecture composed of two subsystems each of which involves energy transfer based on optical near-field interactions, we observe pulsation in the populations based on a model system using a density matrix formalism. The details of the theoretical elements of this paper will be found in Ref. [3].

II. PRINCIPLE OF OPTICAL PULSATION BASED ON OPTICAL NEAR-FIELD INTERACTIONS

Optical excitation transfer via optical near-field interactions is one of the unique attributes available at the nanometer scale, which allows populating even energy levels that are conventionally dipole forbidden [1]. Here we assume two spherical quantum dots whose radii are R_S and R_L, which are denoted by $\mathrm{QD_S}$ and $\mathrm{QD_L}$, respectively in Fig. 1(a). The energy eigenvalues of states specified by quantum numbers (n,l) are given by $E_{nl} = E_g + E_{ex} + \hbar^2 \alpha_{nl}^2 / 2MR^2$ (n=1,2,3,…), where E_g is the band gap energy of the bulk semiconductor, E_{ex} is the exciton binding energy in the bulk system, M is the effective mass of the exciton, and α_{nl} are determined from the boundary conditions. There exists a resonance between the level of quantum number (1,0) of QD_S (S_1) and that of quantum number (1,1) of QD_L (L_2) if $R_L / R_S = 4.49/\pi \approx 1.43$. Due to the large spatial inhomogeneity of the localized optical near-fields at the surface of nanoscale material, an optical transition to the (1,1)-level in QD_L, which is conventionally forbidden, is allowed. Therefore, an exciton in the (1,0)-level in QD_S could be transferred to the (1,1)-level in QD_L. In QD_L, due to the sublevel energy relaxation with a relaxation constant Γ, which is faster than the near-field interaction, the exciton relaxes to the (1,0)-level (L_1), from where it radiatively decays.

Here, when the lower level of QD_L is populated by an external input, the optical excitation occurring in QD_S cannot be transferred to QD_L because the lower energy level in QD_L is populated, which is called the state filling effect [1]. Putting it another way, the population of the (1,0)-level in QD_S is

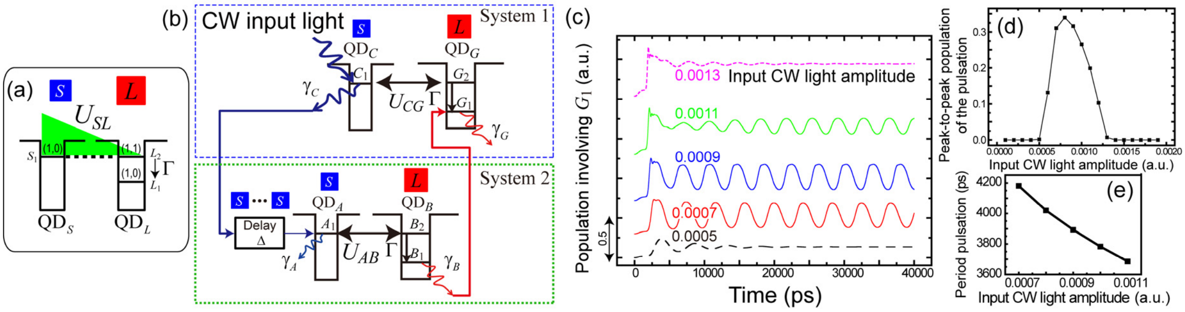

Figure 1. Schematic diagrams of (a) optical excitation transfer from a smaller QD (QD_S) to a larger QD (QD_L) via optical near-field interactions, (b) system architecture of pulsation composed of two subsystems each of which provides optical excitation transfer from QD_S to QD_L. (c) Evolution of population in the lower energy level of QD_G with different CW input light amplitudes where pulsations are observed with adequate parameter range. (d) Peak-to-peak population of the pulsation vs input CW light amplitude. (e) The period of pulsation depends on the input CW light amplitudes.

978-1-61284-318-6/11/$26.00 ©2011 IEEE

changed by the external input applied to L_1 in QD$_L$. Now, the optical pulsation based on optical excitation transfer comes from the idea that the externally applied change induced in L_1 can be provided in a self-induced manner by S_1 with a certain timing delay. If QD$_S$ is irradiated with continuous input light, such a change should repeat with a certain period; that is, a pulsed signal should result.

We consider two quantum dot systems, each of which consists of one smaller and one larger QD, as shown in Fig. 1(b). One system, called *System 1* hereafter, is represented by one smaller dot (QD$_C$) and one larger dot (QD$_G$). A continuous-wave input is provided to the upper level of QD$_C$. The optical near-field interaction between QD$_C$ and QD$_G$ is denoted by U_{CG}. Another system, called *System 2*, provides a delay time by multiple use of smaller and larger dots, as already experimentally realized in Ref. [4]. However, modeling the delay caused by multiple QDs makes the discussion of pulsation mechanisms unnecessarily complicated; thus, we assume an arbitrary delay time applied to the input signal of System 2, denoted by $\varDelta$, followed by the last two quantum dots in the delay system, namely, a smaller QD (QD$_A$) and a larger QD (QD$_B$), as indicated in Fig. 1(b). Here, QD$_A$ accepts radiation from QD$_C$ in System 1; that is, the change of the states in QD$_C$ is transferred to QD$_A$. The optical near-field interaction between QD$_A$ and QD$_B$ is denoted by U_{AB}. The output from QD$_B$ then influences the lower energy level of QD$_G$. We described the details of the above modeling based on a density matrix formalism. For example, regarding System 1, there are in total three energy levels (namely, C_1 in QD$_C$, and G_1 and G_2 in QD$_G$). The radiative relaxation rates from C_1 and G_1 are respectively given by γ_C and γ_G. Then we rigorously derived the quantum master equations for System 1 and System 2, respectively [3].

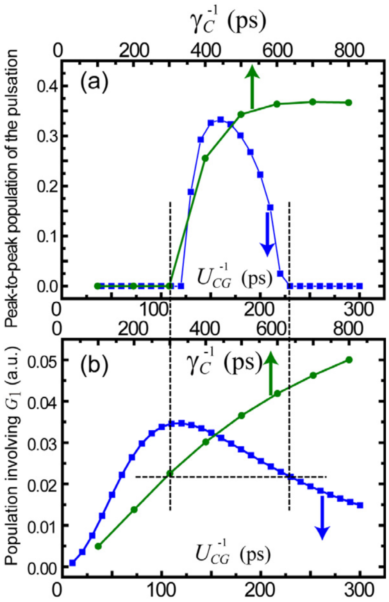

Figure 2. Parameter dependencies to inter-dot optical near-field interactions and the radiation lifetime. (a) Peak-to-peak population of the pulsation. (b) Populations involving G_1.

III. DEMONSTRATION OF THE PULSATIONS

We assume the following typical parameter values based on experimental observations of energy transfer observed in ZnO nanorods [5]; inter-dot optical near-field interactions (144 ps), sublevel relaxation (10 ps), radiative decay times of the smaller dot (443 ps), and the large dot (190 ps). Also, we assume 1 ns for the delay Δ in System 2 in Fig. 1(b). Figure 1(c) demonstrates an example of the evolution of the populations involving the lower level of QD$_G$ (G_1) for different CW input light amplitudes, where optical pulsation is successfully observed with appropriate input light amplitudes, as summarized in Fig. 1(d). The period of the pulsation, or frequency, depends on the input CW light amplitude, which is one of the indications that the pulsation is based on optical excitation transfer among the QDs, as shown in Fig. 1(e). To observe such an effect more clearly, Fig. 2 shows the parameter dependencies on the inter-dot interactions between QD$_C$ and QD$_G$ (U_{CG}) and the radiation lifetime of QD$_C$ (γ_C). The squares and circles in Fig. 2(a) indicate the peak-to-peak value of the pulsations in populations as a function of U_{CG} and the radiation lifetime of QD$_C$, respectively. To seek the origin of such behavior, we investigate the virtually isolated System 1, namely an independent system composed only of QD$_C$ and QD$_G$. Figure 2(b) represents the steady-state populations involving the lower level of QD$_G$ (G_1) as a function of the radiation lifetime of QD$_C$. Increasing the radiation lifetime of QD$_C$ allows an excitation generated in QD$_C$ to be transferrable during that lifetime, thus increasing the possibility of transition to QD$_G$, shown by the circles in Fig. 2(b). On the other hand, increasing the inter-dot interaction time, namely, weaker inter-dot interactions, degrades the populations in QD$_G$, as shown by the squares in Fig. 2(b). Here we should note that the pulsation vanishes, in Fig. 2(a), when U_{CG}^{-1} is larger than 230 ps, corresponding to a population involving G_1 of around 0.02 in Fig. 2(b). In Fig. 2(a), the pulsation also vanishes when γ_C^{-1} is smaller than 300 ps, which also corresponds to a population involving G_1 of around 0.02 in Fig. 2(b). This agreement, or unified understanding, of two different parameter dependencies indicates that the energy transfer via optical near-field interactions plays a crucial role in the optical pulsation at the nanometer scale.

REFERENCES

[1] M. Ohtsu, K. Kobayashi, T. Kawazoe, S. Sangu, and T. Yatsui, "Nanophotonics: Design, Fabrication, and Operation of Nanometric Devices Using Optical Near Fields," *IEEE J. Sel. Top. in Quantum Electron.*, vol. 8, no. 4, pp. 839-862, July/August 2002.

[2] A. Shojiguchi, K. Kobayashi, S. Sangu, K. Kitahara and M. Ohtsu, "Superradiance and Dipole Ordering of an N Two-Level System Interacting with Optical Near Fields," *J. Phys. Soc. Jpn.*, vol. 72, no. 11, pp. 2984-3001, November 2003.

[3] M. Naruse, H. Hori, K. Kobayashi, and M. Ohtsu, *Appl. Phys. B*, in press.

[4] W. Nomura, T. Yatsui, T. Kawazoe, M. Naruse, and M. Ohtsu, "Structural dependency of optical excitation transfer via optical near-field interactions between semiconductor quantum dots," *Appl. Phys. B*, vol. 100, no. 1, pp. 181-187, July 2010.

[5] T. Yatsui, H. Jeong, and M. Ohtsu, "Controlling the energy transfer between near-field optically coupled ZnO quantum dots," *Appl. Phys. B*, vol. 93, no. 5, pp. 199-202, August 2008.

Demonstration of Modulatable Nanophotonics based on modulatable optical near-field interactions between dispersed quantum dots

Naoya Tate[1], Wataru Nomura[1], Makoto Naruse[1,2], Tadashi Kawazoe[1], Takashi Yatsui[1],
Morihisa Hoga[3], Yasuyuki Ohyagi[3], Yoko Sekine[3], Hiroshi Fujita[3], Motoichi Ohtsu[1]

[1]Department of Electrical Engineering and Information Systems, The University of Tokyo,
2-11-16 Yayoi, Bunkyo-ku, Tokyo, 113-8656, Japan

[2]National Institute of Information and Communication Technology,
4-2-1 Nukuikita, Koganei, Tokyo, 184-8795, Japan

[3]Dai Nippon Printing Co. Ltd., Research and Development Center,
250-1 Wakashiba, Kashiwa, Chiba, 277-0871, Japan

***Abstract*- Optical near-field interactions exhibit high-efficiency energy transfer between closely positioned nanometric materials, and the subsequent optical response induced by the transfer can be controlled by modulating the spatial distribution. We experimentally demonstrated the basic concept of such modulatable optical near-field interactions, termed *Modulatable Nanophotonics*, with quantum dots dispersed on a flexible substrate.**

I. INTRODUCTION

Nanophotonics, which utilizes the local interactions between nanometric materials via optical near-fields [1], enables novel photonic devices, fabricated structures, and systems, which can meet the requirements of future optical technologies [2], especially in realizing novel functions and operations in optical devices that cannot be implemented by utilizing any conventional optical techniques. Although there are various applications of nanophotonics, the realization of diverse optical functions from a single device and retrieval techniques using optical far-field responses are likely to be important [3]. In this paper, we describe our concept of *Modulatable Nanophotonics* as one idea to realize this. We experimentally demonstrated the concept by using modulatable optical near-field interactions between randomly dispersed *resonant* quantum dot (QD) pairs on a flexible substrate.

II. MODULATABLE NANOPHOTONICS USING QUANTUM DOTS DISPERSED ON A FLEXIBLE SUBSTRATE

Research in nanophotonic devices has been actively pursued [4]. In device operation, it is essential to transfer a signal and to fix the transferred signal intensity at the output terminal, which can be achieved by transferring optical near-field energy and its subsequent dissipation, respectively. Generally, this operation exhibits a *one-to-one* correspondence with respect to input signals, because the structure and alignment of nanometric materials are essentially constant. In order to realize a *one-to-many* correspondence with a single device, it is necessary to implement modulatable optical near-field interactions and associated modulatable optical functions, a concept we call Modulatable Nanophotonics.

To demonstrate Modulatable Nanophotonics, we utilize the emission from *resonant* QD pairs dispersed on a flexible substrate. Generally, closely positioned resonant QD pairs exhibit high-quantum efficiency, selective energy transfer via induced optical near-fields between QDs. The energy transfer depends on the individual energy levels of each QD. Only if the conditions are matched with each other, that is, if a resonant relation exists, energy can be successfully transferred from small QD to large QD. Transferred energy is immediately dissipated as emission from the large QD. Here, if the substrate has enough flexibility, flexing the substrate can vary the distance between the QDs. Because the extent of the spatial distribution of the optical near-fields depends on the material size, and thus, magnitude of energy transfer decreases rapidly with increasing the separation between the QDs, the resonant relation via optical near-fields is destroyed by flexing the substrate.

Figures 1 show schematic diagrams of comparing emitting processes with non-resonant and resonant QDs. In the case of *non-resonant* QDs as $\mathrm{QD}_{\text{S-NR}}$ and $\mathrm{QD}_{\text{L-NR}}$ in Fig. 1(a), energy transfer does not occur, and each QD emits individually regardless of whether or not the substrate is flexed. Change of the emission spectrum only depends on the number of QDs per unit area. Therefore, rates of change of the spectral peak intensities at before and after the flexion from each QD are obtained as $I_{\text{S-NR2}}/I_{\text{S-NR1}} = I_{\text{L-NR2}}/I_{\text{L-NR1}}$, where $I_{\text{S-NR1}}$, $I_{\text{S-NR2}}$, $I_{\text{L-NR1}}$, and $I_{\text{L-NR2}}$ represent the spectral peak intensities from $\mathrm{QD}_{\text{S-NR}}$ and $\mathrm{QD}_{\text{L-NR}}$ at before and after the flexion, respectively. On the other hand, when using *resonant* QD pairs, as $\mathrm{QD}_{\text{S-R}}$ and $\mathrm{QD}_{\text{L-R}}$ in Fig. 1(b), energy transfer occurs only when the QDs are closely positioned, and emission is obtained only from $\mathrm{QD}_{\text{L-R}}$. Here, if the $\mathrm{QD}_{\text{S-R}}$ and $\mathrm{QD}_{\text{L-R}}$ are separated by flexion of the substrate, the resonant relation is destroyed and $\mathrm{QD}_{\text{S-R}}$ and $\mathrm{QD}_{\text{L-R}}$ emit equivalently, as non-resonant QDs do. Therefore, different rates of change of the spectral peak intensities at before and after the flexion are obtained from $QD_{\text{S-R}}$ and $QD_{\text{L-R}}$ as $I_{\text{S-R2}}/I_{\text{S-R1}} \neq I_{\text{L-R2}}/I_{\text{L-R1}}$, where $I_{\text{S-R1}}$, $I_{\text{S-R2}}$, $I_{\text{L-R1}}$, and $I_{\text{L-R2}}$ represent the spectral peak intensities from $QD_{\text{S-R}}$ and $QD_{\text{L-R}}$ at before and after the flexion, respectively.

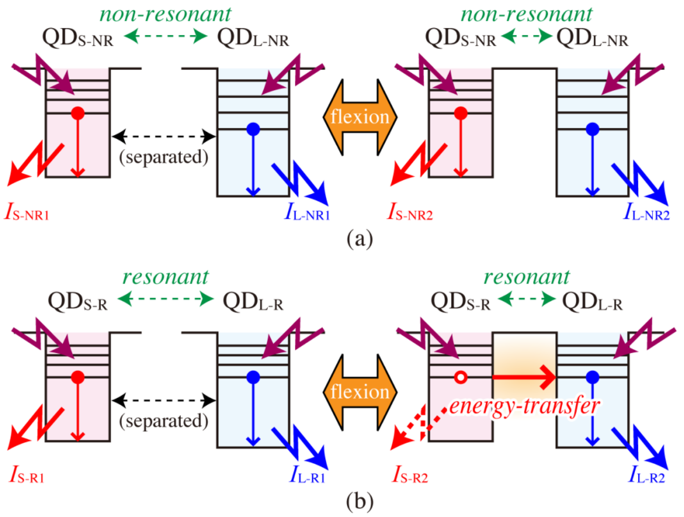

Figure 1 Schematic diagram of modulatable optical response of QDs dispersed on flexible substrates with (a) *non-resonant* QD pairs and (b) *resonant* QD pairs.

III. EXPERIMENTAL DEMONSTRATION

We used commercially available CdSe/ZnS QDs which *non-resonant* and *resonant* relations via optical near-field interactions, which has been experimentally demonstrated [5]. As a flexible substrate, we used polydimethylsiloxane (PDMS), which is optically transparent and is generally considered to be an inert, non-toxic, and non-flammable material. Both non-resonant and resonant QD pairs were dispersed on individual PDMS substrates, and the samples were excited by a 457 nm laser diode. In our experiment, each sample was set on a hole formed in a vacuum desiccator, and substrate flexing was achieved by evacuation.

We observed emission spectra with non-resonant and resonant samples at before and after the flexion of each substrate. From the spectra, peak intensities of the emission spectra from each QD are measured. Figure 2 shows the change rate of each spectrum peak intensity between before and after the flexion. The +50% of the rate is experimentally intended by the change of the number of QDs per unit area. As shown, with the *non-resonant* QD pairs, the rates of $QD_{\text{S-NR}}$ and $QD_{\text{L-NR}}$ are nearly equal ($I_{\text{S-NR2}}/I_{\text{S-NR1}} \cong I_{\text{L-NR2}}/I_{\text{L-NR1}}$). In contrast, with the *resonant* QD pairs, the rates are clearly different ($I_{\text{S-R2}}/I_{\text{S-R1}} \ll I_{\text{L-R2}}/I_{\text{L-R1}}$). These are the expected behaviors as noted above.

In general, the different rates of change of each spectral peak intensity correspond to a change in color tone of the emission from the sample. Our experimental result indicates that the change in color tone of the emission is successfully obtained by the flexion of the substrate.

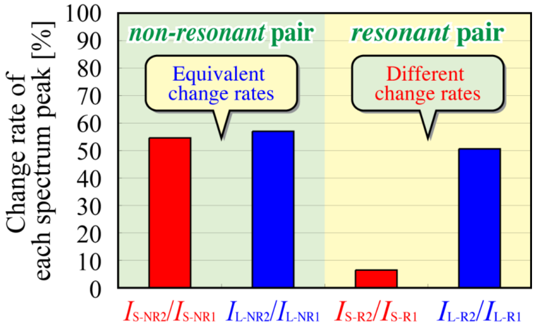

Figure 2 Change rates of each emission spectrum peak intensity between before and after the flexion with *non-resonant* and *resonant* QD pairs.

IV. CONCLUSION

In conclusion, we have described the basic concept of Modulatable Nanophotonics and experimentally demonstrated the concept by utilizing non-resonant and resonant QD pairs dispersed on a PDMS substrate. Moreover, in the point of view of the information retrieval, results of our demonstration indicate that Modulatable Nanophotonics can retrieve effects of optical near-field interactions as modulation of emission spectrum. Selecting appropriate QD pairs can realize various *modulatabilities* of Nanophotonics. By developing the concept further, our idea can be applied to a modulatable multi-spectrum emitting element whose emission spectrum can be switched by modulation on the nanometric scale.

ACKNOWLEDGMENT

This work was supported in part by a comprehensive program for personnel training and industry–academia collaboration based on projects funded by the New Energy and Industrial Technology Development Organization (NEDO), Japan, as well as the Global Center of Excellence (G-COE) “Secure-Life Electronics” and Special Coordination Funds for Promoting Science and Technology sponsored by the Ministry of Education, Culture, Sports, Science and Technology (MEXT), Japan.

REFERENCES

[1] M. Ohtsu, K. Kobayashi, T. Kawazoe, T. Yatsui, and M. Naruse (eds.), *Principles of Nanophotonics*, Taylor and Francis, 2008.

[2] M. Ohtsu, “Nanophotonics in Japan,” Journal of Nanophotonics, vol. 1, pp. 011590 1-7, 2007.

[3] N. Tate, W. Nomura, T. Yatsui, T. Kawazoe, M. Naruse, and M. Ohtsu, “Parallel retrieval of nanometer-scale light-matter interactions for nanophotonic systems,” Natural Computing (Proceedings in Information and Communications Technology), PICT2, pp. 298-307, Springer, 2010.

[4] M. Ohtsu, K. Kobayashi, T. Kawazoe, S. Sangu, and T. Yatsui, “Nanophotonics: design, fabrication, and operation of nanometric devices using optical near fields,” IEEE J. Sel. Top. Quantum Electron., vol. 8, pp. 839-862, 2002.

[5] W. Nomura, T. Yatsui, T. Kawazoe, and M. Ohtsu, “The observation of dissipated optical energy transfer between CdSe quantum dots,” Journal of Nanophotonics, vol. 1, pp. 011591 1-7, 2007.

PROGRAM VIEW : 2011 Spring & Bilateral

MY PROGRAM : 2011 Spring & Bilateral

09 May 2011 | **12 May 2011**

view a

start at **Subject**

14 8 16:00
SYMP
G

Visible light hydrogen generation using ZnO nanorods in a phonon-assisted optical near-field process

Authors : K. Kitamura, T. Yatsui, H. Yasuda, T. Kawazoe, and M. Ohtsu Department of Electrical Engineering and Information Systems, Nanophotonics Research Center, The University of Tokyo

Resume : Because conventional photocatalysts are activated only under ultraviolet light irradiation, the effective use of visible light is a very important goal. We generated hydrogen using visible light in a phonon-assisted optical near-field process. Carrier excitation using propagating light requires photon energy higher than the band gap energy (3.3 eV for ZnO). An optical near-field can excite coherent phonons in nanoscale structures, i.e., a phonon-assisted process. To realize an efficient phonon-assisted process, we introduced ZnO nanorods grown by metal–organic vapor-phase epitaxy (MOVPE) as electrodes. The optical near-field generated around a material depends on the material size. In the MOVPE process, the temperature controls the diameter of the ZnO nanorods. We prepared samples of ZnO nanorods with diameters of 100 and 10 nm. Water was electrolyzed using the electrodes, and hydrogen was generated at the Pt counter electrode. The current was measured under visible light irradiation (2.6 eV). The current was more than 20 times greater using the 10-nm nanorods than using the 100-nm nanorods. Photoluminescence measurements revealed that the visible light excitation did not originate from impurities. We realized a visible-light excitation process due to a phonon-assisted optical near-field by introducing fine ZnO nanorod structures as small as 10 nm in diameter.

14
8

(close full abstract)

Back

PROGRAM VIEW : 2011 Spring & Bilateral

MY PROGRAM : 2011 Spring & Bilateral

09 May 2011 **12 May 2011**

view a

start at	Subject
11 1 08:30 SYMP **G**	**Optimizing the energy transfer between near-field optically coupled ZnO quantum dots** **Authors :** T. Yatsui, Y. Liu, and M. Ohtsu The University of Tokyo, Bunkyo-ku, Tokyo, 113-8656, Japan **Resume :** ZnO quantum dots (QDs) are promising materials for realizing nanophotonic devices at room temperature, owing to their large exciton binding energies. The recent demonstration of QDs has resulted in nanometer-scale signal transmission devices, in which the unidirectional energy flow from a small QD (QDS) to a large QD (QDL) is satisfied by resonant near-field energy transfer and energy dissipation in the QDL. To increase signal transmission efficiency, we optimized the QDS/QDL size ratio. We synthesized ZnO QDs using a Sol-Gel method and then combined a 3.0-nm QDS with a 4.5-nm QDL. For these radii, the first excited state of the QDL resonated with the ground state of the QDS. The mean surface-to-surface separation of the QDs was 3 nm. When the mixing ratio R (=NL [number of QDL]/NS [number of QDS]) of the QDs was less than 4, a photoluminescent (PL) signal was obtained only at 3.41 eV, corresponding to the ground state of the QDL. When the value of R exceeded 4, an additional peak appeared in the PL signal at 3.52 eV, corresponding to the ground state of the QDS. Furthermore, the maximum PL intensity at 3.41 eV was at R=4. If NL increased, the energy transfer from the QDS to the QDL was blocked due to state filling. These results indicate that there is an optimum R value for near-field energy transfer. This assumption is confirmed by the increased energy transfer time from the QDS to the QDL as NL increased. **(close full abstract)**

11 1

Back

European Materials Research Society
23 Rue du Loess - BP 20 - 67037 Strasbourg Cedex 02 - France - Phone:+33-(0)3 88 10 63 72 - Fax:+33-(0)3 88 10 62 93 - emrs@emrs-strasbourg.com

PROGRAM VIEW : 2011 Spring & Bilateral

MY PROGRAM : 2011 Spring & Bilateral

09 May 2011 12 May 2011

view a

start at		Subject	
C 2 SYMP **E**	16:55	**Size control of sol-gel-synthesized ZnO quantum dots using photo-assisted desorption** **Authors :** Y. Liu, T. Yatsui, and M. Ohtsu The University of Tokyo **Resume :** Recently, techniques involving quantum dots (QDs) have been actively studied for producing nanometer-sized optical devices (nanophotonic devices). To realize high performance in a nanophotonic device, it is necessary to resonate the discrete levels of the excitons in the QDs. For this, the size variance of the QD must be reduced to 10% or less. We selected ZnO QDs to fabricate nanophotonic devices, because ZnO has a large exiton binding energy. However, in conventional ZnO QD synthesis in liquid by the sol-gel method, the QD size variance can be as large as 25%. To solve this problem, we developed a new sol-gel method employing light-assisted chemical etching. When synthesized ZnO QDs are irradiated by light with photon energies higher than their bandgap energy, electron-hole pairs trigger an oxidation-reduction reaction in the QDs. Thus, the ZnO atoms depositing on the QD surface are desorbed. The ZnO QD size can be controlled accurately by the absorbed light intensity and wavelength. With this method we succeeded in reducing the QD size variance from 23% to 18%, as was shown in the half bandwidth of the ZnO QD's PL spectrum and TEM image. Furthermore, this technique was found to be effective at reducing the number of defect levels formed due to oxygen defects generated during ZnO QD synthesis. As a result, we succeeded in removing the defect level perfectly.	C 2

(close full abstract)

Back

European Materials Research Society
23 Rue du Loess - BP 20 - 67037 Strasbourg Cedex 02 - France - Phone:+33-(0)3 88 10 63 72 - Fax:+33-(0)3 88 10 62 93 - emrs@emrs-strasbourg.com

Self-organized nanophotonic device

T. Yatsui[1,2] and M. Ohtsu[1,2]
[1] School of Engineering, The University of Tokyo,
[2] Nanophotonics Research Center, The University of Tokyo
2-11-16 Yayoi, Bunkyo-ku, Tokyo 113-8656, Japan

Innovations in optical technology are required for the development of future information processing systems, which includes increasing the integration of photonic devices by reducing their size and levels of heat generation. To meet this requirement, we proposed nanophotonic signal transmission (NST) devices that consist of semiconductor quantum dots (QDs) [1,2]. These NST devices operate using excitons in QDs as the signal carrier, due to optical near-field interactions between closely spaced QDs. The exciton energy transfers to another QD when the exciton energy levels are resonant and, therefore, the optical beam spot may be decreased to be as small as the QD size. To produce the NST device, a new technique is required for positioning and alignment of QDs with precise separation.

Figure 1(a) illustrates our approach for the development of a self-assembling NST device with angstrom-scale controllability in spacing among QDs using silane-based molecular spacers and DNA [3]. First, ZnO QDs 5 nm diameter in diameter were synthesized using the Sol-Gel method [4]. Then, the surfaces of QDs were coated with a silane coupling agent 0.6 nm in length. The function of the agent is to maintain the spacing between QDs, and to be adhesive to anionic DNA, due to its cationic nature. We used λ DNA (stretched length = 16 µm) as a template, and when the QDs are mixed, the QDs are self-assembled onto the DNA by electrostatic interactions. Dense packing of the ZnO QDs along the DNA was obtained, as shown by transmission electron micrography (TEM) (Fig. 1(b)). The separation between QDs (S) was determined by TEM and shown to be 1.2 nm, which was in good agreement with twice the length of silane coupling agents. Such a high density of packing, despite the electrostatic repulsion between ZnO QDs, was due to the quaternary ammonium group of the silane coupling agent [3].

To observe the optical properties of the aligned ZnO QDs, the DNA with QDs was stretched and straightened on the silicon substrate using combing technique [5], where the silicon substrate was terminated with silane coupling agent and the anionic DNA was adsorbed on the cationic silicon substrate. We obtained the isolated chain of ZnO QDs (see Fig. 2(a)). From the polarization dependence of photoluminescence (PL) at a wavelength of 350 nm (Fig. 2(b)), corresponding to the ground state of 5-nm ZnO QDs, the strong PL emission was obtained by excitation of parallel polarization along the QD chains (E_0). Previous studies on the excitation polarization dependence of nanorods [6] indicated that the PL under parallel excitation (E_0) is much greater than that under perpendicular polarization (E_{90}), due to the absorption anisotropy. Similar polarization dependence was observed in our chained structure. It is possible that the dipoles between adjacent QDs are coupled with optical near-field interaction, and QD chains have large dipolar strength (see Fig. 2(b)), indicating that they act as an NST device along the chained QDs.

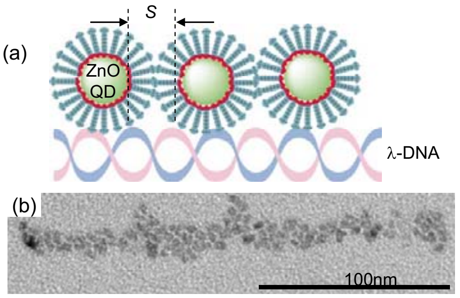

Fig. 1. Fabrication and evaluation of nanophotonic signal transmission device. (a) Schematic of ZnO QD alignment along the λ DNA. S: separation between QDs (b) TEM picture of the aligned ZnO QDs.

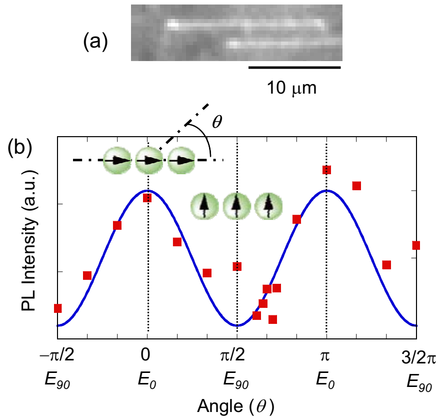

Fig.2. (a) Stretched ZnO QD chain along the λ DNA. (b) Incident light polarization dependence of PL intensity. A 4th-harmonic, Q-switched Nd:YAG laser (λ = 266 nm) was used to excite the ZnO QDs. θ: Polarization angle with respect to the direction along the QD chains.

As optical near-field energy can transmit through the resonant energy level, NST devices have a number of potential applications, such as wavelength division multiplexing using QDs of different sizes.

References

[1] M. Ohtsu, T. Kawazoe, T. Yatsui, M. Naruse, IEEE J. Select. Top. Quant. Electron. **14**, 1404 (2008).
[2] T. Yatsui, Y. Ryu, T. Morishima, W. Nomura, T. Kawazoe, T. Yonezawa, M. Washizu, H. Fujita, and M. Ohtsu, Appl. Phys. Lett., **96**, 133106 (2010).
[3] T. Yonezawa, S. Onoue, N. Kimizuka, Chem. Lett. **31**, 1172 (2002).
[4] E.A. Meulenkamp, J. Phys. Chem. B **102**, 5566 (1998).
[5] H. Oana, M. Ueda, M. Washizu, Biochem. Biophys. Research Commun. **265**, 140-143 (1999).
[6] J. Wang, M. S. Gudiksen, X. Duan, Y. Cui, C.M. Lieber, Science **293**, 1455-1457 (2001)

Autonomous Excitation Transfer in Quantum Dot Mixtures via Network of Optical Near-Field Interactions at the Nanoscale

Makoto Naruse[*1,3], Ferdinand Peper[1], Kenji Leibnitz[1,2], Kouichi Akahane[1], Naokatsu Yamamoto[1],
Wataru Nomura[3], Tadashi Kawazoe[3], Takashi Yatsui[3], Masayuki Murata[2], and Motoichi Ohtsu[3]

[1] National Institute of Information
and Communications Technology
4-2-1 Koganei, Nukui-kita,
Tokyo 184-8749 Japan
* E-mail: naruse@nict.go.jp

[2] Department of Information
Networking, Graduate School
of Information Science and
Technology, Osaka University,
1-5 Yamadaoka, Suita
Osaka, 565-0871 Japan

[3] Department of Electrical Engineering
and Information Systems and the
Nanophotonics Research Center, Graduate
School of Engineering, The University of
Tokyo, 2-11-16 Yayoi, Bunkyo-ku,
Tokyo 113-8656, Japan

***Abstract*—We examine autonomous optical excitation transfer in mixtures of different-sized quantum dots networked via optical near-fields at the nanometer scale. We theoretically and experimentally demonstrate optical excitation transfer via the network of optical near-field interactions among quantum dots. The topology-dependent efficiency of excitation transfer is also investigated. The results of our analysis of autonomous and energy-efficient light–matter interactions at the nanoscale, called nanophotonics, will provide useful insights into the design of robust and energy-efficient information and communications systems and networks.**

***Index Terms*—nanophotonics, nanometer-scale systems, nanostructures, network in the nanometer-scale, new generation network, optical excitation transfer, optical near-fields**

I. INTRODUCTION

OPTICS is expected to play a crucial role in enhancing system performance to handle the continuously growing amount of digital data and new requirements demanded by industry and society [1]. However, there are some fundamental difficulties impeding the adoption of optical technologies in information processing and communication systems [2-6]. One problem is the poor integrability of optical devices in systems due to the diffraction limit of light. This is because the optical wavelength used in a given system is typically around 1 μm, which is about 100 times larger than the gate width of present silicon VLSI hardware.

Nanophotonics, on the other hand, which is based on local interactions between nanometer-scale materials via optical near-fields, is not restricted by conventional diffraction of light, allowing ultrahigh-density integration [2-4]. Optical excitation transfer between quantum dots (QDs) via optical near-field interactions will be one of the most important mechanisms in realizing novel devices and systems [2,3,7,8]. Moreover, qualitatively novel features that are unavailable in conventional optics and electronics are enabled by such optical excitation transfer [9,10].

In this paper, we demonstrate optical excitation transfer in a mixture composed of different-sized (larger and smaller) QDs networked via optical near-fields in their vicinities. We theoretically demonstrate an optimal mixture of two different-sized QDs concerning the optical near-field interaction network based on a density matrix formalism, which agrees well with experimental results obtained using CdSe/ZnS QD mixtures with diameters of 2.0 nm and 2.8 nm. In addition, we theoretically examine the topology-dependent efficiency of optical excitation transfer, which also clearly exhibits autonomous, energy-efficient networking behavior occurring at the nanometer scale.

This paper is organized as follows. In Section II, we describe the physical fundamentals of optical excitation transfer between QDs. In Section III, we discuss a network of optical near-field interactions and analyze the mixture-dependent optical excitation transfer theoretically and experimentally. In Section IV, we investigate the topology-dependency of the excitation transfer. In Section V, we discuss what we can learn from these physical principles and phenomena physically existing at the nanometer scale and their implications for information and communications applications, as well as information networking.

II. OPTICAL EXCITATION TRANSFER VIA OPTICAL NEAR-FIELD INTERACTIONS BETWEEN QUANTUM DOTS

In this section, we first briefly review the fundamental principles of optical excitation transfer involving optical near-field interactions [2,3]. Conventionally, the interaction Hamiltonian between an electron and an electric field is given

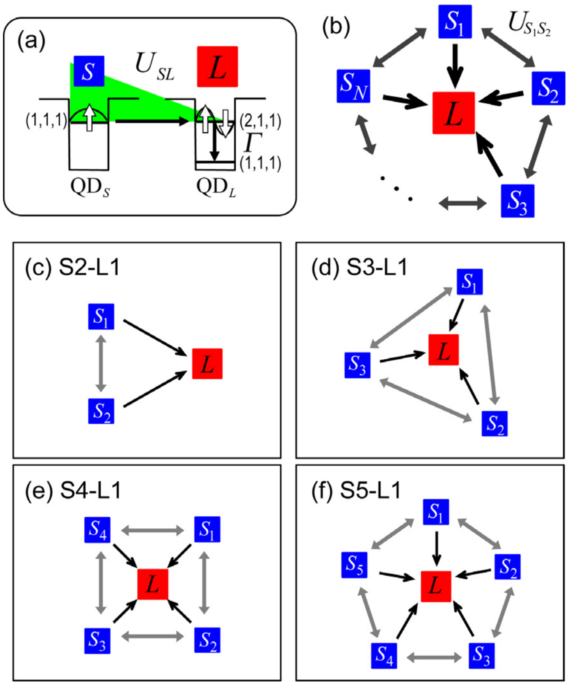

Fig. 1. (a) Optical excitation transfer from smaller quantum dot (QD_S) to larger one (QD_L) via optical near-field interactions. (b) Multiple quantum dot system composed of multiple smaller QDs and one larger QD. (c-f) Example systems.

by

$$\hat{H}_{\rm int} = -\int \hat{\psi}^{\dagger}(\vec{r})\vec{\mu}\hat{\psi}(\vec{r})\bullet\hat{\vec{D}}(\vec{r})d\vec{r} \tag{1}$$

where $\vec{\mu}$ is the dipole moment, $\hat{\psi}^{\dagger}(\vec{r})$ and $\hat{\psi}(\vec{r})$ are respectively creation and annihilation operators of the electron at $\vec{r}$, and $\hat{\vec{D}}(\vec{r})$ is the operator of electric flux density. In usual light–matter interactions, the operator $\hat{\vec{D}}(\vec{r})$ is a constant since the electric field of propagating light is considered to be constant on the nanometer scale. Therefore, one can derive optical selection rules by calculating a transfer matrix of an electric dipole. As a consequence, in the case of cubic QDs, for instance, transitions to states described by quantum numbers containing an even number are prohibited [2]. In the case of optical near-field interactions, on the other hand, due to the steep electric field of optical near-fields in the vicinity of nanometer-scale matter, an optical transition that violates conventional optical selection rules is allowed [2,3].

Optical excitations in nanostructures, such as QDs, can be transferred to neighboring ones via optical near-field interactions [8-10]. For instance, assume that two cubic QDs whose side lengths are a and $\sqrt{2}a$, which are called QD_S and QD_L, respectively, are located close to each other, as shown in Fig. 1(a). Suppose that the energy eigenvalues for the quantized exciton energy level specified by quantum numbers (n_x, n_y, n_z) in the QD with side length a (QD_S) are given by

$$E_{(n_x,n_y,n_z)} = E_B + \frac{\hbar^2\pi^2}{2Ma^2}(n_x^2 + n_y^2 + n_z^2) \tag{2}$$

where E_B is the energy of the bulk exciton, and M is the effective mass of the exciton. According to (2), there exists a resonance between the level of quantum number (1,1,1) in QD_S and that of quantum number (2,1,1) in QD_L. There is an optical near-field interaction, which is denoted by U_{SL}, due to the steep electric field in the vicinity of QD_S. It is known that the inter-dot optical near-field interaction is given by a Yukawa-type potential [2]. Therefore, excitons in QD_S can move to the (2,1,1)-level in QD_L. Note that such a transfer is prohibited for propagating light since the (2,1,1)-level in QD_L contains an even number. In QD_L, the exciton sees a sublevel energy relaxation, denoted by Γ, which is faster than the near-field interaction, and so the exciton goes to the (1,1,1)-level in QD_L.

In Sections III and IV, we apply these theoretical arguments to systems composed of multiple quantum dots and investigate their impact on fundamental features of optical excitation transfer occurring at the nanometer scale.

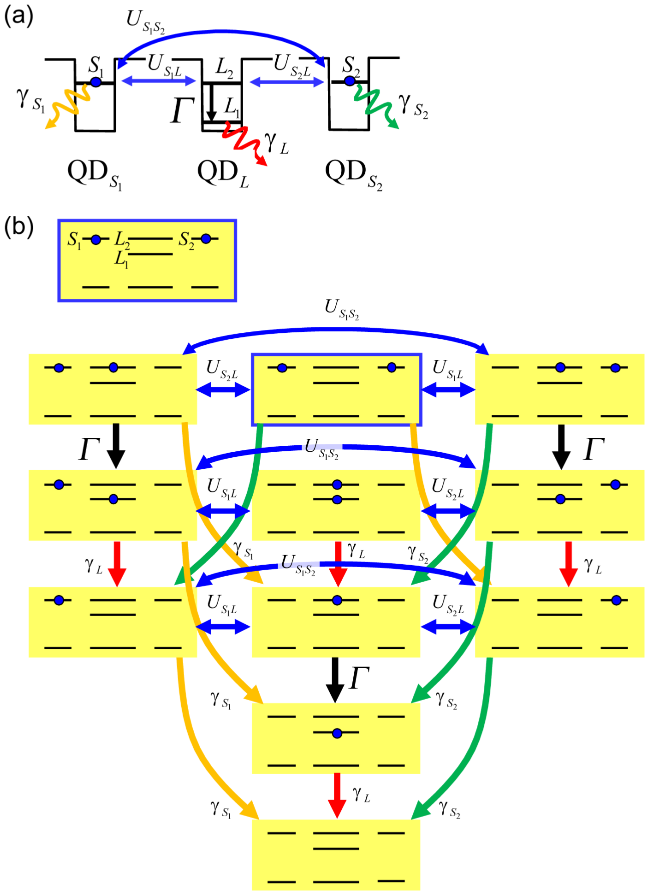

Fig. 2. Example of the system modeling based on a density matrix formalism. (a) Parameterizations for inter-dot near-field interactions, radiative relaxations, and non-radiative relaxations in the **S2-L1** system. (b) Schematic representation of state transitions in the **S2-L1** system.

III. NETWORK OF OPTICAL NEAR-FIELD INTERACTIONS

Here we consider a quantum dot system shown in Fig. 1(b), where multiple smaller dots (denoted by S_i) can be coupled with one larger dot, denoted by L. We also assume inter-dot interactions between adjacent smaller quantum dots; that is, (i) S_i interacts with S_{i+1} (i=1,...,N-1) and (ii) S_N interacts with S_1, where N is the number of smaller QDs. For instance the system shown in Fig. 1(c) consists of two smaller QDs and one larger QD, denoted by **S2-L1**. Similarly, **S3-L1**, **S4-L1**, **S5-L1** systems are composed of three, four, and five smaller QDs in addition to one large QD, which are respectively shown in Figs. 1(d), (e), and (f).

Now, what is of interest is to maximize the flow of excitations from the smaller dots to the larger one. We deal with this problem theoretically based on a density matrix formalism. In the case of the **S2-L1** system, composed of two smaller QDs and one larger QD, the inter-dot interactions between the smaller dots and the larger one are denoted by U_{S_iL}, and that between the smaller dots is denoted by $U_{S_1S_2}$, as schematically shown in Fig. 2(a). The radiations from S_1, S_2, and L are respectively represented by the relaxation constants γ_{S_1}, γ_{S_2}, and γ_L. We suppose that the system initially has two excitations S_1 and S_2. With such an initial state, we can prepare a total of eleven bases where zero, one, or two excitation(s) occupy the energy levels; the state transitions are schematically shown in Fig. 2(b). In the numerical calculation, we assume U_{S_iL} = 200 ps and $U_{S_1S_2}$ = 100 ps as typical parameter values. Following the same procedure, we also derive quantum master equations for the **S3-L1**, **S4-L1**, and **S5-L1** systems with initial states in which all smaller quantum dots have excitations. Finally, we can calculate the population of the lower level of QD_L, the time integral of which we regard as the output signal.

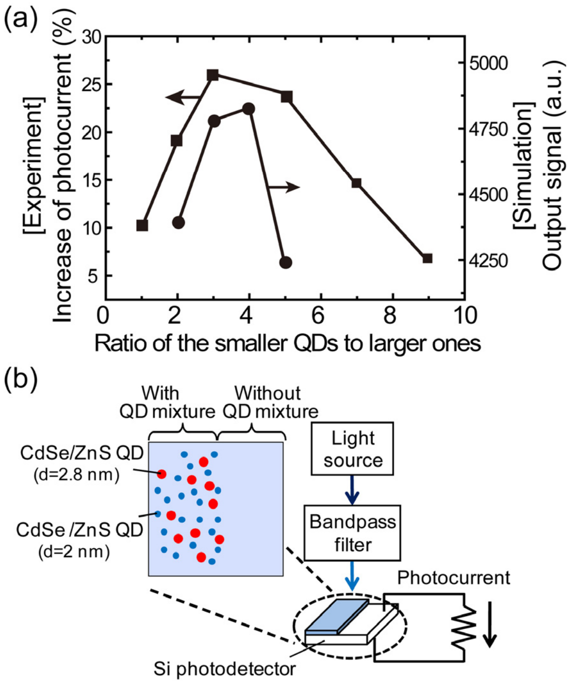

Fig. 3. (a) Optimal ratio of the number of smaller QDs to larger ones so that the optical excitation transfer is the most efficiently induced. (b) Schematic diagram of the experimental demonstration.

We compare the output signal as a function of the *ratio* of the *number* of smaller dots to the larger one assuming that the total number of QDs, regardless of their sizes (smaller or larger), in a give unit area is the same. As shown in the circles in Fig. 3(a), the most efficient transfer is obtained when the ratio of the number of smaller dots to the larger one is 4. That is, increasing the number of smaller quantum dots does not necessarily contribute to increased output signals. Because of the limited radiation lifetime of QD_L, not all of the initial excitations can be successfully transferred to QD_L due to the state filling of the lower level of QD_L. Therefore, part of the input populations must be decayed at QD_S, which results in loss in the transfer from the smaller QDs to the larger one when there are too many excitations in the smaller QDs surrounding one larger QD.

Such an optimal mixture of smaller and larger QDs was experimentally demonstrated by using two kinds of CdSe/ZnS core/shell quantum dots whose diameters were 2.0 nm and 2.8 nm [11,12]. The quantum dots were dispersed in a matrix composed of toluene and ultraviolet curable resin and were coated on the surface of a silicon photodiode (Hamamatsu Photonics K.K., Si Photodiode S2368). As schematically shown in Fig. 3(b), half of the surface of the photodiode was spin-coated with an ultraviolet-curable resin containing a mixture of quantum dots, which was then cured by ultraviolet radiation, whereas the other half of the surface was coated with the same resin without the quantum dot mixture. Input light was selectively radiated onto each area to evaluate the difference in the generated photocurrent. The increase of the induced photocurrent via the QD-coated area with input light wavelengths between 340 nm and 360 nm is shown by the squares in Fig. 3(b). We attribute such an increase to the optical excitation transfer through which the input light wavelength is red-shifted to wavelengths where the photodetector is more sensitive. The maximum increase was obtained when the ratio of the number of smaller QDs to larger ones was 3:1. This agrees with the theoretical optimal ratio discussed above.

IV. TOPOLOGY-DEPENDENT, AUTONOMOUS, EFFICIENT OPTICAL EXCITATION TRANSFER

In the previous section, we observe that the amount of optical excitation transferred from the smaller QDs to the larger one depends on the ratio of the number of smaller and larger QDs. This indicates that we could increase the output by further engineering the network structure among the QDs. In this section, by taking the **S5-L1** system shown in Fig. 1(f) as an example, we demonstrate that the output signal could be increased when the network among the quantum dots is adequately configured.

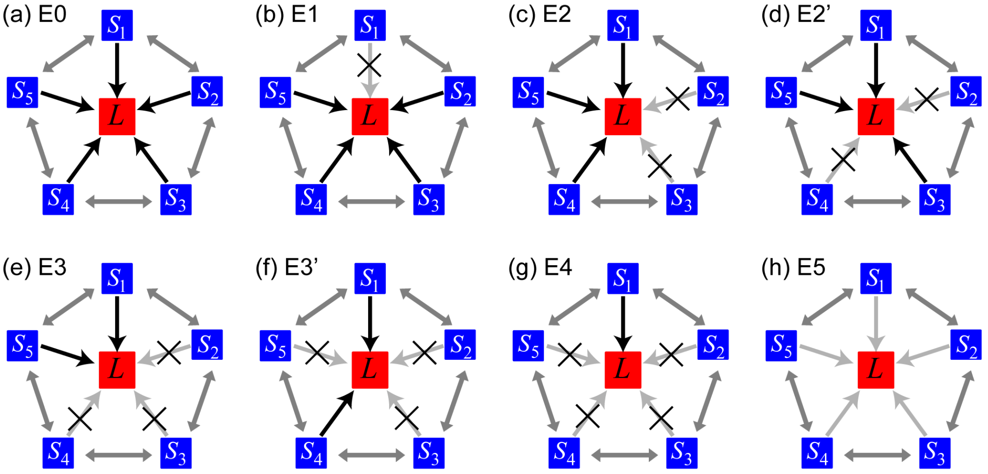

Fig. 4. Eight different network topologies in the **S5-L1** system where some of the interactions between QD$_S$ and QD$_L$ are degraded, or lost. (Degraded interactions are indicated by "X")

Figure 4(a), denoted by **E0,** represents the original **S5-L1** system which is the same as the one shown in Fig. 1(f). Here, assume that some of the interactions between QD$_S$ (denoted by S_1 to S_5) and QD$_L$ are degraded, or lost, due to, for instance, material disorder such as violation of the condition represented by (1). There are in total eight such configurations concerning the symmetry; for instance, when one of the five links between QD$_S$ and QD$_L$ is degraded, such a situation is represented by the system **E1** schematically shown in Fig. 4(b). (The interaction between S_1 and L is indicated by X.) Similarly, when the number of degraded links is two, the system should be represented either by the system **E2** or **E2'** shown respectively in Fig. 4(c) and (d).

Figure 5(a) demonstrates the time evolutions of the populations associated with radiation from QD$_L$. Figure 5(b) summarizes the integrated populations as a function of the network configurations illustrated in Fig. 4. Interestingly, systems with degraded interactions, except the system **E5** which has no valid links between QD$_S$ and QD$_L$, exhibit a higher output signal than the system without link errors, namely, the system **E0**. For example, the system **E2** exhibits an output signal about 1.64 times higher than the system **E0**. This corresponds to the results described in Section III, where the output is maximized when the ratio of the number of QD$_S$ to QD$_L$ is 4, meaning that the excessively high number of excitations in QD$_S$ connected to QD$_L$ cannot be transferred. Thanks to the "limited" interactions between QD$_S$ and QD$_L$, such as in the case of the systems **E2** and **E2'**, the excitations located in QD$_S$ have more chance to be transferred to QD$_L$. In

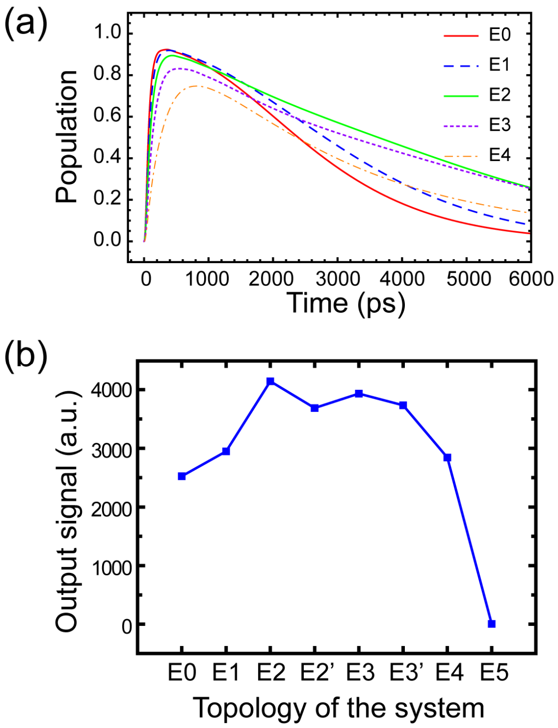

Fig. 5. (a) The time evolution of the populations associated with the QDL in systems E0, E1, E2, E3, and E4 in Fig. 4. (b) Time integrated populations for the systems in Fig. 4, where systems with certain negligible, or essentially nonexistent links result in higher output signal levels.

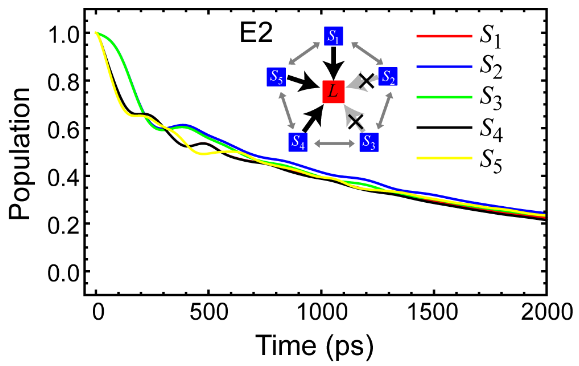

Fig. 6. Time evolutions of the populations associated with the smaller QDs (S1 to S5) in the system **E2** in Fig. 4.

representing such an effect, Fig. 6 summarizes the evolutions of populations associated with S_1 to S_5 in the system **E2,** where the interactions between [S_2 and L] and [S_3 and L] are negligible, or essentially nonexistent. Note that the populations associated with S_2 and S_3 remain at a higher level, indicating that the optical excitations in S_2 and S_3 are effectively "waiting" in the smaller dots until they have the opportunity to be transferred to QD_L by way of the interactions between smaller dots.

V. IMPLICATIONS FOR INFORMATION AND COMMUNICATION SYSTEMS

Finally, we would like to conclude with a few remarks about how these findings in nanometer-scale light–matter interaction networks can be applied to information and communications technologies (ICTs). The first point we would like to address here is the autonomous behavior of the optical excitations. As we could see, there is no "central controller" in the systems, and yet, efficient transport of the optical excitations is realized, as clearly observed in the discussions above. Such an intrinsic, seemingly *intelligent* behavior of the nanometer-scale physical system may also provide valuable lessons for designing self-organizing, distributed, complex ICT systems on Internet-scale. In the wake of the current redesign efforts toward a future Internet, novel distributed and autonomous strategies for *new generation networks* (NwGN) are being considered [13] that are able to cope with the numerous requirements the Internet will be facing in the future. Some of these approaches are based on biological or physical phenomena that exhibit self-* capabilities, e.g., self-organization, self-adaptability, which permit a flexible and autonomous management of the network [14]. Furthermore, using distributed and autonomous network systems helps avoiding unbalanced traffic load and energy consumption [13], as well as reduces the dependence of the network on single points of failure and thus leads to improving the overall sustainability and reliability.

Closely related to this is also the second observation that the increase in the output signal induced by degraded interactions indicates robustness against errors occurring in the system. This point is also of great importance for future communication networks. Since new generation networks are expected to accommodate a large number of heterogeneous end devices, access technologies, network protocols/services, and traffic characteristics, the consideration of failures or sudden fluctuations in performance seems inevitable. Designing robust mechanisms is, therefore, a key issue and utilizing such an intrinsic robustness of nanophotonics, which has the potential to provide superior robustness to errors, while requiring less hardware redundancy than current proposals with redundancies of the order of 10 to 100 [15], may provide helpful guidelines and/or principles for constructing efficient future ICT systems.

Third, it was demonstrated that a single process of optical excitation transfer is about 10^4 times more energy efficient compared with the single bit flip energy required in current electrical devices [16]. A system-level, comprehensive comparison of energy efficiency is an important and timely subject that should be explored in future. These studies will be extremely helpful for developing energy efficient strategies to assist in handling the tremendous growth in traffic and required processing energy anticipated in future communication networks [17,18].

REFERENCES

[1] K. Sato and H. Hasegawa, "Prospects and Challenges of Multi-Layer Optical Networks," *IEICE Trans. Commun.*, vol. E90-B, pp. 1890–1902, August 2007.

[2] M. Ohtsu, K. Kobayashi, T. Kawazoe, S. Sangu, and T. Yatsui, "Nanophotonics: Design, Fabrication, and Operation of Nanometric Devices Using Optical Near Fields," *IEEE J. Sel. Top. Quantum Electron.*, vol. 8, pp. 839–862, 2002.

[3] M. Ohtsu, T. Kawazoe, T. Yatsui, and M. Naruse: "Nanophotonics: Application of Dressed Photons to Novel Photonic Devices, and Systems," *IEEE J. Sel. Top. Quantum Electron.*, vol. 14, pp. 1404–1417, 2008.

[4] H. Hori, "Electronic and Electromagnetic Properties in Nanometer Scales," in *Optical and Electronic Process of Nano-Matters*, M. Ohtsu, ed., Kluwer Academic, 2001, pp. 1–55.

[5] MONA consortium, *A European roadmap for photonics and nanotechnologies*, MONA (Merging Optics and Nanotechnologies Association) consortium, 2008.

[6] National Research Council, *Nanophotonics: Accessibility and Applicability*, National Academies Press, Washington, D.C. , 2008.

[7] T. Unold, K. Mueller, C. Lienau, T. Elsaesser, and A. D. Wieck, "Optical Control of Excitons in a Pair of Quantum Dots Coupled by the Dipole-Dipole Interaction," *Phys. Rev. Lett.*, vol. 94, pp. 137404 1–4, April 2005.

[8] T. A. Klar, T. Franzl, A. L. Rogach, and J. Feldmann, "Super-Efficient Exciton Funneling in Layer-by-Layer Semiconductor Nanocrystal Structures," *Adv. Matter.*, vol. 17, pp. 769–773, March 2005.

[9] M. Naruse, T. Miyazaki, F. Kubota, T. Kawazoe, K. Kobayashi, S. Sangu, and M. Ohtsu, "Nanometric summation architecture based on optical near-field interaction between quantum dots," *Opt. Lett.*, vol. 30, pp. 201–203, January 2005.

[10] M. Naruse, H. Hori, K. Kobayashi, and M. Ohtsu, "Tamper resistance in optical excitation transfer based on optical near-field interactions," *Opt. Lett.* vol. 32, pp. 1761–1763, June 2007.

[11] M. Naruse, T. Kawazoe, R. Ohta, W. Nomura, and M. Ohtsu, "Optimal mixture of randomly dispersed quantum dots for optical excitation transfer via optical near-field interactions," *Phys. Rev. B*, vol. 80, pp. 125325 1–7, September 2009.

[12] W. Nomura, T. Yatsui, T. Kawazoe, and M. Ohtsu, "The observation of dissipated optical energy transfer between CdSe quantum dots," *J. Nanophotonics*, vol. 1, pp .011591 1–7, November 2007.

[13] H. Harai, K. Fujikawa, V.P. Kafle, T. Miyazawa, M. Murata, M. Ohnishi, M. Ohta, and T. Umezawa, "Design Guidelines for New Generation Network Architecture," *IEICE Trans. Commun.*, vol. E93–B, no. 3, pp. 462–465, March 2010.

[14] S. Balasubramaniam, D. Botvich, J. Mineraud, W. Donnelly, N. Agoulmine, "BiRSM: bio-inspired resource self-management for all IP-networks," IEEE Network, vol. 24, no. 3, pp. 20–25, May-June 2010.

[15] A. S. Sadek, K. Nikolić, M. Forshaw, "Parallel information and computation with restitution for noise-tolerant nanoscale logic networks," Nanotechnology, vol. 15, no. 1, pp. 192–210, November 2003.

[16] M. Naruse, H. Hori, K. Kobayashi, P. Holmström, L. Thylén, and M. Ohtsu, "Lower bound of energy dissipation in optical excitation transfer via optical near-field interactions," Opt. Express, vol. 18, pp. A544–A553, October 2010.

[17] M. Gupta, S. Singh, "Greening the Internet," in Proc. of ACM SIGCOMM '03, Karlsruhe, Germany, August 2003.

[18] A. Qureshi, R. Weber, H. Balakrishnan, J. Guttag, and B. Maggs. "Cutting the electric bill for internet-scale systems," ACM SIGCOMM Comput. Commun. Rev., vol. 39, no. 4, August 2009.

Nanophotonic Hierarchical Hologram: Hierarchical information processing and nanometric data retrieval based on nanophotonics

Naoya Tate[a,b], Makoto Naruse[a,b,c], Takashi Yatsui[a,b], Tadashi Kawazoe[a,b], Morihisa Hoga[d], Yasuyuki Ohyagi[d], Tokuhiro Fukuyama[e], Yoko Sekine[d], Mitsuru Kitamura[d], and Motoichi Ohtsu[a,b]

[a] Department of Electrical Engineering and Information Systems, The University of Tokyo,
2-11-16 Yayoi, Bunkyo-ku, Tokyo, 113-8656, Japan;
[b] Nanophotonics Research Center, The University of Tokyo,
2-11-16 Yayoi, Bunkyo-ku, Tokyo, 113-8656, Japan;
[c] National Institute of Information and Communications Technology,
4-2-1 Nukuikita, Koganei, Tokyo, 184-8795 Japan;
[d] Dai Nippon Printing Co. Ltd., Research and Development Center,
250-1 Wakashiba, Kashiwa, Chiba, 277-0871 Japan;
[e] Dai Nippon Printing Co. Ltd., Corporate R&D Division,
1-1 Ichigaya-kagacho, Shinjuku-ku, Tokyo, 162-8001 Japan

ABSTRACT

A *nanophotonic hierarchical hologram* works in both optical far-fields and near-fields, the former being associated with conventional holographic images, and the latter being associated with the optical intensity distribution based on a nanometric structure that is accessible only via optical near-fields. In principle, a structural change occurring at the subwavelength scale does not affect the optical response functions, which are dominated by propagating light. Therefore, the visual aspect of the hologram is not affected by such a small structural change on the surface, and retrieval in both fields can be processed independently. We propose embedding a *nanophotonic code*, which is retrievable via optical near-field interactions involving nanometric structures, *within* an embossed hologram. Due to the one-dimensional grid structure of the hologram, evident polarization dependence appears in retrieving the code. Here we describe the basic concepts, numerical simulations, and experimental demonstrations of a prototype nanophotonic hierarchical hologram with a nanophotonic code and describe its optical characterization.

Keywords: Holography, Optical data processing, Nanostructure fabrication, Optical devices, Nanophotonics and photonic crystals

1. INTRODUCTION

Holography, which generates natural three-dimensional images, is one of the most common anti-counterfeiting techniques [1]. In the case of a volume hologram, the surface is ingeniously formed into microscopic periodic structures, which diffract incident light in specific directions. A number of diffracted light beams can form an arbitrary three-dimensional image. Generally, these microscopic structures are recognized as being difficult to duplicate, and therefore, holograms have been widely used in the anti-counterfeiting of bank notes, credit cards, etc. However, conventional anti-counterfeiting methods based on the physical appearance of holograms are less than 100% secure [2]. Although they provide ease of authentication, adding other security functions without degrading the appearance is quite difficult.

Here, we propose a *nanophotonic hierarchical hologram*, which is created by applying nanometric structural changes to the surface structure of a conventional hologram [3]. The physical scales of the nanometric structural changes and the elemental structures of the hologram are less than 100 nm and larger than 100 nm, respectively. In principle, a structural change occurring at the subwavelength scale does not affect the optical response functions, which are dominated by propagating light. Therefore, the visual aspect of the hologram is not affected by such a small structural change on the surface. Additional data can thus be written by engineering structural changes in the subwavelength regime so that they are only accessible via optical near-field interactions (we call such information retrieval *near-mode* retrieval) without

Practical Holography XXV: Materials and Applications, edited by Hans I. Bjelkhagen,
Proc. of SPIE Vol. 7957, 79570M · © 2011 SPIE · CCC code: 0277-786X/11/$18 · doi: 10.1117/12.873535

having any influence on the optical responses obtained via the conventional far-field light (what we call *far-mode* retrieval). By applying this hierarchy, new functions can be added to conventional holograms.

As such additional data for the near-mode retrieval, we propose embedding a *nanophotonic code*, which is physically a subwavelength-scale shape-engineered metal nanostructure, in a hierarchical hologram to implement a near-mode function [4]. The basic concept of the nanophotonic code and fabrication of a sample device are described. In particular, since our proposed approach is to embed a nanophotonic code *within* the patterns of the hologram, which is basically composed of one-dimensional grating structures, it yields clear polarization dependence compared with the case where it is not embedded within the hologram or arrayed structures.

In this paper, we numerically and experimentally demonstrate these features of a nanophotonic hierarchical hologram with an embedded nanophotonic code for hierarchical information retrieval. Section 2 describes the basic concept of our nanophotonic hierarchical hologram design and fabrication of the prototype device. Section 3 shows numerical characterizations, and Section 4 gives experimental results. Section 5 concludes the paper.

2. BASIC CONCEPT AND FABRICATION OF NANOPHOTONIC HIERARCHICAL HOLOGRAM WITH NANOPHOTONIC CODE

A nanophotonic hierarchical hologram can be created by adding a nanometric structural change to a conventional embossed hologram. Figure 1 shows the basic composition of the hierarchical hologram.

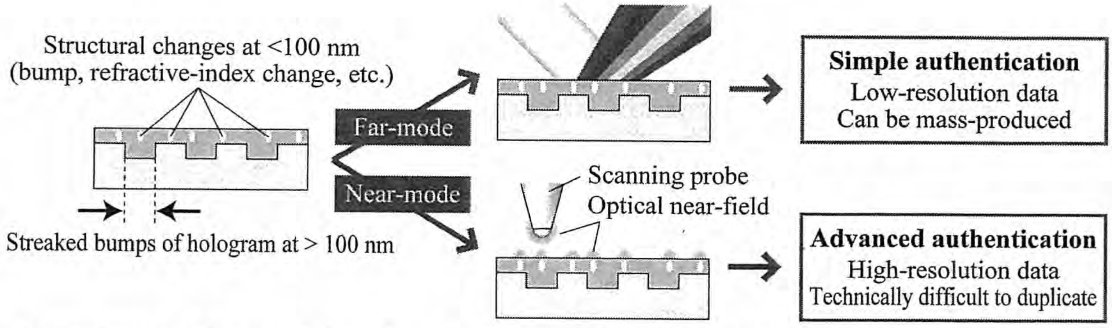

Figure 1. Basic concept of functional hierarchy of nanophotonic hierarchical hologram. In principle, no interference occurs between the two layers, the far-mode and the near-mode.

The physical scale of the nanometric structural changes is less than 100 nm, and that of the elemental structures of the hologram is larger than 100 nm. In principle, a structural change occurring at the subwavelength scale does not affect the optical response functions, which are dominated by propagating light. Therefore, the visual aspect of the hologram is not affected by such a small structural change on the surface. Additional data can thus be written by engineering structural changes in the subwavelength regime so that they are only accessible via optical near-field interactions, that is to say, with *near-mode* retrieval, without having any influence on the optical responses obtained via the conventional far-field light, or *far-mode* retrieval. By applying this hierarchy, new functions can be added to conventional holograms.

Our *nanophotonic code* is defined by induced optical near-fields for the near-mode retrieval, which are generated by irradiating a nanometric structure with light. An optical near-field is a non-propagating light field generated in a space extremely close to the surface of a nanometric structure [5]. Because the light distribution depends on several parameters of the structure and the retrieval setup, various types of coding can be considered. Moreover, several novel features of nanophotonics, such as energy transfer [6] and hierarchy [7], may be exploited.

As shown in Fig. 2, we created a sample device to experimentally demonstrate the retrieval of a nanophotonic code within an embossed hologram. The entire device structure, whose size was 15 mm × 20 mm, was fabricated by electron-beam lithography on a Si substrate, followed by sputtering a 50 nm-thick Au layer, as schematically shown in the cross-sectional profile in Fig. 2(b).

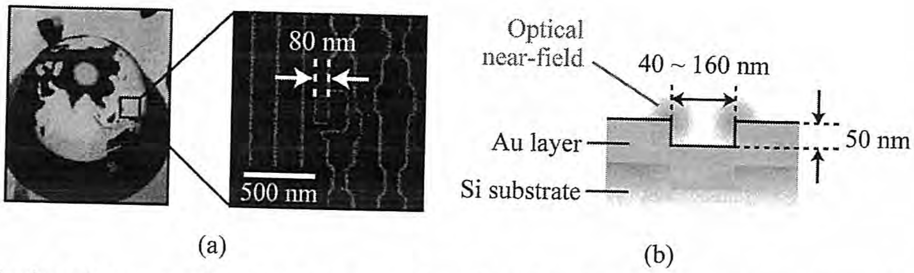

Figure 2. (a) Fabrication of a nanometric structure as a nanophotonic code within the embossed structure of Virtuagram®, and (b) schematic diagram of fabricated sample device.

As indicated in the left-hand side of Fig. 2(a), we can observe a three-dimensional image of the earth from the device. More specifically, our prototype device was essentially based on the design of *Virtuagram®*, developed by Dai Nippon Printing Co., Ltd., Japan, which is a high-definition computer-generated hologram composed of binary-level one-dimensional modulated gratings (see Fig. 2(a)). Within the device, we slightly modified the shape of the structure so that near-mode information is accessible only via optical near-field interactions. As shown in the right side of Fig. 2(a), nanometric structures with varying shapes, whose associated optical near-fields correspond to the near-mode information, were embedded in the original hologram structures as nanophotonic codes. The unit size of the nanophotonic codes ranged from 40 nm to 160 nm. No difference was evident in a comparison between the unprocessed hologram and the processed hologram. The compared results indicate the independence of the far-mode retrieval from nanometric fabrication of the hierarchical hologram.

Note that the original hologram was composed of arrays of one-dimensional grid structures, spanning the vertical direction. To embed the nanophotonic codes, the grid structures were partially modified in order to implement the nanophotonic codes. Nevertheless, the grid structures remained topologically continuously connected along the vertical direction. On the other hand, the nanophotonic codes were always isolated from the original grid structures. Those geometrical characteristics provide interesting polarization dependence, which is discussed in detail in Sections 3 and 4.

3. NUMERICAL EVALUATIONS

First, electric fields at the surface of nanometric structures were numerically calculated by a finite-difference time-domain (FDTD) method based on electromagnetic simulation with *Poynting for Optics*, a product of Fujitsu, Japan.

As shown in Figs. 3 and 4, two types of calculation models were created in order to examine polarization dependencies due to the existence of environmental structures when retrieving the nanophotonic code. The calculated layer was set 10 nm above the surface of the structures. The nanophotonic code was represented by a square-shaped Au structure with a side length of 150 nm and a depth of 100 nm, which is shown near the center in Figs. 2(a) and 3(a).

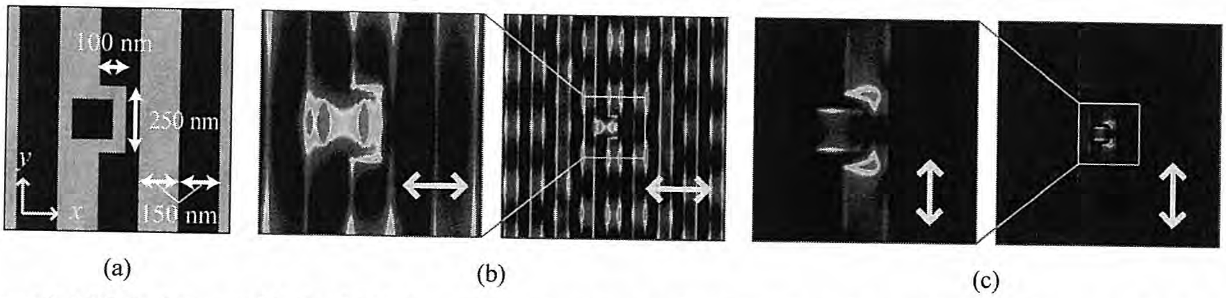

Figure 3. (a) Calculation model of embedded nanophotonic code with environmental structures and calculated intensity distribution of electric field produced by (b) x-polarized input light and (c) y-polarized input light.

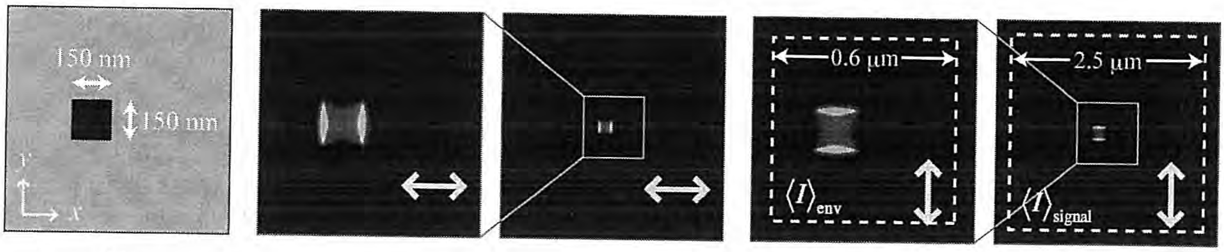

(a) (b) (c)

Figure 4. (a) Calculation model of isolated nanophotonic code and calculated intensity distribution of electric field produced by (b) x-polarized input light and (c) y-polarized input light. In (c), the definitions of average electric field intensities $\langle I \rangle_{\mathrm{signal}}$ and $\langle I \rangle_{\mathrm{env}}$ are indicated for quantitative evaluation

As shown in Fig. 3, the square-shaped structure was embedded in a periodic one-dimensional wire-grid structure, whose pitch was 150 nm, which models the typical structure of an embossed hologram. On the other hand, as shown in Fig. 4, the square-shaped structure, whose size was the same as that in Fig. 3(a), was not provided with any grid structure. By comparing those two cases, we can evaluate the effect of the environmental structures around the nanophotonic code. Also, we chose the square-shaped structure that is isotropic in both the x and y directions in order to clearly evaluate the effects of environmental structures and ignore the polarization dependency originating in the structure of the nanophotonic code itself. Periodic-conditioned computational boundaries were located 1.5 μm away from the center of the square-shaped structure. The wavelength was set to 785 nm.

Figures 3(b) and 3(c) and Figures 4(b) and 4(c) show the electric field intensity distribution on the surface of the structure assuming x-polarized and y-polarized input light irradiation, respectively. We then investigated how the environmental structures affected the electric fields in the vicinity of the nanophotonic code and the influence of the input light polarization. For these purposes, we first evaluated the average electric field intensity in the area of the nanophotonic code, denoted by $\langle I \rangle_{\mathrm{signal}}$, and that in the area including the surroundings, denoted by $\langle I \rangle_{\mathrm{env}}$. More specifically, $\langle I \rangle_{\mathrm{signal}}$ represents the average electric field intensity in the 0.6 μm × 0.6 μm area covering the nanophotonic code, whereas $\langle I \rangle_{\mathrm{env}}$ indicates that in the 2.5 μm × 2.5 μm area marked by the dashed squares in the left and right of Fig. 4(c), respectively. Figure 5(a) summarizes the calculated $\langle I \rangle_{\mathrm{signal}}$ and $\langle I \rangle_{\mathrm{env}}$, respectively shown by the red and blue bars.

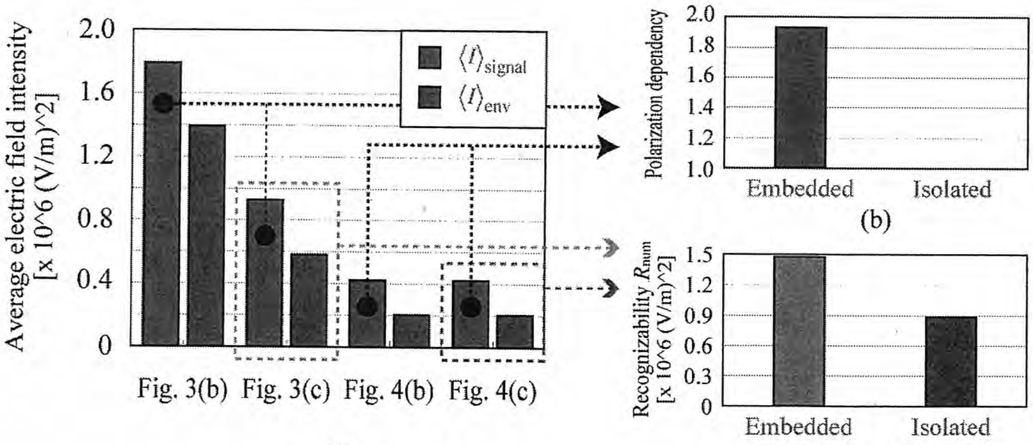

(a) (b) (c)

Figure 5. (a) Graphical representations of $\langle I \rangle_{\mathrm{signal}}$ and $\langle I \rangle_{\mathrm{env}}$ in each calculation model. (b) Numerical polarization dependency, expressed as the ratio of $\langle I \rangle_{\mathrm{signal}}$ with x-polarized input to that with y-polarized input light, for the embedded and isolated structures. Evident polarization dependency was exhibited in the case of a nanometric code embedded in environmental structures. (c) Numerical recognizability, R_{num}, in both types of models with y-polarized input light. The result indicates that the recognizability of the nanophotonic code was enhanced by embedding it in the environmental structure.

We first investigated the polarization dependencies. In the case of the nanophotonic code embedded in environmental periodic structures, evident polarization dependency was observed for both $\langle I \rangle_{\mathrm{signal}}$ and $\langle I \rangle_{\mathrm{env}}$. For example, $\langle I \rangle_{\mathrm{signal}}$ with x-

polarized input was about two times larger than $\langle I\rangle_{\mathrm{signal}}$ with y-polarized input light. On the other hand, the isolated nanophotonic code did not show any polarization dependency. Figure 5(b) compares the ratio of $\langle I\rangle_{\mathrm{signal}}$ with x-polarized input light to that with y-polarized input light for the embedded and isolated structures.

Second, from the viewpoint of facilitating recognition of the nanophotonic code embedded in the hologram, it is important to obtain a kind of higher *recognizability* for the signals associated with the nanophotonic codes. In order to evaluate such recognizability, here we define a figure-of-merit, R_{num}, as

$$R_{\mathrm{num}} = \frac{\langle I\rangle_{\mathrm{signal}}}{\langle I\rangle_{\mathrm{env}}} \times \langle I\rangle_{\mathrm{signal}}, \tag{1}$$

which yields a higher value with higher contrast with respect to $\langle I\rangle_{\mathrm{signal}}$ and $\langle I\rangle_{\mathrm{env}}$ (indicated by the term $\langle I\rangle_{\mathrm{signal}}/\langle I\rangle_{\mathrm{env}}$) and with higher signal intensity (indicated by $\langle I\rangle_{\mathrm{signal}}$). Figure 5(c) shows the calculated R_{num} in the case of y-polarized light input to the two types of models. The result indicates that the nanophotonic code embedded in the environmental structure is superior to that of the isolated code in terms of the recognizability defined by eq. (1).

We consider that such polarization dependency and recognizability of nanophotonic codes are based on the environmental grid structures that span along the vertical direction. The input light induces oscillating surface charge distributions due to the coupling between the light and electrons in the metal. In the present case, the y-polarized input light induces surface charges along the vertical grids; since the grid structure continuously exists along the y-direction, there is no chance for the charges to be concentrated. However, in the area of the embedded nanophotonic code, we can find structural discontinuity in the grid; this results in higher charge concentrations at the edges of the embedded nanophotonic code.

On the other hand, the x-polarized input light sees structural discontinuity along the horizontal direction due to the vertical grid structures, as well as in the areas of the nanophotonic codes. It turns out that charge concentrations occur not only in the edges of the nanophotonic codes but also at other horizontal edges of the environmental grid structures. In contrast to these nanophotonic codes embedded in holograms, for the isolated square-shaped nanophotonic codes, both x- and y-polarized input light beams have equal effects on the nanostructures.

These mechanisms indicate that such nanophotonic codes embedded in holograms could also exploit these polarization and structural dependences, not only for retrieving near-mode information via optical near-field interactions. For instance, we could facilitate near-mode information retrieval using suitable input light polarization and environmental structures.

4. EXPERIMENT

In the experimental demonstration, optical responses during near-mode observation were detected using a near-field optical microscope (NOM). A schematic diagram of the detecting setup is shown in Fig. 6(a), in which the NOM was operated in an illumination-collection mode with a near-field probe having a tip with a radius of curvature of 5 nm. The fiber probe was connected to a tuning fork. Its position was finely regulated by sensing a shear force with the tuning fork, which was fed back to a piezoelectric actuator. The observation distance between the tip of the probe and the sample device was set at less than 50 nm. The light source used was a laser diode (LD) with an operating wavelength of 785 nm, and scattered light was detected by a photomultiplier tube (PMT). A Glan–Thomson polarizer (extinction ratio 10^{-6}) selected only linearly polarized light as the radiation source, and a half-wave plate (HWP) rotated the polarization.

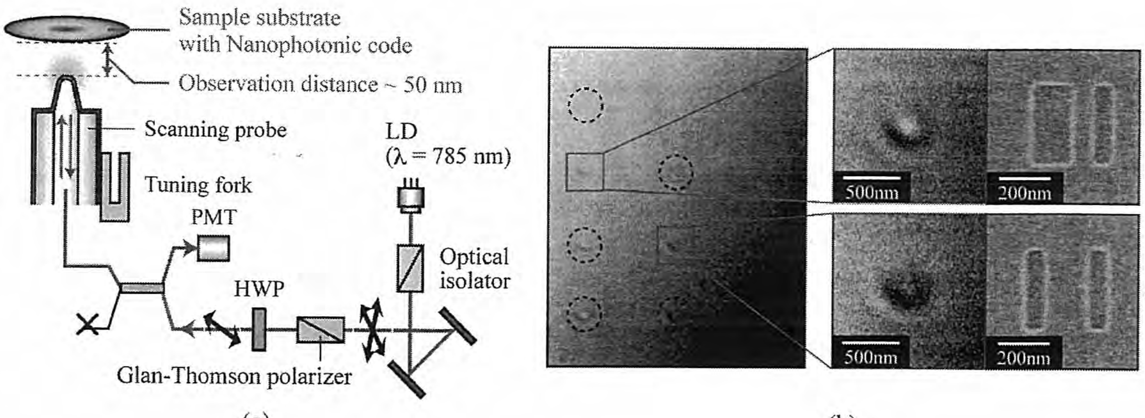

(a) (b)

Figure 6. (a) Schematic diagram of the experimental setup for retrieving a nanophotonic code, and (b) observed optical image showing basic retrieval results.

Figure 6(b) summarizes the experimental results obtained in retrieving nanophotonic codes which were *not* embedded in the hologram. In this demonstration, nanophotonic codes with different shapes were formed at the positions marked by the dashed circles in Fig. 6(b). For the first step of our demonstration, the device was irradiated with randomly polarized light by removing the polarizer from the experimental setup. Clear near-field optical distributions that depended on the structures of the nanophotonic codes were obtained.

Figures 7 (a) and (b) and Figures 7(c) and (d) show other retrieved results of nanophotonic codes that were embedded in the hologram and not embedded in the hologram, respectively, using a linearly polarized radiation source. Figures 7(a) and 7(b) respectively show observed NOM images of the nanophotonic code that was embedded in the hologram with a reference polarization (defined as 100-degree polarization) and 60-degree-rotated polarization. Also, Figs. 7(c) and 7(d) represent the NOM images of the nanophotonic code that was not embedded in the hologram. As is evident, in the case of the nanophotonic code embedded in the hologram, clear polarization dependence was observed; for example, from the area of the nanophotonic code located in the center, a high-contrast signal intensity distribution was obtained with polarizations around 80 degree.

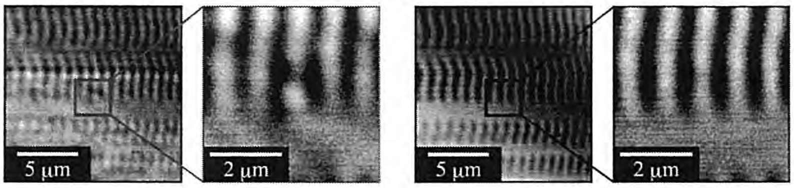

Reference (100 deg) 60 deg-rotated

(a) (b)

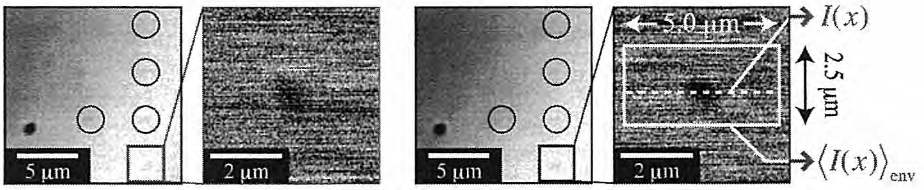

Reference (100 deg) 60 deg-rotated

(c) (d)

Figure 7. (a) Observed NOM images of optical intensity distributions of retrieved nanophotonic codes embedded in environmental structures with (a) reference polarization (100 deg) and (b) 60 deg-rotated polarization. Observed NOM images of optical intensity distributions of retrieved isolated nanophotonic codes with (c) reference polarization (100 deg) and (d) 60 deg-rotated polarization. (d) shows the definitions of $I(x)$ and $\langle I(x)\rangle_{\mathrm{env}}$ for numerical evaluation.

To quantitatively evaluate the polarization dependency of the embedded nanophotonic code, we investigated two kinds of intensity distribution profiles from the NOM images observed. One is a horizontal intensity profile along the dashed line in Fig. 7(d), which crosses the area of the nanophotonic code, denoted by $I(x)$, where x represents the horizontal position. The other was also an intensity distribution as a function of horizontal position x; however, at every position x, we evaluated the average intensity along the vertical direction within a range of 2.5 μm, denoted by $\langle I(x)\rangle_{\mathrm{env}}$, which indicates the environmental signal distribution. When a higher intensity is obtained selectively from the area of the nanophotonic code, the difference between $I(x)$ and $\langle I(x)\rangle_{\mathrm{env}}$ can be large. On the other hand, if the intensity distribution is uniform along the vertical direction, the difference between $I(x)$ and $\langle I(x)\rangle_{\mathrm{env}}$ should be small. Thus, the difference between $I(x)$ and $\langle I(x)\rangle_{\mathrm{env}}$ indicates the recognizability of the nanophotonic code. We define an experimental recognizability, R_{exp}, as

$$R_{\mathrm{exp}} = \sum_{x} \left| I(x) - \langle I(x)\rangle_{\mathrm{env}} \right| \tag{2}$$

Figures 8(a) and 8(b) show R_{exp} as a function of the input light polarization based on the observed NOM results for the embedded and isolated nanophotonic codes, respectively. The nanophotonic code embedded in the hologram exhibited much greater polarization dependency, as shown in Fig. 8(a), where the maximum R_{exp} was obtained at 80-degree input polarization, whereas only slight polarization dependency was observed with the isolated nanophotonic code, as shown in Fig. 8(b). Such polarization dependence in retrieving the nanophotonic code agrees well with the results of the simulations in Figs. 3 and 4.

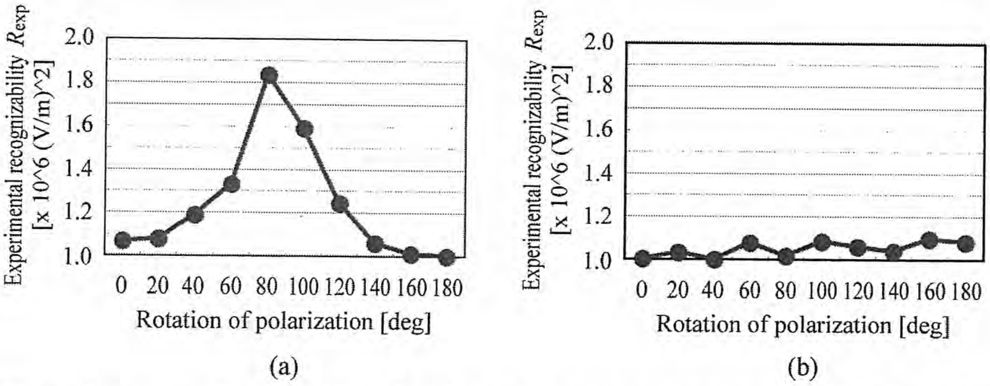

Figure 8. (a) Calculated experimental recognizability R_{exp} of embedded nanophotonic code and (b) that of isolated nanophotonic code. Evident recognizability and polarization dependency were exhibited.

5. SUMMARY

We described the basic concept of a nanophotonic hierarchical hologram and a nanophotonic code embedded in a hologram as an implementation of a nanophotonic hierarchical hologram, and we demonstrated its features by numerical simulations, experimental fabrication of prototype devices, and optical characterization. One of the most notable characteristics of our proposed approach is embedding a nanophotonic code within the patterns of a hologram composed of one-dimensional grating structures; it yields clear polarization dependence compared with an isolated nanophotonic code that is not embedded within a grid structure. These features were successfully demonstrated both numerically and experimentally. Also, because embedding and retrieval of a nanophotonic code requires highly advanced technical know-how, this approach can also improve the strength of anti-counterfeiting measures. Another major benefit is that we can fully utilize the existing industrial facilities and fabrication technologies that have been developed so far for conventional holograms, yet adding novel new functionalities to the hologram.

Our concept can be applied not only to a hologram but also to other media, such as lenses and jewelry. Adding extra functions creates value-added media with only a slight impact on the primary functions. However, a trade-off occurs between the nanometric fabrication conditions (e.g., size and pitch) and the impact on the primary functions. We are currently investigating these trade-offs for several types of media in actual use. Moreover, the number of layers can be increased in the near-mode observation to further extend the hierarchical function. An optical near-field interaction between multiple nanometric structures produces a characteristic spatial distribution depending on the size, the alignment, etc. Therefore, various optical signal patterns can be observed depending on the size of the fiber probe, and another layer can be added in the near-mode observation [7,10].

Our results indicated that the environmental structure provides interesting polarization dependency, and more interestingly, facilitates the retrieval of near-field information. In our future research, we may come to more deeply understand the relation between the retrieved optical intensity distributions and the design of the nanometric structures, including their environmental conditions. Such insights should allow us to propose, for instance, an optimized strategy for implementing nanophotonic codes or a strategy robust to errors that possibly occur in the fabrication and/or retrieval processes [8]. Moreover, a simpler method for retrieving the nanophotonic code is required, without using optical fiber probe tips [11]. We are currently investigating these aspects.

ACKNOWLEDGEMENT

This work was supported in part by a comprehensive program for personnel training and industry–academia collaboration based on projects funded by the New Energy and Industrial Technology Organization (NEDO), Japan, the Global Center of Excellence (G-COE) "Secure-Life Electronics" project, and Special Coordination Funds for Promoting Science and Technology sponsored by the Ministry of Education, Culture, Sports, Science and Technology (MEXT), Japan.

REFERENCES

[1] R. L. Van Renesse (ed), [Optical document scanning], Altech House Optoelectronics Library (1998).

[2] S. P. McGrew, "Hologram counterfeiting: problems and solutions," *Proc. SPIE, Optical Security and Anticounterfeiting Systems* **1210**, 66-76 (1990).

[3] N. Tate, W. Nomura, T. Yatsui, M. Naruse, and M. Ohtsu, "Hierarchical Hologram based on Optical Near- and Far-Field Responses," Optics Express **16**, 607-612 (2008).

[4] N. Tate, M. Naruse, T. Yatsui, T. Kawazoe, M. Hoga, Y. Ohyagi, T. Fukuyama, M. Kitamura, and M. Ohtsu, "Nanophotonic code embedded in embossed hologram for hierarchical information retrieval," Optics Express **18**, 7497-7505 (2010).

[5] M. Ohtsu, K. Kobayashi, T. Kawazoe, T. Yatsui, and M. Naruse (ed), [Principles of Nanophotonics], Taylor and Francis, Boca Raton (2008).

[6] M. Ohtsu, T. Kawazoe, T. Yatsui, and M. Naruse, "Single-photon emitter using excitation energy transfer between quantum dots," *IEEE J. Sel. Top. Quantum Electron.* **14**, 1404-1417 (2008).

[7] M. Naruse, T. Yatsui, W. Nomura, N. Hirose, and M. Ohtsu, "Hierarchy in optical near-fields and its application to memory retrieval," Optics Express **13**, 9265-9271 (2005).

[8] M. Naruse, H. Hori, K. Kobayashi, M. Ishikawa, K. Leibnitz, M. Murata, N. Tate, and M. Ohtsu, "Information theoretical analysis of hierarchical nano-optical systems in the subwavelength regime," J. Opt. Soc. Am. B **26**, 1772-1779 (2009).

[9] N. Tate, H. Tokoro, K. Takeda, W. Nomura, T. Yatsui, T. Kawazoe, M. Naruse, S.-I. Ohkoshi and M. Ohtsu, "Transcription of optical near-fields by photoinduced structural change in single crystal metal complexes for parallel nanophotonic processing," Appl. Phys. B: Lasers and Optics **98**, 685-689 (2010).

[10] M. Naruse, T. Inoue, and H. Hori, "Analysis and Synthesis of Hierarchy in Optical Near-Field Interactions at the Nanoscale Based on Angular Spectrum," Jpn. J. Appl. Phys. **46**, 6095-6103 (2007).

[11] N. Tate, W. Nomura, T. Yatsui, M. Naruse, and M. Ohtsu, "Hierarchy in optical near-fields based on compositions of nanomaterials," Appl. Phys. B: Lasers and Optics **96**, 1-4 (2009).

Investigation of Phonon-assisted Optical Near-Field Effect on Nanostructured TiO_2 Thin Film

Thu. H. H. Le[1*], Kazuma Mawatari[1], Kokoro Kitamura[2], Takashi Yatsui[2], Tadashi Kawazoe[2]
Motoichi Ohtsu[2], Takehiko Kitamori[1]
[1]*Department of Applied Chemistry, the University of Tokyo, JAPAN and*
[2] *Department of Electrical Engineering and Information Systems, the University of Tokyo, JAPAN*

In this study, we investigated a novel process to excite TiO_2 using sub-bandgap photon via the phonon-assisted optical near-field(ONF). Recently it has been reported by Ohtsu et al. that the optical near-field generated at nanomeric materials allows the excitation of dipole forbidden phonon states, coincident with the excitation of electronic levels, which is called as non-adiabatic process. This process has been confirmed to be able to excite electrons with sub-bandgap photons in many material systems. For the nanostructure of materials plays an important role in the generation of ONF, we introduced nano-structured TiO_2 thin film with different grain sizes by CVD method. TiO_2 thin film was grown directly onto FTO substrate by CVD method with the thickness of 1.0, 0.5, 0.3, 0.1 μm, respectively. The size and the protrusion of TiO_2 grains were controlled by the film thickness. The SEM images showed that the thicker film has larger grains of TiO_2. The photocatalytic activity of TiO_2 thin films under UV and visible laser (488nm) irradiation were investigated by PEC measurement in 0.5M $NaClO_4$ buffered with phosphate buffer (pH=7.4). Compared with UV irradiation, under visible irradiation, the more significant differences between samples with different grain sizes, have been observed. For example, the 1μm-thick sample showed a double higher IPCE under UV irradiation, while a 3 times higher IPCE under 488nm irradiation, compared with the 100nm-thick sample. From these results, we suggest that for all samples, the observed visible photo response is the combination of surface defects effect and the phonon-assisted optical near-field effect. And it is likely that the larger protrusion structure the surface possesses, the larger the visible response could be obtained. Towards improving the effect of ONF, the growth of TiO_2 nanorod with sufficient size by the so-called GLAD (Glancing Angle Deposition) method and the PEC evalution are under investigation.

SUBJECT AREA: (5) Physical, Theoretical & Computational **SYMPOSIA:** (171) The Nanostructure-Enhanced Photochemical Reactions

Presenter Details **PRESENTER PERSON INFORMATION:** Kazuma Mawatari, Hongo 7-3-1, Bunkyo-ku, Tokyo, Japan, 113-8656

PRESENTER (E-MAIL ONLY): kmawatari@icl.t.u-tokyo.ac.jp

TITLE: Development of local surface-modification method for fluidic control in extended-nano space using nanopillar and optical near-field

AUTHORS (LAST NAME, FIRST NAME): Mawatari, Kazuma [1]; Hasumoto, Naosuke [1]; Kitamura, Kokoro [2]; Yatsui, Takashi [2]; Kawazoe, Tadashi [2]; Ohtsu, Motoichi [2]; Kitamori, Takehiko [1]

INSTITUTIONS (ALL): 1. Department of Applied Chemistry, Graduate School of Enginnering, The University of Tokyo, Tokyo, Japan.

2. Department of Electrical Engineering and Information Systems, Graduate School of Enginnering, The University of Tokyo, Tokyo, Japan.

ABSTRACT BODY: Integration of various and complex chemical processes on a microfluidic chip was realized by our basic technique for general micro-integration: micro unit operations (MUOs) and continuous flow chemical processing (CFCP). The high performances have been demonstrated in analysis, diagnosis and synthetic systems. In order to support the concept, multiphase parallel flow is important fluidic control method to form complex chemical networks. Recently, our focus has been centered on an even smaller space, extended-nano space (10-1000 nm). In this space, we found unique physicochemical water properties such as higher viscosity and higher proton mobility than those in microspace. The new chemical operations utilizing these unique properties are expected which leads to novel functional devices. Similar to microspace, multiphase parallel flow is also key method to realize complex chemical processes in extended-nano space. Extended-nano space has extremely high surface-to-volume ratio, and surface properties (hydrophilic/hydrophobic) affect the stabilization of multiphase parallel flow. Therefore, partial surface modification is important methodology. So far, there were several methods for partial surface modification: light, electron beam, SPM. Especially, optical method is essential for closed extended-nano space. However, partial surface modification with spatial resolution less than optical diffraction limit (~500 nm) is usually difficult and conventional optical method cannot be applied to the extended-nano space. Then, I focus on optical near-field. As the optical near-field is nanometer-scale light formed around the nano-object and behave as high energy photon (exciton-phonon polariton). By combining the near-filed light and nanostructure in extended-nano space, the partial surface modification smaller than diffraction limit is expected. In this research, we developed a new method for partial surface modification in extended-nano channel. Photocatalytic reaction of TiO_2 by optical near-field visible light was induced to partially remove the octadecyltrimethoxysilane (ODS) on

TiO_2/glass nanopillar surface. The nanostrucuture made the photochemical reaction by visible light (488nm). The experimental results for the principle verification will be presented.

MEET5 - 1
Invited

Increased Spatial Homogeneity in a Light-Emitting InGaN Thin Film Using a Phonon-Assisted Optical Near-Field Process

Takashi Yatsui*,** **and Motoichi Ohtsu***,**

* School of Engineering, The University of Tokyo, Bunkyo-ku, Tokyo, 113-8656 Japan
** Nanophotonic Research Center, Graduate school of Engineering, The University of Tokyo, Bunkyo-ku, Tokyo 113-8656, Japan

ABSTRACT

We report a self-assembly method that produces greater spatial uniformity in InGaN thin films using optical near-field desorption. Spatial homogeneity in the In fraction was reduced by introducing additional light during the photo-enhanced chemical vapour deposition of InGaN.

1. INTRODUCTION

The control of light-emitting-diode (LED) colour is important in many applications, including the generation of white light [1] and in optical communications [2]. The photon energy, $h\nu_{em}$, emitted from a composite semiconductor can be tailored by adjusting its composition. White light-emitting diodes (WLEDs) were developed using gallium nitride (GaN)-based LEDs because the $h\nu_{em}$, from GaN can be shifted from 400 nm to 1.5 µm by adjusting the indium (In) content in $In_xGa_{1-x}N$ from x = 0 to 1, respectively [1,3]. Although some commercial WLEDs combine the emission of three coloured LEDs, the resulting colour-rendering index over a broad spectrum is low due to the low spatial uniformity of In. As a result, this type of WLED has yet to replace fluorescent lamps in many applications. Here we report a self-assembly method that yields greater spatial uniformity of In in InGaN thin film using optical near-field desorption. The spatial heterogeneity of the In fraction was reduced by introducing an additional light source (*i.e.*, a desorption light source) during the photo-enhanced chemical vapour deposition (PECVD) of InGaN thereby causing near-field desorption of InGaN nanoparticles. The degree of nanoparticle desorption depended on In content of the film, and the photon energy of the desorption light source ultimately determined the emitted photon energy of the thin film [4].

2. CONTROLLING THE THIN FILM COMPOSITION USING THE OPTICAL NEAR-FIELD

Figures 1(a) and 1(b) illustrate the approach to obtaining a more spatially uniform device composition using optical near-field effects. During the initial stages of $In_{x1}Ga_{1-x1}N$ nanoparticle growth (bandgap energy E_{x1}), a lattice vibrational mode can be excited by far-field light originating from an optical near field caused by coupling of exciton-polaritons and phonons (Fig. 1(a)) [5]. If the nanoparticles are concurrently illuminated by a desorption source with photon energy of $h\nu_{x2}$ ($< E_{x1}$), a strong optical absorption due to a multistep excitation of lattice vibrational modes induces desorption of a fraction of the nanoparticle population [6]. The absorption is enhanced by increasing the In content. As the deposition proceeds with desorption source illumination, the growth is governed by a trade-off between In deposition (where the In content $x < x_1$) and In desorption (where $x > x_1$). Thus, the resulting In content in the film is a function of $h\nu_{x2}$, and both spatial heterogeneity of the In fraction and spectral broadening (Fig. 1b) are avoided.

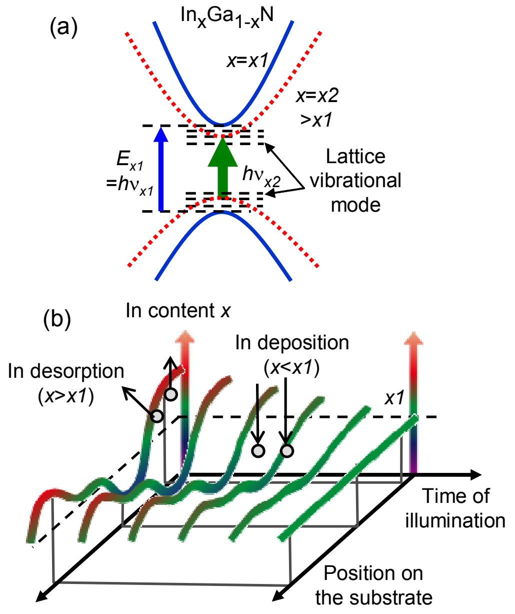

Fig. 1
Controlling the thin film composition using the optical near field. (a) A schematic diagram shows the energy dispersion and the generation of lattice vibrational modes induced by an optical near field on InGaN nanoparticles. (b) Spatial distributions of x are shown as a function of deposition time for $In_xGa_{1-x}N$ whilst illuminated with the desorption light source.

3. EXPERIMENT

A spectral change was observed upon introduction of the desorption light source during PECVD of InGaN at room temperature [7] in which $h\nu_{em}$ was determined by the photon energy $h\nu_{x2}$. A 5th-harmonic, Q-switched Nd:YAG laser ($h\nu_{depo}$ = 5.82 eV, λ = 213 nm) was used to excite and photodissociate trimethylgallium (TMG), triethylindium (TEI) and ammonia (NH_3, 99.999 %). The choice of laser was based on the strong photo-absorptions of gas-phase TMG ($E_g > 4.59$ eV), TEI ($E_g > 4.77$ eV) and NH_3 ($E_g > 5.66$ eV), respectively [8,9]. The desorption light source was introduced through an optical window, and H_2 gas was introduced around the window to prevent GaN deposition onto the window. The substrate was placed at the centre of the reaction chamber and irradiated with a 2-mm spot size of excitation light. The total pressure in the reaction chamber was 5.4 Torr, and the deposition time was 60 min.

4. RESULTS AND DISCUSSION

The morphology of the GaN sample was investigated with a scanning electron microscope (SEM). Figures 2(a) through 2(c) show magnified SEM images. Similar morphologies, consisting of 100-nm lines, were observed at different TEI flow rates, r_{TEI}. The relative atomic compositions of indium, gallium and nitrogen were obtained by monitoring photoluminescence (PL) induced by a continuous wave He–Cd laser (3.81 eV, $\lambda = 325$ nm), in which the PL peak was shifted by changing r_{TEI} (Fig. 2(d)). The In content, x, was determined according to

$$E = 3.42\text{-}4.95\,x, \qquad (1)$$

where E refers to the PL peak energy [10]. Figure 2(e) shows that x was a linear function of r_{TEI}, which agrees with results obtained using low-temperature metal-organic chemical vapour deposition (MOCVD) [11].

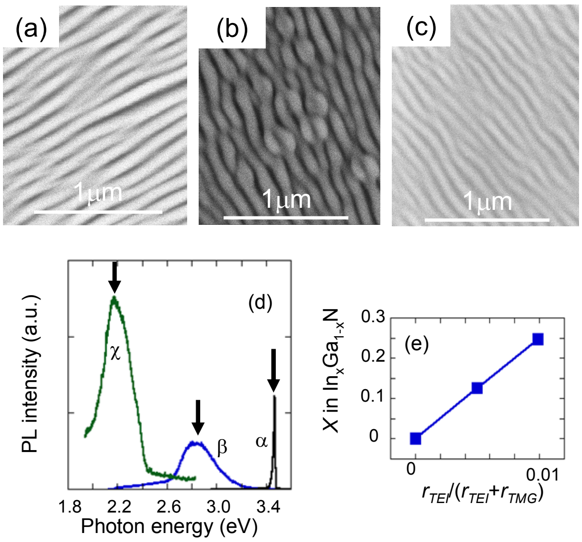

Fig.2

Magnified images show films fabricated with $r_{TEI} = 0$ (a), 2.5×10^{-3}(b), 5.0×10^{-3} (c) sccm. Spectral control by adjusting the TEI flow rate, r_{TEI}, at room temperature. (d) PL spectra obtained at 5 K were acquired following room-temperature film deposition with $r_{TEI} = 0$ (α), 2.5×10^{-3} (β), 5.0×10^{-3} (χ) sccm with $r_{TMG} = 0.5$ sccm. (e) The indium content of InGaN is shown as a function, r_{TEI}. Spectral control by adjusting the TEI flow rate, r_{TEI}, at room temperature.

Based on the above results, a spectral shift was induced by introducing desorption light during PECVD. InGaN was grown with $r_{TEI} = 2.5 \times 10^{-3}$ sccm and under illumination with a desorption light source of $h\nu_{x2} = 2.71$ eV. As shown in Fig. 3(a), the PL intensity in the region $h\nu_{em} < h\nu_{x2}$ (curve X') decreased relative to that observed in the absence of desorption light (curve X). The difference in PL intensity, I_{diff}, between X and X' (Fig. 3(b)) clearly shows the decrease in the PL intensity of X' at energies less than $h\nu_{x2}$, indicating near-field desorption as described in Fig. 1(a). Using a desorption light source with $h\nu_{x2} = 2.33$ eV, which is lower in energy than the peak PL of deposited InGaN (2.5 eV) in the absence of desorption light, similar decreases in PL intensity were observed for $r_{TEI} = 2.5 \times 10^{-3}$ sccm and $r_{TEI} = 5.0 \times 10^{-3}$ sccm (curves Y' and Z' in Fig. 3(c), respectively). The difference in PL between Y and Y', and Z and Z, as indicated by curves Y" and Z" in Fig. 3(d), respectively, shows that the PL intensity of both Y' and Z' decreased at energies below $h\nu_{x2} = 2.33$ eV. In addition, Fig. 3(d) shows that higher levels of r_{TEI} (curve Z") resulted in increased I_{diff} values at $h\nu_{x2} > 2.33$ eV relative to those obtained at lower r_{TEI} (curve Y"). This further indicates In desorption. This result confirms that the use

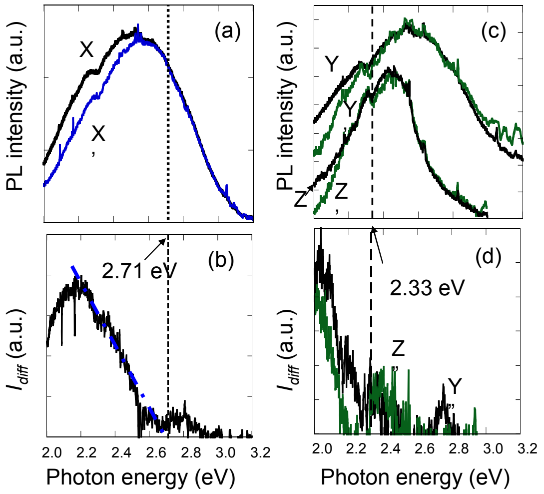

Fig. 3

Spectral changes induced by desorption light illumination at 2.71 eV during PECVD. (a) PL spectra were obtained at 5 K using room-temperature PECVD with $r_{TEI} = 2.5 \times 10^{-3}$ (curves X and X') and a desorption source energy of $h\nu_{x2} = 2.71$ eV. (b) The difference spectrum is shown for X – X'.

Spectral changes induced by desorption light illumination at 2.33 eV during PECVD. (c) PL spectra were obtained at 5 K using room-temperature PECVD with $r_{TEI} = 2.5 \times 10^{-3}$ (curves Y and Y') and $5.0 \text{ x } 10^{-3}$ (curves Z and Z') sccm and a desorption source energy of $h\nu_{x2} = 2.33$ eV. (d) The PL difference spectra are shown for Y – Y' (curve Y") and Z – Z' (curve Z").

of the desorption light source during film deposition did not permit additional In doping other than that determined by the photon energy of the desorption light source itself. This effect resulted in a film with a more spatially uniform In content.

5. CONCLUSION

Since the deposition method described herein is based on a photo-desorption reaction, it can be applied with other deposition techniques, such as MOCVD [1], molecular beam epitaxy [12] and pulsed-laser depositions [13], and can also be applied with other compound semiconductors such as InGaAs [14].

6. ACKNOWLEDGEMENT

The authors gratefully acknowledge Drs S. Yamazaki and T. Kawazoe (University of Tokyo), K. Ito, H. Kawamura (Nitto Optical Co., Ltd.), and Dr. M. Mizumura (V-Technology Co., Ltd.), for their help in the experiment and their useful discussions.

REFERENCES

[1] S. Nakamura, Science **281**, 956 (1998).
[2] K. J. Vahala, Nature **424**, 839 (2003).
[3] S. Nizamoglu, T. Ozel, E. Sari, H. V. Demir, Nanotech. **18**, 065709 (2007).
[4] T. Yatsui S. Yamazaki, K. Ito, H. Kawamura, M. Mizumura, T. Kawazoe, and M. Ohtsu, Appl. Phys. B, **97**, 375 (2009)
[5] T. Kawazoe, K. Kobayashi, S. Takubo, M. Ohtsu, J. Chem. Phys. **122**, 024715 (2005).
[6] T. Yatsui, W. Nomura, M. Ohtsu, Nano Lett. **5**, 2548 (2005).
[7] S. Yamazaki, T. Yatsui, M. Ohtsu, Appl. Phys. Exp. **1**, 061102 (2008).
[8] H. Okabe, M.K. Emadi-Babaki, V.R. McCrary, J. Appl. Phys. **69**, 1730 (1991).
[9] K. Watanabe, J. Chem. Phys. **22**, 1564 (1954).
[10] M.D. McCluskey, C.G. Van de Walle, C.P. Master, L.T. Romano, N.M. Johnson, Appl. Phys. Lett. **72**, 2725 (1998).
[11] A. Koukitu and H. Seki, Jpn. J. Appl. Phys. **35**, L1638 (1996).
[12] R. Singh, D. Doppalapudi, T.D. Moustakas, L.T. Romano, Appl. Phys. Lett. **70**, 1089 (1997).
[13] A. Kobayashi, J. Ohta, H. Fujioka, J. Appl. Phys. **99**, 123513 (2006).
[14] K. Akahane, N. Ohtani, Y. Okada, M. Kawabe, J. Cryst. Growth **245**, 31 (2002).

Nanophotonics: Dressed photon science and technology

M. Ohtsu
Dept. Electrical Eng. and Information Systems, the University of Tokyo
2-11-16 Yayoi, Bunkyo-ku ,Tokyo 113-8656, Japan
Email: ohtsu@ee.t.u-tokyo.ac.jp

This presentation reviews the recent progress of *nanophotonics*, which was proposed by the author in the year 1993[1,2]. The key is to utilize optical near-fields in order to realize novel nanometric device operation, fabrication, and energy conversion, etc., by the control of an intrinsic interaction between nanometer-sized materials. The nature of optical near-fields was studied by regarding the optical near-field as an electromagnetic field that mediates the interaction between nanometric materials. As a result, the physically intuitive concept of a *dressed photon* was established to describe optical near-fields, *i.e.*, the interaction between nanometric materials is mediated by exchanging dressed photons. The principles of device operation are reviewed considering the excitation energy transfer via the optical near-field interaction and subsequent relaxation. The operations of logic gates, an optical nano-fountain, a nano-coupler, a pulse generator, a phonon-assisted light emitter, etc. are described as well as their single photon emission and extremely low power consumption capability. Experimental results using quantum dos at the room temperature are described. Using a systems-perspective approach, the principles of content-addressable memory for optical router, a multilayer memory retrieval system, etc. are demonstrated.

This presentation also reviews nanophotonic fabrications based on phonon-assisted processes triggered by optical-near-field interactions. These processes represent *qualitative* innovation in photochemical vapor deposition and photolithography, suggesting that large, expensive ultraviolet light sources are no longer required, although they are indispensable for conventional adiabatic methods. A prototype of the commercial lithography system has been produced in collaboration with industry, and has been used for fabricating a diffraction grating and a Fresnel zone plate for the soft X-ray. Furthermore, phonon-assisted photochemical etching and sputtering were developed for realizing ultra-flat surfaces of glass and polycrystalline ceramics, respectively, in a self-organized manner. Phonon-assisted deposition will be also reviewed in order to increasing spatial homogeneity of the mol fractional ratio of In in a light emitting InGaN film.

References

[1]M. Ohtsu and K. Kobayashi, *Optical Near Fields*, Springer Verlag, Berlin, 2004.
[2]M. Ohtsu, et al., *Principles of Nanophotonics*, Tayler & Francis, London, 2008.

INVESTIGATION OF PHONON-ASSISTED OPTICAL NEAR-FIELD EXCITATION ON NANOSTRUCTURED TiO_2 TOWARDS ON-CHIP FUEL CELL APPLICATION

Thu. H. H. Le[1*], Kazuma Mawatari[1], Kokoro Kitamura[2], Takashi Yatsui[2], Tadashi Kawazoe [2] and Motoichi Ohtsu[2], Takehiko Kitamori[1]

[1]*Department of Applied Chemistry, the University of Tokyo, JAPAN and*
[2] *Department of Electrical Engineering and Information Systems, the University of Tokyo, JAPAN*

ABSTRACT

We report herein the investigation of a novel non-adiabatic optical near-field (ONF) excitation on nanostructured TiO_2 photo-anode. The usage of ONF allows the transition to the dipole forbidden phonon states, which is called the phonon-assisted ONF transition, and hence allows us to excite TiO_2 by sub-bandgap photon. Here, we investigated the usage of ONF to induce the photocatalytic activity of TiO_2 with visible light instead of conventional UV light. By introducing nanostructure into TiO_2 photo-anode to generate optical near-field at the surface of electrode, we confirmed the enhancement of photo current in the visible range, and this current is attributed to the phonon-assisted ONF excitation. This study should lead to a novel approach to excite TiO_2 by sub-bandgap photon, consequently improve its visible-light response photocatalytic performance. It also suggest that this kind of nanostructured semiconductor photocatalyst have promising properties for hydrogen production from water splitting.

KEYWORDS: Nanostructured titaninum dioxide, visible-light response photocatalyst, optical near-field(ONF), phonon-assisted excitation, overall water splitting.

INTRODUCTION

Over the past decades, due to the increasing need for clean energy, significant effort has been made to investigate semiconductor photocatalysts such as TiO_2, ZnO, and WO_3 that can efficiently produce hydrogen from water splitting. Yet the large bandgaps of those materials and the lack of absorption in visible range of solar spectrum is the major limitation so far. To overcome this, there have been approaches to manipulate the bandgaps of metal oxides by doping both transition metals as well as nitrogen, or carbon. The doping enhances the visible absorption whereas it makes recombination centers for photogenerated holes and electrons that conversely reduce the photocatalytic performance[1-2]. The visible-light response photocatalyst still remains a big issue. In this study, we report a novel approach to excite TiO_2 with visible light by using optical near-field without changing the electronic band structure of material. Thus unlike in the case of doping, it is expected to hav1e no influence on the photocatalytic performance of TiO_2.

Recently it has been reported by Ohtsu et al. that the optical near-field generated at nanomeric surface of material allows the transition of electric dipole forbidden states, together with the conventional excitation of electronic levels. This novel excitation has been confirmed to be able to excite the carriers by sub-bandgap photons in many kinds of materials and has already been applied in the development of novel photochemical vapor deposition [3], photolithography [4], self-organized photochemical etching [5], etc. Herein, we studied for the first time the usage of this novel property of optical near-field to excite photocatalyst TiO_2 by visible light. Besides, the enhancement of proton conductivity in nanochannels suggested us the usage of nanochannel-array as a novel class of proton exchange membrane for micro fuel cell application[6]. In the future, taking the advantages of these two effects, we are also simultaneously developing the integration of the investigated visible-light response photocatalyst into micro device and realizing the overall water splitting reactor and fuel cell in micro/nanofluidic device.

CONCEPT

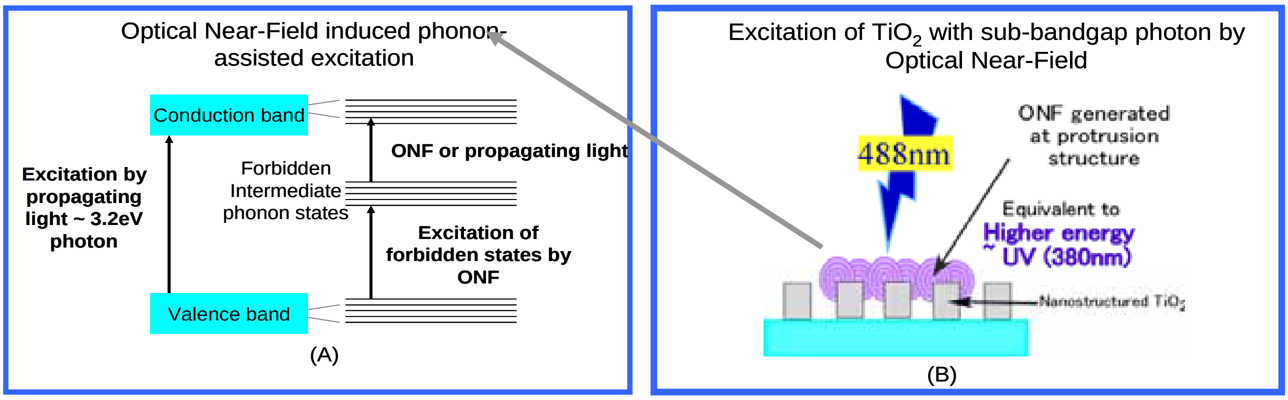

Fig 1. (A) Schematic diagram of ONF-induced phonon-assisted excitation (B) In case of TiO_2

Fig. 1 shows the schematic diagram of the excitation of titanium dioxide with sub-bandgap photon by two-step phonon-assisted process. The first step is the excitation of electrons from valence band to intermediate phonon states by optical near-field. The intermediate phonon states exist in the bandgap are dipole-forbidden levels that can not be excited by conventional propagating light, and hence optical near-field is indispensable for the transition to such levels. In the second step, electrons can be excited from phonon states to conduction band by both optical near-field and propagating light, since this is a dipole-allowed transition[3]. We have studied this multi-step phonon assisted excitation on TiO_2 thin film by introducing nanostructures into TiO_2 film and evaluating the visible light response of TiO_2 thin film in photocatalytic water splitting reaction based on photo electro chemical (PEC) cell.

EXPERIMENTAL

Since the nanostructure and morphology of materials play important roles in the generation of ONF, especially the protrusion surface structure[3], we introduced nanostructures into TiO_2 thin film by both (1)Top-down and (2) bottom-up approach. For the top-down method, the nano-pillar pattern was fabricated onto quartz substrate by EB lithography and dry etching process. We have reached the limitation of pillar sizes as 200nm, and pitch between pillars and depth as 200nm and 300nm. Two layers of Ti (50nm) (conducting layer) and TiO_2 (100nm) were deposited onto the quartz substrate to form a TiO_2 electrode. For the bottom-up approach, TiO_2 thin films were grown directly onto transparent conducting substrate SnO_2:F by CVD method with the thickness of 1.0, 0.5, 0.3, 0.1 μm, respectively. The morphology of films were controlled by film thickness. The morphology and the surface average roughness(Ra) of the films were characterized by scanning electron microscope (SEM) and atomic force microscope (AFM). The photocatalytic performance of TiO_2 photo anode was evaluated by PEC measurement with a 3-electrode cell setup, as shown in Fig. 2A. For comparison, the photo anode were irradiated by UV (SP-9 Spot Cure UV source) and 488nm laser. The electrolyte used in all measurement was 0.5M $NaClO_4$. A bias voltage of 0.5V vs Ag/AgCl was applied to all measurements.

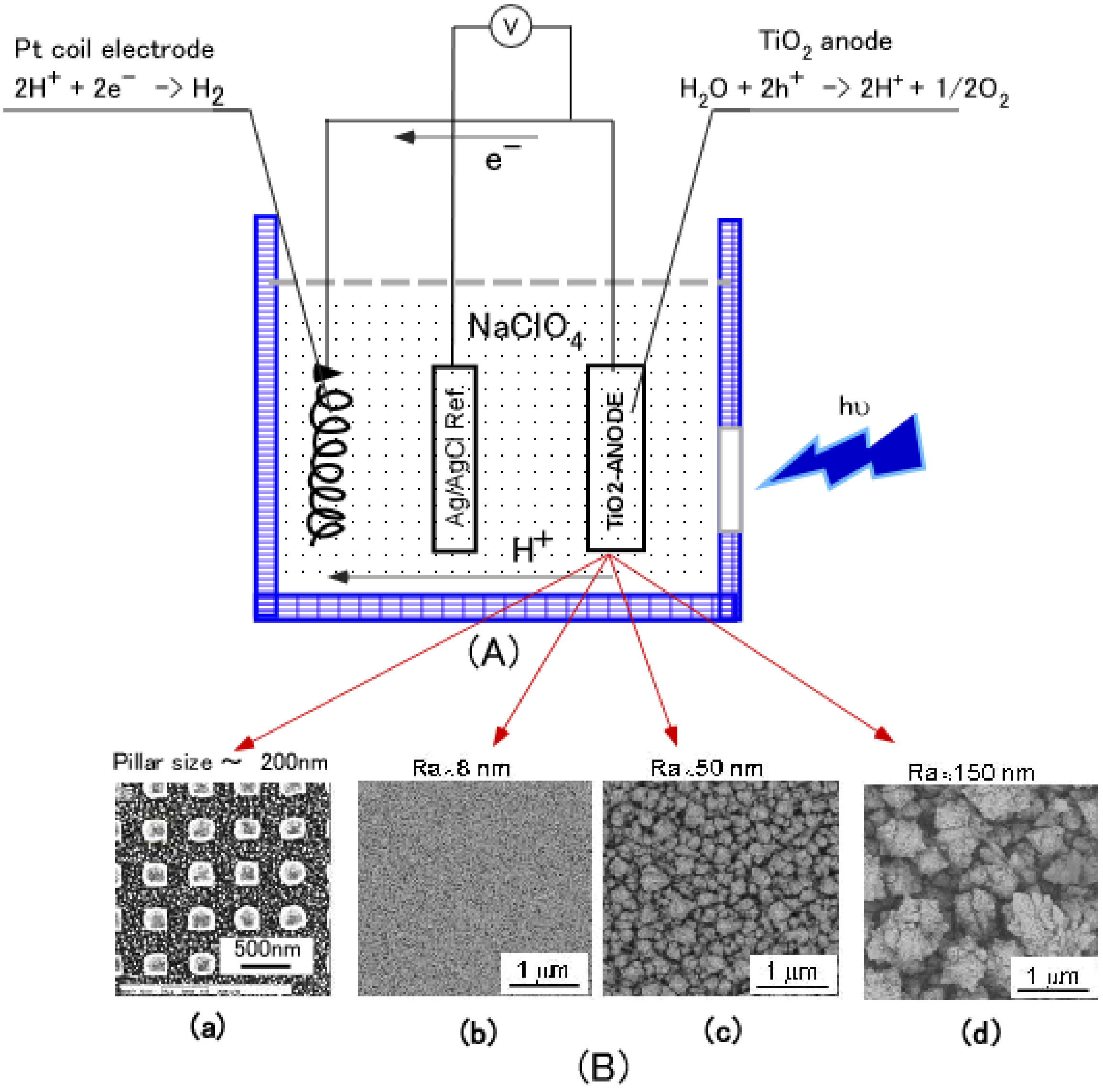

Fig. 2 (A) PEC cell set up (B) SEM images of (a) nano-pillar and thickness (b) 0.1 μm, (c) 0.5 μm, (d) 1.0 μm CVD samples respectively

RESULTS AND DISCUSSION

Fig. 2B shows the SEM images of nano-pillar samples and CVD samples. In case of CVD samples, the thicker film shows the larger grain size and protrusion structure that promise a better ONF effect.

The X-ray diffraction (XRD) spectra show that, TiO_2 thin film in nano-pillar sample was a mixed phases of rutile and anatase at the ratio 5:1, while the film deposited by CVD showed all anatase crystal phase.

For nano-pillar samples, under both UV and visible irradiation, there was no significant difference in photo-response current between nano-pillar fabricated and non-fabricated film. This result suggested that the nano-scale of nano-pillar was not sufficient to generate optical near-field and consequently not able to contribute the effect large enough to be observed in our measurement. However, we could not introduce the finer nanostructure by this top-down method. The visible response of both patterned and non-patterned samples can be attributed to the absorption of surface defects such as oxygen vacancies.

Fig. 3 shows the UV and 488nm photo response of CVD samples. Under UV irradiation, the TiO_2 films with the larger grains showed the larger photo currents due to the enhancement of specific surface area(Fig. 3A), while under visible irradiation, the more significant difference between samples with different surface roughness has been observed. For example, the 1μm-thick sample showed a double higher Incident-photon-to-current conversion efficiency (IPCE) under UV irradiation, while a 3 times higher IPCE under 488nm irradiation, compared with the 100nm-thick sample. This enhancement could be attributed to the optical near-field nonadiabatic multi-step excitation process.

The investigation to separate the photo response current derived from absorption of surface defect and optical near-field effect is undergoing. Besides, towards the improvement of optical near-field generation, the Glancing Angle Deposition (GLAD) sputtering method is being introduced to control the fine TiO_2 nanorod structure with optimized size, and the size dependence of the optical near-field effect is under investigation.

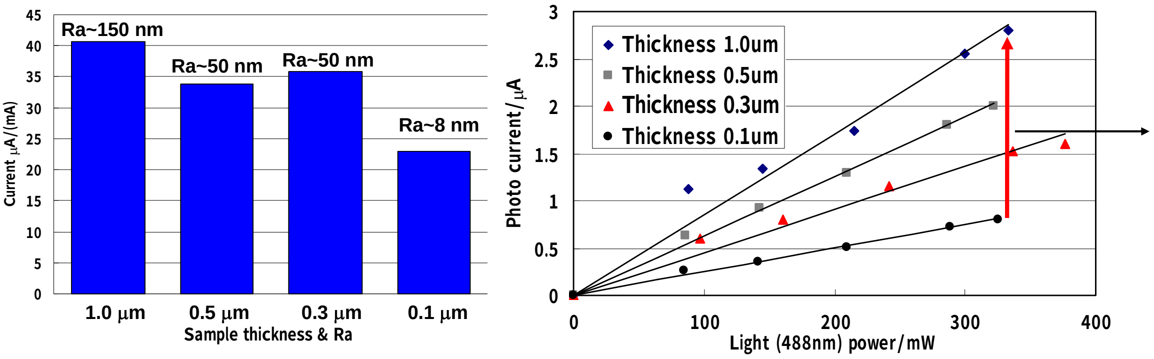

(A) (B)

The enhancement of visible response current by introducing nanoscale protrusion structure

Fig. 3 Photo response current of CVD samples under(A) UV & (B) 488nm irradiation

CONCLUSION

We have prepared nanostructured TiO_2 thin film and investigated the phonon-assisted optical near-field excitation by PEC measurement. Our results confirmed the excitation of TiO_2 with sub-bandgap photon by using the novel non-adiabatic transtition property of optical near-field. The fine nanomeric surface structure of the materials was realized to be the most significant factor in this effect. This study suggested a novel approach to develop visible-light reponse photocatalytic materials using optical near-field by merely introducing nanoscale structure and morphology.

ACKNOWLEDGEMENTS

This work was supported by JSPS Core-to-core program, and Grant-in-Aid for Specially Promoted Research.

REFERENCES

[1] V. N. Kuznetsov, et al, *J. Phys. Chem. C.* , **113** , 15110-15123 (2009)
[2] X. F. Qiu, et al. *Adv. Mater.* **19**, 3995-3999 (2007)
[3] T. Kawazoe, et al. *J. Chem. Phys* **122**, 024715 (2005)
[4] T. Kawazoe, et al. *J. Nanophoton* **1**, 011595 (2007)
[5] T. Yatsui, et al. *Appl. Phys B* **93**, 55 (2008)
[6] S. Liu *et al.*, *Nano Lett.*, **5**, 7 (2005)

Nanophotonics: Dressed photon science and technology

Motoichi Ohtsu

Graduate School of Engineering, The University of Tokyo, Tokyo 113-8656, Japan
Nanophotonics Research Center, The University of Tokyo, Tokyo 113-8656, Japan

Nanophotonics, proposed by the author in 1993 [1-3], is a novel optical technology that utilizes the optical near-field. The optical near-field is the dressed photons that mediate the interaction between nanometric particles located in close proximity to each other. Nanophotonics allows the realization of qualitative innovations in photonic devices, fabrication techniques, and systems by utilizing novel functions and phenomena enabled by optical near-field interactions that would otherwise be impossible if only conventional propagating light were used. In this sense, the principles and concepts of nanophotonics are completely different from those of conventional wave-optical technology, encompassing photonic crystals, plasmonics, metamaterials, and silicon photonics.

By combining the concepts of quantum field theory, optical science, and condensed-matter physics, the author has studied nanometric materials and optical energy transfer in nanometric space. Through these studies, a theoretical picture of dressed photons was obtained. Based on this picture, the exchange of dressed photons was studied, revealing energy transfer to electric dipole-forbidden energy levels. Furthermore, the possibility of coupling a dressed photon with a coherent phonon was found, revealing a novel phonon-assisted process in light-matter interactions in nanometric space. These discoveries were applied to develop novel technologies, such as devices, fabrication techniques, energy conversion, information systems, architectures and algorithms.

Fundamental concepts such as the behavior of photons in nanometric space, excitation transfer and relaxation in a nanometric space, and the primary mechanisms of the phonon-assisted process should be delved into more deeply. Such fundamental studies are expected to bring about further discoveries involving the coupling of dressed photons with various elementary excitations besides coherent phonons, leading to the discovery of novel applications. This marriage of basic studies and technological applications is expected to establish a new field of dressed photon science and technology in the near future.

Dressed photons can be utilized to establish fundamental new technologies that can replace a wide range of conventional optical technologies. Even though users will not notice their existence, it is expected that technologies exploiting dressed photons will be widely used in everyday life in the near future. This is because dressed photons can be generated universally on the surface of illuminated nanometric materials.

[1] M. Ohtsu, T. Kawazoe, T. Yatsui, and M. Naruse, IEEE J. Selected Topics in Quantum Electron., **14**, 1404 (2008).

[2] M. Ohtsu, K. Kobayashi, T. Kawazoe, T. Yatsui, and M. Naruse, Principles of Nanophotonics, (Tailor and Francis, Florida, 2008).

[3] M. Ohtsu, Preface to Volume V, in Progress in Nano-Electro-Optics V, ed. by M. Ohtsu, (Springer, Berlin, 2006).

Extended Abstracts of the 2010 International Conference on Solid State Devices and Materials, Tokyo, 2010, pp1281-1282

Energy transfer in multi-stacked InAs quantum dots

Kouichi Akahane[1], Naokatsu Yamamoto[1], Makoto Naruse[1,2,3], Tadashi Kawazoe[2,3], Takashi Yatsui[2,3] and Motoichi Ohtsu[2,3]

[1]National Institute of Information and Communications Technology
4-2-1, Nukui-kitamachi, Koganei, Tokyo 184-8795, Japan
Phone: +81-42-327-6804 E-mail: akahane@nict.go.jp
[2]Department of Electrical Engineering and Information Systems, Graduate School of Engineering, the University of Tokyo
2-11-16 Yayoi, Bunkyo-ku, Tokyo 113-8656, Japan
[3]Nanophotonics Research Center, Graduate School of Engineering, the University of Tokyo
2-11-16 Yayoi, Bunkyo-ku, Tokyo 113-8656, Japan

1. Introduction

A great deal of research interest exists in the excitation energy transfer between semiconductor quantum dots (QDs), and many investigations of interlayer excitation energy transfer between QDs have been conducted based on carrier tunneling [1-4], dipole-dipole interactions [5], optical near-field interaction [6,7], and carrier hopping [8,9] in self-assembled QDs systems. It is important to evaluate the energy transfer length for applications such as signal processors and solar cells because the performance of these devices is based on these phenomena. However, it is difficult to evaluate energy transfer length systematically in a self-assembled QD system, because QDs are distributed randomly on the semiconductor surface. Even with QDs aligned vertically in a stacked structure, fabrication of a stacking structure with multiple layers is difficult because of the accumulation of strain energy.

We have developed a method of stacking InAs QDs grown on InP(311)B using a strain compensation scheme. In this scheme, spacer layers with a lattice constant slightly smaller than that of the substrate are used to embed the QD layers. Using this method, we successfully stacked 150 InAs QD layers without any degradation in QD quality. We believe that there is no limit to the number of QD layers that can be stacked using this method [10], [11]. This enable use of the optimum number of QD layers for any given application. In addition, we can change emission wavelength by changing QDs growth thickness without degrading crystal quality, as long as the strain compensation condition is satisfied. Therefore, this material system is considered to be ideal for investigating energy transfer length among QDs. In this paper we investigate energy transfer in highly stacked QDs using the photoluminescence (PL) method.

2. Experiments

All samples were fabricated using conventional solid-source molecular beam epitaxy (MBE). We fabricated the stacked QD structures on an InP(311)B substrate. The value of the lattice constant of InP lies between the values of those of GaAs and InAs. This means that the lattice constant of InGaAlAs can be varied continuously around that of InP by controlling its composition. Thus, strain compensation can be achieved by capping the InAs QDs with an InGaAlAs layer whose lattice constant is slightly smaller than that of the InP substrate. We defined the strain-compensation conditions as:

$$d_{QD} \cdot \varepsilon_{QD} = - d_s \cdot \varepsilon_s \qquad (1)$$

$$\varepsilon_{QD} = (a_{QD} - a_{sub})/a_{sub} \qquad (2)$$

$$\varepsilon_s = (a_s - a_{sub})/a_{sub} \qquad (3)$$

where d_{QD} and d_s are the thicknesses of the deposited QDs and spacer layers, respectively, and a_{QD}, a_{sub}, and a_s are the lattice constants of the InAs, InP, and InGaAlAs spacer layers, respectively. This definition is based on the simple approximation that the total strain energy of a set, containing one layer of QDs and one spacer layer, is zero. First, we fabricated two 60-layer stacked samples with d_{QD}/d_s = 3-ML/15 nm and d_{QD}/d_s = 4-ML/20 nm to check the emission wavelength. We then fabricated modulated sample, continuously stacked N layers/one layer/ N+1 layers where N and N+1 layers correspond to a 3-ML QD layer and one layer corresponds to a 4-ML QD layer. We fabricated three samples of N=5, 10 and 20. Post-growth surface morphology was observed using an atomic force microscope (AFM) under normal atmospheric conditions. Photoluminescence (PL) measurements were carried out using the 532-nm line of a YVO laser, 250-mm monochromator, and an electrically cooled PbS detector.

3. Results and discussions

Figure 1 shows the PL spectra of 3-ML and 4-ML QDs measured at room temperature. Four-ML QDs shows longer wavelength emissions at 1607 nm, which corresponds to the ground state of 4-ML QDs depending on size of QDs. The larger size of 4-ML QDs is also confirmed by AFM measurements. There are small peaks in the shorter wavelength region of the main peak corresponding to the excited states of 4-ML QDs. This peak energy is the same as the main emission of 3-ML QDs (ground state, 1484 nm). Therefore, the energy transfer from 3ML QDs to 4-ML QDs is enhanced when 3-ML and 4-ML QDs exist in the same sample.

Figure 2 shows the PL spectrum for modulated samples N=5, 10 and 20. The ground state emission of 4-ML QDs shows a large intensity even if there is only one layer of 4-ML QDs in these samples. This clearly shows that energy transfer occurs from small QDs to large QDs. These amplified PL emission of 4-ML QDs were observed in all samples we fabricated (N= 5, 10 and 20).

We evaluated a ratio of PL intensity per dot layer as follows,

$$\frac{PL(\text{large } QD)/layer}{PL(\text{small } QD)/layer} \tag{4}$$

Where PL(small QD) and PL(large QD) means PL intensity of 3-ML QDs and 4-ML QDs. Figure 3 shows the N dependence of the ratio of PL intensity per dot layer. The ratio of PL intensity per dot layer increased with increasing N then decreased with increasing N. The maximum ratio of PL intensity per dot layer is around N=10. This result implies that long-range energy transfer should occur in these samples. The energy transfer length should depend on the condition of excitation intensity and temperature, and this should be the subject of a detailed investigation in the near future.

4. Conclusions

We fabricated a modulated stacked QD structure to investigate energy transfer among QDs. Energy transfer from small QDs to large QDs was clearly observed. Long-range energy transfer can be considered from the measurement of N dependence of PL intensity.

Acknowledgements

We would like to acknowledge the staff of the Photonic Device Laboratory at NICT for their technical support in device fabrication.

References

[1] R. Heitz, I. Mukhametzhanov, P. Chen, and A. Madhukar, Phys. Rev. B **58** (1998) R10151.

[2] A. Tackeuchi, T. Kuroda, K. Mase, Y. Nakata, and N. Yokoyama, Phys. Rev. B **62** (2000) 1568.

[3] Yu. I. Mazur, Zh. M. Wang, G. G. Tarasov, M. Xiao, G. J. Salamo, J. W. Tomm, V. Talalaev, and H. Kissel, Appl. Phys. Lett. **86** (2005) 063102.

[4] Yu. I. Mazur, X. Wang, Z. M. Wang, G. J. Salamo, M. Xiao, and H. Kissel, Appl. Phys. Lett. **81** (2002) 2469.

[5] C. R. Kagan, C. B. Murray, M. Nirmal, and M. G. Bawendi, Phys. Rev. Lett. **76** (1996) 1517.

[6] M. Ohtsu and H. Hori, *Near-Field Nano-Optics: From Basic Principles to Nano-Fabrication and Nano-Photonics* _Kluwer, Dordrecht, (1999).

[7] M. Ohtsu, K. Kobayashi, T. Kawazoc, S. Sangu, and T. Yatsui, IEEE J. Sel. Top. Quantum Electron. **8** (2002) 839.

[8] Z. Y. Xu, Z. D. Lu, X. P. Yang, Z. L. Yuan, B. Z. Zheng, J. Z. Xu, W. K. Ge, Y. Wang, J. Wang, and L. L. Chang, Phys. Rev. B **54** (1996) 11528.

[9] A. Polimeni, A. Patanè, M. Henini, L. Eaves, and P. C. Main, Phys. Rev. B **59** (1999) 5064.

[10] K. Akahane, N. Ohtani, Y. Okada, and M. Kawabe, J. Cryst. Growth, vol. **245** (2002) 31.

[11] K. Akahane, N. Yamamoto, S. Gozu, A. Ueta, N. Ohtani, and M. Tsuchiya, Conference Proceedings of International Conference on Indium Phosphide and Related Materials (IPRM'06) (2006) 192.

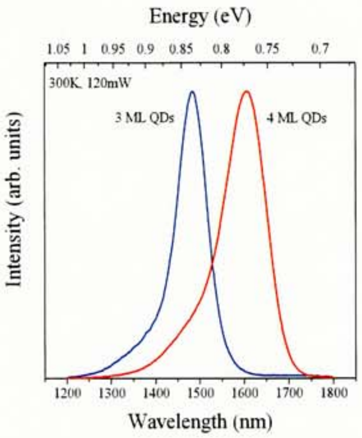

Fig. 1 PL spectra of 60 layer stacked QDs with thickness of 3-ML and 4-ML.

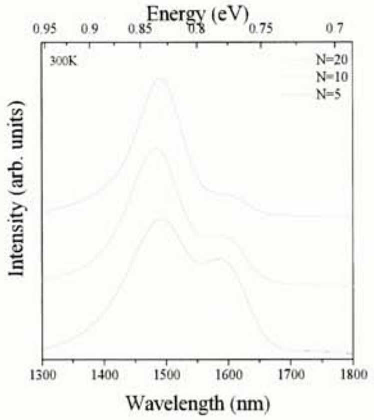

Fig. 2 N dependence of PL spectra of modulated stacking structure of QDs.

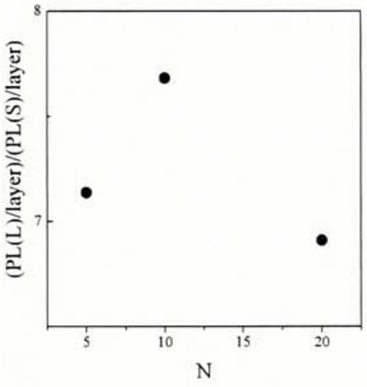

Fig. 3 N dependence of the ratio of PL intensity per QD layers

Photon modes and second harmonic generation in ZnO nano-needle arrays

David Leipold[1], **Manfred Maschek**[2], **Slawa Schmidt**[2], **Martin Silies**[2], **Takashi Yatsui**[3], **Kokoro Kitamura**[3], **Motoichi Ohtsu**[3], **Erich Runge**[1], **and Christoph Lienau**[2]

[1] *Institut für Physik und Institut für Mikro- und Nanotechnologien, Technische Universität Ilmenau, Germany*
[2] *Institut für Physik, Carl von Ossietzky Universität Oldenburg, Germany*
[3] *School of Engineering, University of Tokyo, 113-8656, Japan*

Localization of visible light is a fascinating topic in modern physics. Not only is it of fundamental interest in itself, but the resulting strong electromagnetic field enhancements concentrated to dimensions below the diffraction limit allow for novel ultrafast, non-linear, nano-optical experiments and applications.

Weak localization and strong light-matter interaction can be achieved in disordered dielectric materials [1]. In recent experiments, some of the present authors illuminated a densely packed array of ZnO nanorods fabricated by metal-organic vapor phase epitaxy. Ultrashort (6-fs) laser pulses around 800 nm are focused onto the sample with a Cassegrain objective. Pronounced spatial fluctuations of the resulting second-harmonic emission by more than an order of magnitude are seen, see Figure 1.

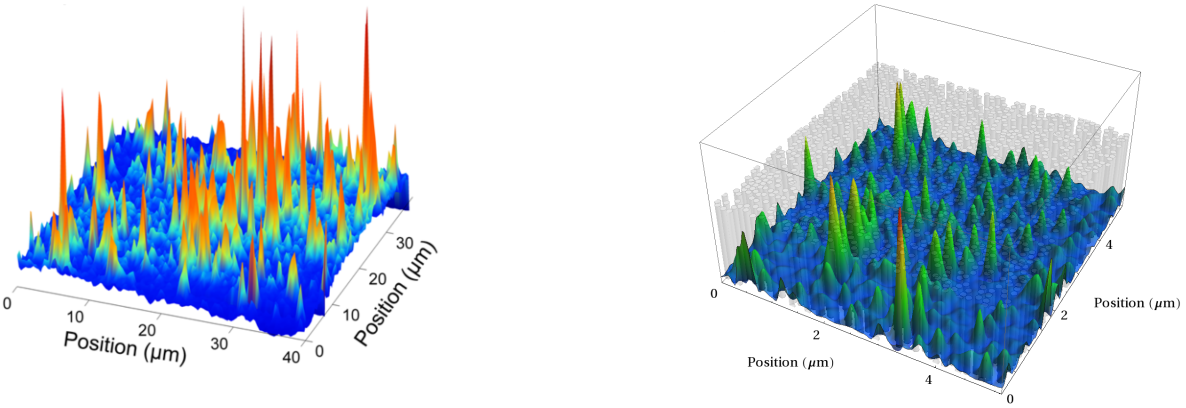

Figure 1: Experimental (left) and calculated (right) spatially resolved $|\mathbf{E}|^4$ patterns show strong field enhancements on a sub-wavelength sizescale. Model parameters: The nano needles (transparently overlayed) have an average distance of about 40 nm; the needle radius is 50 nm; the source is a 5 fs pulse centered at 780 nm.

In our calculations, we algorithmically create random spatial distributions of cylinders which are very similar to those seen in SEM images of the actual sample. These distributions are then used as input to a finite difference time-domain (FDTD) Maxwell solver. In our contribution, we present field distributions obtained from 2-D calculations (i.e., cylinders extent infinitly in their axial direction) showing strong, localized field enhancements which we compare with the experimental results. Additionally, we show first results of full 3-D calculations of our complete model system (i.e., substrate layer, nano-needles, and air) which provide detailed insight in the dynamics and spatial distribution of the second harmonic generation.

References

[1] Cefe Lopez, “News and Views, Anderson localization of light: A little disorder is just right”, *Nature Physics* **4**, 755 (2008).

Minimum Energy Dissipation in Signal Transfer via Optical Near-Field Interactions in the Subwavelength Regime

Makoto Naruse(1),(2), Hirokazu Hori(3), Kiyoshi Kobayashi(3), and Motoichi Ohtsu(2)

(1) Photonic Network Group, New Generation Network Research Centre, National Institute of Information and Communications Technology, 4-2-1 Nukui-kita, Koganei, Tokyo 184-8795, Japan, naruse@nict.go.jp

(2) Department of Electrical Engineering and Information Systems and Nanophotonics Research Centre, School of Engineering, The University of Tokyo, 2-11-16 Yayoi, Bunkyo-ku, Tokyo 113-8656, Japan

(3) Interdisciplinary Graduate School of Medicine and Engineering, University of Yamanashi, Kofu, Yamanashi 400-8511, Japan

Abstract *We theoretically demonstrate that the minimum energy dissipation required for optical excitation transfer in quantum dot systems on the nanometer-scale via optical near-field interactions could be about 25 μeV, nearly 10^4 times more energy-efficient than conventional electrically wired devices.*

Introduction

Energy efficiency is one of the most important requirements in today's information and communications technology (ICT) in order to abate CO_2 production. Various approaches have been intensively studied regarding energy efficiency, ranging from analysis of fundamental physical processes to system-level smart energy management[1,2].

The fundamental physical attributes of photons exploited so far are, however, typically just the ability to utilize fully optical end-to-end connections and the multiplexing nature of propagating light. The primary objective of this paper is to note another unique attribute available on the nanometer-scale, that is, optical near-field interactions[3]. Here we theoretically demonstrate that the minimum energy dissipation in optical excitation transfer via optical near-field interactions could be around 25 μeV, which is 1000 times as low as the thermal fluctuations, and is significantly smaller than in conventional electrically wired devices.

Optical Excitation Transfer for Communication on the Nano-scale

Optical excitations could be transferred from smaller quantum dots to larger ones via optical near-field interactions that allow even transitions to conventionally electric-dipole forbidden energy levels. The electric field is homogeneous on the nanometer scale in conventional light–matter interactions due to to diffraction-limited propagating light. As a consequence, we can derive optical selection rules where, in the case of cubic quantum dots for instance, transitions to states containing an even quantum number are prohibited. On the other hand, in the case of optical near-field interactions, the steep electric field of optical near-fields in the vicinity of nano-scale material allow optical transitions that are prohibited in propagating light[3]. For instance, assume two cubic quantum dots whose side lengths are a and $\sqrt{2}a$, which we call $\mathrm{QD_S}$ and $\mathrm{QD_L}$, respectively, as shown in Fig. 1(a). Suppose that the energy eigenvalues for the quantized exciton energy level specified by quantum numbers (n_x,n_y,n_z) in a QD with side length a are given by

$$E_{(n_x,n_y,n_z)} = E_B + \frac{\hbar^2\pi^2}{2Ma^2}(n_x^2+n_y^2+n_z^2), \tag{1}$$

(a)

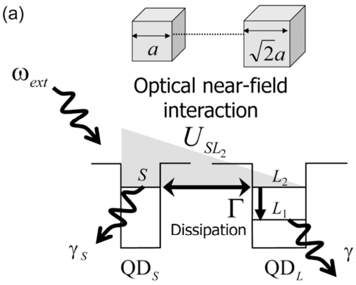

(b) System A (*intended* system) **(c) System B (*unintended* system)**

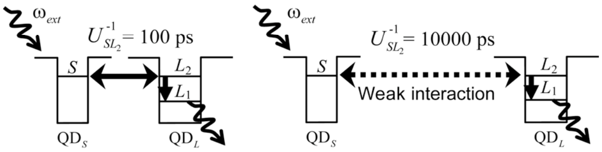

Fig. 1: (a) Optical near-field interaction in a two-QD system. (b,c) *Intended* and *unintended* systems where an optical excitation transfer does and does not occur, respectively.

where E_B is the energy of the bulk exciton, and M is the effective mass of the exciton. According to eq. (1), there exists a resonance between the

978-1-4244-8534-5/10/$26.00 ©2010 IEEE

level of quantum number (1,1,1) for QD_S and that of quantum number (2,1,1) for QD_L. Hereafter, the (1,1,1)-level of QD_S is denoted by S, and the (2,1,1)-level of QD_L is called L_2. There is an optical near-field interaction, which is denoted by U_{SL_2} , in the vicinity of QD_S. Therefore, excitons in S can move to L_2 in QD_L. Note that such a transfer is prohibited in propagating light since the identifier (2,1,1) of the level in QD_L contains an even number. In QD_L, the exciton sees a sublevel energy relaxation, denoted by Γ, which is faster than the near-field interaction, and so the exciton goes to the (1,1,1)-level of QD_L, which is called L_1 hereafter.

The energy dissipation in such an optical excitation transfer from a smaller QD to a larger one is the energy relaxation processes occuring at the larger QD, which guarantees the unidirectionality of the signal transfer[1]. We quantitatively examine how such energy dissipation at the larger QD could be minimized.

We introduce quantum mechanical modeling of the total system based on a density matrix formalism. There are in total eight states where either zero, one, or two exciton(s) can sit in the energy levels S, L_1, and L_2 in the system. Here, the interactions between QD_S and QD_L are denoted by U_{SL_i} (i=1,2), and the radiative relaxation rates from S and L_1 are respectively given by γ_S and γ_L. Also, we assume far-field input light irradiation at the optical frequency ω_{ext} , which could couple to the (1,1,1)-level in QD_S (S) and QD_L (L_1) because those levels are electric dipole-allowed energy levels.

Such optical excitation transfers have been experimentally demonstrated in various materials, such as CuCl, CdSe, CdTe, InAs QDs, and ZnO nanorods[4-6]. These principles have also been applied to basic applications in ICT, such as logic gates[6], interconnects[7], and energy concentration[4].

Minimum Energy Dissipation in Optical Excitation Transfer

Here we introduce two different system setups to investigate the minimum energy dissipation in the optical excitation transfer modeled above. In the first one, System A in Fig. 1(b), two quantum dots are located close together where the optical excitation transfer from QD_S to QD_L occurs. We assume $U_{SL_2}^{-1}$ of 100 ps in System A, which is a typical interaction time between closely separated quantum dots[4]. In System B on the other hand, shown in Fig. 1(c), the two quantum dots are located far away from each other. Therefore, the interactions between QD_S and QD_L are negligible, and thus the optical excitation transfer from QD_S to QD_L does not occur, and the radiation from QD_L should normally be zero. We assume $U_{SL_2}^{-1} = 10{,}000$ ps for System B, indicating that there are effectively no interactions between the quantum dots.

The energy dissipation in the optical excitation transfer from QD_S to QD_L is the sublevel relaxation in QD_L. Therefore, the issue is to derive the minimum of such dissipation. When the dissipation, given by the energy difference between L_1 and L_2, denoted by Δ, is too small, the input light may directly couple to L_1, resulting in output radiation from QD_L even in System B. In other words, we would not be able to recognize the origin of the output radiation from QD_L if it involves the optical excitation transfer from QD_S to QD_L in System A, or if it directly couples to L_1 in System B. Therefore, the proper system behavior is to observe higher populations from L_2 in System A while at the same time observing lower populations from L_2 in System B.

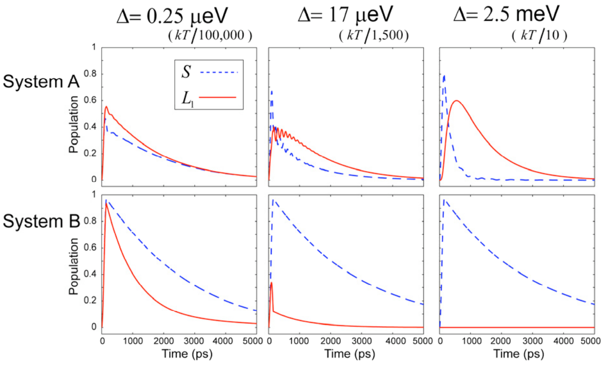

Fig. 2: Evolutions of the populations in Systems A and B as a function of energy dissipation.

We first assume pulsed input light irradiation with a duration of 150 ps at 3.4 eV (wavelength 365 nm), and assume that the energy level S is resonant with the input light. Also, we assume the radiation lifetime of QD_L to be γ_L^{-1}=1 ns and that of QD_S to be γ_S^{-1}=2.83 ns, since it is inversely proportional to the volume of the QD. The sublevel relaxation time is given by Γ^{-1}=10 ps. The solid and dashed curves in Fig. 2 respectively represent the evolutions of populations related to the radiation from the energy levels L_1 and S for both System A and System B, assuming three different values of Δ: (i) $\Delta = 0.25\ \mu\text{eV}$, (ii) $\Delta = 17\ \mu\text{eV}$, and (iii) $\Delta = 2.5\ \text{meV}$, which respectively correspond to about $kT/10$, $kT/1500$, and $kT/100000$, where k is the Boltzmann constant and T represents room temperature.

In the case of (i), there is nearly zero population in System B from L_1, which is the expected proper behavior of the system since there are no interactions between the quantum dots. The radiation from QD_S is observed with its radiation decay rate (γ_S). In System A, on the other hand, populations from L_1 do appear. Note that the population involving the output energy level L_1 is only 0.17 when the input pulse is terminated (t=150 ps), whereas the population involving S at t=150 ps is 0.81. Therefore the increased population from L_1 after t=150 ps is due to the optical excitation transfer from QD_S to QD_L. In the case of (iii), due to the small energy difference, the input light directly couples with L_1; therefore, both System A and System B yield higher populations from L_1, which is an unintended system behavior. Finally, in the case of (ii), the population from L_1 in System B is not as large as in case (iii), but it exhibits a non-zero value compared with case (i), indicating that the energy difference ($\Delta = 17\ \mu\text{eV}$) may be around the middle of the intended and unintended system operations involving optical excitation transfer between QD_S and QD_L.

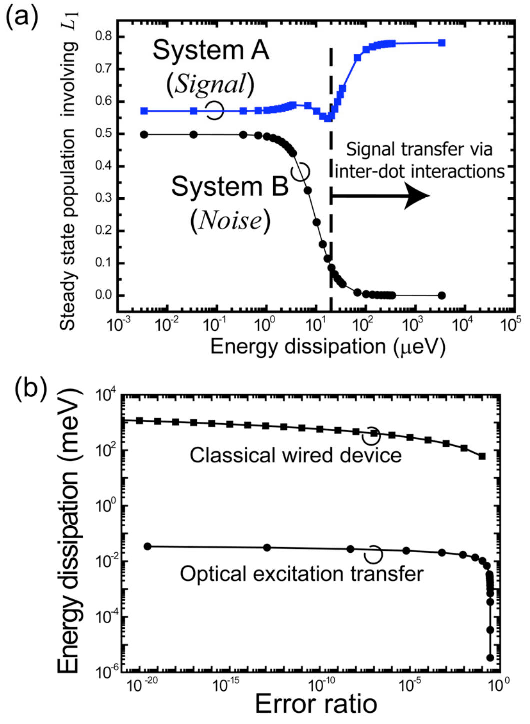

Fig. 3: Output populations in System A and B as a function of the energy dissipation. (b) Energy dissipation as a function of error ratio in optical excitation transfer and electrically wired device.

When we assume a longer duration of the input light, the population converges to a steady state. When radiating a pulse with a duration of t=150 ps at the same wavelength (365 nm), Fig. 3(a) summarizes the steady state output populations involving energy level L_1 evaluated at t=10 ns as a function of the energy dissipation. The intended system behavior, that is, a higher output population in System A and a lower one in System B, is obtained in the region where energy dissipation is larger than around 25 μeV.

If we treat the population from System A as the "signal" amplitude and that from System B as “noise”, the signal-to-noise ratio (SNR) can be evaluated based on the numerical values obtained in Fig. 3(a). With SNR, the error ratio (P_E) is derived by the formula $P_E = (1/2)erfc\left(\sqrt{SNR}/2\sqrt{2}\right)$ where $erfc(x)$ represents the complementary error function[8]. The circles in Fig. 3(b) represent the energy dissipation as a function of the error ratio assuming the photon energy used in the above study (3.4 eV). According to Ref. 2, the minimum energy dissipation (E_d) in classical electrically wired devices (specifically, energy dissipation required for a single bit flip in a CMOS logic gate) is given by $E_d = kT\ln(\sqrt{3}P_E/2)$, which is indicated by the squares in Fig. 3(b). For example, when the error ratio is 10^{-6}, the minimum energy dissipation in optical excitation transfer is about 0.024 meV, whereas that of the classical electrical device is about 303 meV; the former is about 10^4 times more energy efficient than the latter.

Conclusion

In summary, we investigated the minimum energy dissipation required for optical excitation transfer from smaller quantum dots to larger ones via optical near-field interactions. We demonstrate that the minimum energy dissipation could be around 25 μeV, which is about 10^4 times more energy efficient than conventional electrically wired devices. We will further investigate the minimum energy required to operate nanophotonic systems, including technological and experimental limitations.

References

1 R. S Tucker, et al., J. Lightwave Technol. **27**, 243 (2009).
2 L. B. Kish, IEE Proc. Circuits Devices Syst. 151, 190 (2004).
3 M. Ohtsu, et al., *Principles of Nanophotonics*, Taylor and Francis (2008).
4.M. Naruse, et al., Phys. Rev. B **80**, 125325 (2009).
5 T. Franzl, et al., Nano Lett. **4**, 1599 (2004).
6 T. Yatsui, et al., Appl. Phys. Lett. **90**, 223110 (2007).
7 M. Naruse, et al., Opt. Express **14**, 306 (2006).
8 S. Haykin, *Communication Systems*, John Wiley & Sons (1983).

I 7: Phonon-assisted nanophotonic fabrication and its application (Invited)

Presenter : Motoichi OHTSU

Motoichi OHTSU, (The University of Tokyo)

This presentation reviews novel nanophotonic fabrication techniques based on a phonon-assisted process triggered by optical-near-field interactions. This process represents qualitative innovation in photochemical vapor deposition and photolithography, suggesting that large, expensive ultraviolet light sources will no longer be required, although they are indispensable for conventional adiabatic photochemical vapor deposition, photolithography, and photochemical etching. It also suggests that phonon-assisted photochemical vapor deposition can even dissociate optically inactive molecules (i.e., inactive to propagating light), which is advantageous for environmental protection because most optically inactive molecules are chemically stable and harmless. For example, optically inactive Zn(acac)2 molecules have been dissociated to deposit nanometric Zn particles. In addition, in the case of phonon-assisted photolithography, an optically inactive resist film for electron-beam lithography has been used to fabricate fine patterns. A prototype commercial lithography system has been produced in collaboration with industry, and has been used for fabricating diffraction gratings and Fresnel zone plates for soft X-rays. Furthermore, phonon-assisted photochemical etching has realized an ultra-flat glass surface with a roughness as low as 0.13 nm without using any photomasks.

SESSION 12

Room: Conv. Ctr. 6B . . . . Wed. 10:30 am to 12:05 pm

Ultrafast and Strong Field Plasmonics

Session Chair: **Yeshaiahu Fainman,** Univ. of California, San Diego

10:30 am: **High harmonic generation by guided surface plasmon polaritons** *(Keynote Presentation)*, Seung-Woo Kim, In-Yong Park, Seungchul Kim, Joonhee Choi, Korea Advanced Institute of Science and Technology (Korea, Republic of) . . . . [7757-46]

11:15 am: **Electron and XUV light emission probes of ultrafast nano-localized plasmonic fields** *(Invited Paper)*, Matthias F. Kling, Max-Planck-Institut für Quantenoptik (Germany) . . . . [7757-47]

11:45 am: **Probing ultrafast nano-localised plasmonic fields via XUV light generation,** Sarah L. Stebbings, Frederik Süßmann, Ying Ying Yang, Max-Planck-Institut für Quantenoptik (Germany); Roswitha Graf, Alexander Apolonskiy, Ludwig-Maximilians-Univ. München (Germany); Alexander Weber-Bargioni, Lawrence Berkeley National Lab. (United States); Mark I. Stockman, Georgia State Univ. (United States); Ferenc Krausz, Matthias F. Kling, Max-Planck-Institut für Quantenoptik (Germany) . . . . [7757-48]

Lunch/Exhibition Break . . . . 12:05 to 1:30 pm

SESSION 13

Room: Conv. Ctr. 6B . . . . Wed. 1:30 to 3:10 pm

Infrared and Terahertz Plasmonics

Session Chair: **Anatoly V. Zayats,**
Queen's Univ. Belfast (United Kingdom)

1:30 pm: **Experimental observation of infrared spoof plasmons** *(Invited Paper)*, Gennady Shvets, Alexander B. Khanikaev, Hossein Mousavi, Dmitriy V. Korobkin, Burton Neuner III, The Univ. of Texas at Austin (United States) . . . . [7757-49]

2:00 pm: **Nanoconcentration of terahertz radiation,** Maxim Durach, Anastasia Rusina, Mark I. Stockman, Georgia State Univ. (United States) . . . . . . [7757-50]

2:20 pm: **Active terahertz nano resonators with full transmission control** *(Invited Paper)*, Dai-Sik Kim, Minah Seo, Jisoo Kyoung, Hyeong-Ryeol Park, Kwang Jun Ahn, H. S. Kim, Sukmo Koo, Seoul National Univ. (Korea, Republic of); B. J. Kim, Electronics and Telecommunications Research Institute (Korea, Republic of); Y. H. Ahn, Ajou Univ. (Korea, Republic of); Hyun Tak Kim, Electronics and Telecommunications Research Institute (Korea, Republic of); Namkyoo Park, Seoul National Univ. (Korea, Republic of) . . . . [7757-51]

2:50 pm: **Electrically tunable surface plasmon for THz emission, detection and other applications,** Jed Khoury, Bahareh Haji-Saeed, Walter R. Buchwald, Charles L. Woods, Air Force Research Lab. (United States) . . . . [7757-52]

Coffee Break . . . . 3:10 to 3:30 pm

SESSION 14

Room: Conv. Ctr. 6B . . . . Wed. 3:30 to 6:05 pm

Nanoantennas II

Session Chair: **Olivier J. F. Martin,**
Ecole Polytechnique Fédérale de Lausanne (Switzerland)

3:30 pm: **Nano-antenna control of single photon emitters** *(Keynote Presentation)*, Niek F. van Hulst, ICFO - Instituto de Ciencias Fotónicas (Spain) . . . . [7757-53]

4:15 pm: **Effect of grain boundaries on nanoantenna performance,** Vladimir P. Drachev, Kuo-Ping Chen, Joshua D. Borneman, Alexander V. Kildishev, Vladimir M. Shalaev, Purdue Univ. (United States) . . . . [7757-54]

4:35 pm: **Plasmonic sensor based on perfect absorption,** Na Liu, Thomas Weiss, Martin Mesch, Harald W. Giessen, Univ. Stuttgart (Germany) . [7757-55]

4:55 pm: **Spoof surface plasmons shape terahertz laser beams** *(Invited Paper)*, Federico Capasso, Harvard Univ. (United States) . . . . [7757-56]

5:25 pm: **Plasmonic resonator antennas for enhanced light emission and detection,** Edward S. Barnard, Mark L. Brongersma, Stanford Univ. (United States) . . . . [7757-57]

5:45 pm: **Manipulating the local symmetry and geometry of bowtie optical antennae for controlling spectral properties while maintaining the near-field enhancement,** Alexander Weber-Bargioni, Scott Dhuey, Frank Ogletree, Jim Schuck, Stefano Cabrini, Lawrence Berkeley National Lab. (United States) . . . . [7757-58]

Thursday 5 August

SESSION 15

Room: Conv. Ctr. 6B . . . . Thurs. 8:00 to 10:25 am

Nanoplasmonic Confinement and Related Subjects

Session Chair: **Niek F. van Hulst,**
ICFO - Instituto de Ciencias Fotónicas (Spain)

8:00 am: **Plasmonic, semiconductor, and dielectric building blocks for nanophotonics** *(Keynote Presentation)*, Mark L. Brongersma, Stanford Univ. (United States) . . . . [7757-59]

8:45 am: **Optical resonances and nanofocusing in triangular metal nano-grooves,** Thomas Søndergaard, Aalborg Univ. (Denmark); Sergey I. Bozhevolnyi, Jonas Beermann, Sergey M. Novikov, Univ. of Southern Denmark (Denmark); Eloïse Devaux, Thomas W. Ebbesen, Univ. de Strasbourg (France); Jens Rafaelsen, Aalborg Univ. (Denmark) . . . . [7757-60]

9:05 am: **Plasmonic assisted confinement of electromagnetic energy** *(Invited Paper)*, Uriel Levy, Gilad Lerman, Avner Yanai, Boris Desiatov, Ilya Goykhman, The Hebrew Univ. of Jerusalem (Israel) . . . . [7757-61]

9:35 am: **Plasmonic nanostructures: Local versus non-local response,** Niels A. Mortensen, Martijn Wubs, Giuseppe Toscano, Sanshui Xiao, Technical Univ. of Denmark (Denmark); Min Yan, Royal Institute of Technology (Sweden); Z. Fatih Öztürk, Istanbul Teknik Üniv. (Turkey); Antti-Pekka Jauho, Aalto Univ. School of Science and Technology (Finland) . . . . [7757-62]

9:55 am: **Cooperative effects in plasmonics** *(Invited Paper)*, Tigran V. Shahbazyan, Jackson State Univ. (United States) . . . . [7757-63]

Coffee Break . . . . 10:25 to 10:55 am

SESSION 16

Room: Conv. Ctr. 6B . . . . Thurs. 10:55 am to 12:05 pm

Surface Enhanced Photochemistry and Spectroscopy

Session Chair: **Mark L. Brongersma,** Stanford Univ.

10:55 am: **Information theoretical aspects in nanophotonics** *(Invited Paper)*, Makoto Naruse, National Institute of Information and Communications Technology (Japan); Naoya Tate, Motoichi Ohtsu, The Univ. of Tokyo (Japan) . . . . [7757-75]

11:25 am: **Radiative engineering of nanoantenna arrays for ultrasensitive vibrational spectroscopy of proteins,** Ronen Adato, Ahmet A. Yanik, Boston Univ. (United States); Jason J. Amsden, David Kaplan, Fiorenzo Omenetto, Tufts Univ. (United States); Mi Kyung Hong, Shyamsunder Erramilli, Hatice Altug, Boston Univ. (United States) . . . . [7757-65]

11:45 am: **Optical properties and surface-enhanced Raman scattering of quasi-3D gold plasmonic nanostructures,** Qiuming Yu, Jiajie Xu, Univ. of Washington (United States) . . . . [7757-66]

Lunch/Exhibition Break . . . . 12:05 to 1:35 pm

SESSION 17

Room: Conv. Ctr. 6B . . . . Thurs. 1:30 to 3:05 pm

Engineering Plasmonic Spectra and Enhancement I

Session Chair: **Uriel Levy,** The Hebrew Univ. of Jerusalem (Israel)

1:30 pm: **Studies of plasmon hybridization via electron and optical spectroscopies in designer plasmon nanocavities** *(Keynote Presentation)*, Stefan A. Maier, Imperial College London (United Kingdom) . . . . [7757-67]

2:15 pm: **Manipulating field enhancement in gaps and at tips,** Calin Hrelescu, Siji Wu, Weihai Ni, Ludwig-Maximilians-Univ. München (Germany); Tapan K. Sau, International Institute of Information Technology (India); Ludovic Douillard, Fabrice Charra, Guillaume Laurent, Commissariat à l'Énergie Atomique (France); Severin Habisreutinger, Ludwig-Maximilians-Univ. München (Germany); Andrey L. Rogach, Ludwig-Maximilians-Univ. München (Germany) and City Univ. of Hong Kong (China); Frank Jäckel, Jochen Feldmann, Ludwig-Maximilians-Univ. München (Germany) . . . . [7757-68]

2:35 pm: **Optical resonator in gap plasmon waveguide** *(Invited Paper)*, Masanobu Haraguchi, Hidenori Sokabe, Masamichi Taniguchi, Tatsuya Okuno, Toshihiro Okamoto, Masuo Fukui, Univ. of Tokushima (Japan) . . . . . . [7757-69]

Coffee Break . . . . 3:05 to 3:35 pm

Recent advances in nanophotonics allow the design of optical devices and systems at densities beyond those conventionally limited by the diffraction of light. In addition to physical principles and experimental technologies of nanophotonics, system-level fundamentals from the viewpoint of information are also indispensable in order to grasp the limitations of nanophotonic systems and to exploit their optimal performances. Here we demonstrate information theoretic and information-network theoretic approaches to nanophotonic systems while assessing the optical near-field interactions in the nanometer-scale via angular-spectrum frameworks and dressed photon models. We analyze the information capacity of hierarchical nanophotonic systems using mutual information. Also, we show optimized optical near-field interactions network among quantum dots for efficient energy concentration. Such insights contribute to further progress of nanophotonics for information and communications applications.

[III] REVIEW PAPERS

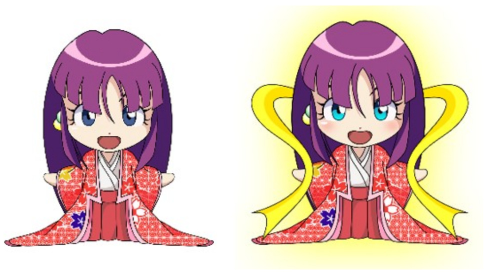

Laser Review

ZnOナノ構造のナノフォトニックデバイスへの応用

八井 崇，大津 元一
東京大学（〒113-8656 東京都文京区弥生2-11-16）

Nanophotonic Device Using ZnO Nanostructures

Takashi YATSUI and Motoichi OHTSU
University of Tokyo, 2-11-16 Yayoi, Bunkyo-ku, Tokyo 113-8656

(Received September 17, 2010)

This paper reviews recent progress in nanophotonic devices using optical near-field interaction. ZnO nanocrystallites are potentially ideal components for realizing room-temperature operation of nanophotonic devices because of their high exciton-binding energy and great oscillator strength. To confirm this promising optical property in ZnO, we report here the near-field time-resolved spectroscopy of ZnO nanorod double-quantum-well structures (DQWs). We successfully demonstrated switching dynamics by a dipole-forbidden optical energy transfer among resonant exciton states. Furthermore, we developed a self-assembly method that aligns nanometer-sized quantum dots (QDs) into a straight line along which photonic signals can be transmitted by optically near-field effects. ZnO QDs were bound electrostatically to DNA to form a one-dimensional QD chain. The photoluminescence intensity under parallel polarization excitation along the QDs chain was much greater than under perpendicular polarization excitation, indicating an efficient signal transmission along the QD chain.

Key Words: Near-field energy transfer, ZnO nanorod quantum-well-structure, ZnO quantum dot, Nanophotonic device, Virtual exciton polariton

1. はじめに

情報通信の高速化・大容量化により，演算素子の微細化が急務となっている．現在の演算素子を支えるシリコン電子デバイスにおいても，配線などにおける熱の発生が大きな問題となり，微細化の限界が見え始めている．このような状況においてMIT Microphotonics Centerにより取りまとめられた2005年版Communications Technology Roadmapに予想されるように，回路の微小化だけでなく既存の電子デバイスから光デバイスの移行が，PC内部のチップ間配線などにおいても必要となってきている．このような光デバイスに求められる寸法は10年以内には100 nm以下になると予測されており，現状の光デバイスを単純に微細化するだけでは，光の回折限界の壁を乗り越えられない．つまり，単に小寸法化という「量的変革」ではなく，伝搬光を用いたのでは実現しないデバイス機能の開発という「質的変革」が求められている[1,2]．

この問題を解決する有効な手段として，近年，量子ドット(QD)によって構成され近接場光によって動作するナノフォトニックデバイスが提案されている[3]．その一例がナノフォトニックスイッチ(波長変換素子)であり，その基本原理を，Fig. 1を用いて説明する．このデバイスでは共鳴する量子準位間での「近接場光エネルギー移動および散逸」を利用する．近接場光エネルギー移動とは，一方のQDにおいて再結合により消滅した励起子が，他方のQDに吸収される過程ではない．励起子がQDに生成されると，かかるQDの周りには近接場光が発生する．その近接場光は光子と励起子の混ざり合った状態であり，仮想励起子ポラリトンと呼ばれる．この仮想励起子ポラリトンの広がり内に別のQDが存在すると，トンネル効果により励起子が移動する．この，仮想励起

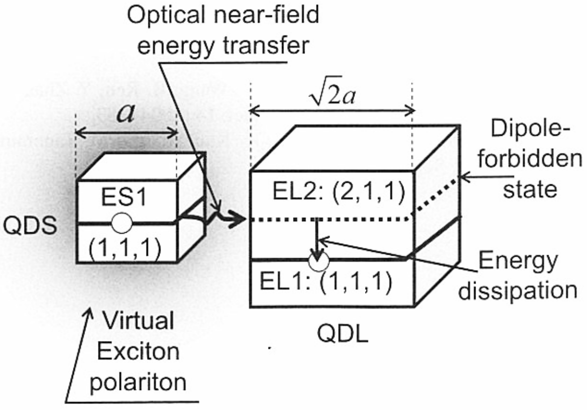

Fig. 1 Energy transfer and dissipation.

子ポラリトンを介した励起子の移動のことを近接場光エネルギー移動と呼ぶ[1,2]．このように，近接場光エネルギー移動は，発光・吸収過程とは異なり，トンネル効果による移動であるため，高いエネルギー移動効率が実現する．

近接場光エネルギー移動を利用することにより，従来の光デバイスでは実現不可能であった全く新しい機能が実現する．その一つの機能が，光学禁制準位への励起が許容となることである．この機能によって，従来の波動光学デバイスでは実現不可能であった，一方向エネルギー伝送が可能となる．寸法比が1：$\sqrt{2}$のQDSとQDLにおいて，QDSの励起子の基底準位ES1と，QDLの第一励起準位EL2はエネルギー的に共鳴する（Fig. 1）．ここで，EL2は光学禁制準位となるため従来の伝搬光では励起することができない．しかし，2つのQDを寸法サイズであるa程度に近接して配置すると，QDSに励起される近接場光（局所場）によって，EL2は励起可能となる．結果として，ES1とEL2間で近接場光エネルギー移動が発生するが，EL2からEL1への高速のサブレベル間緩和（散逸）が発生するために，ES1に励起されたエネルギーは全てEL1に移動し，ES1に逆流することはない．つまり一方向なエネルギー伝送が実現する[1-3]．

ナノフォトニックデバイスを室温で安定に動作させるために，本稿では近年，著者らが研究を進めているZnOを用いた取り組みについて紹介する．電子デバイスとしても良質な特性を示すZnO[5]の光デバイスとしての特長は（1）励起子結合エネルギーが大きい[6]（60 meV．量子構造にした場合には，110 meVまで大きくなることが報告されている），（2）振動子強度が大きい[7]，ことから室温において強い励起子発光強度が得られることである．

2. ZnOナノロッド量子井戸構造[8]

ZnOからなる量子構造の一つとして，Metal Vapor Phase Epitaxy（MOVPE）法により作製されたZnOナノロッド先端に作製されている[9]．この手法により，ナノロッド先端の単一量子井戸構造とした場合でも，井戸幅に依存して強い励起子発光が観測されている[10]．この手法では，量子井戸の幅および間隔を原子層レベルでを自在に制御することができるため任意のナノフォトニックデバイス作製が可能となる．

Fig. 1で説明した一方向エネルギー伝送を実現させるために，2つの量子井戸構造からなる，2重量子井戸構造（DQWs）の作製を行った．井戸の幅を調整し，拡い井戸幅を有する量子井戸（QW$_B$）の励起子第一励起準位（EB_2）と狭い井戸幅を有する量子井戸（QW$_A$）の励起子基底準位（EA_1）が共鳴する寸法でDQWsを作製した（Fig. 2 (a)およびFig. 2 (b)）．それぞれの井戸幅L_wは3.2 nm（QW$_A$）および3.8 nm（QW$_B$）であり，E_{A1}（E_{B2}）およびE_{B1}に相当する波長は361 nm，362 nmである（Fig. 2 (c)）．これにより，QW$_A$にポピュレーションを生成させた場合でも，共鳴するエネルギー準位を介してポピュレーションが移動し，この際に失うサブバンド間エネルギーにより，励起が逆流することなくQW$_B$の基底準位（E_{B1}）からの発光のみ観測されることになると期待される．この際，QW$_B$の第一励起準位は光学禁制であるために，基底準位からの発光しか観測されないと考えられる．

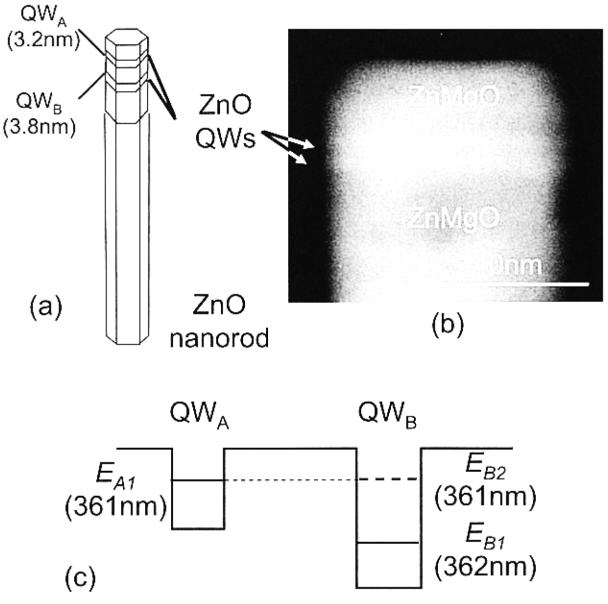

Fig. 2 (a) Schematic and (b) TEM image of ZnO nanorod DQWs. (c) Energy diagram of DQWs.

近接場エネルギー移動の一方向性を確認する実験として，まず両者の井戸を励起するために，入力光としてHe-Cdレーザー（$\lambda = 325$ nm）による励起を行った結果に

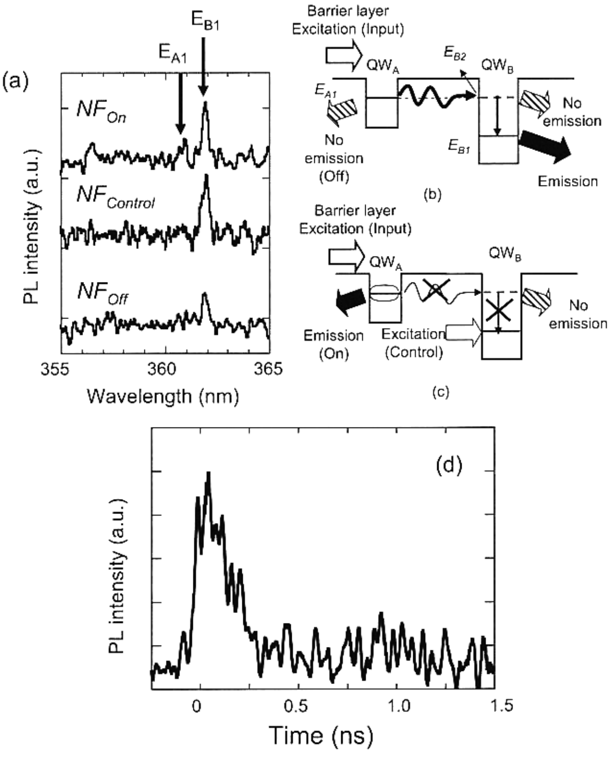

Fig. 3 (a) Near-field spectra. NF_{Off}: Excitation with input light only, $NF_{Control}$: Excitation with control light only, NF_{On}: Excitation with both input and control light. (b) On state. (c) Off state. (d) Near-field time-resolved PL signal with "On" state.

ついて説明する．この状態で得られた近接場光スペクトル（Fig. 3 (a) の曲線NF_{Off}）から，362 nm付近に発光のピークを有するスペクトル（E_{B1}）が観測された．QW_AとQW_Bの井戸が孤立して存在した場合には，それぞれの基底準位に対応する波長361 nmおよび362 nmでの発光ピークが観測されるが，この場合には，QW_Bの基底準位に相当するピークからの発光しか観測することができなかった．これは，先に予測したように，共鳴する励起子準位間でのエネルギー移動を示す結果であるといえる（Fig. 3 (b)．"Off"状態．）．次に，このエネルギーの流れを止めるために，制御光としてE_{B1}を共鳴励起（Fig. 3 (a) の曲線$NF_{Control}$．制御光はTi:Sapphireレーザーの2次高調波：波長362 nm・パルス幅2 ps）させた状況下において，He-Cdレーザー光を照射したスペクトルをFig. 3 (a)の曲線NF_{On}に示す．この結果，He-Cdレーザー単独励起では観測されなかったE_{A1}（$\lambda = 361$ nm）に相当する発光ピーク（出力光）が観測された（Fig. 3 (c)．"On"状態．）．以上の結果は前述した近接場エネルギー移動制御によるナノフォトニックスイッチの基本的動作原理を実証するものである[8]．

さらに，ナノフォトニックスイッチの動的特性評価を行った．バリア層励起用光源，および制御光同時照射下における，波長361 nmでの時間分解発光強度信号をFig. 3 (d)に示す．信号の立ち上がり時間から，スイッチの動作時間が約100 psであることが示された．

3. 量子ドットナノ光伝送路[11]

上記の成果を発展させるため，QDを用いたデバイス開発について紹介する．QDは化学的な手法による安価かつ大量の合成が可能であり，ナノロッド構造と異なり三次元的な空間配列自由度が大きいため，多重度の高いエネルギー伝送路作製に適した材料であると期待される．

室温で動作可能なエネルギー伝送路を実現するには，室温で良好な発光特性を有するZnO QDを作製する必要がある．ZnO量子ドットの合成にはゾル・ゲル法を用いた[12,13]．これによって，単結晶の量子ドットが簡便に得られる．

光電子工学で従来使われているトップダウン的作成技術ではQDを直線配列することは不可能なので，DNAに沿ってQDを固定する方法を用いた（Fig. 4 (a)）．2本鎖DNAはアニオン性であるので，ZnO QD表面にカチオン性のシランカップリング剤（長さ0.6 nm）を付与した[14]．配列後の様子を透過型電子顕微鏡（TEM）により観測した結果をFig. 4 (b) に示す．この結果，ZnO QD（直径5 nm）がDNA全長（λ-DNA，16.4 μm）に渡り等間隔（1.2 nm）に配列されることが確認され（Fig. 4 (b)およびFig. 4 (c)）QD間隔がシランカップリング剤の2倍の長さと一致していることがわかる．シランカップリング剤はCH_2基の数を制御することで0.15 nm毎に長さを変化させることが可能であるため，本手法によってQD間隔をÅ寸法で制御可能であると言える．

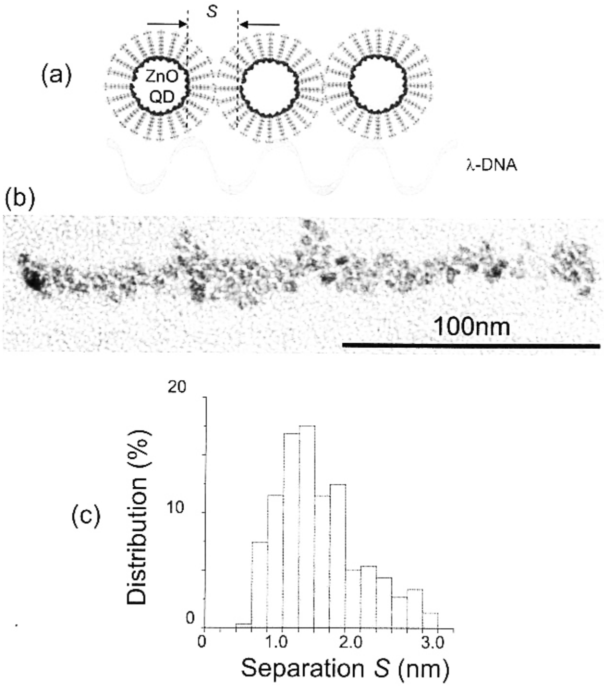

Fig. 4 (a) Schematic of ZnO QD alignment along the λ DNA. S: separation between QDs. (b) TEM image of the aligned ZnO QDs. (c) Separation (S) distribution.

続いて，QD列からの発光特性を評価するために，QD付きDNAを基板上に伸長固定した．基板にはシリコンを用い，表面をカチオン性のシランカップリング剤により修飾することで，アニオン性のDNAを固定した．その際，DNAが伸長固定されるように，コミング法を用いた[15]．その結果Fig. 5 (a)の蛍光像に示されるように，

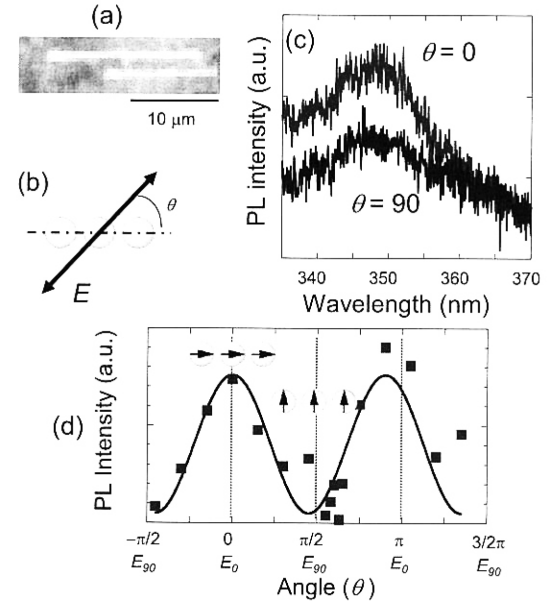

Fig. 5 (a) Charge-coupled device image of the stretched λ DNA. (b) Incident light polarization dependence of PL intensity. θ: Polarization angle with respect to the direction along the QD chains. (c) Typical PL spectra obtained at θ = 0 and 90. (d) Incident light polarization dependence of the PL intensity obtained at $\lambda = 350$ nm. Schematics of the equivalent total dipole strength under d E_{90} and e E_0.

DNA上に配列されたQD列が孤立して直線上に配列されていることがわかる．

さらにこのQD列の偏光特性を測定した．QD列の方向に対して，入射光の偏光方向とのなす角度(θ)とする．$\theta = 90°$の場合と比較して，$\theta = 0°$となったときに，発光強度が強くなった(Fig. 5 (c))．ここで，得られた発光スペクトルのピーク波長である350 nmは直径5 nmのZnO QDからの基底準位からの発光に対応している．そこで，波長350 nmにおける発光強度について，入射角依存性を調べた結果をFig. 5 (d)に示す．この偏光依存性からも，QD列に対して入射偏光が平行であるときに，発光強度が強くなることが明らかになった．QD列に対して平行偏光の時に発光強度が強くなる理由は，各QDに励起された双極子が，QD列間で結合し，大きな強度の双極子となり，強い発光強度が得られたと考えられる．このことは，言い換えるとQD間でエネルギー移動が発生したことを意味している．

5. あとがき

本稿ではZnO量子構造を用いたナノフォトニックデバイスへの応用について解説した．本稿で述べたデバイスの特長は，半導体量子構造による「量的」に変革された微小なデバイスということだけではなく，伝搬光を用いたのでは駆動することのできない機能を持つ「質的」に変革されたデバイスということである1,2)．QD列については同一寸法でのエネルギー伝送の確認を行ったが，本構造は，結晶性・寸法の制御性にも非常に優れており，ナノフォトニックスイッチに限らず，さらに複雑で高機能なナノフォトニック機能デバイス(集光器16)やパルス発生器17)など)の実現に理想的な系であると考えられる．

謝　辞

本稿をまとめるにあたり，有益な議論を頂いた川添 忠氏(東京大学)，小林 潔教授(山梨大学)，ZnOナノロッド量子構造を提供頂いた李 奎哲教授(韓国ソウル大学校)，ZnO QDの配列実験を行ってくれた劉 洋氏(東京大学)，森島 哲氏(東京大学)，ZnO QDの合成および配列のご助言を頂いた米澤 徹教授(北海道大学)，鷲津 正夫教授(東京大学)，藤田 博之教授(東京大学)に感謝します．

参考文献

1) M. Ohtsu, K. Kobayashi, T. Kawazoe, S. Sangu, and T. Yatsui: IEEE J. Sel. Top. Quant. Electr. **8** (2002) 839.

2) M. Ohtsu, K. Kobayashi, T. Kawazoe, S. Sangu, and T. Yatsui: EEE J. Sel. Top. Quant. Electr. **14** (2008) 1404.

3) T. Kawazoe, K. Kobayashi, J. Lim, Y. Narita, and M. Ohtsu: Phys. Rev. Lett. **88** (2002) 067404.

4) T. Kawazoe, K. Kobayashi, S. Sangu, and M. Ohtsu: Appl. Phys. Lett. **82** (2003) 2957.

5) W. I. Park, J. S. Kim, G.-C. Yi, and H.-J. Lee: Adv. Mater. **17** (2005) 1393.

6) H. D. Sun, T. Makino, Y. Segawa, M. Kawasaki, A. Ohtomo, K. Tamura, and H. Koinuma: J. Appl. Phys. **91** (2002) 1993.

7) D. C. Reynolds, D. C. Look, B. Jogai, C. W. Litton, G. Cantwell, and W. C. Harsch: Phys. Rev. B **60** (1999) 2340.

8) T. Yatsui, S. Sangu, T. Kawazoe, M. Ohtsu, S. J. An, J. Yoo, and G.-C. Yi: Appl. Phys. Lett. **90** (2007) 223110.

9) W. I. Park, G.-C. Yi, M. Y. Kim, and S. J. Pennycook: Adv. Mater. **15** (2003) 526.

10) W. I. Park, S. J. An, J. Long, G.-C. Yi, S. Hong, T. Joo, and M. Y. Kim: J. Phys. Chem. B **108** (2004) 15457.

11) T. Yatsui, Y. Ryu, T. Morishima, W. Nomura, T. Kawazoe, T. Yonezawa, M. Washizu, H. Fujita, and M. Ohtsu: Appl. Phys. Lett. **96** (2010) 133106.

12) E. A. Meulenkamp: J. Phys. Chem. B **102** (1998) 5566.

13) T. Yatsui, H. Jeong, and M. Ohtsu: Appl. Phys. B **93** (2008) 199.

14) T. Yonezawa, S. Onoue, and N. Kimizuka: Chem. Lett. **31** (2002) 1172.

15) H. Oana, M. Ueda, and M. Washizu: Biochem. Biophys. Res. Commun. **265** (1999) 140.

16) T. Kawazoe, K. Kobayashi, and M. Ohtsu: Appl. Phys. Lett. **86** (2005) 103102.

17) A. Shojiguchi, K. Kobayashi, S. Sangu, K. Kitahara, and M. Ohtsu: J. Phys. Soc. Jpn. **72** (2003) 2984.

レーザーワード

励起子ポラリトン(exciton polariton)

光によって物質中に励起された価電子帯の正孔と伝導帯の電子とがクーロン力によって結びつき，一つの粒子のように振舞うと考えることができる．このような正孔と電子を一つの粒子のようにみなしたものが励起子である．さらに，この励起子と光の混ぜ合わさった状態のことを励起子ポラリトンと言い，電磁場と励起子の分極場が作る練成波である．この励起子ポラリトンを媒介として，ナノ系中の一方の微粒子から，他方の微粒子へのエネルギー移動するとき，巨視系のいろいろなエネルギー状態(中間状態)を経由する．ナノ領域では，さらに，エネルギー移動を伴わない量子力学的遷移，つまり仮想励起子ポラリトンを介した遷移が発生する可能性がある．このような仮想励起子ポラリトンの交換は，近接場光が媒介する．

(八井 崇)

一枚の写真

東京大学
大津 元一

ついに室温動作したナノフォトニック論理ゲートデバイス

ナノフォトニクスの原理にもとづく論理ゲートデバイスは日本で提案され，その低温動作が確認されていたが，このたび室温動作が実現し，実用化にむけて大きな一歩が踏み出された。**図 1(a)**はデバイス構造の断面で，メサ構造（底辺の寸法は一辺 200nm）の半導体の中に特定の寸法比をもつ微小な半導体微粒子（量子ドット：QD）が二つ含まれている。図 1(b)の写真はデバイス断面の電子顕微鏡像である。メサ構造の上辺には，出力信号光取り出し用の金ナノ微粒子が作りつけられている。このデバイスに信号光を加えると，近接場光（ドレスト光子）を介した QD 間の局所的相互作用により論理ゲート動作する。図 1(c)は半導体基板上に二次元的に高密度配列した多数のデバイスからの出力信号光スポット像の写真である。この配列中のいくつかのデバイスは NOT ゲートであり，“入力 2”の信号光があると出力信号光はない。したがってこの写真中では，そのデバイスからの光スポットは暗い。その他のデバイスは AND ゲート（光スイッチ）であり，“入力 1”と“入力 2”の信号光により出力信号光が発生するので光スポットは明るい。

QD の応用例として，センサー，太陽電池，レーザーなどが知られているが，それらは多数の QD を集団として使う技術であり，個々の QD の特性とそれらの相関を生かした応用は今までなかった。しかし，レーザー発明から 50 周年を迎える今年，上記のようにレーザーとはまったく異なる原理に基づく革新的デバイスができたことは感慨深く，光技術の新時代の到来を感じさせる。

このデバイスの構造はかくも単純なのに，なぜ今まで作られなかったのだろうか？　それは近接場光の原理を研究し，それを信号の担い手として使う発想がなかったためである。例えば，レーザーに使われる光は伝搬光であり，多数の QD を使うため，基板上にできるだけ多数の QD を高密度で成長させる必要があった。それに対しこのデバイスでは近接場光を使うので，二つの QD があれば十分である。したがって，基板の上には低密度の QD を成長させればよいが，その寸法を調節する必要がある。そこで従来技術とは大きく異なる新技術が開発された。QD 作製時の温度・原料供給量・作製時間の精密制御，QD 間の中間層形成条件の精密制御，作製条件と発光強度・発光エネルギーとの関係の系統的検討手法，メサ構造作製における加工歪みによる発光強度劣化を回避する加工技術などである。これらを実現するには忍耐強い作業が必要であったが，いったんできあがってしまうと，その構造が非常に単純・小型，かつ消費電力が従来の LSI 用電子デバイスの一万分の一と極めて低くほとんど発熱しないため，高い集積度が実現した。また作製の歩留まりも非常に高い。

従来の伝搬光を信号の担い手として使ったのでは光の回折のためデバイス寸法は小さくならず，その構造は複雑かつ消費電力は大きい。すなわち，製作のための匠（たくみ）の技を高めることのみに注力しても，従来の原理をそのまま信奉する限り，でき上がったものの性能と構造はトレードオフの関係になってしまう。それに対し今回の技術開発は，「革新的に異なる原理を考え出せば性能の高さと構造の単純さは両立する」という典型的な例であろう。

このデバイスのための新しい概念・原理は大学での基礎研究により生まれ，これに呼応して新しい作製技術手法が産業界で育ったため，このたび両者の産学連携によって世界で初めて実用化デバイスが生まれた。これは，全光動作 IC/LSI，通信用光スイッチアレイ，モバイル機器・情報機器・車載用コンピューターおよびそれらの入出力部，高感度光検出器，高効率太陽電池，フォトンコンピューター，光 FPGA，高速画像演算，超高精細超小型内視鏡用カメラ・光源などへ応用されると考えられており，その産業化の検討も始まった。なお，ナノフォトニクスの原理はデバイス応用のみでなく，微細加工，太陽電池・燃料電池などを含むエネルギー・環境技術，レアメタル代替技術，情報セキュリティー，ディスプレイなどの幅広い応用が展開されており，その実用化への取り組みも加速している。

本稿で紹介したデバイスは，新エネルギー・産業技術総合開発機構（NEDO）「低損失オプティカル機能部材技術開発」事業により開発された。

参考文献

1) 川添忠，大津元一，麻生三郎，沢渡義規，細田康雄，吉沢勝美，赤羽浩一，山本直克：“メサ構造 InAs 量子ドットを用いたナノ光論理ゲートの室温動作”，第 71 回応用物理学会学術講演会，2010 年 9 月 14–17 日，長崎大学，講演番号 16a–NK–11（光分科会内招待講演）

2) T. Kawazoe, M. Ohtsu, S. Aso, Y. Sawado, Y. Hosoda, K. Yoshizawa, K. Akahane, and N. Yamamoto: “Room–temperature nanophotonic logic gate using InAs QDs in mesa structure,” The third German–Japanese Seminar on Nanophotonics, Ilmenau, Germany, September 26–29, 2010, paper number 1 in the session: Control and logic elements

一枚の写真

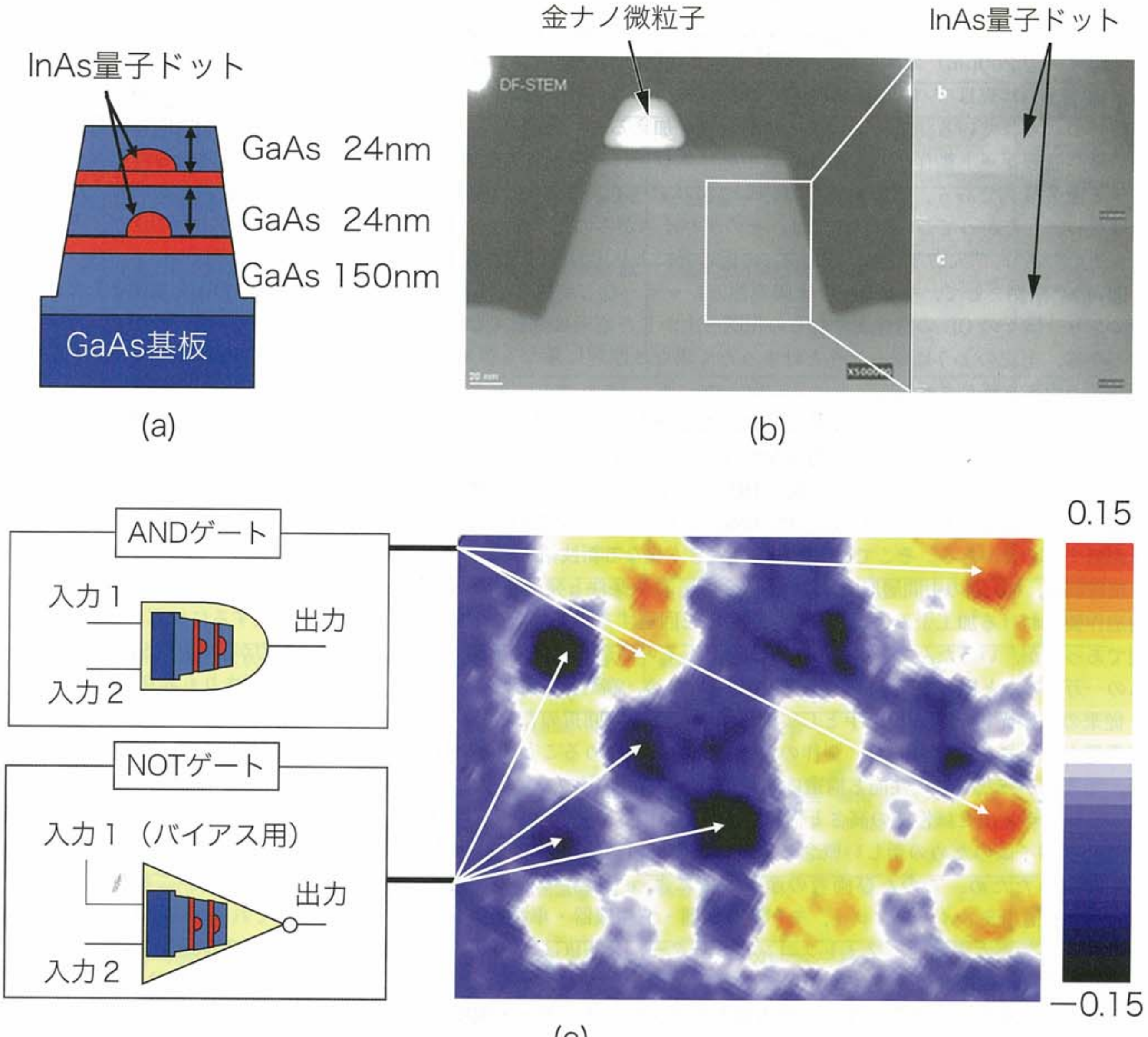

(a)　(b)　(c)

図1　開発された論理ゲートデバイスの二次元アレイ
(a) デバイスの構造，(b)断面の電子顕微鏡写真，(c)二次元アレイからの出力信号光スポットの光学顕微鏡写真

東京大学
大津 元一

日本写真学会誌 2010年73巻6号：297–302

特　集：新しい光励起系の科学　　解　説

近接場光を利用した新しい光励起系によるナノ材料加工技術

Nano-Scale Fabrication Using Optical-Near-Field

八井　崇*・大津元一*,**

Takashi YATSUI* and Motoichi OHTSU*,**

要　旨　本稿では近接場光の本質であるドレスト光子の原理について概説した後，このドレスト光子を用いたナノ加工について解説する．そして，このドレスト光子を利用した加工技術であるナノフォトニクスを用いることで，伝搬光では原理的に不可能な形態の微細光加工の実際について列挙する．

Abstract　This paper reviews the specific nature of nanophotonics, i.e., a novel optical nano-technology, utilizing dressed photon excited in the nano-material. As examples of nanophotnic fabrication, optical near-field etching and increased spatial homogeneity of contents in compound semiconductors is demonstrated with a self-organized manner.

キーワード：近接場光，ナノフォトニクス，ドレスト光子，自己組織的
Key words: optical near field, nanophotonics, dressed photon, self-organized manner

1.　まえがき

近接場光を加工に用いることで，光の回折限界を超えた微細加工が可能となっている．応用例として，超高速・超高密度光記録1)，近接場光リソグラフィー2) などがある．上記の手法では，光の局在性を利用しており超高分解能を達成している．しかしながら，これらの技術開発は寸法を微細化したいわば「量的変革」である．これに対して，近年伝搬光とは異なる近接場光特有な性質を活かした「質的に変革」された加工技術が達成されている．一例として，寸法依存共鳴現象の発見により3)，従来はいわゆる一筆書き加工であった微細加工の分野において一括大面積加工の可能性をもたらした4)．本稿では，このような一括加工技術のうち，フォノン援用励起過程の特長を積極的に活かした一括加工技術について紹介する．

2.　フォノン援用励起過程を用いた光化学反応

本節ではナノフォトニクス特有な反応であるフォノン援用励起過程を用いた光化学反応について概説する．まず，ナノ寸法物質に光を照射したときに発生した分極が，周囲に大きな機械的ひずみを誘起し，その結果，コヒーレントフォノンを局所的に生成する場合がある（Fig. 1 (a)）5–6)．これは熱源とはならず，励起子ポラリトンとフォノンとの混合状態である励起子フォノンポラリトン，言い換えるとナノ寸法物質間の近接場光相互作用を媒介する仮想励起子フォノンポラリトン（ドレスト光子）を形成する．すなわち，ナノ寸法物質の励起子ポラリトンのエネルギーとフォノンのエネルギーが，近接するナノ寸法物質に移動可能となる．

このエネルギー移動を使うと，入射光の光子エネルギーが近接するナノ寸法物質中の電子を励起準位に励起させるほど高くなくとも（すなわち断熱過程による光化学反応が起こらなくとも），フォノンのエネルギー移動により近接物質中の分子振動が誘起され，分子振動エネルギー準位を介した多段階励起により電子が励起される（フォノン援用励起過程，Fig. 1 (b)）．従って，従来の加工で使われる紫外光などの短波長光源が不要となる．さらには，ドレスト光子が励起されるナノ物質の周りのみで反応が励起されるため，従来の伝播光加工において必要であった近接場光発生用のためファイバプローブやマスクが不必要となり，高効率に一括加工を実現することが可能となる．

この非断熱励起過程の現象は，近接場光化学気相堆積（Chemical Vapor Deposition: CVD）において最初に実証された7)．近接場光CVD法の一例として，亜鉛（Zn）ナノ微粒子

平成22年11月18日受付・受理　Received and accepted 18th, November 2010

* 東京大学大学院工学系研究科電子工学専攻　〒113-8656　東京都文京区弥生 2-11-16
School of Engineering, The University of Tokyo, 2-11-16 Yayoi, Bunkyo-ku, Tokyo 113-8656, Japan
** 東京大学大学院工学系研究科ナノフォトニクス研究センター　〒113-8656　東京都文京区弥生 2-11-16
Nanophotonics Research Center, The University of Tokyo, 2-11-16 Yayoi, Bunkyo-ku, Tokyo 113-8656, Japan

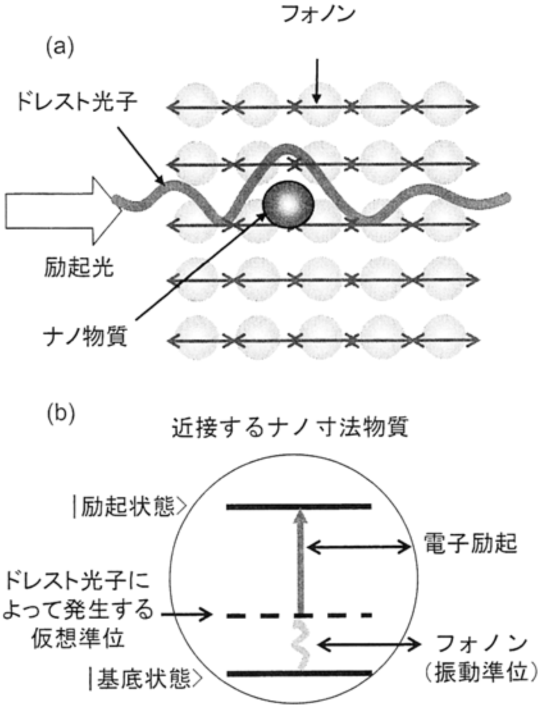

Fig. 1 (a) ナノ物質におけるドレスト光子生成の概念図. (b) 隣接するナノ物質におけるフォノン援用励起過程.

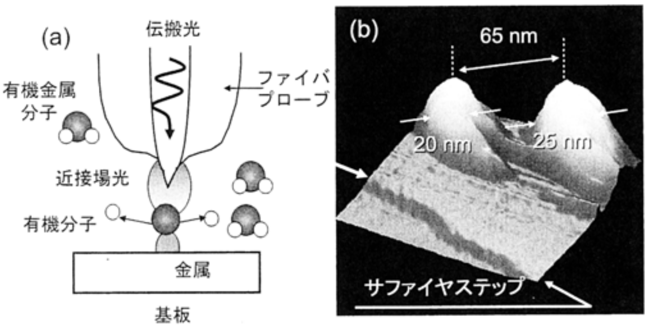

Fig. 2 (a) 近接場光 CVD の概念図. (b) 波長 325 nm の光によって堆積された Zn 原子の表面形状像.

の堆積が行われた．亜鉛の原料としてジエチル亜鉛（Diethyl Zinc: DEZn）分子を用い，DEZn 雰囲気中のチャンバーに近接場光発生するための先鋭化ファイバを導入する（Fig. 2 (a)）．ここで DEZn の吸収端波長は波長 300 nm であるが，これよりも長い波長である 325 nm の光を導入した場合でも，亜鉛ナノ微粒子の堆積が確認された（Fig. 2 (b)）[8]．これは，先鋭化ファイバ先端にドレスト光子が発生し，その結果 DEZn が分解され Zn ナノ微粒子が堆積した．また，堆積結果の表面形状像から，Zn ナノ微粒子近傍での堆積は発生しておらず，堆積前のサファイヤ基板の原子ステップが観測されていることからも，近接場光はナノ物質近傍のみ発生していることがわかる．

以上述べた非断熱光化学反応の原理を利用した一括加工の例について以下に紹介する．

3. 非断熱光化学反応によるオングストローム平坦化[9]

近年の光産業は目覚しい発展を遂げており，この発展を支えるレーザ機器において，高出力化，短波長化，短パルス化への要望が強まっている．このような産業界の要請に答える為には，レーザ機器を構成するレンズやミラー等の光学素子の高性能化を達成する必要がある．光学素子の高性能化にとって現在一番の問題となるのが表面粗さ（以下 R_a 値）の低減である．これは，表面粗さが大きいと，

①光学素子表面での散乱損失が大きくなる
②レーザ損傷閾値が上げられない

などの問題が生じるためである．ここで，R_a 値は平均線（面）からの絶対値偏差の平均値として下記の式（1）で表される（Fig. 3）．

$$R_a = \frac{1}{l}\int_0^l |f(x)|dx \cong \frac{1}{n}\sum_{i=1}^{n} |f(x_i)| \qquad (1)$$

（l：測定長さ，dx：AFM 測定時の面内分解能に対応，$|f(x)|$：平均線からの表面高さの絶対値，n：評価時の測定点数.）

しかしながら，市販されている光学素子の R_a 値は 2 ～ 5 Å 程度であり，近年，下げ止まりを余儀なくされている．その原因のひとつは，光学素子の製造方法にある．現在，光学素子は機械化学方式と呼ばれる方法により製作されており，その手法は，研磨パットの間に，被研磨材料であるガラスを挟み，研磨剤（酸化セリウム等）を流しながら擦る．この方法では，研磨パットの平坦性や研磨剤の粒径などの制限から，R_a 値は 2 Å 程度が限界になっている．さらに，細かい領域での凹凸だけでなく，大面積に渡る溝（スクラッチ）や数十 nm の穴（ディグ）が発生する．以上の現状より，光学素子の高性能化（R_a 値低減）の為には，全く新しい手法による研磨方法が必要となっている．上記の問題を解決するために，従来の機械化学的手法ではなく，近接場光エッチングを使うことにより，次世代レーザ用光学素子向けの平坦化基板を実現する技術について説明する．

紫外領域を中心に，ミラー基板として最も需要の大きい合成石英を用いて，近接場光エッチングの詳細を紹介しよう．合成石英をエッチングする気体としては塩素ラジカル（Cl^*：

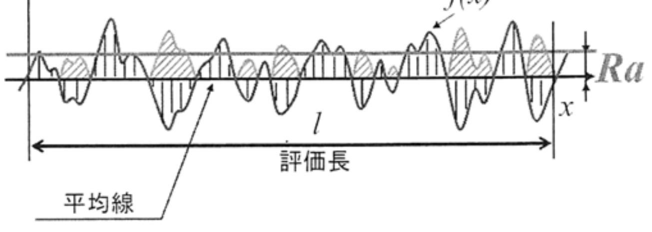

Fig. 3 表面粗さ R_a の定義.

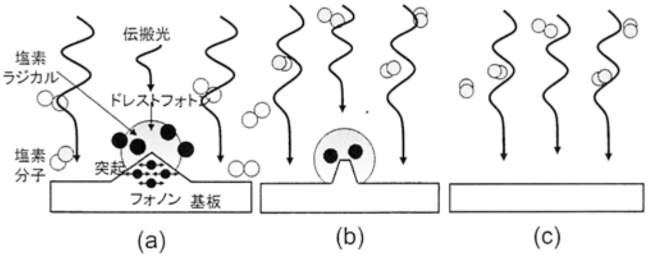

Fig. 4　近接場光エッチングの概念図.

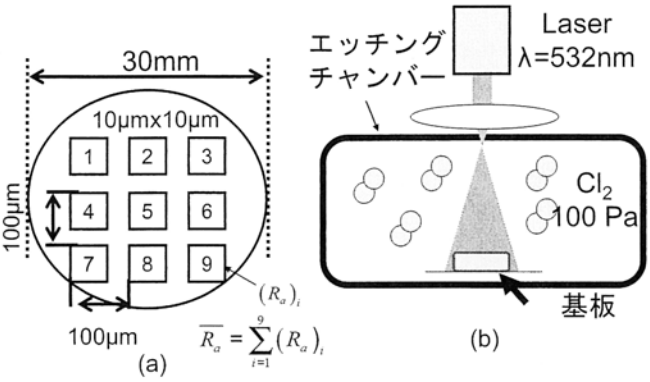

Fig. 5　(a) 表面形状測定の概念図. $(R_a)_i$：領域 i における R_a.
(b) 近接場光化学エッチング実験の概念図.

塩素分子が分解されたもの）がある．合成石英とは反応しない不活性な塩素分子（光吸収端波長 400 nm [10]）雰囲気中に基板を導入し，レーザ光（波長 532 nm）を照射する（Fig. 4 (a)）．この光の波長は光吸収端波長より長いので，塩素分子に吸収されず基板とは反応しない．一方，この光により，基板表面の局所的な凹凸部に近接場光が発生すると非断熱光化学過程 [9][11][12] により塩素分子は分解し，塩素ラジカルが発生する（Fig. 4 (a)）．その結果，この塩素ラジカルが合成石英表面と反応し，凹凸構造のみがエッチングされ基板が平坦化される（Fig. 4 (b)）．そして，最終的に基板に凹凸部がなくなると近接場光は発生しなくなるため，反応が自動的に停止し余計なエッチングを防ぐことが可能となる（Fig. 4 (c)）．

R_a 値の評価方法には，原子間力顕微鏡（AFM）を用いる．従来，R_a 値の観測には，白色干渉計が用いられているが，横分解能が波長程度と大きく，また R_a 値の測定限界能が 5 Å 程度であるため，横分解能が 10 nm 程度で，凹凸の分解能が 0.1 A程度であるAFMを使用する．AFMでは走査範囲が10 μm と狭いため，測定領域による誤差が大きくなる．そこで，平行平面基板の中心付近 9 点を 100 μm ピッチでAFMにより測定を行い（Fig. 5 (a)），各エリアで算出される表面粗さ $(R_a)_i$ の値を得る．その値を平均した

$$\overline{R_a}=\sum_{i=1}^{9}(R_a)_i \tag{2}$$

によってその基板の表面粗さ R_a 値を決定する．基板エッチングのためのガスには塩素を選択し，塩素導入後のチャンバーの圧力を 100 Pa とする．照射光源についてはレーザ（波長 532 nm）を使用する（Fig. 5 (b)）．

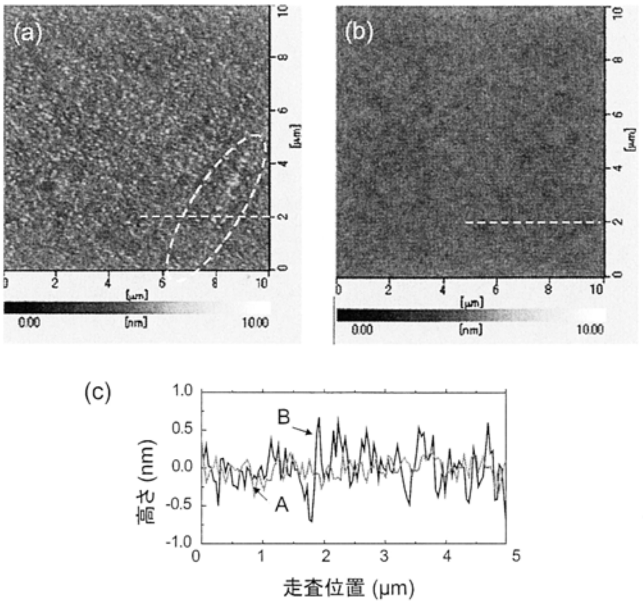

Fig. 6　堆積前 (a) および堆積後 (b) の AFM 像. (c) AFM 像の断面図.
曲線 A：堆積前，曲線 B：堆積後.

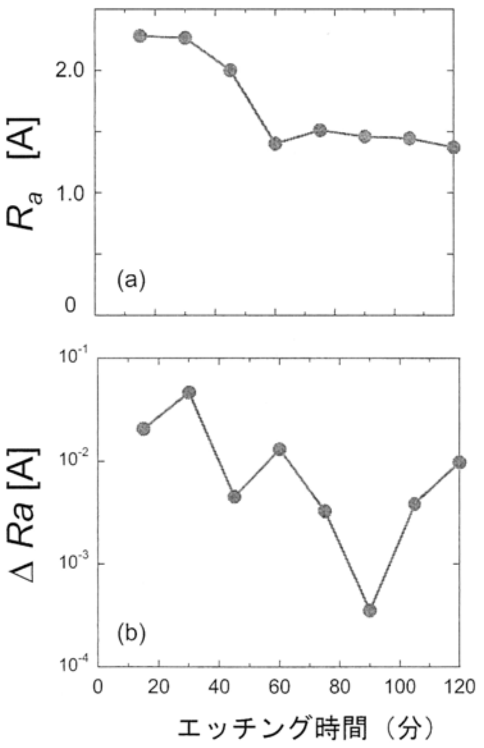

Fig. 7　エッチング時間依存性. (a) R_a の平均値（$\overline{R_a}$），(b) R_a の標準偏差（ΔR_a）.

Fig. 6は近接場光エッチング前後のAFM像の比較を示している．この比較像より表面の凹凸が低減することが明らかである．さらに，Fig. 6 (a) に示されるように，近接場光エッチング前には多く見られたスクラッチ（白楕円の内側）がなくなっていることが分かる．このAFM図の変化をより詳細に比較するために，それぞれの像における白破線を通る断面図を Fig. 6 (c) に示す．この図からピーク–バレー値が近接場光エッチングによって 1.2 nm から 0.5 nm に減少していることが分かる．

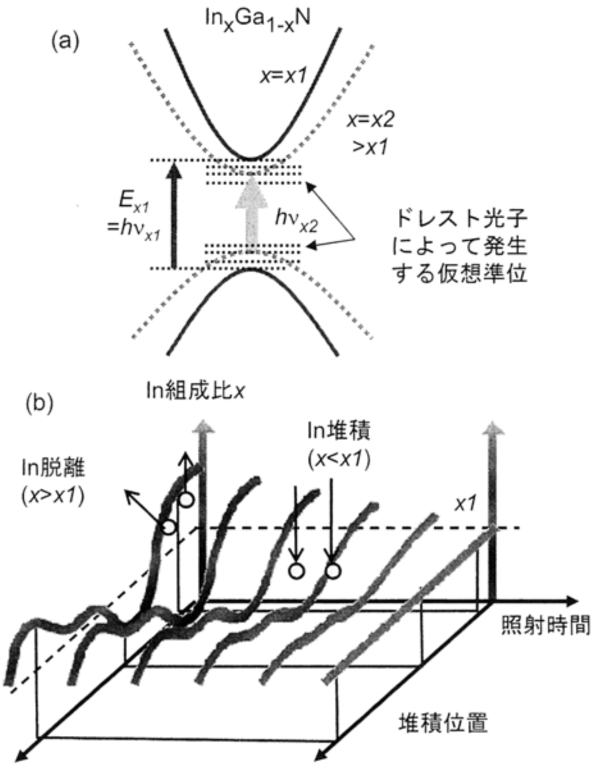

Fig. 8　(a) 非断熱光励過程による In 組成比制御の概念図．(b) 脱離用光源を照射して堆積される $In_xGa_{1-x}N$ の組成 (x) 分布の場所依存性．

最後に R_a 値の平均値のエッチング時間依存性を Fig. 7 (a) に示す．この結果より，基板への光照射時間に応じて単調に表面粗さ R_a 値が減少する結果となっている．光照射時間 120 分では，R_a 値は 1.4 Å まで減少する．この値は 9 点での平均であり，その中で得られた R_a 値として最小 1.1 Å である．また，各照射時間における R_a 値の分散（Fig. 7 (b)）も光を照射することで減少することが分かる[9]．

本手法は光化学反応を利用したものであるため，平坦基板のみならずレンズやミラーなどの曲率を有する基板や，中空レンズの内壁の平坦化など，従来の研磨技術では全く不可能な加工法への応用にも展開が期待される．

4.　非断熱光化学反応に基づく組成制御[13]

2 節で述べた非断熱光化学反応を多元系物質の堆積に利用すると組成制御が可能となる．薄膜堆積中のナノ粒子では近接場光により物質内に格子モードが励起されるため，この格子モードに共鳴する光を照射しながら堆積を行うと，その光がバンド端よりも低い光子エネルギーであっても強く吸収される（Fig. 8 (a) 参照）．このため堆積物質中において，In の組成比が高くなろうとすると，In 組成比の高い粒子が選択的に近接場光を吸収されるため脱離が発生する[3)4)]．上記の結果，脱離用に用いた光源のフォトンエネルギーよりも高いバンド端を有する InGaN（In 組成比としては低い）のみが堆積され，堆積場所による In 組成比の均一化が実現する（Fig. 8 (b) 参照）．

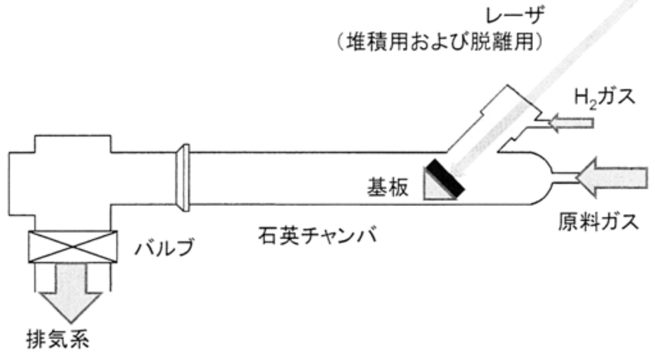

Fig. 9　光 CVD による InGaN 堆積の実験系．

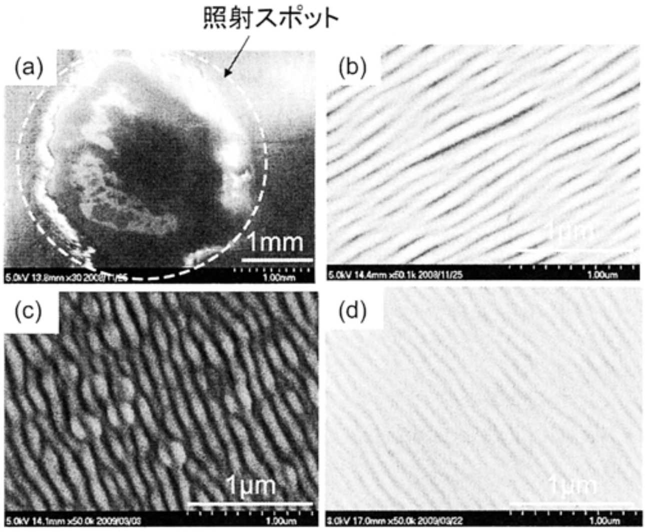

Fig. 10　堆積結果の SEM 像．(a) 全体像．TEI 流量 r_{TEI} 依存性：(b) $r_{TEI}=0$ sccm, (c) $r_{TEI}=2.5\times10^{-3}$ sccm, (d) $r_{TEI}=5.0\times10^{-3}$ sccm.

脱離用光源を用いた InGaN 中の In 組成比制御の実験の予備実験として，通常の光 CVD による InGaN の成長を行った（Fig. 9）．光 CVD における堆積用光源には Nd:YAG レーザの 5 倍波（波長 213 nm，パルス幅 3 ns，繰り返し周波数 20 Hz，出力 10 mJ）を用いた．サファイア（0001）基板を使用し室温で堆積を行った．原料ガスは，V/III 比が 40,000 となるようにアンモニア（NH_3）およびトリメチルガリウム（TMG）の流量を，2000 sccm・0.5 sccm とした．堆積はいずれも 60 分であった．

Fig. 10 に In 原料となるトリエチルインジウム（TEI）の流量（r_{TEI}）を変化させて堆積した結果を示す．この結果，光照射スポット内部への堆積が確認された（Fig. 10 (a)）．また，In 流量を変化させた場合の表面形状の電子顕微鏡像（SEM）から（Fig. 10 (b)–(d)），何れの場合にも縞状形状が確認された．

次に，堆積物の組成比を見積もるために，発光スペクトルを測定した．励起には CW の He-Cd レーザ（波長 325 nm）を用い，基板温度 5 K で測定を行った．その結果を Fig. 11 (a) に示す．この結果から，TEI の流量（r_{TEI}）の増大に伴い，発光スペクトルのピークエネルギーが低エネルギー側にシフトする結果が得られた．このピーク値から In 組成比を推定し[14]，この In 組成比と，原料ガスの TEI・TMG の供給流量比との

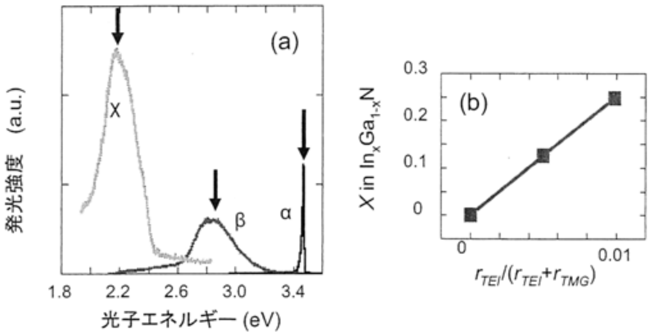

Fig. 11　(a) PL スペクトル．r_{TEI}=0 sccm（曲線 α），r_{TEI}=2.5×10^{-3} sccm（曲線 β），r_{TEI}=5.0×10^{-3} sccm（曲線 γ）．測定温度 5 K.（b）原料ガス供給流量比（$r_{TEI}/(r_{TEI}+r_{TMG})$）と In 組成比.

関係を Fig. 11 (b) に示す．その結果，両者には比例関係が見られ，光 CVD においても，原料ガスの流量比によって In 組成比が制御可能であるという結果が得られた．ガス流量による In の組成制御は熱を用いた有機金属 CVD（Metal-organic chemical vapor deposition; MOCVD）においては報告があったが，光 CVD においては世界初の成果である．

以上の実験に続いて，光 CVD に脱離用光源を導入した場合の堆積結果について述べる．光 CVD による堆積用光源には Nd:YAG レーザの 5 倍波を用い，基板をサファイア（0001）とし室温で堆積（60 分）を行った．原料ガスは，NH_3，TMG の流量を，2000 sccm・0.5 sccm とした．

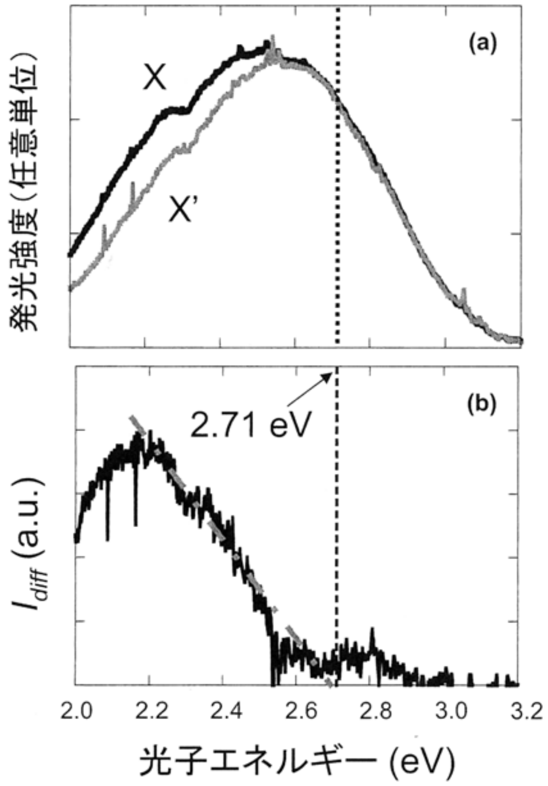

Fig. 12　脱離用光源を同時照射して堆積した InGaN からの PL スペクトル．(a) 曲線 X：堆積用光源のみ，曲線 X'：堆積用光源＋脱離用光源（2.71 eV），TEI：2.5×10^{-3} sccm．(b) 曲線 X と曲線 X' の差スペクトル．

以上の堆積用光源に加えて，脱離用光源として，2.71 eV（波長 457 nm：青色）を照射した結果を曲線 X'（Fig. 12 (a)，r_{TEI}=2.5×10^{-3} sccm）に示す．脱離用光源を照射しなかった場合の結果（Fig. 12 (a) の曲線 X）との差分強度曲線 I_{diff} から（Fig. 12 (b)），脱離用光源の光子エネルギー以下において発光強度の低減が見られた．この結果，スペクトルの半値幅として 50 meV 程度の減少を確認した．すなわち，Fig. 8 で説明した通り，脱離用光源によって，In 組成比の高い（つまりは発光のフォトンエネルギーが低い）成分が脱離され，In 組成比の均一化が達成されたことを示す結果が得られた．同様な結果は，脱離用光源のフォトンエネルギーを変化させた場合でも観測された．Fig. 13 に，脱離用光源として 2.33 eV（波長 532 nm：緑色）を用いた場合の結果を示す（曲線 Y'［Fig. 13 (a)］：r_{TEI}=2.5×10^{-3} sccm，および曲線 Z'［Fig. 13 (a)］：r_{TEI}=5.0×10^{-3} sccm）．それぞれの場合についての脱離用光源を照射しなかった場合の結果（Fig. 13 (a) の曲線 Y および Z）との差分強度曲線 I_{diff} から（Fig. 13 (b)），脱離用光源の光子エネルギーに応じて，発光強度が低減される波長領域の変化が観測された．

本実験で示された結果は光脱離反応に起因するため，MOCVD 法[15] や，分子線エピタキシー法[16]，パルスレーザ堆積法[17] など他のあらゆる堆積法にも適用可能であると期待される．また，同時に InGaAs[18] などの他の化合物半導体の堆積についても同様な効果が期待される．

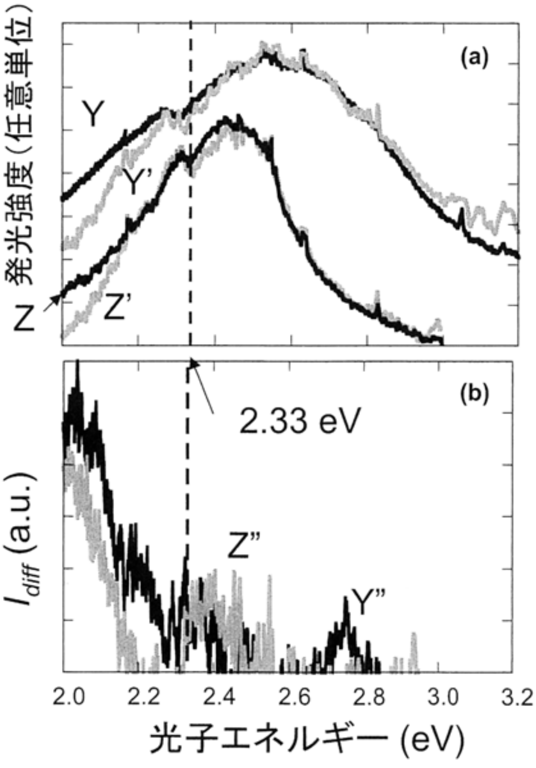

Fig. 13　脱離用光源を同時照射して堆積した InGaN からの PL スペクトル．(a) 曲線 Y：堆積用光源のみ，曲線 Y'：堆積用光源＋脱離用光源（2.33 eV），TEI：2.5×10^{-3} sccm．曲線 Z：堆積用光源のみ，曲線 Z'：堆積用光源＋脱離用光源（2.33 eV），TEI：5.0×10^{-3} sccm．(b) 曲線 Y"：曲線 Y と曲線 Y' の差スペクトル．曲線 Z"：曲線 Z と曲線 Z' の差スペクトル．

5. あとがき

本稿では，ナノフォトニック加工の例として「表面平坦化」と「組成制御」について紹介した．これらは，全く異なる応用例であるが，「フォノン援用励起過程に基づく光化学反応」であり，従来の伝搬光の概念では達成し得ない，「質的に変革」された革新技術である．このように，ナノフォトニック加工は，多様な光システム実現のための基盤技術として発展しており，今後は多様な分野に波及すると考えられる．当面は，これらの応用分野を精選して技術レベルをさらに高めることが重要であろう．

謝辞

本研究を遂行するにあたり，多大なる協力を頂いた川添忠（東京大学），野村航（東京大学）の各氏に深く感謝致します．本稿で紹介させていただいたオングストローム平坦化の研究についてデータをご提供下さった多幡能徳，平田和也（シグマ光機株式会社）の各氏，および組成制御の研究についてデータをご提供下さった伊藤圭一，川村博（日東光器株式会社），水村通伸（株式会社ブイ・テクノロジー）の各氏に深く感謝致します．

参考文献

1) T. Yatsui, M. Kourogi, K. Tsutsui, J. Takahashi, M. Ohtsu, Opt. Lett., **25**, 1279 (2000).
2) Y. Inao, S. Nakasato, R. Kuroda, M. Ohtsu, Science Direct Microelectronic Engineering, **84**, 705 (2007).
3) T. Yatsui, S. Takubo, J. Lim, W. Nomura, M. Kourogi, M. Ohtsu, Appl. Phys. Lett., **83**, 1716 (2003).
4) T. Yatsui, W. Nomura, M. Ohtsu, Nano Lett., **5**, 2548 (2005).
5) T. Kawazoe, K. Kobayashi, S. Takubo, M. Ohtsu, J. Chem. Phys., **122**, 024715 (2005).
6) Y. Tanaka, K. Kobayashi, J. Microsc., **229**, 228 (2008).
7) T. Kawazoe, Y. Yamamoto, M. Ohtsu, Appl. Phys. Lett., **79**, 1184 (2001).
8) T. Yatsui, T. Kawazoe, M. Ueda, Y. Yamamoto, M. Kourogi, M. Ohtsu, Appl. Phys. Lett., **81**, 3651 (2002).
9) T. Yatsui, K. Hirata, W. Nomura, Y. Tabata, M. Ohtsu, Appl. Phys. B: Lasers and Optics, **93**, 55 (2008).
10) R. Kullmer, D. Büerle, Appl. Phys. A, **43**, 227 (1987).
11) T. Kawazoe, M. Ohtsu, Y. Inao, R. Kuroda, J. Nanophotonics, **1**, 011595 (2007).
12) H. Yonemitsu, T. Kawazoe, K. Kobayashi, M. Ohtsu, J. Luminescence, **122–123**, 230–233 (2007).
13) T. Yatsui, S. Yamazaki, K. Ito, H. Kawamura, M. Mizumura, T. Kawazoe, M. Ohtsu, Appl. Phys. B: Lasers and Optics, **97**, 375 (2009).
14) M. D. McCluskey, C. G. Van de Walle, C. P. Master, L. T. Romano, N. M. Johnson, Appl. Phys. Lett., **72**, 2725 (1998).
15) S. Nakamura, Science, **281**, 956 (1998).
16) R. Singh, D. Doppalapudi, T. D. Moustakas, L. T. Romano, Appl. Phys. Lett., **70**, 1089 (1997).
17) A. Kobayashi, J. Ohta, H. Fujioka, J. Appl. Phys., **99**, 123513 (2006).
18) K. Akahane, N. Ohtani, Y. Okada, M. Kawabe, J. Cryst. Growth, **245**, 31 (2002).

低消費エネルギーを実現するナノフォトニクス技術

成瀬　誠*,**，川添　忠**，大津　元一**

Nanophotonics for Energy Applications

Makoto NARUSE*,**, Tadashi KAWAZOE** and Motoichi OHTSU**

This paper reviews the principles of nanophotonics and their impacts to energy applications. Optical near-fields, appearing in the vicinity of nano-scale materials, break through the spatial density restrictions posed by the diffraction of conventional propagating lights. In addition, further unique features have been developed by the dressed photon model that unifies photons and material excitations on the nanometer scale. This article demonstrates that the dress photon, thanks to its abilities in realizing optical excitation transfer and phonon-assisted processes, leads to another breakthrough in overcoming the limitations of conventional optical technologies. Their impacts to energy-related applications are shown in (1) information and communications devices and systems based on optical excitation transfer, (2) phonon-assisted visible light emission by infrared light excitations, (3) phonon-assisted photovoltaic devices sensitive to conventionally transparent wavelengths, and (4) phonon-assisted optical near-field lithography realizing nanostructures without the use of short-wavelength light irradiation. These demonstrations indicate that nanophotonics provides versatile qualitatively novel functions into optical technologies for green innovations.

Key words: nanophotonics, dressed photon, optical near-field, optical excitation transfer, phonon-assisted process, energy efficiency, energy applications, wavelength conversion, photovoltaic device

波長より微小な寸法での光と物質の相互作用を活用するナノフォトニクス[1]には，広範な応用に対する多大なインパクトが予測されている[2,3]．物質近傍の近接場光を用いることで従来の光（伝搬光）に不可避の回折限界が打破され，「光の微小化」が実現された．さらに，近接場光とはナノ寸法において光子と物質中の励起が結合した場であり，物質励起の衣をまとった光子（dressed photon，以下ドレスト光子と記す）ととらえることで，光の微小化にとどまらない新しい機能が可能になった[4,5]．本稿は，低消費エネルギー化を機軸に，ドレスト光子が可能にする原理と技術を，① processing（処理），② transformation（信号変換），③ energy harvesting（エネルギー生成），④ manufacturing（加工）という4つの応用に整理しつつ，現状と今後を展望する．

ドレスト光子はナノ寸法程度に局在しているため，伝搬光での光電子相互作用に用いられてきた光の長波長近似が成り立たない．その結果，従来は電気双極子禁制なエネルギー遷移もドレスト光子では許容されることとなる[5]．これに基づいてドレスト光子を信号の担体とした光デバイスが可能になる．1章では，従来の電子デバイスとの原理的な差異を踏まえながらドレスト光子に基づいたデバイスのエネルギー消費性能を議論する．

ドレスト光子は格子振動（フォノン）と結合することも可能であり，ナノ寸法での物質の形状や寸法によっては，入力となる伝搬光の光子エネルギーよりも大きなエネルギー状態へ物質中の電子を励起できる．これを本稿では「ドレスト光子によるフォノン援用過程」とよぶ．これを生かして，赤外光から可視光へのエネルギー変換（2章），従来受光感度のなかった波長の光に対する光電流生成（3章），短波長光を必要としない微細加工（4章）などの応用

---

*(独)情報通信研究機構新世代ネットワーク研究センター（〒184-8795 小金井市貫井北町 4-2-1）　E-mail: naruse@nict.go.jp
**東京大学大学院工学系研究科電気系工学専攻；ナノフォトニクス研究センター（〒113-8656 東京都文京区弥生 2-11-16）

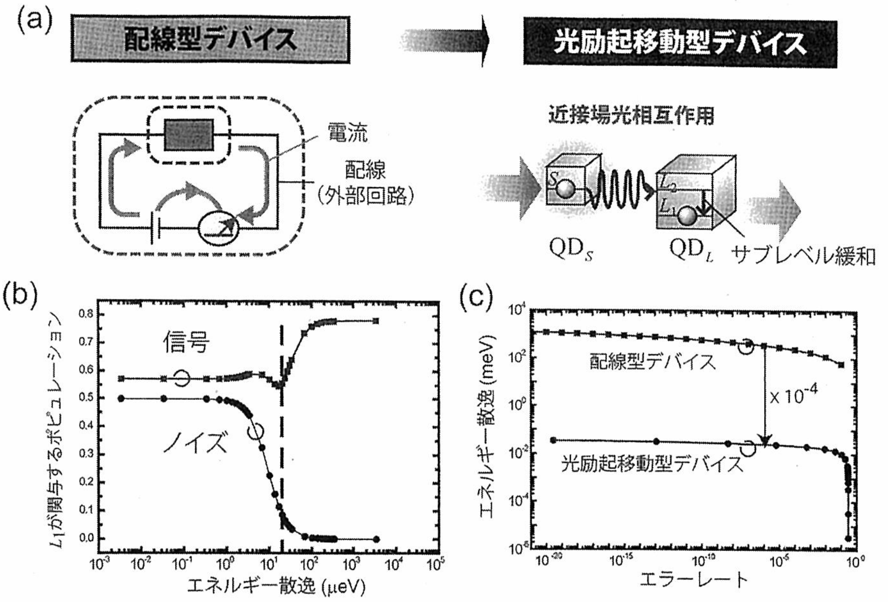

図1　ドレスト光子による「processing」と消費エネルギー性能．(a) ドレスト光子に基づいた「配線型」から「光励起移動型」への構造の転換．(b) (c) 光励起移動型デバイスにおける信号輸送の必要最小エネルギー散逸．理論上は配線型デバイスより約10^4の改善が可能．

が示されており，各々低消費エネルギー化へのインパクトとともに議論する．

1.　ドレスト光子によるprocessing（処理）とエネルギー

情報通信技術における省エネルギー化の旗手として光技術への期待は非常に高く，世界的に研究開発が活発化している6)．そこでは，伝搬光（自由光子）には質量がなく，きわめて広帯域であること，抽象的には光の「透明性」を最大限に生かすこと，具体的には光電変換過程を可能な限り省略し，電気処理に不可避の膨大な電力消費を削減することが，省エネルギー化に向けた最も重要なポイントのひとつになる（そのため例えば全光型のルーティング技術7)やアーキテクチャー技術8)が期待されている）．このことは，同時に，電子技術が主たる役割を担っているデータ処理（processing）については，従来の光技術が不十分であり，また微細化限界に迫りつつある電子技術がエネルギー消費削減の危機を迎えていることの表出でもある6)．この問題を根本から解決するには，信号の輸送に必要な最小エネルギー散逸が何によって支配されるかという基本原理に立ち返る必要がある．ドレスト光子の技術は「配線型から励起移動型へ」というデバイスの基本構造の転換を可能にしており（図1 (a)），これが消費エネルギーの低減に結びつく．

一般に，信号の輸送を確定するにはエネルギー散逸が必要である9)．電気配線を必要とするナノ電子デバイスにおける必要エネルギー散逸は，ナノ電子デバイス自身の性質ではなく，それを取り巻く外部回路が決定づけている（そのために，外部回路において発生するエネルギー散逸を傍受することで内部回路の秘密情報を読み出し得るという，耐タンパー性とよばれるセキュリティー上の重要な問題も生じる10)）．これに対し，ドレスト光子による信号輸送は，輸送先となるナノ微粒子において生じるエネルギー散逸が決定づけている10)．これを図1 (a) 右の模型で掘り下げる．半径がR_Sおよび$R_L=1.43R_S$である球形型の量子ドットQD_SおよびQD_Lが近接配置されたシステムにおいて，QD_Sの (1, 0) 準位 (S) に存在する励起子は近接場光相互作用を介して伝搬光では禁制されていたQD_Lの (1, 1) 準位 (L_2) へ遷移できる1)．QD_Lでは (1, 1) 準位の下方に (1, 0) 準位 (L_1) が存在し，上準位から下準位への緩和は量子ドット間の相互作用時間よりも相対的に早いのでQD_Lに移動した励起子は下準位に緩和する．このような光励起移動におけるエネルギー散逸は，QD_Lの上準位L_2から下準位L_1へのサブレベル緩和に相当する．したがってL_2とL_1のエネルギー差が信号輸送に必要なエネルギー散逸である．従来の配線型デバイスと異なり，いわば「電源と信号を一体としながら」信号の輸送が行われるので，外部システムでの傍受が事実上不可能となる10)．さらに，理論上はこの最小エネルギー散逸はきわめて小さく抑えることができる．以下これを簡単に示す．上記のエネルギー差が過度に微小となればSへの入力光が直接にL_1と結合し得ることになり，L_1からの出力信号が，量子ドット間の相互作用の結果として生じる「信号」(図1 (b) の■) か「ノ

イズ」（同図●）かの区別がつかない．これをエラーレートに対するエネルギー散逸として評価すると図１（c）が得られるが，ドレスト光子に基づく方式は，従来の電子デバイス（具体的にはCMOSロジックにおけるビットフリップに必要なエネルギー散逸[11]）よりも，およそ10^4倍小さい[12]．ドレスト光子による信号輸送過程は，光合成におけるエネルギー移動過程とも類似しており[13]，このようなナノ領域におけるエネルギー輸送過程の効率の高さは，ナノ寸法における複雑システム（complex system）が創発する新規なシステム機能[14,15]としても注目されている．このように，ドレスト光子の原理は「配線型から励起移動型へ」というデバイス原理の転換を可能にし，省エネルギー性能の飛躍的低減の可能性を与える．

2．ドレスト光子によるtransformation（信号変換）とエネルギー

通常，光と物質を相互作用させるには，入力となる光子のエネルギーが物質中の電子を励起するためのバンドギャップエネルギー（E_g）より大きい必要がある．E_gは材料により異なり，利用する光の波長に応じて適切な材料を選択する必要がある．このような非常に基本的な原則は，省エネルギー化に向けた根本的なハードルとなる．例えば赤外光センサーの課題を取り上げてみる．赤外光センサーには，通常InGaAsやMCT（HgCdTe）等が用いられる．ところが，これらのセンサーはノイズが大きく，検出感度を上げるためにペルチェ素子や液体窒素などの冷却機構が必要であり，結果として多大な消費電力と装置の大型化を招いている．一方，赤外光センサーの適応領域は昨今の環境問題の高まりを受け環境センサーネットワークなど急速に広がりつつある（例えば，国内携帯電話大手は全国規模で花粉やCO_2濃度等を観測し情報配信する計画の試験運用を開始した[16]．なお，環境センシング自体も情報通信ネットワークの省エネルギー化にとってきわめて重要とされている[17]）．このようなネットワークシステムは，新興国への普及も含めて大規模化が必至であり，端末となる光センサーの省エネルギー化は急務といえるが，上記のように根本的な限界があった．

この問題のブレイクスルーとなるのがドレスト光子によるフォノン援用過程である．後述のように，ナノ寸法の物質の形状に依存して発生する近接場光を介して，入力となる赤外光を波長の短い可視光に変換する．可視光に変換されれば，冷却不要で安価で小型なシリコンフォトダイオード等との組み合わせが可能になり，結果として，エネルギー消費の軽減が可能になる．従来より非線形光学結晶を用いた和周波発生による短波長変換手法が知られているが，使用波長や位相整合条件など適応条件に制約があり，高強度レーザー光源の波長変換などには有効だが，光センサーに対してはほとんど利用されていない．

フォノン援用過程を用いた赤外光–可視光の変換原理を図２（a）に示す[18]．物質系は色素微結晶等のナノ寸法の形状を有した構造である．これに赤外光が入射すると，ナノ寸法物質の突起部などの形状に依存して近接場光が発生する．近接場光は周囲の物質中の分子振動（フォノン）を励起することができる．この状態（基底状態の電子と励起状態にあるフォノン）を中間状態にして，さらに赤外光の入射によって，物質中の電子を励起状態に至らせることができる．励起された電子が再結合発光するときに可視光が発生する．図２（b），（c）に，DCM色素をナノ物質として，フォノン援用過程を用いた赤外光–可視光変換の実験例を示す．サンプルAは材料の一辺の大きさが１μm以下であり，波長800 nmの赤外光を入射させると波長700 nmの可視光が生じる．図２（b）はサンプルAのSEM像およびサンプル表面の可視発光部を画像化したものである．白色部が可視発光部を示す．一方，図２（c）のサンプルBは長さ５μmのロッド形状を有する同様のDCM色素結晶である．サンプルAに対して可視発光部が少なく，変換量は前者のおよそ10分の1に過ぎない．このように物質系の形状・寸法を制御することで近接場光とフォノンを結合させ，光エネルギーを変換するフォノン援用過程によって，従来技術が抱えていた省エネルギー化の基本的な限界をブレイクスルーできる．

なお，以上のフォノン援用過程は「長波長から短波長への変換」となるが，「短波長から長波長への変換」は１章の光励起移動で実現される（サイズ大のナノ微粒子における散逸による）．この場合には，図１（a）右における大小のナノ微粒子間の個数比を適切に制御して，微粒子間の相互作用のネットワークを最適化することで変換効率の向上が実現される[14]．また，固体照明において短波長の光が強すぎると不眠などの健康障害に結びつくことが指摘されており[19]，ドレスト光子による光エネルギー変換は「発光スペクトルのエンジニアリング」の手段にもなる．固体照明は光技術における省エネルギー化の最重要技術のひとつだが，ドレスト光子による技術は照明とヘルスケアの橋渡しなど新たな付加価値を提供する．

3．ドレスト光子によるenergy harvestingとエネルギー

２章の方式をさらに発展させ，光エネルギーを直接に電気エネルギーとして取り出し可能になれば，利用形態はさ

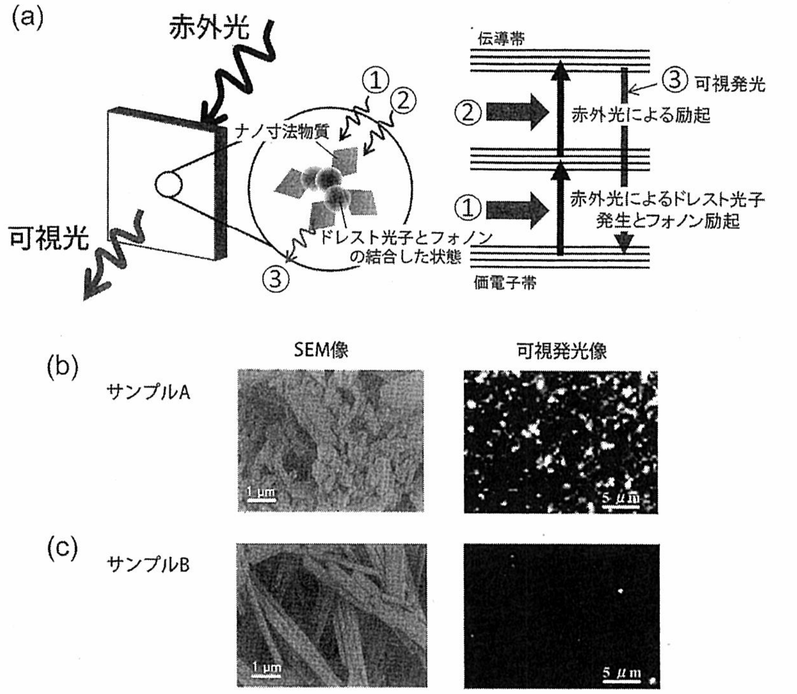

図2　ドレスト光子による「transformation」(信号変換) の例. (a) フォノン援用過程により赤外光を可視光に変換. これにより電力消費および環境負荷の大幅な低減が可能. (b) (c) フォノン援用過程は物質の形状・寸法に依存し, (b) では可視発光が多く生じているが, (c) の構造に対してはほとんど生じていない.

らに広がる. 例えば, 従来は受光感度がゼロであった帯域において光エネルギー変換の感度が生じれば, より多くの光エネルギーを回収できる. 受光の帯域を広げるという目標自体は一般的であり, 従来, 種類の異なる材料を積層するなどのアプローチがとられている. ただし, 作製プロセスの複雑化, 複数材料利用による環境負荷増大などの課題があり, その根底には, バンドギャップエネルギーが材料固有に与えられるという, 2章と同様の伝搬光と物質の相互作用の制約がある. これに対しドレスト光子によるフォノン援用過程は, 物質の形状・寸法制御で同等の機能を実現する. 加えて, フォノン援用過程による光電変換素子として機能するナノ構造を, 感度を発現させたい波長の光によるフォノン援用過程を用いて作製することで, フォノン援用過程による光電変換の効率を所望の波長において選択的に発現できる. 具体的な実証実験を参照しながら説明する[20].

有機太陽電池としてよく使用されているP3HT (poly (3-hexylthiophene)) を材料とした発電デバイスの作製プロセス (具体的にはP3HT上への電極作製プロセス) において, 逆バイアスをかけ, かつ「光を照射しながら」電極材料である銀のスパッタリングを行う. ここで, 照射する光の波長をP3HTの光吸収端波長である約570 nmよりも長波の660 nmに設定する. すなわち伝搬光に対してはP3HTが透明である波長の光を照射する. このとき, P3HTにおいて前章と同じ原理でフォノン援用の電子励起が起きるが, 逆バイアスのため電子正孔対は分離し, 堆積した銀電極表面には正孔が現れる. RFスパッタリングで堆積するAgは正に帯電しており, 銀電極表面の正孔と反発し, 正孔の存在しない領域へと優先的に堆積することになる. この結果, 銀電極の表面は上記のフォノン援用過程を反映した特徴的モルフォロジーに至る. このようにして作製されたデバイスは, 通常のP3HTでは感度を有さない長波長の光に対して感度を示し, 作製時に用いた波長近辺において最大感度を示す[20] (最大感度を与える波長は620 nmで, 作製時波長660 nmから40 nmだけ短波にシフトするが, これはシュタルク効果で説明できる[20]).

このように, フォノン援用過程による効果を最大化するには, 作製時にもフォノン援用過程を用いるという「循環型の発想」の有効性が示唆される. このような作製プロセスは, システムの形態と制御を同時に考慮することによって, 所望の機能をより効率的に実現する技術として注目を集めている「モルフォロジカルコンピューティング」とよばれる概念がナノスケールにおいて具現したものとみることもでき, 今後のさらなる適応領域の広がりが期待される.

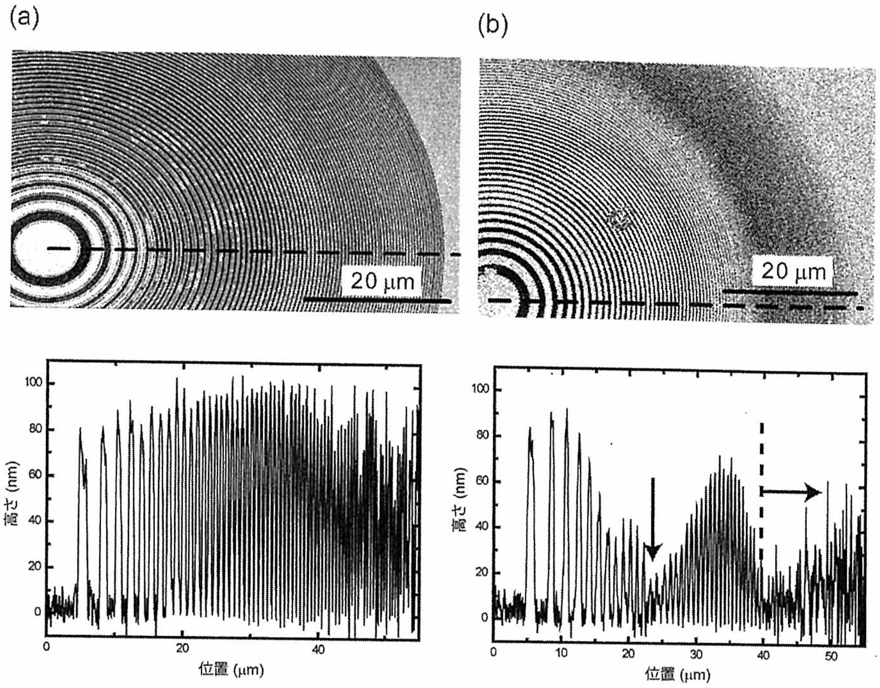

図3　ドレスト光子による「manufacturing」（加工）の例：近接場光リソグラフィー．(a) 露光光源波長（長波長光源）に対して感度を有さないレジストとマスクパターンを近接させ，フォノン援用過程を介して作製したフレネルゾーンプレート．外周まで微細パターンが明瞭に形成されている．(b) レジストが感度を有する短波長光源を用いて (a) と同じマスクパターンとレジストを近接させて作製したパターン．伝搬光の影響のため外周ではパターンが不明瞭になっている．

4.　ドレスト光子による manufacturing（加工）とエネルギー

光リソグラフィーにおける最小寸法の微細化では，伝搬光の回折現象のため極端紫外（EUV）光に代表される露光用光源の短波長化が必要である．しかしながら，このようなきわめて短波長の光源開発には膨大なコストが必要なことに加え，空調等を含めたシステム全体の装置運用のエネルギーも膨大である．これに対し，フォトマスクとフォトレジストを近接させフォトマスクの形状に依存して発生する近接場光を用いた露光戦略をとれば，短波長化光源なしで微細化を実現できる[21]．ただし，光源の波長に対してフォトマスクが露光の感度を有していれば，フォトマスクから必ず漏れ出ている伝搬光の回折成分の影響を完全に回避することは難しい．一方，「フォトレジストが感度を有さない」長波長の光を照射し，フォトレジストに対して2章，3章と同様のフォノン援用過程が生じれば，フォトマスクに対応して発生する近接場光（ドレスト光子）のみに対してパターンが生成される．

中心波長550 nm，帯域80 nmのXeランプを露光光源として，500 nmより長波長の伝搬光に対して感度がないことを確認しているFH-SP-3CLというレジストを用いて，X線光学素子用のフレネルゾーンプレート（FZP）が実現されている[22]．図3 (a) に，作製したFZPのSEM像とAFM（原子間力顕微鏡）による断面図を示す．辺縁部まで明瞭な輪帯が形成され，干渉パターンもなく，回折現象の影響を受けていないことがわかる．一方，図3 (b) に，上記レジストが伝搬光に対して感度のある450 nmのHgランプを露光光源として作製した，同パターンのSEM像および断面図を示す．このFZPの最小輪帯幅は190 nmであり，輪帯幅が光の回折限界以下になる辺縁領域において加工断面が不明瞭になっている（図3 (b) 中の右矢印）．また，輪帯幅の周期が光と干渉を起こす領域も断面が不明瞭になっている（図3 (b) 中の下矢印）．以上のように，微細なパターンを生成するには，短波長よりも長波長の光を用いたほうがむしろ有利であるという，これまでの光とは全く逆の傾向が得られている．このような微細パターンを安価な可視光源で作製可能である特徴を生かし，緑色LED 1個を光源とした低コストかつ低消費電力（5 Wh以下）の露光装置が実用化されている[23]．なお，上記で作製物としたX線光学素子は，通常，電子ビームリソグラフィー等による個別の製造工程を必要とするなど単価が高かった．上記のフォノン援用過程を用いたリソグラフィーによる大量一括加工によれば，従来の製造プロセスに必要な製造のエネルギーを劇的に低減することもできる．これは，原料採取，製造，使用，廃棄まで含め，製品が経験する全行程を通じての環境負荷を問うライフサイクルアセスメント（LCA）

とよばれる環境影響評価手法の立場からも重要である．なお，2章および3章における波長変換およびエネルギー変換デバイスが物質の形状・寸法制御で実現されたことは，稀少材料を必要とせずに同等の機能が達成できることに相当し，LCAの立場からもきわめて効果が高い．また，フォノン援用過程を用いた加工は光リソグラフィーに限定されない．ドレスト光子が突起部に強く発生することを利用した光化学エッチングによる超平坦化技術[24]が実現され，エネルギー消費の低減が見込まれている．

ナノフォトニクスが可能にする低消費エネルギー化への影響を，物質励起の衣をまとった光子（ドレスト光子）の概念を踏まえ，4つの応用領域における事例を参照しながら議論した．光技術は，情報通信，ライフサイエンス・健康，照明・ディスプレイ，セキュリティー・センサー，環境・エネルギー，加工などのきわめて広い分野に及ぶ重要技術であり，ナノフォトニクスに限らず省エネルギー化への重要課題が存在する．ただし，本稿でもたびたび指摘しているように，従来の光技術には，回折限界という空間軸にかかわる限界，物質のバンドギャップエネルギーに代表されるエネルギー軸上の原理上の限界等があり，また，適応先となる応用がシステムとして抱えている構造的課題も存在している．環境の世紀へと急速に舵が切られた昨今，ナノメートル寸法の光と物質の相互作用の本質を生かし，従来技術の基本的限界を打破する科学と技術を真剣に見据えていく必要がある．

本稿に掲載の技術は，東京大学大津研究グループの職員・学生各位ならびに産学連携研究に参画いただいている企業・独立行政法人等の関連研究員各位との共同成果による．

文　　献

1) M. Ohtsu, K. Kobayashi, T. Kawazoe, S. Sangu and T. Yatsui: "Nanophotonics: Design, fabrication, and operation of nanometric devices using optical near fields," IEEE J. Sel. Top. Quantum Electron., **8** (2002) 839–862.

2) MONA consortium: *A European roadmap for photonics and nanotechnologies* (Merging Optics and Nanotechnologies Association (MONA) consortium, 2008).

3) National Research Council: *Nanophotonics: Accessibility and Applicability* (National Academies Press, Washington DC, 2008).

4) M. Ohtsu, T. Kawazoe, T. Yatsui and M. Naruse: "Nanophotonics: Application of dressed photons to novel photonic devices and systems," IEEE J. Sel. Top. Quantum Electron., **14** (2008) 1404–1417.

5) M. Ohtsu, K. Kobayashi, T. Kawazoe, T. Yatsui and M. Naruse: *Principles of Nanophotonics* (Taylor and Francis, Boca Raton, 2008).

6) オプトロニクス2010年1月号「ネットワークの省エネ化を実現する光技術」．

7) H. Furukawa, N. Wada and T. Miyazaki: "640 Gbit/s (64-wavelength × 10 Gbit/s) data-rate wide-colored NRZ-DPSK optical packet switching and buffering demonstration," J. Lightwave Technol., **28** (2010) 336–343.

8) K. Sato and H. Hasegawa: "Prospects and challenges of multi-layer optical networks," IEICE Trans. Commun., **E90-B** (2007) 1890–1902.

9) H. Hori: "Electronic and electromagnetic properties in nanometer scales," *Optical and Electronic Process of Nano-Matters*, ed. M. Ohtsu (Kluwer Academic, Dordrecht, 2001) pp. 1–55.

10) M. Naruse, H. Hori, K. Kobayashi and M. Ohtsu: "Tamper resistance in optical excitation transfer based on optical near-field interactions," Opt. Lett., **32** (2007) 1761–1763.

11) L. B. Kish: "Moore's law and the energy requirement of computing versus performance," IEE Proc. Circ. Dev. Syst., **151** (2004) 190–194.

12) M. Naruse, H. Hori, K. Kobayashi, P. Holmstrom, L. Thylen and M. Ohtsu: "Lower bound of energy dissipation in optical excitation transfer via optical near-field interactions," Opt. Express, **18** (2010) A544–A553.

13) H. Imahori: "Giant multiporphyrin arrays as artificial light-harvesting antennas," J. Phys. Chem. B, **108** (2004) 6130–6143.

14) M. Naruse, T. Kawazoe, R. Ohta, W. Nomura and M. Ohtsu: "Optimal mixture of randomly dispersed quantum dots for optical excitation transfer via optical near-field interactions," Phys. Rev. B, **80** (2009) 125325.

15) N. Johnson: *Simply Complexity* (Oneworld Publications, Oxford, 2007).

16) NTTドコモ，報道発表資料，2009年11月．

17) 南　正輝，川村龍太郎，森川博之，平原正樹："省電力志向新世代ネットワーク"，電子情報通信学会論文誌，**J92-B** (2009) 605–614.

18) T. Kawazoe, H. Fujiwara, K. Kobayashi and M. Ohtsu: "Visible light emission from dye molecular grains via infrared excitation based on the nonadiabatic transition induced by the optical near field," J. Sel. Top. Quantum Electron., **15** (2009) 1380–1386.

19) B. A. Akins, G. Medina, T. A. Memon, A. C. Rivera, G. A. Smolyakov and M. Osiński: "Nanophosphors based on CdSe/ZnS and CdSe/SiO_2 colloidal quantum dots for daylight-quality white LEDs," *Conference on Lasers and Electro-Optics (CLEO) and the Quantum Electronics and Laser Science Conference (QELS)*, CTuNN7 (Optical Society of America, Washington DC, 2010).

20) S. Yukutake, T. Kawazoe, T. Yatsui, W. Nomura, K. Kitamura and M. Ohtsu: "Selective photocurrent generation in the transparent wavelength range of a semiconductor photovoltaic device using a phonon-assisted optical near-field process," Appl. Phys. B, **99** (2010) 415–422.

21) H. Yonemitsu, T. Kawazoe, K. Kobayashi and M. Ohtsu: "Nonadiabatic photochemical reaction and application to photolithography," J. Lumin., **122-123** (2007) 230–233.

22) T. Kawazoe, T. Takahashi and M. Ohtsu: "Evaluation of the dynamic range and spatial resolution of nonadiabatic optical near-field lithography through fabrication of Fresnel zone plates," Appl. Phys. B, **98** (2010) 5–11.

23) ナノフォトニクス工学推進機構：ドレストフォトン微細加工装置．http://www.nanophotonics.info/

24) T. Yatsui, K. Hirata, W. Nomura, Y. Tabata and M. Ohtsu: "Realization of an ultra-flat silica surface with angstrom-scale average roughness using nonadiabatic optical near-field etching," Appl. Phys. B, **93** (2008) 55–57.

(2010年6月2日受理)

[Ⅳ] PUBLISHED BOOKS

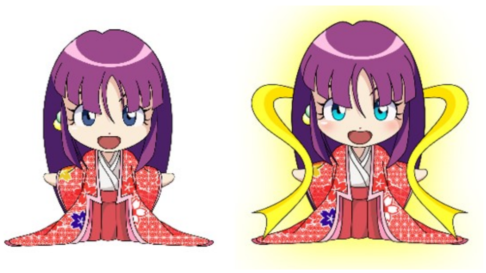

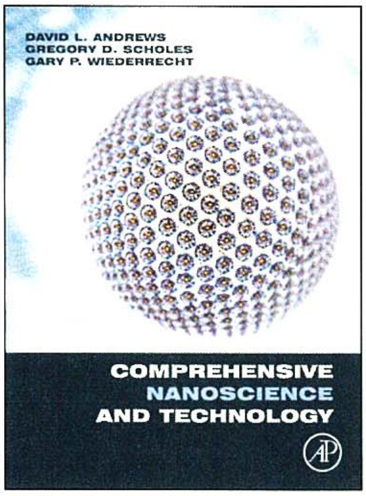

G-C Yi, T Yatsui and M Ohtsu (2011) ZnO Nanorods and their Heterostructures for Electrical and Optical Nanodevice Applications. In: Andrews DL, Scholes, GD and Wiederrecht GP (eds.), *Comprehensive Nanoscience and Technology*, volume 1, pp. 335–374 Oxford: Academic Press.

1.12 ZnO Nanorods and their Heterostructures for Electrical and Optical Nanodevice Applications

G-C Yi, Seoul National University, Seoul, Republic of Korea

T Yatsui and M Ohtsu, The University of Tokyo, Tokyo, Japan

Comprehensive Nanoscience and Technology, 2011, Vol. 1, 335-374

HANDBOOK OF NANOPHYSICS

6

Nanoelectronics and Nanophotonics

Edited by

Klaus D. Sattler

CRC Press
Taylor & Francis Group
Boca Raton London New York

CRC Press is an imprint of the
Taylor & Francis Group, an **informa** business

Contents

PART I Computing and Nanoelectronic Devices

PART II Nanoscale Transistors

PART III Nanolithography

PART IV Optics of Nanomaterials

PART V Nanophotonic Devices

PART VI Nanoscale Lasers

35

Nanophotonics for Device Operation and Fabrication

Tadashi Kawazoe
The University of Tokyo

Motoichi Ohtsu
The University of Tokyo